frontiers | Research Topics

Advances in noise reduction and feature extraction of acoustic signal

Edited by
Govind Vashishtha and Rajesh Kumar

Published in
Frontiers in Physics

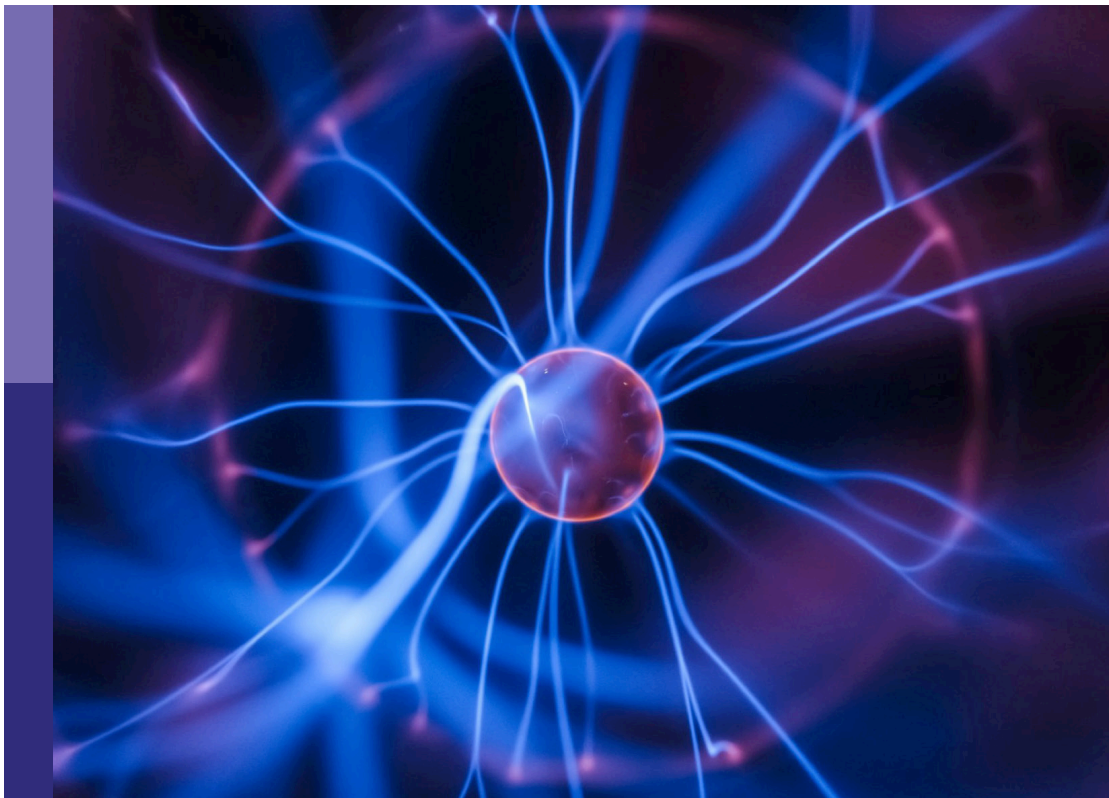

ISSN 1664-8714
ISBN 978-2-8325-3578-3
DOI 10.3389/978-2-8325-3578-3

About Frontiers

Frontiers is more than just an open access publisher of scholarly articles: it is a pioneering approach to the world of academia, radically improving the way scholarly research is managed. The grand vision of Frontiers is a world where all people have an equal opportunity to seek, share and generate knowledge. Frontiers provides immediate and permanent online open access to all its publications, but this alone is not enough to realize our grand goals.

Frontiers journal series

The Frontiers journal series is a multi-tier and interdisciplinary set of open-access, online journals, promising a paradigm shift from the current review, selection and dissemination processes in academic publishing. All Frontiers journals are driven by researchers for researchers; therefore, they constitute a service to the scholarly community. At the same time, the *Frontiers journal series* operates on a revolutionary invention, the tiered publishing system, initially addressing specific communities of scholars, and gradually climbing up to broader public understanding, thus serving the interests of the lay society, too.

Dedication to quality

Each Frontiers article is a landmark of the highest quality, thanks to genuinely collaborative interactions between authors and review editors, who include some of the world's best academicians. Research must be certified by peers before entering a stream of knowledge that may eventually reach the public - and shape society; therefore, Frontiers only applies the most rigorous and unbiased reviews. Frontiers revolutionizes research publishing by freely delivering the most outstanding research, evaluated with no bias from both the academic and social point of view. By applying the most advanced information technologies, Frontiers is catapulting scholarly publishing into a new generation.

What are Frontiers Research Topics?

Frontiers Research Topics are very popular trademarks of the *Frontiers journals series*: they are collections of at least ten articles, all centered on a particular subject. With their unique mix of varied contributions from Original Research to Review Articles, Frontiers Research Topics unify the most influential researchers, the latest key findings and historical advances in a hot research area.

Find out more on how to host your own Frontiers Research Topic or contribute to one as an author by contacting the Frontiers editorial office: frontiersin.org/about/contact

Advances in noise reduction and feature extraction of acoustic signal

Topic editors

Govind Vashishtha — Sant Longowal Institute of Engineering and Technology, India

Rajesh Kumar — Sant Longowal Institute of Engineering and Technology, India

Citation

Vashishtha, G., Kumar, R., eds. (2023). *Advances in noise reduction and feature extraction of acoustic signal*. Lausanne: Frontiers Media SA.

doi: 10.3389/978-2-8325-3578-3

Table of contents

05 Editorial: Advances in noise reduction and feature extraction of acoustic signal
Govind Vashishtha and Rajesh Kumar

07 Feature extraction method of ship radiated noise based on BOA-VMD and slope entropy
Yingmin Yi and Ge Tian

21 Present status and challenges of underwater acoustic target recognition technology: A review
Lei Zhufeng, Lei Xiaofang, Wang Na and Zhang Qingyang

28 A comparative study of four types of multi-scale entropies in feature extraction of underwater acoustic signals for potential GNSS positioning applications
Danning Zhao, Yu Lei, Jinsong Xu and Hongbing Cai

38 Revising the application of cross-spectrum processing in motion parameter estimation for harmonic sources
Ningning Liang, Jianbo Zhou and Yixin Yang

50 A new conjugate gradient algorithm for noise reduction in signal processing and image restoration
Pan Huang and Kaiping Liu

60 A simplified model for acoustic focalization in environments with seabed uncertainties
Ke Qu, Zhenyi Ou, Xin Huang and Liwen Liu

69 Feature extraction method of ship-radiated noise based on dispersion entropy: A review
Guanni Ji

78 Variational Bayesian cardinalized probability hypothesis density filter for robust underwater multi-target direction-of-arrival tracking with uncertain measurement noise
Boxuan Zhang, Xianghao Hou, Yixin Yang, Jianbo Zhou and Shengli Xu

89 A method of underwater sound source range estimation without prior knowledge based on single sensor in shallow water
Xiaoman Li, Hongyun Chen, Hongyu Lu, Xuejie Bi and Yaxiao Mo

102 Analysis of the synergistic complementarity between bubble entropy and dispersion entropy in the application of feature extraction
Xinru Jiang, Yingmin Yi and Junxian Wu

112 Triple feature extraction method based on multi-scale dispersion entropy and multi-scale permutation entropy in sound-based fault diagnosis
Nina Zhou and Li Wang

120 Adaptive noise suppression for low-S/N microseismic data based on ambient-noise-assisted multivariate empirical mode decomposition
Zhichao Yu, Yingkun Huang, Zisen Fang, Yuyang Tan and Chuan He

frontiers | Frontiers in Physics

TYPE Editorial
PUBLISHED 13 September 2023
DOI 10.3389/fphy.2023.1287956

OPEN ACCESS

EDITED AND REVIEWED BY
Michele Meo,
University of Southampton,
United Kingdom

*CORRESPONDENCE
Govind Vashishtha,
govindyudivashishtha@gmail.com

RECEIVED 03 September 2023
ACCEPTED 06 September 2023
PUBLISHED 13 September 2023

CITATION
Vashishtha G and Kumar R (2023), Editorial: Advances in noise reduction and feature extraction of acoustic signal. *Front. Phys.* 11:1287956. doi: 10.3389/fphy.2023.1287956

Editorial: Advances in noise reduction and feature extraction of acoustic signal

Govind Vashishtha [1,2]* and Rajesh Kumar [2]

[1]Faculty of Geoengineering, Mining and Geology, Wroclaw University of Science and Technology, Wroclaw, Poland, [2]Precision Metrology Laboratory, Department of Mechanical Engineering, Sant Longowal Institute of Engineering and Technology, Sangrur, India

KEYWORDS

acoustic signal, entropy, wavelet analysis, emprical mode decomposition, variational mode decomoposition (VMD)

Editorial on the Research Topic
Advances in noise reduction and feature extraction of acoustic signal

It is our pleasure to introduce the Research Topic on *advances in noise reduction and feature extraction of acoustic signals* in Frontiers in physics. Acoustic signal processing and its analysis is one of the hot topics of research in physics and has been studied by many engineers and scientists in various real-world fields, including underwater acoustics, architectural acoustics, engineering acoustics, physical acoustics, environmental acoustics, psychological acoustics, and so on. Noise reduction is the foundation of acoustic signal pre-processing in order to extract useful features from the acoustic signal, which is the linchpin for pattern recognition, target detection, tracking, and localization.

The real-world acoustic signals are usually non-linear and accompanied by intense background noise, and features extracted directly from these signals generally contain a large volume of useless as well as noisy information leading to ambiguous results. Therefore, the study of noise reduction methods of acoustic signals is the first step to effectively utilize this signal, including but not restricted to wavelet analysis, integrated empirical mode decomposition, variational mode decomposition, and consequential improvements. In addition, whether the extracted features contain sufficient useable information also determines the performance of the results of acoustic signal research. For weak signals present in many application areas, it is extremely difficult to precisely describe certain physical meanings of the signal utilizing specified features. In recent years, some researchers have used entropy to characterize the dynamics of the signal, but there are also issues such as missing scale and distance information as well as fractional order differential information. In a word, it is urgent to put forward more advanced features to solve the problem of missing information.

This Research Topic welcomed the research and review articles on advanced acoustic signal noise reduction and feature extraction in various fields. This Research Topic brought together a Research Topic of articles that addresses these challenges and/or showcase the latest real-world applications and enabling algorithmic advances in intelligent control and optimisation, as they pertain to system identification, intelligent control, and optimisation of dynamical systems.

The call for papers was launched in September 2022 and closed in April 2023. In total, 12 papers were finally selected for inclusion in the Research Topic.

Yi and Tian have utilised the butterfly optimization algorithm (BOA) to optimize the parameters of the variational mode decomposition. The proposed method BOA-VMD has also been incorporated with novel slope entropy for extracting the features from ship-radiated noise (SNR).

Zhufeng et al. presented advances in the mechanism of underwater target radiation noise generation and analyzed the research progress. Further, they applied machine learning in underwater target radiation applications from three perspectives: signal acquisition, feature extraction, and signal recognition. The authors elaborated the challenges of underwater target-radiated noise recognition technology against the backdrop of rapid computing science development.

Huang and Liu proposed a new conjugate gradient method for noise reduction in signal processing and image restoration. The superiority of this method lies in its employment of the ideas of accelerated conjugate gradient methods in conjunction with a new adaptive method for choosing the step size. The authors have demonstrated the effectiveness and superiority of the proposed method through numerical simulation.

Zhao et al. have used four types of multi-scale entropies, including multi-scale sample entropy (MSE), multi-scale fuzzy entropy (MFE), multi-scale permutation entropy (MPE), and multi-scale dispersion entropy (MDE) to extract more effective information from underwater acoustic signals.

Liang et al. introduced enhanced cross-spectrum processing to improve the computational efficiency of time-frequency analysis (TFA) for passive source localization and train-bearing fault diagnosis. Through results, it has been shown that an improvement up to 85% can be achieved without a noticeable impact on the accuracy of parameter estimates.

Qu et al. have shown the effect of parameter mismatch on source localization in cases involving environments and seabed uncertainties. To address these issues, the authors have developed the simplified seabed model for focalization using two geoacoustic parameters *viz.*, the amplitude F and phase of reflection C_F.

Li et al. proposed a method based on a single hydrophone that can jointly identify the mode order and estimate the propagation range in an unknown marine environment. The method uses Bayesian theory as the main methodology and applied to broadband pulse sound sources in shallow seas with long-range propagation. The dispersion curves extracted from the data and those calculated by the dispersion formula are the input signal and the replica of the methods, respectively. Accurate identification of the normal mode order and estimation of the propagation range can be achieved by establishing the joint cost function.

Zhang et al. proposed the robust underwater multi-target direction-of-arrival (DOA) tracking method to address the issues of typical multi-target problems under unknown underwater environments with missing detection, false alarms, and uncertain measurement noise.

Ji presented an exhaustive review of the research progress of dispersion entropy (DE) in the feature extraction of ship radiated noise (SRN). He first described the DE and its improved algorithms. Then the traditional and DE-based SRN feature extraction methods are summarized, and the application of DE in SRN feature extraction methods is concluded from two aspects: methods that apply DE algorithms only and methods that combine DE with mode decomposition algorithms.

Jiang et al. suggested that most researchers have ignored the relationship between one entropy with another. Inspired by this point, they proposed the synergistic relationship between bubble entropy (BE) and permutation entropy (PE). Through experimentation, it has been demonstrated that the synergistic complementarity between BE and PE increases the recognition rate of sea state signals by 10.5% and the recognition rate of bearing signals reaches 99.5%.

Zhou and Wang proposed the triple feature extraction and classification method based on multi-scale dispersion entropy (MDE) and multi-scale permutation entropy (MPE) to extract the features from the rolling bearing and used them in K nearest neighbour classification algorithm to determine whether there is a fault in the bearing and the type of the fault.

Yu et al. proposed an ambient-noise-assisted multivariate empirical mode decomposition (ANA- MEMD) method for adaptively suppressing noise in low signal-to-noise (S/N) microseismic data encountered during data processing.

Author contributions

GV: Writing–original draft, Writing–review and editing. RK: Methodology, Supervision, Visualization, Writing–original draft, Writing–review and editing.

Acknowledgments

We hope that this Research Topic will inspire readers to explore the possibilities in noise reduction and feature extraction of acoustic signals and to contribute to the ongoing efforts to create a more sustainable and equitable future. We would like to thank all the authors and reviewers who have contributed to the Research Topic. We would also like to express our gratitude to the Editor-in-Chief Prof. Alex Hansen and the Frontiers editorial team. Without their support, this Research Topic would not have been successful.

Conflict of interest

The authors declare that they have no known competing financial interests or personal relationships that could have appeared to influence the work reported in this paper.

Publisher's note

frontiers | Frontiers in Physics

TYPE Original Research
PUBLISHED 17 October 2022
DOI 10.3389/fphy.2022.1043070

OPEN ACCESS

EDITED BY
Govind Vashishtha,
Sant Longowal Institute of Engineering and Technology, India

REVIEWED BY
Sumika Chauhan,
National Institute of Technology Delhi, India
Xiaohui Yang,
Inner Mongolia University of Science and Technology, China
Xiao Chen,
Shaanxi University of Science and Technology, China

*CORRESPONDENCE
Ge Tian,
2220320083@stu.xaut.edu.cn

SPECIALTY SECTION
This article was submitted to Physical Acoustics and Ultrasonics, a section of the journal Frontiers in Physics

RECEIVED 13 September 2022
ACCEPTED 03 October 2022
PUBLISHED 17 October 2022

CITATION
Yi Y and Tian G (2022), Feature extraction method of ship radiated noise based on BOA-VMD and slope entropy.
Front. Phys. 10:1043070.
doi: 10.3389/fphy.2022.1043070

Feature extraction method of ship radiated noise based on BOA-VMD and slope entropy

Yingmin Yi[1,2] and Ge Tian[1]*

[1]School of Automation and Information Engineering, Xi'an University of Technology, Xi'an, China, [2]Shaanxi Key Laboratory of Complex System Control and Intelligent Information Processing, Xi'an University of Technology, Xi'an, China

Although the technical requirements for the feature extraction of ship radiated noise (SRN) in the fields of national defense and economy increase with each passing day, the complexity of the marine environment makes the feature extraction of SRN difficult. The traditional feature extraction method based on variational mode decomposition (VMD) is widely used in the feature extraction of SRN. Nevertheless, the use of VMD is greatly affected by parameters. In this paper, the butterfly optimization algorithm (BOA) is introduced to optimize VMD, which is called BOA-VMD algorithm, and realizes the optimal selection of VMD parameters K and α. To further improve the efficiency of feature extraction method, combined with slope entropy (SE), a feature extraction method of SRN based on BOA-VMD and SE is proposed. The experimental results of the simulated signal show that the BOA-VMD algorithm has a smaller envelope entropy value and better decomposition effect than the genetic algorithm (GA) and particle swarm optimization (PSO). The experimental results of feature extraction of SRN show that the highest recognition rate of the four entropy values improve with the increase of the number of extracted features, compared with the three entropy values of dispersion entropy (DE), fluctuation dispersion entropy (FDE) and permutation entropy (PE), the SRN feature extraction method based on BOA-VMD and SE has the highest recognition rate under different quantity features, and the recognition rate has reached 100% under three features.

KEYWORDS

ship radiated noise, slope entropy, feature extraction, variational mode decomposition, butterfly optimization algorithm

1 Introduction

Due to the complexity of the generation principle of underwater acoustic signals and the diversity of components, it is difficult to identify ship radiated noise (SRN) [1, 2]. The key to the recognition of SRN lies in the feature extraction method [3]. Traditional feature extraction methods usually use DEMON spectral analysis, wavelet transform, Fourier transform, empirical mode decomposition (EMD) and other signal processing algorithms, which are based on feature differences to classify and identify SRN. However, wavelet transform cannot guarantee time accuracy and frequency accuracy at the same time.

Fourier transform has trouble in dealing with non-stationary signals, and EMD has modal aliasing in the processing of SRN signals.

To overcome the above shortcomings, Konstantin Dragomiretskiy et al. proposed the variational mode decomposition (VMD) in 2014 [4], which adaptively decomposes the complex signal into several intrinsic mode functions (IMF), thereby overcoming the mode mixing [5, 6]. VMD is suitable for processing complex hydroacoustic signal, such as feature extraction of SRN [7]. However, its decomposition effect is greatly affected by the number of decompositions K and the penalty factor α. In order to solve the parameter selection problem of VMD, many scholars have combined intelligent optimization algorithms [8] with VMD [9–13], and proposed some modified algorithms for VMD, such as using genetic algorithm (GA) to optimize VMD in the field of SRN and using particle swarm optimization algorithm (PSO) to optimize VMD in the field of fault detection [14, 15]. These methods have proved to be able to solve the problem of parameter selection of VMD and improve the decomposition effect of VMD. In 2019, the butterfly optimization algorithm (BOA) [16] was proposed, which is a butterfly-based foraging strategy that uses its sense of smell to locate food. Compared with GA and PSO, BOA has higher convergence accuracy and faster convergence speed. However, it has not yet been applied to optimize the parameter selection of VMD.

In the field of underwater acoustic signal processing, entropy is used to describe the complexity of the time series and is often used as eigenvalues for feature extraction [17–20], among which permutation entropy (PE) [21], dispersion entropy (DE) [22], fluctuation dispersion entropy (FDE) [23] and others have been widely used in this field. Moreover, a large number of experimental studies have also proved that the entropy-based feature extraction method [24] is more effective than traditional methods [25–27]. Slope entropy (SE) [28], as a new type of entropy estimator, was proposed by David Cuesta-Frau in 2019. It assigns symbols based on the slope between two continuous data samples, and has good time series classification performance [29]. In 2022, SE was applied for the first time, and combined with PE to achieve double feature extraction of SRN [30], which verifies the effectiveness of SE. However, the feature extraction methods still are based on the original signal, and the features of each mode of the signal are not deeply excavated. To solve this problem, a method combining VMD and SE is proposed to extract the features of SRN [31], which is more effective than the method based on SE of the original signal. However, intelligent optimization algorithm has not been introduced to improve the decomposition efficiency of VMD.

In order to solve the parameters selection problem of VMD and further improve the feature extraction efficiency of SRN, BOA is introduced to optimize the parameters of VMD, called BOA-VMD, in addition, combined with SE, a feature extraction method of SRN based on BOA-VMD and SE is proposed. The structure of this paper is as follows. Section 2 expounds the principle and step of various algorithms used in this paper. Section 3 exhibits the steps of the feature extraction method proposed in this paper. In Section 4, the simulation signal decomposition experiment and result analysis are introduced. Section 5 demonstrates the experiment and result analysis of single feature, dual feature and three feature extraction of SRN. Finally, the last Section draws the conclusion of this paper.

2 Algorithm

2.1 Butterfly optimization algorithm-variational mode decomposition algorithm

Since the parameters K and α of VMD directly affect the result of signal decomposition, we add BOA to optimize the parameters selection of VMD, called the BOA-VMD. The fitness function of the BOA-VMD is the average envelope entropy value of all IMF components after decomposition. The smaller the envelope entropy value, the better the decomposition effect. On the contrary, the larger the envelope entropy value, the worse the decomposition effect. The expression for the average envelope entropy is as follows:

$$Y_i = \frac{1}{K}\sum_{j=1}^{K} H_{en}(j) \tag{1}$$

where, K represents the number of IMF components after decomposition, $H_{en}(j)$ is the envelope entropy value of the jth IMF component.

The expression for the envelope entropy value $H_{en}(j)$ of the signal p_j is as follows:

$$\begin{cases} H_{en}(j) = -\sum_{j=1}^{N} p_j \lg p_j \\ p_j = a(j) \Big/ \sum_{j=1}^{N} a(j) \end{cases} \tag{2}$$

where, N represents the sampling point, $a(j)$is the envelope signal obtained by Hilbert modulation of the signal IMF(j), and $p_j$denotes the normalized sequence of $a(j)$.

The algorithm steps of BOA-VMD are as follows:

(1) Set the range of parameters in VMD, with the parameter [K, α] as the position of the butterfly.
(2) Initialize the parameters in BOA, including population size G, number of iterations N, sensory modality C, stimulus intensity I, etc.
(3) Initialize the population, and use the average envelope entropy value of all IMF components as the fitness function for optimization.

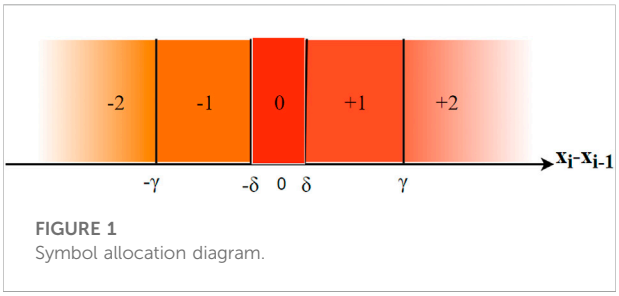

FIGURE 1
Symbol allocation diagram.

(4) Calculate the fitness value of each butterfly under VMD decomposition, compare the size of the fitness value, and update the range of parameters $[K, \alpha]$ and the position and fragrance of the butterfly.
(5) Repeat step (4) until the number of iterations reaches the set maximum value, and output the optimal parameter combination $[K, \alpha]$ of VMD.

2.2 Slope entropy

SE, as a new type of entropy estimator, was proposed by David Cuesta-Frau in 2019. Its purpose is to solve the problem that the time series amplitude information is ignored in the calculation of permutation entropy. SE uses a new encoding method that is based on the slope of two consecutive data samples and maintains the symbolic representation of subsequences. The SE contains five symbols, namely (± 2), (± 1), and 0. The configuration rule of symbols stipulates that the horizontal increment between consecutive samples is 1, and the vertical increment, that is, the difference, is represented by the parameter γ threshold. In this paper, γ is taken as 1 (45°). It is represented by the parameter δ threshold near 0, and the value of δ in this paper is 1×10^{-3}.

For two continuous values x_i, x_{i-1} in a continuous time series, if $x_i - x_i > +\gamma$, the sign is +2; if $+\delta < x_i - x_{i-1} \leq +\gamma$, the sign is +1; if $|x_i - x_{i-1}| \leq \delta$, the sign is 0; if $-\gamma \leq x_i - x_{i-1} \leq -\delta$,

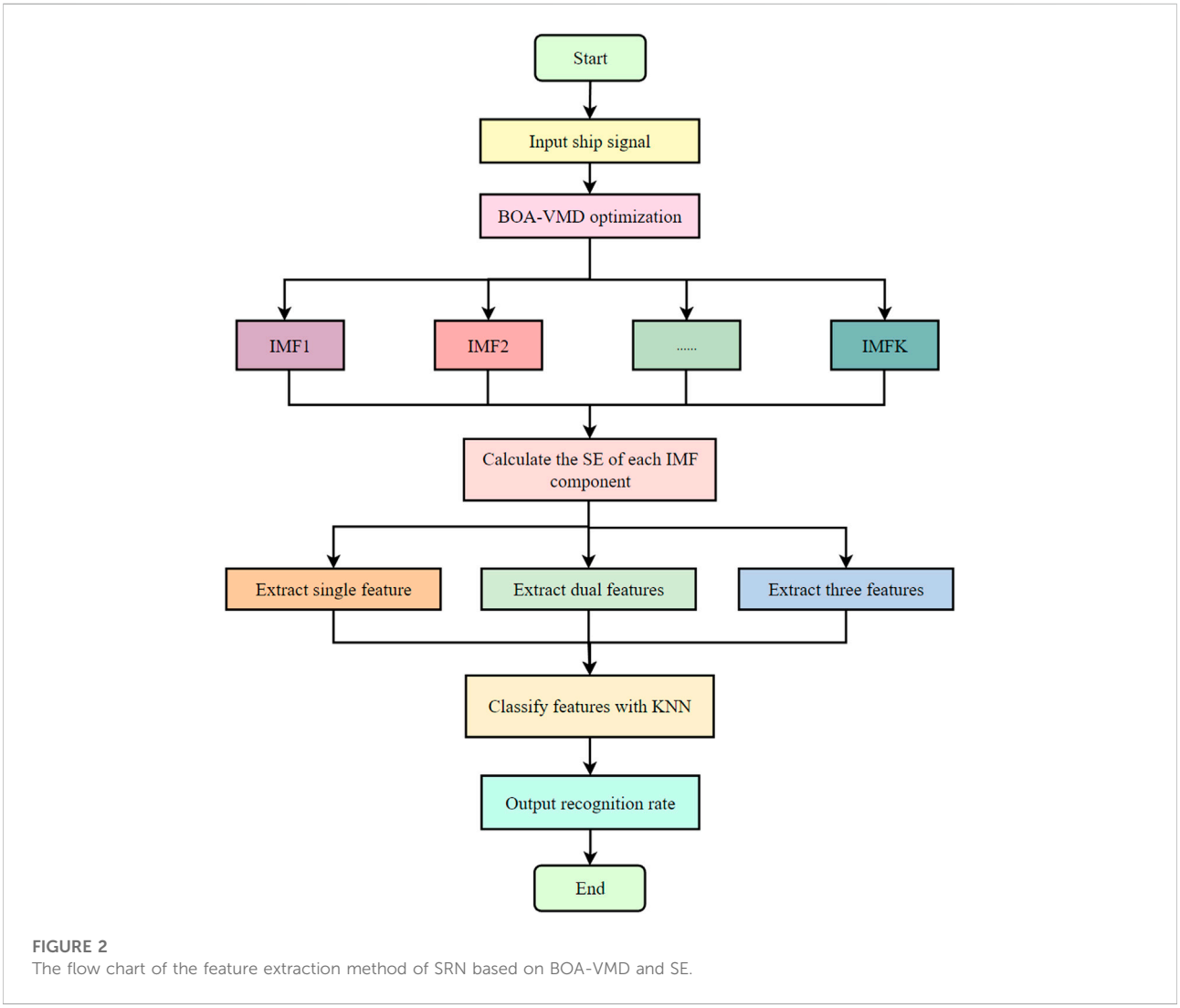

FIGURE 2
The flow chart of the feature extraction method of SRN based on BOA-VMD and SE.

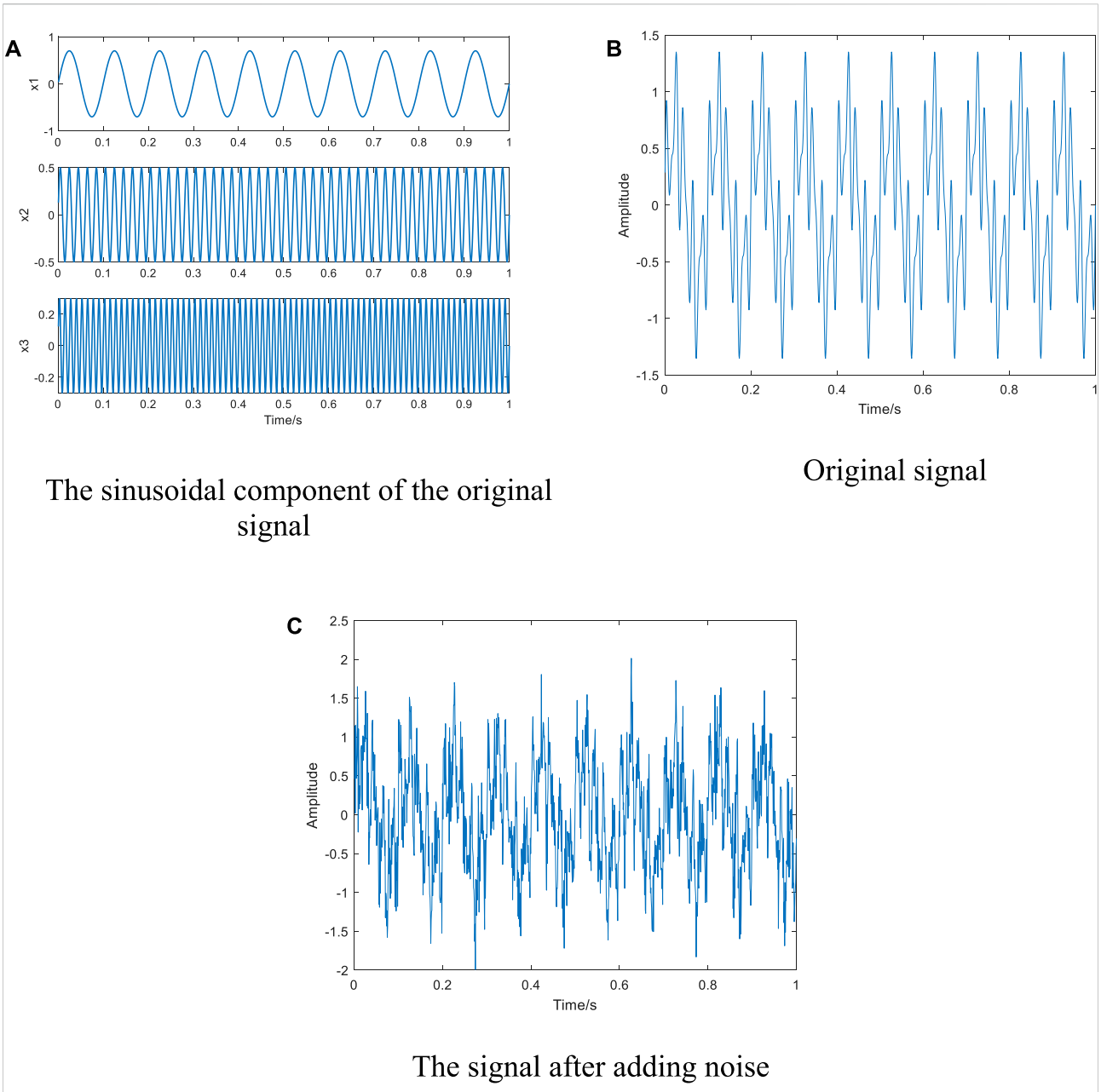

FIGURE 3
The waveform of the simulated signal: **(A)** The sinusoidal component of the original signal; **(B)** Original signal; **(C)** The signal after adding noise.

the sign is −1; if $x_i - x_{i-1} < -\gamma$, the sign is −2. The symbol allocation diagram is shown in Figure 1.

The symbols cover the range of slopes of line segments for two consecutive input data samples, and the relative frequency of each pattern found is then mapped to a true value using the method of Shannon entropy. The calculation steps are as follows.

(1) Input a time series of length N: $X = \{x_1, x_2, x_3 \dots x_N\}$, set the embedding dimension to m, so that K subsequences of length m can be extracted:$X_1 = \{x_1, x_2 \dots x_m\}$, $X_2 = \{x_2, x_3 \dots x_{m+1}\}$ $\dots$ $X_k = \{x_k, x_{k+1} \dots x_N\}$,where $k = N - m + 1$

(2) Calculate $x_i - x_{i-1}$, and then compare the calculated results with γ and δ by the principle of symbol assignment to obtain the k new sequences. The new sequence is:$S_1 = \{s_1, s_2 \dots s_{m-1}\}$, $S_2 = \{s_2, s_3 \dots s_m\} \dots S_k = \{s_k, s_{k+1} \dots s_{N-1}\}$.Where $k = N - m + 1$, $s_k = x_{k+1} - x_k$. The new sequence contains $n = 5^{m-1}$ of different types, and the number of occurrences of each type is $k_1, k_2 \dots k_n$.

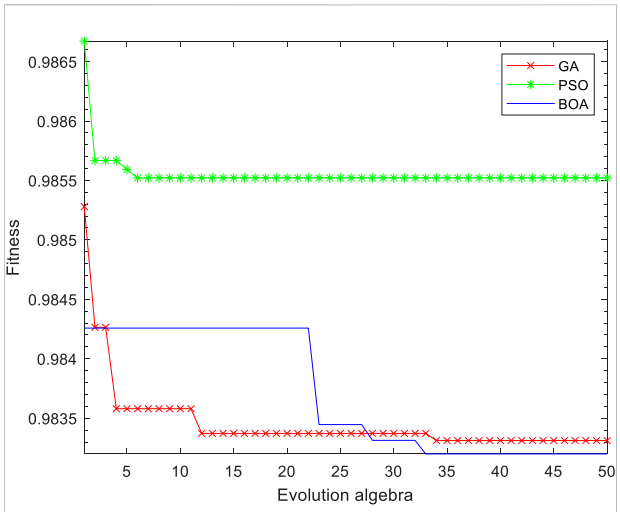

FIGURE 4
The iteration results of the three types of optimization algorithms.

TABLE 1 Optimization results of three types of optimization algorithms.

Optimal results	Optimization		
	GA	PSO	BOA
Iteration time	404.14s	324.98s	399.35s
Min envelope entropy	0.9842	0.9848	0.9832
[K, α]	[8,1393]	[8,919]	[6,1541]

(3) Calculate the probability of each type, $P_1 = \frac{k_1}{k}$, $p_2 = \frac{k_2}{k} \ldots P_n = \frac{k_n}{k}$. On the basis of Shannon entropy, the definition formula of SE is as follows.

$$H_s(m) = -\sum_{j=1}^{n} P_j \ln P_j \tag{3}$$

3 Feature extraction method

In this section, the BOA-VMD is proposed to select the best parameter combination of VMD, and combined with SE, we propose a feature extraction method based on BOA-VMD and SE to extract single, dual and three features of SRN.

The flow chart of the feature extraction method of SRN based on BOA-VMD and SE is shown in Figure 2. The specific implementation steps of the proposed feature extraction method for SRN are as follows:

(1) Different types of SRN signals are input and normalized.
(2) The SRN is decomposed by the BOA-VMD algorithm, and K IMF components are obtained.
(3) The SE of each decomposed IMF component is calculated.
(4) SE is taken as the feature value, the feature extraction experiments of single feature, dual feature and three feature are carried out respectively.
(5) The KNN classifier is introduced for classification of feature values.
(6) The recognition rate is obtained.

4 Simulation

Two parameters of VMD, namely the number of decompositions K and the penalty factor α, will affect its decomposition effect. In this section, a set of simulation signals are set up to optimize VMD parameters by BOA, GA and PSO, and the optimization results of the three optimization algorithms are compared and analyzed.

4.1 Simulation signal

To verify the optimization effect of the three optimization algorithms on VMD parameters, a set of simulation signals are set up for analysis, and the specific expressions are as follows:

$$X = x_1 + x_2 + x_3 \tag{4}$$

$$\begin{cases} x_1 = 0.7\sin(2\pi f_1 t) \\ x_2 = 0.5\sin(2\pi f_2 t) \\ x_3 = 0.3\sin(2\pi f_3 t) \end{cases} \tag{5}$$

$$Y = X + f \tag{6}$$

here, X is the original signal, which consists of three sinusoidal components with different amplitudes and center frequencies, x_1, x_2 and x_3. f_1, f_2, f_3 are the center frequencies of each sinusoidal component, $f_1 = 10$ Hz, $f_2 = 50$ Hz, $f_3 = 80$ Hz. f is Gaussian white noise, and Y is the noise-added signal with a signal-to-noise ratio of 6 dB after adding noise.

Figure 3 shows the waveform of the simulated signal. It can be seen from the figure that the time-domain waveform of the noise-added signal is complex, so signal decomposition is required.

4.2 Parameter optimization variational mode decomposition

In this section, BOA-VMD is used to optimize the modal component $K$and the penalty factor α. To verify the effect of the BOA-VMD algorithm, the optimization experiments of GA and PSO on VMD parameter selection are designed, so as to carry out comparison and analysis. For the convenience of comparison, the

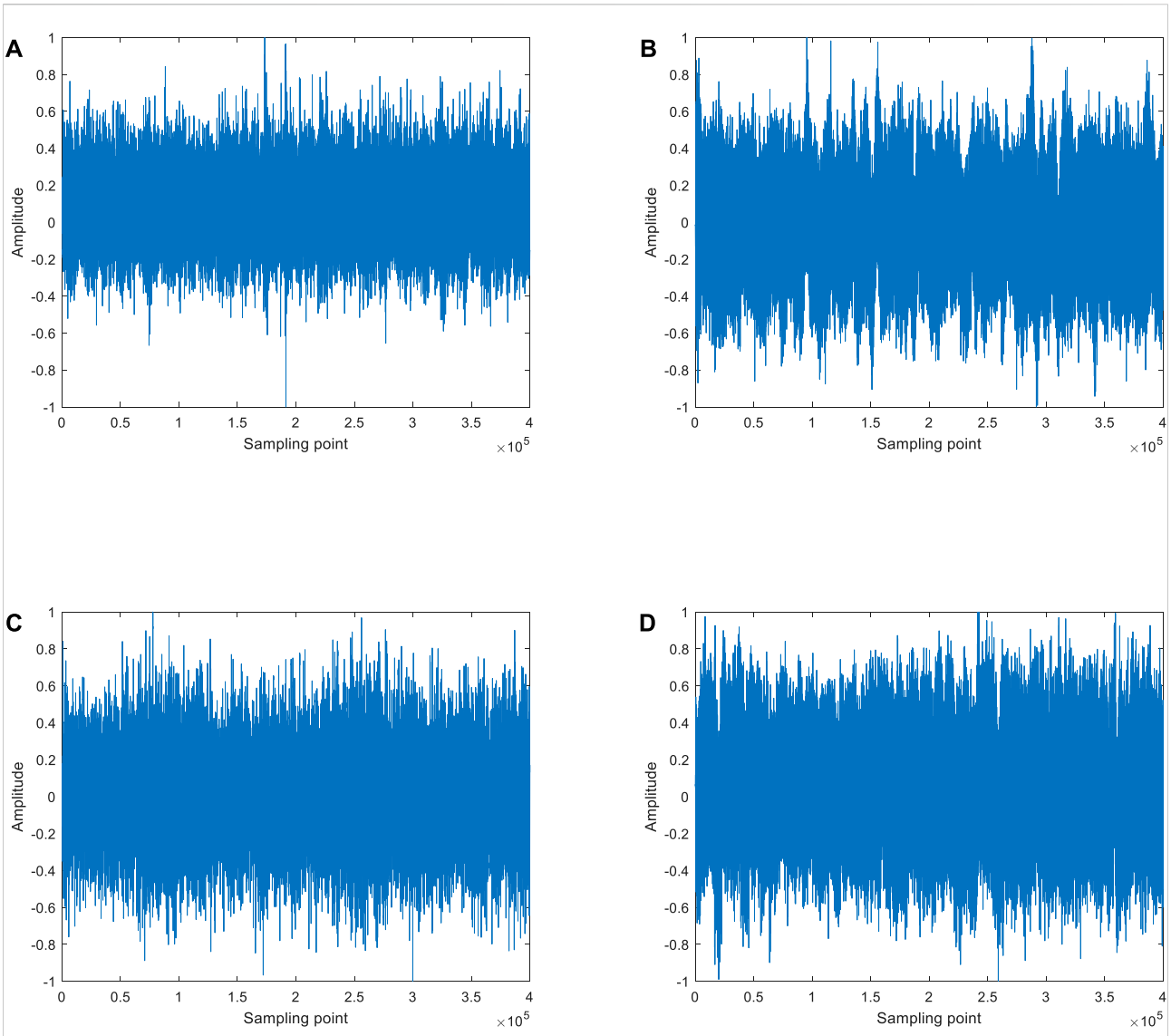

FIGURE 5
The normalized four types of SRN: **(A)** SRN-I; **(B)** SRN-II; **(C)** SRN-III; **(D)** SRN-IV.

initial population of the three optimization algorithms is 10, and the number of iterations is 50.

After several optimizations for the three types of algorithms, the average value of the iteration time and the minimum envelope entropy value are obtained. The iteration results of the three types of optimization algorithms are shown in Figure 4.

From Figure 4, it can be concluded that GA and BOA begin to converge after about the 35th iteration, and PSO begins to converge after about the 6th iteration. The convergence speed of PSO is much faster than that of BOA and GA. BOA has the smallest fitness value, which is about 0.9820, while the minimum fitness value of PSO and GA is approximately 0.9850 and 0.9830, which are larger than BOA.

By calculating the iteration time and minimum envelope entropy of the three types of optimization algorithms for comparison, the optimization results of the three types of optimization algorithms are shown in Table 1.

As shown in Table 1, PSO has the least iteration time and GA has the most iteration time, that is, PAO has the fastest optimization speed. But in terms of optimization results, BOA has the smallest envelope entropy value, which is 0.9832. The minimum envelope entropy values of GA and PSO are bigger than BOA. The experimental results show that BOA's optimization speed is second only to that of PSO, and has the smallest envelope entropy value. Considering comprehensively, the parameter combination obtained by BOA search is the most reliable.

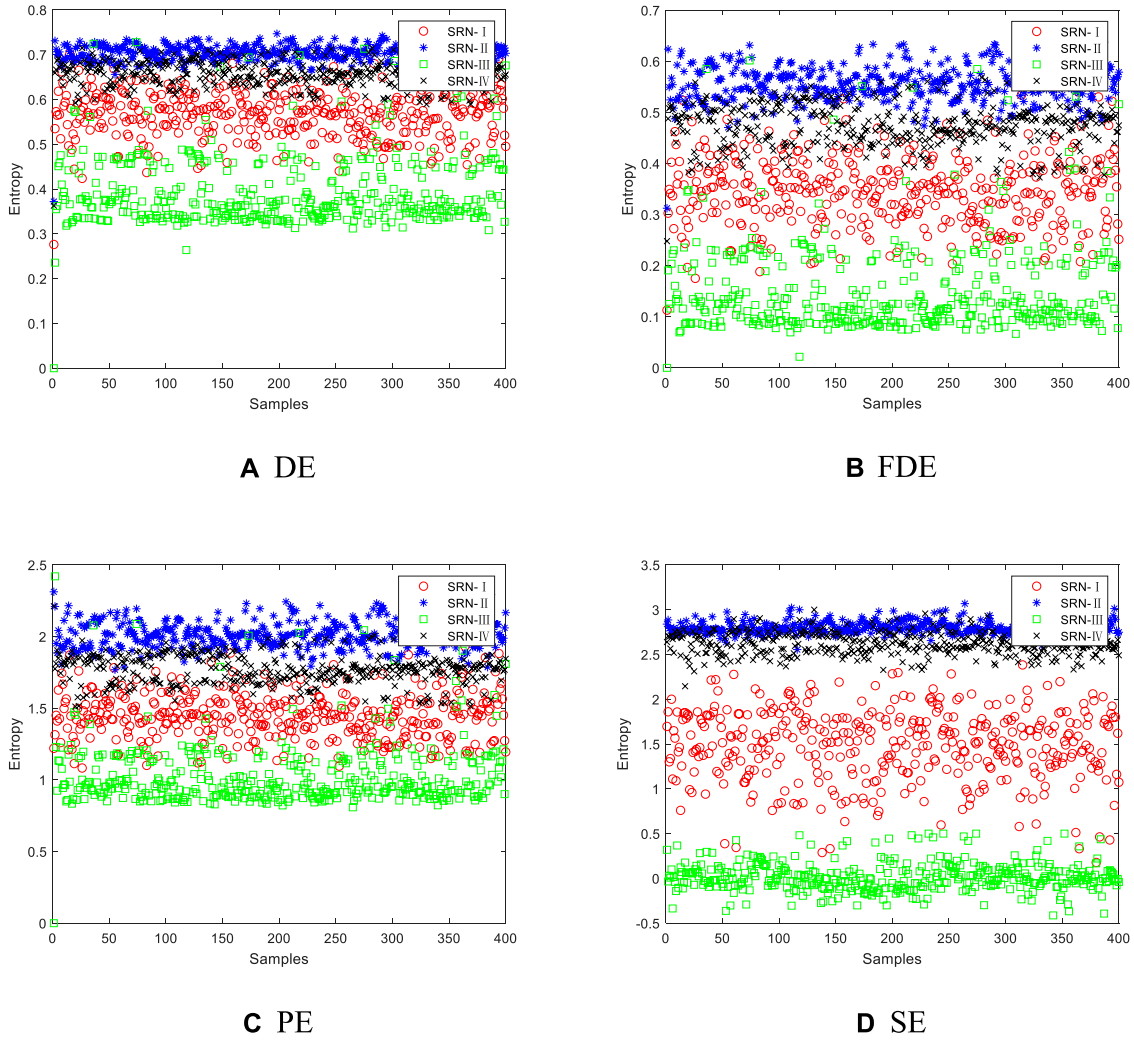

FIGURE 6
Single feature distribution of the IMF corresponding to the highest classification accuracy of the four types of SRN. **(A)** DE **(B)** FDE **(C)** PE **(D)** SE.

5 Experiment on feature extraction of ship radiated noise

This section uses four types of SRN from the United States Park Service, which are ferries, freighters, cruise ships, and engine-driven ships [32]. The four types of SRN are coded as SRN-I, SRN-II, SRN-III, and SRN-IV. The data lengths of the four types of SRN are 1379568, 1641072, 5314800, and 446448, respectively. Each SRN sampling segment is [3001, 403000], containing 400,000 data points, and the sampling frequency is 44100Hz. The normalized four types of SRN are shown in Figure 5.

According to the BOA-VMD algorithm proposed in Section 3, the VMD decomposition results of four types of SRN are optimized. The optimal number of IMF $K$is 9, and the penalty factors α are 6165, 1000, 5746 and 4374, respectively.

5.1 Single feature extraction and classification

5.1.1 Single feature extraction

In this single feature extraction experiment, 400 samples are selected for each type of SRN with 3001 as the starting point, and each sample contains 1000 data points. In order to compare with SE, FDE, DE and PE of each IMF are calculated at the same time. All entropies have two parameters in common, the embedding dimension m is set to 4 and delay time τ is set to 1. There are two common parameters of DE and FDE, which are the number of categories c is set to 3, and the mapping method uses NCDF. SE has two thresholds that need to be set, where γ is set to 0.1666 and $\delta$is set to 0.0222. Figure 6 shows the single feature distribution of the IMF corresponding to the highest classification accuracy of the four types of SRN.

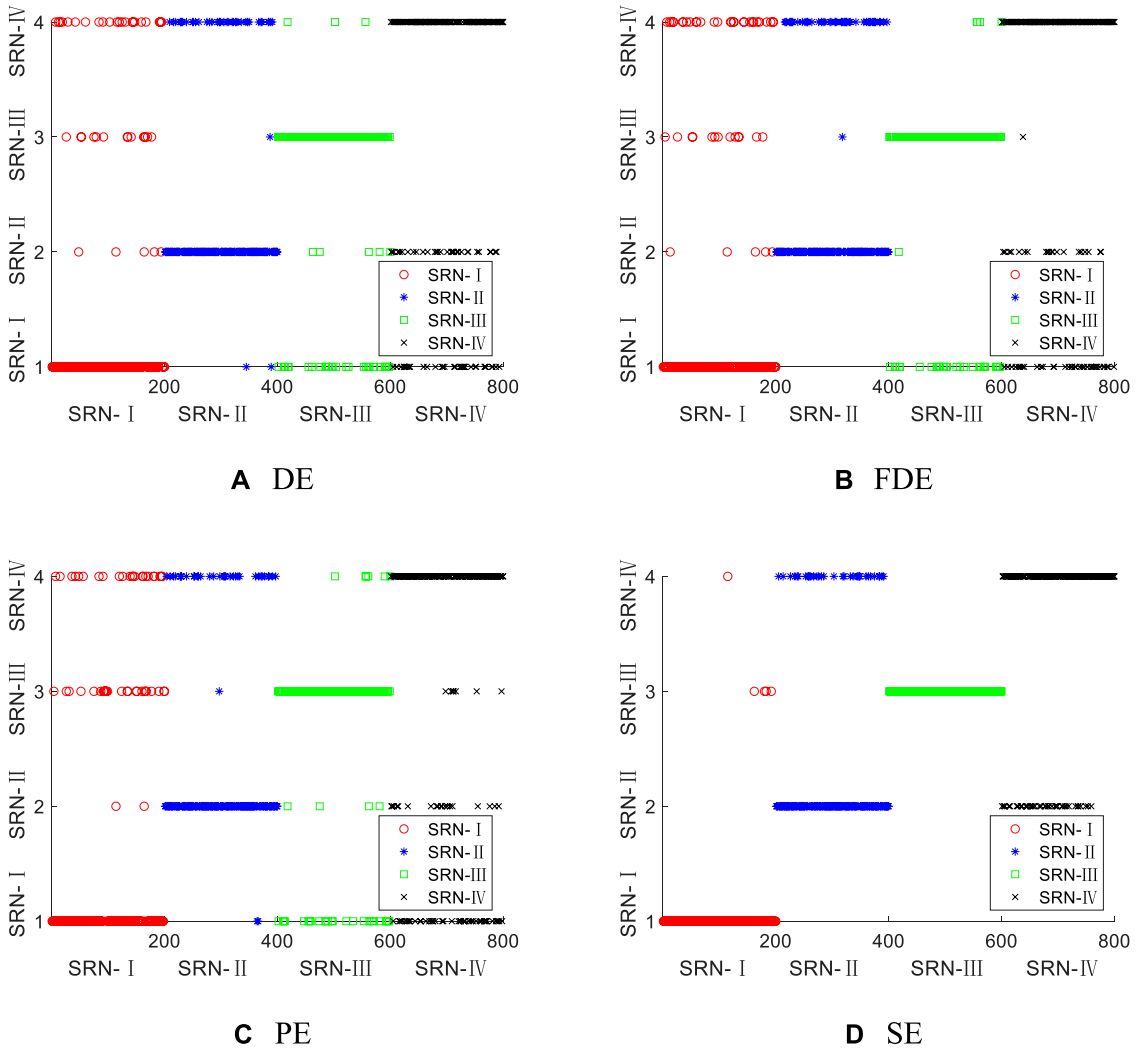

FIGURE 7
Single feature classification results of four types of entropy for four types of SRN. **(A)** DE **(B)** FDE **(C)** PE **(D)** SE.

It can be gained from Figure 6 that the single feature distributions of the four types of SRN all fluctuate within a certain range, and the DE mixing of SRN-II and SRN-IV is the most serious; DE, FDE and PE of SRN-I and SRN-III have different degrees of aliasing, and only a few samples of their SE are aliased; the FDE of SRN-I and SRN-IV is the most aliased, and their SE has only very little eigenvalue mixing. Experiments show that SE is the best for feature extraction of the four types of SRN.

5.1.2 Single feature classification

A KNN classifier is added to perform single-feature classification of four types of SRN [33, 34]. For the four types of SRN, 400 samples are selected, the first 200 samples are taken as training samples, and the remaining 200 samples are used as test samples for classification. Figure 7 shows the single feature classification results of four types of entropy for four types of SRN.

As shown in Figure 7, DE, FDE, PE and SE have different degrees of error in the classification of the four types of SRN samples; DE, FDE and PE have more classification errors for SRN-I, SRN-II and SRN-IV samples, but less for SRN-III samples; this indicates that DE, FED and PE have a stronger ability to identify SRN-III samples than the other three samples; compared with these three types of features, the SE has only four wrong classifications for SRN-I, and all the classifications for SRN-III are correct; this suggests that SE has the strongest recognition ability for SRN-III samples, but poor recognition ability for SRN-II and SRN-IV, which is stronger than the other three features. Experiments show that SE is better than DE, FDE and PE for

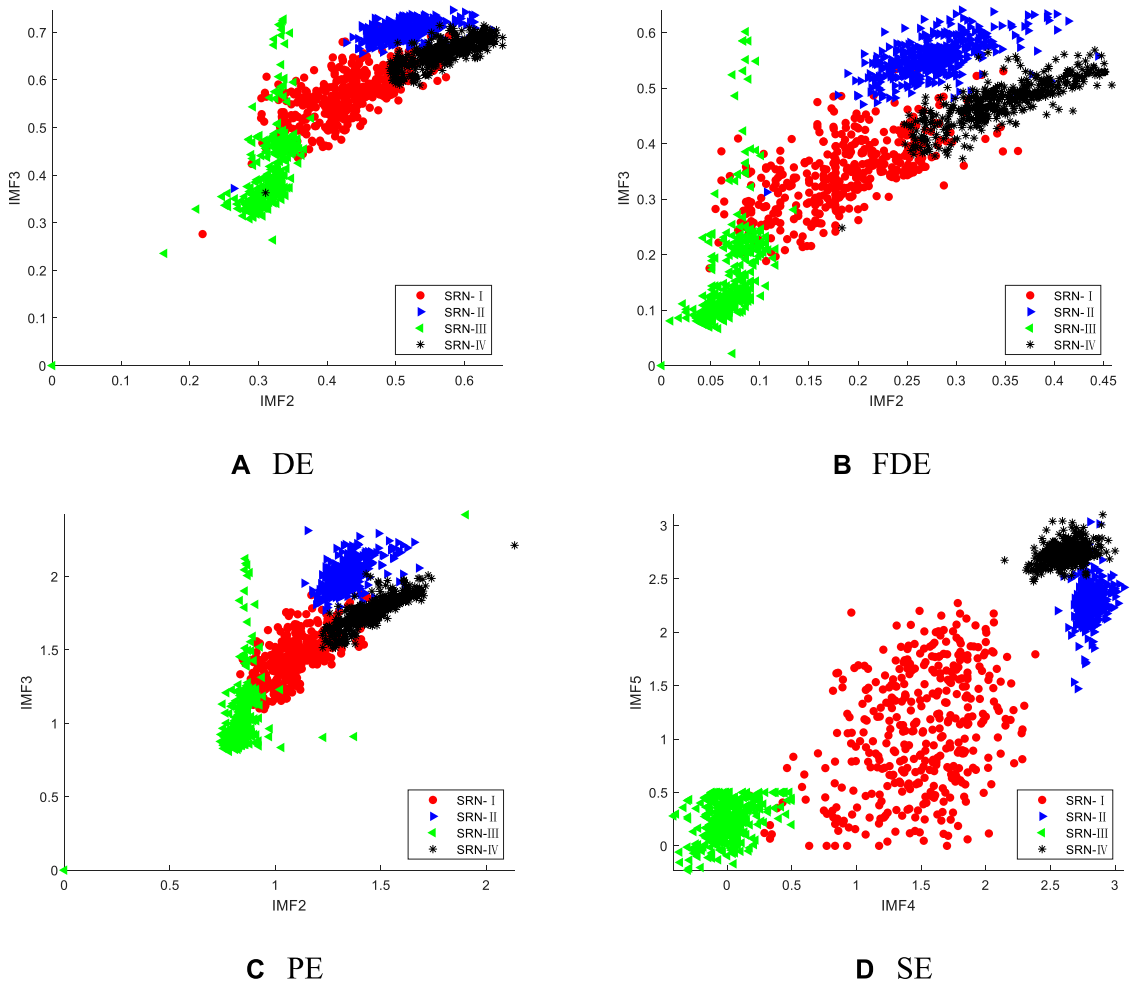

FIGURE 8
Dual feature distribution of the IMF combination corresponding to the highest recognition accuracy of the four types of SRN. **(A)** DE **(B)** FDE **(C)** PE **(D)** SE.

TABLE 2 The highest average recognition rate of four kinds of entropy under single-feature.

Entropy	Average recognition rate (%)
DE	76.88
FDE	76.75
PE	76.38
SE	90.38

the classification of the four types of SRN. The highest average recognition rate of the four types of entropy under single-feature is shown in Table 2.

According to Table 2 can be obtained that the highest recognition rate of SE is 90.38%. Among DE, FDE and PE, the highest recognition rate did not exceed 80%. The highest recognition rates corresponding to DE, FDE and PE are 13.5%, 13.63%, and 14% lower than the highest recognition rates for SE, respectively. The experimental results show that under single feature extraction, the average recognition rate of SE is the highest compared with the other three entropies.

However, under single feature extraction, there are still many samples of four types of entropy that are not correctly identified and classified, and only the highest recognition rates of SE reach more than 90%. To further improve the recognition rates, we adopt dual feature extraction, that is, identifying two IMF components at the same time.

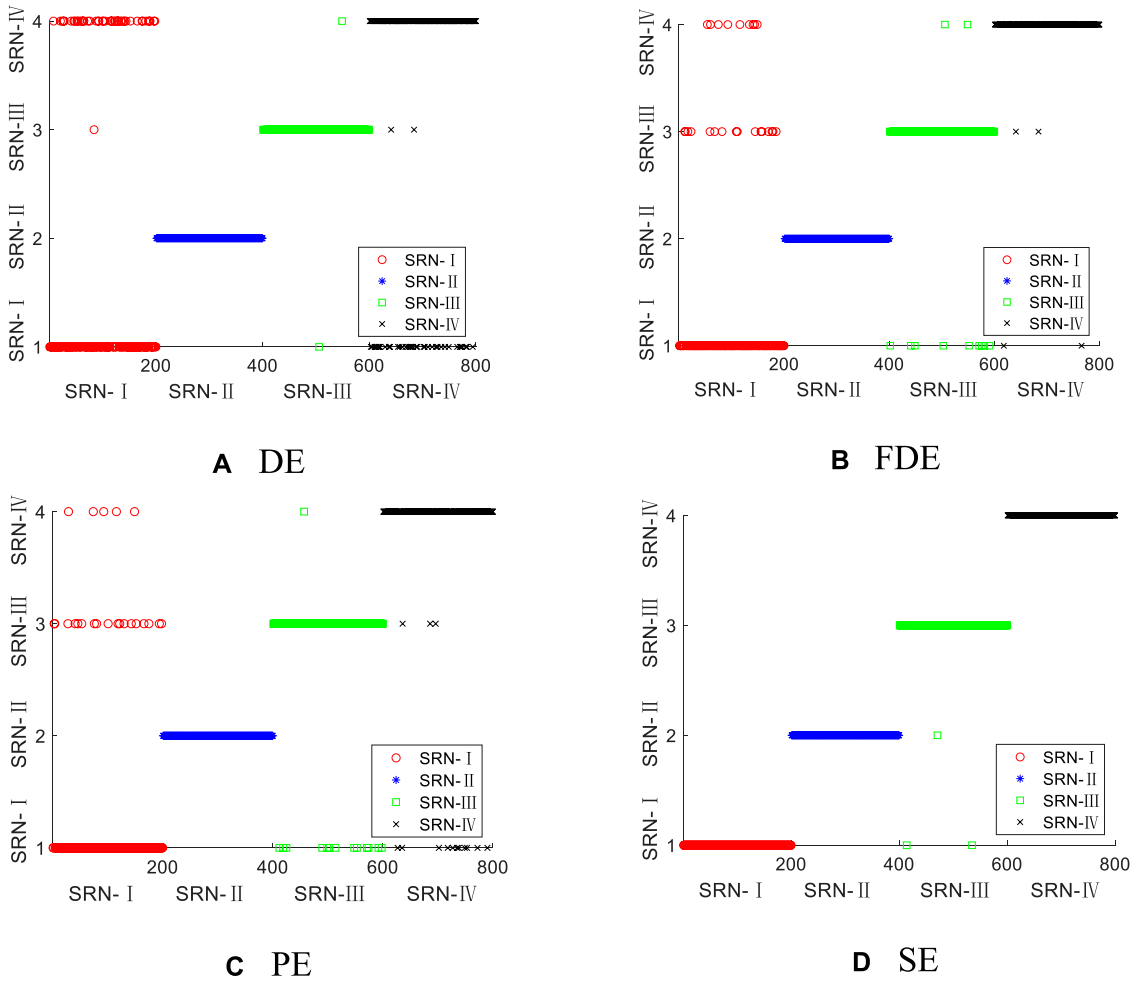

FIGURE 9
Dual feature classification results of four types of entropy for four types of SRN. **(A)** DE **(B)** FDE **(C)** PE **(D)** SE.

5.2 Dual feature extraction and classification

5.2.1 Dual feature extraction

In the dual feature extraction experiment, all parameters used in the experiment are the same as the data listed in Section 5.1. According to the principle of permutation and combination, the IMF components are combined in pairs, and a group of IMF components with the highest recognition rate is selected for feature extraction. Figure 8 shows the dual feature distribution of the IMF combination corresponding to the highest recognition accuracy of the four types of SRN, where the abscissa and ordinate are the corresponding IMF components.

From Figure 8 we can obtain that, the mixing phenomenon of entropy value of the four types of SRN is significantly reduced under dual feature extraction; compared with the entropy values of the other three types of samples, the SRN-III samples have obvious differences; in DE, FDE and PE, the SRN-I sample is close to the other three types of samples in terms of partial entropy, which may lead to errors in sample identification; the entropy values of the four types of samples in SE are significantly different, which is easier to distinguish in sample identification. Experiments show that, compared with the other three types of features, the SE has better separability for the four types of SRN samples.

5.2.2 Dual feature classification

In order to prove that the identification effect of simultaneously identifying the SE of two IMF components is better under dual feature extraction, KNN classifier is also adopted to perform dual feature extraction classification of four types of SRN. The selection of training samples and test samples is the same as in Section 5.1. The dual feature classification results of the four types of entropy for four types of SRN are shown in Figure 9.

It can be seen from Figure 9 that under the dual feature extraction, the four types of entropy have improved the classification accuracy for the four types of SRN samples, and

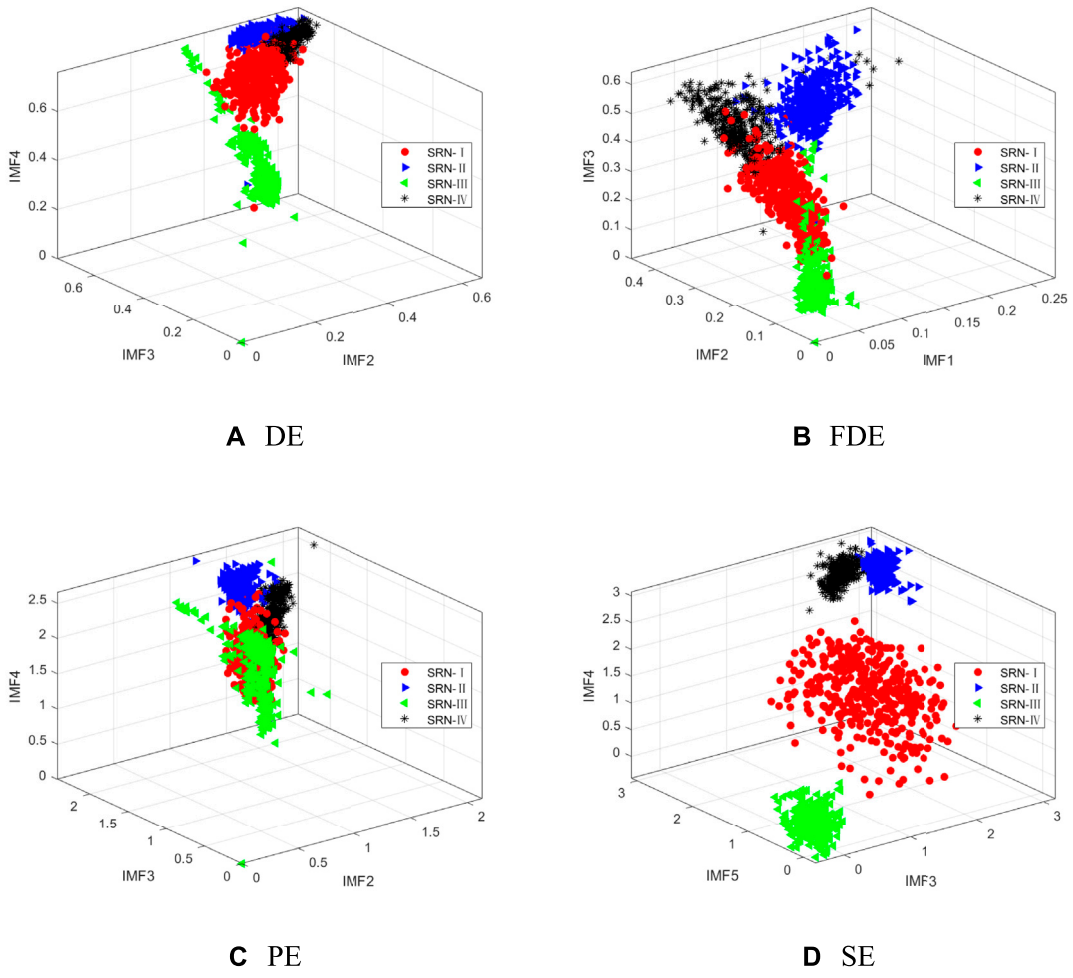

FIGURE 10
Three-feature distribution of the IMF combination corresponding to the highest recognition accuracy of the four types of SRN. **(A)** DE **(B)** FDE **(C)** PE **(D)** SE.

TABLE 3 The highest average recognition rates of the four entropies under dual features.

	DE	FDE	PE	SE
Selected IMF component	(2,3)	(2,3)	(2,5)	(3,4)
Average recognition rate (%)	97.50	95	93.63	99.63

the SE samples have the highest classification accuracy; the classification of SRN-II samples in DE, FDE and PE is completely correct, but some errors are found in SRN-I, SRN-III and SRN-IV samples; in SE, only three samples of SRN-III are classified incorrectly, and the other three SRN samples are classified correctly. Through program operation, the highest average recognition rates of the four entropies under dual features are shown in Table 3, where (2, 3) in the table represents the selected modal components are IMF2 and IMF3, and so on.

As can be seen from the data in Table 3, the recognition rates of the four types of entropy for SRN all reach more than 90%. The SE has the highest recognition rate for the four types of SRN, up to 99.63%, which is 2.13%, 4.63%, and 6% higher than the recognition rates of DE, FDE and PE, respectively. This shows that the recognition effect of SE is the most significant.

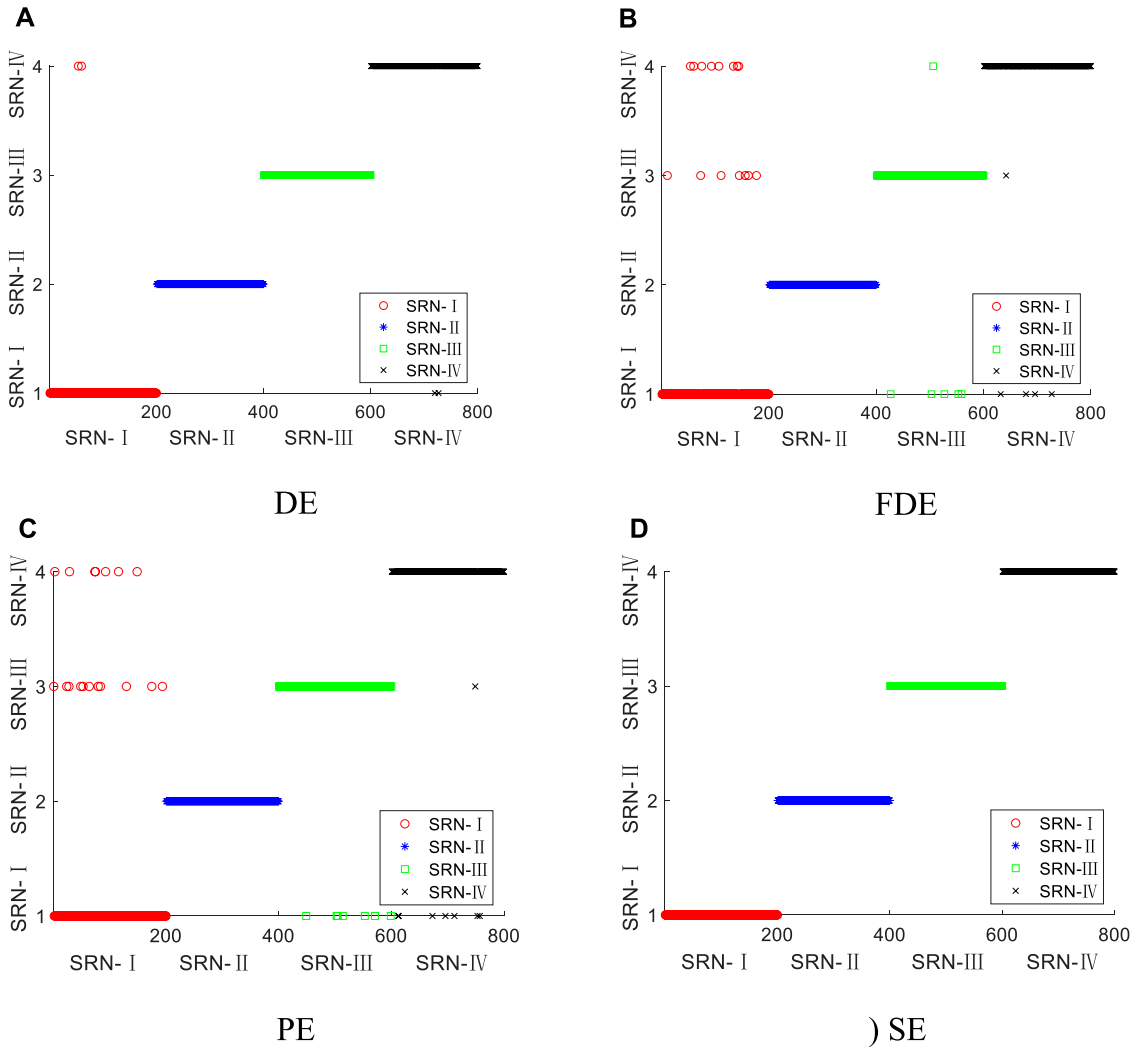

FIGURE 11
Three-feature classification results of the four types of entropy for the four types of SRN. **(A)** DE **(B)** FDE **(C)** PE **(D)** SE.

To sum up, under dual feature extraction, although there are still some sample errors in the classification for the four types of SRN samples by the four types of entropy, the average recognition rate is greatly improved compared with the single feature extraction. The highest average recognition rate under dual feature extraction is still SE, which is 9.25% higher than the average recognition rate of 90.38% under single feature extraction.

5.3 Three feature extraction and classification

5.3.1 Three feature extraction

In view of the fact that the recognition rate of four kinds of entropy in dual feature extraction is greatly improved compared with single feature extraction, SE still has the highest recognition rate. Therefore, in order to further improve the recognition rate, this section classifies the four types of SRN by identifying the three IMF components. All parameters used in the experiment are the same as the data listed in Section 5.1. In the three-feature extraction experiment, according to the principle of permutation and combination, three IMF components are selected for combination, and a group of IMF components with the highest recognition rate is selected for feature extraction. Figure 10 shows the three-feature distribution of the IMF combination corresponding to the highest recognition accuracy of the four types of SRN, where the x, y, and z coordinates are the corresponding IMF components.

As shown in from Figure 10, under the three-features extraction, the SRN-I, SRN-II and SRN-IV samples in the DE and the FDE have

partial entropy distributions overlapping, the SRN-III sample has a small amount of entropy mixed with SRN- I distribution; the four types of SRN in the PE have partial entropy aliasing; in the SE, only a few samples of SRN-II and SRN-IV have close entropy values. Experiments show that under the three-feature extraction, for the four types of SRN samples, the difference in the entropy value of the SE is the most obvious, so it has better distinguishing ability than the other three types of features.

5.3.2 Three feature classification

In order to prove that the identification effect of SE is better under three-feature extraction, KNN classifier is also introduced to perform three-feature classification of four types of SRN. The selection of training samples and test samples is the same as that in Section 5.1. The three-feature classification results of the four types of entropy for the four types of SRN are shown in Figure 11.

It can be seen from Figure 11 that under the three-feature extraction, the classification and recognition ability of the four types of entropy is greatly improved; the DE classification of SRN-II and SRN-III samples is completely correct, and only a few samples have errors in the DE classification of SRN-I and SRN-IV; the FDE and PE are completely correct for the classification of SRN-II samples, but some samples are wrong for SRN-I, SRN-III and SRN-IV; the classification of the four types of SRN samples by the SE is all correct. Experiments show that, compared with DE, FDE and PE, SE has a better ability to distinguish four types of SRN.

Through program operation, the highest average recognition rates of the four types of entropy under three-feature are shown in Table 4, where (1, 2, 7) in the table represents the selected IMF components are IMF1, IMF2 and IMF7, and so on.

From the data in Table 4, we can get that under the three-feature extraction, the four types of entropy have more than 95% recognition rates for SRN samples. Among them, the SE has the highest recognition rate of 100%, which is much higher than the SE under the single feature, and is also higher than the SE under the dual feature.

To sum up, under three feature extraction, the four types of entropy can greatly improve the recognition rate for the four types of SRN samples, and the classification performance of the SE is better than other entropies.

6 Conclusion

In this paper, BOA algorithm is introduced to realize the optimization of VMD parameters selection, and then BOA-VMD algorithm is proposed. Combined with the SE, a feature extraction method of SRN based on BOA-VMD and SE is proposed. The feasibility of the method is verified by simulation experiments and features extraction experiments of four SRNs. The main conclusions reached are as follows:

(1) In order to achieve the optimal selection of VMD parameters, the BOA algorithm is adhibited to optimize the VMD, called BOA-VMD. Compared with GA and PSO, the algorithm is more accurate and reliable, and can realize adaptive decomposition of signals in simulation experiments.
(2) In order to improve the effect of feature extraction and classification of SRN, this paper proposes a feature extraction method based on BOA-VMD and SE. Under single feature, the method achieves a remarkable effect on feature extraction, and the average recognition rate of SE is 90.38%, which is much higher than DE, FDE and PE.
(3) Compared with single feature, dual features and three features further improve the recognition rate of SRN. Compared with the other three entropies, the feature extraction method based on BOA-VMD and SE can obtain the highest recognition rate under the same number of features, furthermore, the three-feature recognition rate has reached 100%.

TABLE 4 The highest average recognition rates of four kinds of entropy under three-feature.

	DE	FDE	PE	SE
Selected IMF component	(2,3,4)	(1,2,3)	(2,3,4)	(2,4,5)
Average recognition rate (%)	99.50	96.75	95.88	100

Data availability statement

The original contributions presented in the study are included in the article/Supplementary Material; further inquiries can be directed to the corresponding author.

Author contributions

YY and GT designed research, performed research, and analyzed data, and GT wrote the paper.

Funding

Key Research and Development Plan of Shaanxi Province (2020ZDLGY06-01) Key Scientific Research Project of Education Department of Shaanxi Province (21JY033) Science and Technology Plan of University Service Enterprise of Xi'an (2020KJRC0087).

Conflict of interest

The authors declare that the research was conducted in the absence of any commercial or financial relationships that could be construed as a potential conflict of interest.

Publisher's note

References

1. Wang S, Zeng X. Robust underwater noise targets classification using auditory inspired time–frequency analysis. *Appl Acoust* (2014) 78:68–76. doi:10.1016/j.apacoust.2013.11.003

2. Yang S, Li Z, Wang X. Ship recognition via its radiated sound: The fractal based approaches. *The J Acoust Soc America* (2002) 112(1):172–7. doi:10.1121/1.1487840

3. Esmaiel H, Xie D, Qasem ZAH, Sun H, Qi J, Wang J. Multi-stage feature extraction and classification for ship-radiated noise. *Sensors* (2022) 22(1):112. doi:10.3390/s22010112

4. Dragomiretskiy K, Zosso D. Variational mode decomposition. *IEEE Trans Signal Process* (2014) 62(3):531–44. doi:10.1109/tsp.2013.2288675

5. Mohanty S, Gupta KK, Raju KS. Hurst based vibro-acoustic feature extraction of bearing using EMD and VMD. *Measurement* (2018) 117:200–20. doi:10.1016/j.measurement.2017.12.012

6. Lei Z, Lei X, Zhou C, Qing L, Zhang Q, Chao W. Research on feature extraction of ship-radiated noise based on compressed sensing and center frequency. *IEEE Access* (2021) 9:128679–86. doi:10.1109/access.2021.3113042

7. Li Y, Li Y, Chen X, Yu J. A novel feature extraction method for ship-radiated noise based on variational mode decomposition and multi-scale permutation entropy. *Entropy* (2017) 19(7):342. doi:10.3390/e19070342

8. Chauhan S, Vashishtha G, Kumar A. A symbiosis of arithmetic optimizer with slime mould algorithm for improving global optimization and conventional design problem. *J Supercomput* (2022) 78(5):6234–74. doi:10.1007/s11227-021-04105-8

9. Li Y, Tang B, Jiang X, Yi Y. Bearing fault feature extraction method based on GA-VMD and center frequency. *Math Probl Eng* (2022) 2022:1–19. doi:10.1155/2022/2058258

10. Guo Z, Liu M, Wang Y, Qin H. A new fault diagnosis classifier for rolling bearing united multi-scale permutation entropy optimize VMD and cuckoo search SVM. *IEEE Access* (2020) 8:153610–29. doi:10.1109/access.2020.3018320

11. Li C, Peng T, Zhu Y. A novel approach for acoustic signal processing of a drum shearer based on improved variational mode decomposition and cluster Analysis. *Sensors* (2020) 20(10):2949. doi:10.3390/s20102949

12. Zhou F, Yang X, Shen J, Liu W. Fault diagnosis of hydraulic pumps using PSO-VMD and refined composite multiscale fluctuation dispersion entropy. *Shock and Vibration* (2020) 2020:1–13. doi:10.1155/2020/8840676

13. Xu W, Hu J. A novel parameter-adaptive VMD method based on grey wolf optimization with minimum average mutual information for incipient fault detection. *Shock and Vibration* (2021) 2021:1–14. doi:10.1155/2021/6640387

14. Ding J, Xiao D, Li X. Gear fault diagnosis based on genetic mutation particle swarm optimization VMD and probabilistic neural network algorithm. *IEEE Access* (2020) 8:18456–74. doi:10.1109/access.2020.2968382

15. Vashishtha G, Chauhan S, Kumar A, Kumar R. An ameliorated African vulture optimization algorithm to diagnose the rolling bearing defects. *Meas Sci Technol* (2022) 33(7):075013. doi:10.1088/1361-6501/ac656a

16. Arora S, Singh S. Butterfly optimization algorithm: A novel approach for global optimization. *Soft Comput* (2019) 23(3):715–34. doi:10.1007/s00500-018-3102-4

17. Li Z, Li Y, Zhang K, Guo J. A novel improved feature extraction technique for ship-radiated noise based on IITD and MDE. *Entropy* (2019) 21(12):1215. doi:10.3390/e21121215

18. Li Y, Jiao S, Geng B, Jiang X. Rcmfrde: Refined composite multiscale fluctuation-based reverse dispersion entropy for feature extraction of ship-radiated noise. *Math Probl Eng* (2021) 2021:7150921–18. doi:10.1155/2021/7150921

19. Yang H, Li L-L, Li G-H, Guan Q-R. A novel feature extraction method for ship-radiated noise. *Defence Tech* (2022) 18(4):604–17. doi:10.1016/j.dt.2021.03.012

20. Li Y, Geng B, Jiao S. Dispersion entropy-based lempel-ziv complexity: A new metric for signal analysis. *Chaos Solitons Fractals* (2022) 161:112400. doi:10.1016/j.chaos.2022.112400

21. Bandt C, Pompe B. Permutation entropy: A natural complexity measure for time series. *Phys Rev Lett* (2002) 88(17):174102. doi:10.1103/physrevlett.88.174102

22. Rostaghi M, Azami H. Dispersion entropy: A measure for time-series analysis. *IEEE Signal Process Lett* (2016) 23(5):610–4. doi:10.1109/lsp.2016.2542881

23. Azami H, Escudero J. Amplitude- and fluctuation-based dispersion entropy. *Entropy* (2018) 20(3):210. doi:10.3390/e20030210

24. Vashishtha G, Chauhan S, Yadav N, Kumar A, Kumar R. A two-level adaptive chirp mode decomposition and tangent entropy in estimation of single-valued neutrosophic cross-entropy for detecting impeller defects in centrifugal pump. *Appl Acoust* (2022) 197:108905. doi:10.1016/j.apacoust.2022.108905

25. Li Y-X, Li Y-A, Chen Z, Chen X. Feature extraction of ship-radiated noise based on permutation entropy of the intrinsic mode function with the highest energy. *Entropy* (2016) 18(11):393. doi:10.3390/e18110393

26. Li G, Hou Y, Yang H. A novel method for frequency feature extraction of ship radiated noise based on variational mode decomposition, double coupled Duffing chaotic oscillator and multivariate multiscale dispersion entropy. *Alexandria Eng J* (2022) 61(8):6329–47. doi:10.1016/j.aej.2021.11.059

27. Li Z, Li Y, Zhang K. A feature extraction method of ship-radiated noise based on fluctuation-based dispersion entropy and intrinsic time-scale decomposition. *Entropy* (2019) 21(7):693. doi:10.3390/e21070693

28. Cuesta-Frau D. Slope entropy: A new time series complexity estimator based on both symbolic patterns and amplitude information. *Entropy* (2019) 21(12):1167. doi:10.3390/e21121167

29. Cuesta-Frau D, Schneider J, Bakštein E, Vostatek P, Spaniel F, Novák D. Classification of actigraphy records from bipolar disorder patients using slope entropy: A feasibility study. *Entropy* (2020) 22(11):1243. doi:10.3390/e22111243

30. Li Y, Gao P, Tang B, Yi Y, Zhang J. Double feature extraction method of ship-radiated noise signal based on slope entropy and permutation entropy. *Entropy* (2022) 24(1):22. doi:10.3390/e24010022

31. Li Y, Tang B, Yi Y. A novel complexity-based mode feature representation for feature extraction of ship-radiated noise using VMD and slope entropy. *Appl Acoust* (2022) 196:108899. doi:10.1016/j.apacoust.2022.108899

32. National Park Service Available online: https://www.nps.gov/glba/learn/nature/soundclips.htmhttps://www.nps.gov/glba/learn/nature/soundclips.htm (Accessed July 10, 2022).

33. Venkatesan C, Karthigaikumar P, Varatharajan R. A novel LMS algorithm for ECG signal preprocessing and KNN classifier based abnormality detection. *Multimed Tools Appl* (2018) 77(8):10365–74. doi:10.1007/s11042-018-5762-6

34. Li G, Liu F, Yang H. Research on feature extraction method of ship radiated noise with K-nearest neighbor mutual information variational mode decomposition, neural network estimation time entropy and self-organizing map neural network. *Measurement* (2022) 199:111446. doi:10.1016/j.measurement.2022.111446

frontiers | Frontiers in Physics

TYPE Review
PUBLISHED 18 October 2022
DOI 10.3389/fphy.2022.1044890

OPEN ACCESS

EDITED BY
Yuxing Li,
Xi'an University of Technology, China

REVIEWED BY
Bo Geng,
Xi'an University of Technology, China
Junde Guo,
Xi'an Technological University, China
Lihang Wang,
Changzhou Institute of Technology, China

*CORRESPONDENCE
Lei Zhufeng,
leizhufeng@xaau.edu.cn

SPECIALTY SECTION
This article was submitted to Physical Acoustics and Ultrasonics, a section of the journal Frontiers in Physics

RECEIVED 15 September 2022
ACCEPTED 27 September 2022
PUBLISHED 18 October 2022

CITATION
Zhufeng L, Xiaofang L, Na W and Qingyang Z (2022), Present status and challenges of underwater acoustic target recognition technology: A review. *Front. Phys.* 10:1044890. doi: 10.3389/fphy.2022.1044890

Present status and challenges of underwater acoustic target recognition technology: A review

Lei Zhufeng[1]*, Lei Xiaofang[2], Wang Na[1] and Zhang Qingyang[1]

[1]National Joint Engineering Research Center for Special Pump Technology, Xi'an Aeronautical Institute, Xi'an, China, [2]China National Heavy Machinery Research Institute Co.,Ltd., Xi'an, China

Future naval warfare has placed high demands on underwater targets' target detection, target recognition, and opposition resistance, among other things. However, the ocean's complex underwater acoustic environment and the evolving "stealth" technology of underwater targets pose significant challenges to target detection systems, which has become a hot topic in the field of underwater acoustic signal processing in various countries. This study introduced the mechanism of underwater target radiation noise generation, analyzed the research progress and development of underwater target radiation noise recognition by applying machine learning from three perspectives: signal acquisition, feature extraction, and signal recognition at home and abroad, and elaborated on the challenges of underwater target-radiated noise recognition technology against the backdrop of rapid computing science development, and finally, an integrated signal processing method based on the fusion of traditional feature extraction methods and deep learning is proposed for underwater target radiation noise recognition, which improves the low recognition rate of traditional methods and also circumvents the problem of deep learning requiring high computational cost, and is an important direction for future hydroacoustic signal processing.

KEYWORDS

underwater acoustic target, radiated noise recognition, feature extraction, feature selection, machine learning

1 Introduction

The ocean will be the primary battlefield of future high-tech warfare, and future naval weaponry will inevitably include information and intelligence. With the advancement of equipment countermeasure and counter-countermeasure technology, the complete application of underwater acoustic countermeasure and counter-countermeasure technology in recent battles has demonstrated its value in naval combat. Target detection and target recognition refer to the use of signal processing technology for underwater acoustic signal processing in order to complete target detection, parameter estimation, and target recognition, as well as other military tasks, in the complex marine battlefield environment of underwater acoustic countermeasure and counter-countermeasure. Target recognition is also the foundation of underwater acoustic

countermeasure and counter-countermeasure, and many subsequent tasks can only be completed by precisely recognizing hostile targets.

The future of naval warfare places great demands on underwater targets' target detection, target recognition, and anti-resistance capabilities, among other things. However, the ocean's complex underwater acoustic environment and evolving "stealth" technology of underwater targets pose significant challenges to target detection systems, particularly for counter-countermeasure equipment, under strong noise and small aperture conditions, to detect different types of underwater target radiation noise and accurate positioning from the complex navigation noise and ocean environment noise, which has been a difficult problem of underwater target detection [1]. The reverberant background in the underwater acoustic complex environment increases the complexity of underwater acoustic active target detection, and remote detection is difficult to achieve, especially with the constant advancement of underwater acoustic countermeasure technology. At the same time, due to the complexity of the underwater target radiation noise creation and radiation mechanism, its composition is different, as is the water acoustic channel [2]. The detection system's original good performance will not be satisfactory, and detection performance will be severely deteriorated.

This study analyzes the mechanism of underwater target radiation noise generation, then reviews the progress and challenges in underwater target radiation noise feature extraction and feature recognition, introduces the shortcomings of traditional underwater target radiation noise signal processing methods, and proposes a method combining traditional underwater target radiation noise feature extraction and deep learning, which not only improves the recognition rate but also circumvents the high computational cost.

The rest of this article is organized as follows: the mechanism of underwater target radiation noise generation is introduced in Section 2. The development trend of underwater target radiation noise recognition is introduced in Section 3. Future research directions and future prospects are introduced in Section 4. Section 5 concludes this article.

2 The mechanism of underwater target radiation noise generation

In navigation and operation, propellers and other machinery produce vibration through the shell to the water radiation acoustic waves, resulting in radiation noise. Underwater targets have a variety of distinct characteristics, and radiation noise sources are classified into three types: mechanical noise, propeller noise, and hydrodynamic noise. There are two types of radiation noise spectrum: continuous spectrum and line spectrum. Mechanical noise should be regarded as a superposition of a strong line spectrum and weak continuous spectrum, which is the main component of radiation noise in the low-frequency band. Propeller noise is made up of two components: propeller cavitation noise and propeller rotation noise. Cavitation noise is a continuous spectrum component, while propeller rotation noise is primarily expressed as a line spectrum superimposed on the continuous spectrum, and it is the main component of noise in the low-frequency band. In terms of intensity, hydrodynamic noise is frequently masked by mechanical noise and propeller noise. However, in some cases, hydrodynamic noise may become the primary noise source in the range in which the line spectrum appears. Due to high mechanical speed, the line spectrum shifts to high frequencies, and with these radiation noise differential features, underwater targets provide a theoretical basis for target recognition and estimation [3, 4].

The electric power system was once the main source of power for underwater targets in order to improve the quietness and delay the target warning time, and its main shortcoming was its range. The Swedish TP2000, the United States MK50, and the British "sailfish" have all adopted quiet thermodynamic systems that are 80 percent quieter than electric systems at the same speed, thanks to the development of closed cycle thermodynamic systems.

Underwater target radiation noise is typically generated using an excitation or vibration source, transmitted through the underwater target shell, and radiated outward through the water medium, as illustrated in Figure 1, for two types of underwater target radiation noise generation models.

The thermodynamic underwater target excitation source consists of a high-speed rotating body, a reciprocating motion body, a high-speed gear reducer, a high-speed pump, and other motion mechanisms, but its radiation noise is dependent on the vibration of the shell; as long as the thermodynamic underwater target vibration isolation method is appropriate, its radiation noise is less than that of an electric power underwater target; thus, the detection of underwater target radiation noise discrepancy is possible.

3 Development trend of underwater target radiation noise recognition

Underwater target detection and recognition technology evolves in tandem with military requirements, economic development, and the advancement of other disciplines. It is to use underwater target radiation noise as the research object and advanced signal processing technology to extract multi-directional and multi-level high-quality target difference features and then build an artificial intelligence target recognition model based on the features to achieve accurate underwater target recognition. It primarily consists of the links depicted in Figure 2.

1) Underwater target radiation noise information analysis and preferential difference feature extraction: using underwater

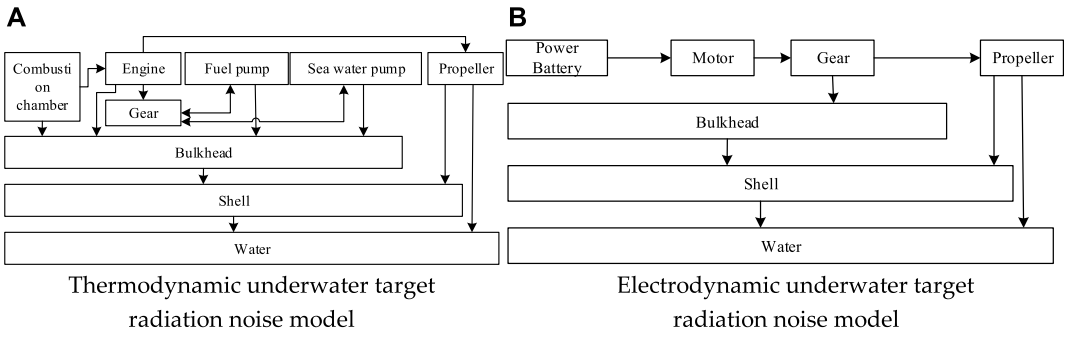

FIGURE 1
Two types of underwater target radiation noise generation models.

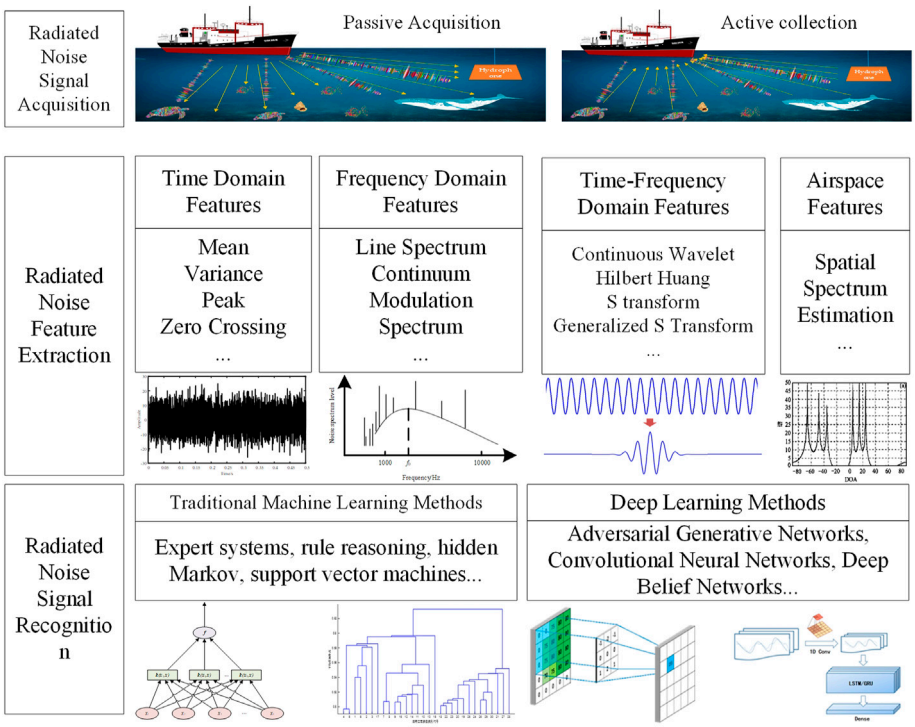

FIGURE 2
Flow chart of underwater target radiation noise recognition [4, 5].

acoustic signal processing methods, eliminate noise interference, retain information reflecting the target's features, and then obtain the underwater target's key information using feature extraction and preferential selection.

2) Accurate recognition of underwater target radiation noise: establish an underwater target detection and recognition method, based on an artificial intelligence model, and then determine the type of underwater targets and motion parameter information to evaluate the advantages and disadvantages of the different feature extraction methods.

3.1 Development trend of underwater target radiation noise feature extraction

Underwater target radiation noise feature extraction is an important way to realize underwater target radiation noise

information representation, which lays an important foundation to realize effective underwater target radiation noise recognition, and good "extractable" features are both good separability and can maintain good similarity between the same kind, so feature extraction is important for underwater target radiation noise recognition.

3.1.1 Underwater target radiation noise statistical feature extraction

In 1996, A. Passamante proposed time series characterization using the repeatability of similar sequences [6], and Chen Xiangdong et al. [7] applied the repeatability of similar sequences to underwater acoustic signal processing and then realized the feature extraction of ship-radiated noise. Meng et al. [8, 9] constructed a nine-dimensional feature vector of ship-radiated noise using statistical features, including over-zero wavelength, tachistoscopic amplitude, over-zero wavelength difference, wave train region, and wave column region. Tian et al. [10] used underwater acoustic target-radiated noise signal waveforms as features to achieve effective recognition of underwater acoustic targets. Wang et al. [11] proposed a new statistical complexity measure to achieve underwater target radiation noise recognition.

3.1.2 Underwater target radiation noise frequency domain feature extraction

Xu Yuanchao et al. [12] rearranged the logarithmic spectrum frequency points and proposed a double logarithmic spectrum feature for ship radiation noise classification. Nan Lin et al. [13] analyzed the cepstrum features of the periodic impulse signal and ship-radiated noise and improved the non-cooperative detection performance of ship-radiated noise using a cepstrum-wavelet. Bing-Yang Wang [14] proposed a control algorithm to simulate the spectrum of ship radiation noise based on the study of the ship radiation noise characteristics, combined with the power spectrum feature. Bo-Bin Rao [15] used the Detection of Envelope Modulation on Noise (DEMON) method to obtain broadband modulation features of ship radiation noise. Shen et al. [16] used the poles of the AR model to extract the short-time frequency peak of the signal and proposed a new multiple frequency shift keying (MFSK) signal modulation recognition method using clustering features.

3.1.3 Underwater target radiation noise time–frequency feature extraction

Chen et al. [17] implemented the signal detection of ship noise using the wavelet packet transform method. Wu Chengxi et al. [18] extracted multiple features of ship-radiated noise in frequency bands using the wavelet packet decomposition technique and improved the ship recognition accuracy. Li et al. [19] and Hong et al. [20] achieved effective recognition of underwater target-radiated noise using complete ensemble empirical mode decomposition with adaptive noise (CEEMDAN). Fang et al. [21] proposed a selective noise-assisted empirical mode decomposition method for the classification and recognition of underwater targets. Xie et al. [22] proposed a new feature extraction method in which the hybrid features of underwater target-radiated noise are extracted based on an improved variational mode decomposition method for underwater target-radiated noise recognition.

3.1.4 Other feature extraction methods of underwater target radiation noise

Guo Zheng et al, [23] proposed a generalized multiscale pattern erosion spectrum entropy (GMPESE) nonlinear underwater target-radiated noise feature extraction method based on the mathematical morphology method. Gaunaurd et al. [24] discussed a method for time–frequency image detection of underwater radar and sonar target echoes. Hui Junying et al. [25] combined pressure and particle velocity to propose an acoustic composite sensor for low-intensity radar noise measurement. Li et al. [26–28] carried out research on complexity analysis of time series signals, discrimination of bearing fault diagnosis, and identification of hydroacoustic target radiation noise using dispersion entropy, fractional slope entropy, and VMD, respectively, with good results, demonstrating the feasibility of entropy in the field of signal identification.

In summary, scholars have conducted a lot of research on underwater target radiation noise feature extraction and achieved gratifying results, which provide a basis for underwater target radiation noise recognition under strong background environmental noise interference and weak information extraction conditions. However, the existing feature extraction methods are closely associated with recognition methods which restricts their engineering progress, and few feature extraction methods that can be applied to actual underwater target radiation noise recognition have been reported.

3.2 Underwater target radiation noise recognition

Using artificial intelligence methods to input the extracted underwater target radiation noise features to achieve underwater target classification recognition is the goal of conducting underwater target radiation noise classification. A good classification model is one that does not depend on a certain feature and is applicable to many types of underwater targets, that is, robustness and generalization.

3.2.1 Underwater target radiation noise recognition based on traditional machine learning

Meng et al. [29], Li et al. [30], and Ke et al. [31] achieved the recognition of underwater targets using a support vector machine

model with kernel functions as radial basis functions as classifiers. Hui Jiang [32] used the Gaussian mixture model (GMM) for ship and island bird acoustic signal recognition. Wang et al. [33] used a decision tree to achieve the recognition of underwater target-radiated noise. Yang et al. [34] used an underwater acoustic signal processing model based on the gray wolf optimized kernel extreme learning machine model to achieve classification recognition of underwater target-radiated noise. Li et al. [35] calculated the recognition rate of ship-radiated noise using the K-nearest neighbor algorithm and validated the ship-radiated noise feature extraction method. Zhou et al. [36] proposed a wavelet domain-hidden Markov tree model to achieve underwater target radiation noise classification.

3.2.2 Underwater target radiation noise recognition based on deep learning

Luo et al. [37–39] used the normalized spectrum of the signal as input and completed the space–frequency joint detection of the line spectrum of underwater acoustic signals using a restricted Boltzmann machine. Yang et al. [40] proposed a new cooperative deep learning method for underwater acoustic target recognition by combining deep long- and short-term memory networks and deep self-coding neural networks. Satheesh et al. [41] constructed a data-efficient underwater target classifier using the generative modeling capability of an auxiliary classifier generative adversarial network to achieve underwater target radiation noise classification. Cao et al. [42] used sparse self-encoders to learn invariant features from underwater target spectra, combined with stacked autoencoders and softmax to achieve underwater target classification. Cai et al. [43–46] introduced multi-perspective light field reconstruction into the field of underwater target recognition and implemented multi-target recognition based on a generative adversarial network. Feng et al. [47] proposed a fusion feature and 18-layer residual network method to achieve the classification of underwater targets. Liu et al. [48] used a 1D-CNN model to identify the envelope-modulated line spectrum on the DEMON spectrum of underwater target radiation noise with good generalization capability. Yang et al. [49] proposed a deep neural network classification system, which can automatically learn more discriminative advanced features in the wavelet packet component energy and then realized the classification and recognition of underwater targets. Wu et al. [50] addressed the problem of small samples in underwater target recognition, a matching model with multiple target feature extraction methods, and a deep neural network model is constructed to achieve automatic, efficient, and accurate underwater target recognition.

In conclusion, researchers both at home and abroad have conducted useful investigations and achieved significant results in underwater target radiation noise recognition using artificial intelligence models. Traditional machine learning methods rely more on the signal acquisition and signal feature extraction, whereas deep learning methods have greater robustness and generalization ability, but the problems of poor physical interpretation and higher computational cost remain.

4 Future research directions and future prospects

At the moment, China is aggressively implementing marine strategy, underwater target recognition technology in both military and civilian domains will be a big show, and a large number of demands will undoubtedly give rise to a large number of scientific and technological achievements output. The traditional method of underwater target radiation noise feature extraction recognition can no longer meet China's economic and social development. Artificial intelligence has emerged as one of the strategic technologies driving China's future scientific and technological development. Combining artificial intelligence and underwater target radiation noise recognition to provide a reliable foundation and means for underwater target radiation noise recognition will be a significant future development direction.

1) Develop more efficient deep learning models

The introduction of deep learning methods into the field of underwater acoustic signal processing has greatly improved underwater target radiation noise recognition methods. In the short term, deep learning does not appear to require the use of features such as line spectra and frequency spectra that are used in traditional underwater target radiation noise processing, because deep learning methods are a completely data-based processing method, but the characterization of its features is a serious problem; however, the excessive computational cost and poor physical interpretability severely limit the engineering applications of deep learning methods, thus, the development of deep learning frameworks with more concise computational frameworks and lower computational costs and the improvement of their physical interpretability is the next work to focus on.

2) Combining traditional machine learning methods and deep learning methods

Deep learning methods rely on a large amount of raw data, but due to the confidentiality policy, it is difficult or even impossible to obtain a large amount of underwater target radiation noise, and the data collected from semi-physical simulation tests cannot truly restore the underwater target radiation noise, although some deep learning methods can generate some feature information, but the authenticity of these feature information cannot be verified; therefore, combining traditional machine learning methods and deep learning methods, integrating and extracting a large amount

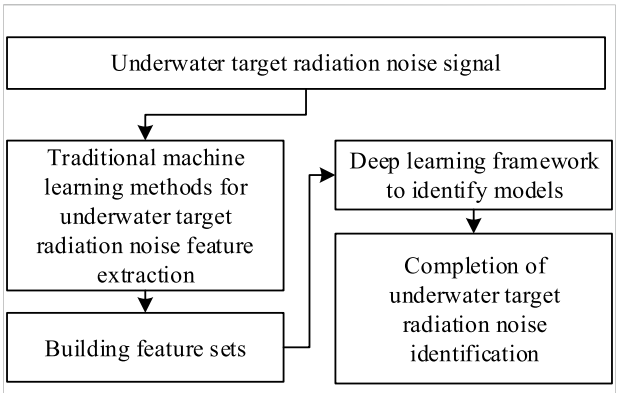

FIGURE 3
Flow chart of deep learning methods and traditional machine learning methods for underwater target radiation noise recognition.

of feature information under small sample conditions, and then using deep learning to improve the recognition rate of underwater target radiation noise will be an important direction for future research. The process of combining deep learning methods and traditional machine learning methods for underwater target radiation noise recognition is shown in Figure 3.

5 Conclusion

With the continuous development of the national economy, the recognition of underwater target radiation noise has become one of the hot topics that scholars are currently concerned about the recognition of underwater target radiation noise. This study first introduced the mechanism of underwater target radiation noise generation, then analyzed the necessity of underwater target radiation noise recognition, then composed the underwater target radiation noise feature extraction methods and underwater target radiation noise recognition methods commonly used at present, and clarified the main problems and challenges of existing methods by reviewing the research progress at home and abroad, and finally, the future development direction in the field of underwater target radiation noise recognition was also analyzed to meet the demand for underwater target radiation noise recognition in the rapid development of the national economy.

Author contributions

Writing—original draft preparation, LZ; investigation, LX; and reviewed and edited the manuscript, WN and ZQ.

Funding

This work was supported in part by the National Natural Science Foundation of China (Nos. 52105068 and 11902236), China Postdoctoral Science Foundation (No. 2021M692509), Natural Science Basic Research Program of Shaanxi Province (No. 2021JQ-860), and Science Foundation of Xi'an Aeronautical Institute (Nos. 2020KY0223 and 2020KY1228).

Conflict of interest

LX was employed by China National Heavy Machinery Research Institute Co., Ltd.

The remaining authors declare that the research was conducted in the absence of any commercial or financial relationships that could be construed as a potential conflict of interest.

Publisher's note

All claims expressed in this article are solely those of the authors and do not necessarily represent those of their affiliated organizations, or those of the publisher, the editors, and the reviewers. Any product that may be evaluated in this article, or claim that may be made by its manufacturer, is not guaranteed or endorsed by the publisher.

References

1. Yang H, Lee K-H, Choo Y, Kookhyun K. Underwater acoustic research trends with machine learning: General background. *J Ocean Eng Technol* (2020) 34(2): 147–54. Cited in: Pubmed; PMID KJD:ART002580627. doi:10.26748/ksoe.2020.015

2. Huang T, Wang T. Research on analyzing and processing methods of ocean sonar signals. *J Coastal Res* (2019) 94:208–12. Cited in: Pubmed; PMID WOS: 000485711600045. doi:10.2112/si94-044.1

3. Naval Weapons Engineering (2020). Introduction to naval weapons engineering. Available from: https://fas.org/man/dod-101/navy/docs/es310/asw_sys/asw_sys.htm [accessed on 4 May 2020].

4. Yang H, Lee K-H, Choo Y, Kookhyun K. Underwater acoustic research trends with machine learning: Passive SONAR applications. *J Ocean Eng Technol* (2020) 34(3):227–36. Cited in: Pubmed; PMID KJD:ART002596748. doi:10.26748/ksoe.2020.017

5. Yang H, Byun S, Lee K-H, Choo Y, Kookhyun K. Underwater acoustic research trends with machine learning: Active SONAR applications. *J Ocean Eng Technol* (2020) 34(4): 277–84. Cited in: Pubmed; PMID KJD:ART002615997. doi:10.26748/ksoe.2020.018

6. Passamante A, Bromely D, Farrell ME. Time series characterization using the repeatability of similar sequences. *Physica D: Nonlinear Phenomena* (1996) 96(1-4):100–9. Cited in: Pubmed; PMID WOS:A1996VJ20400009. doi:10.1016/0167-2789(96)00015-2

7. Chen X, Gao X, Lu J. Research on time domain characteristics of ship radiated noise based on repeatability of similar sequences. *J Southeast Univ* (1998) 1998: 17–23.

8. Meng Q, Yang S, Piao S. The classification of underwater acoustic target signals based on wave structure and support vector machine. *The J Acoust Soc America* (2014) 136(4):2265. doi:10.1121/1.4900181

9. Meng Q, Yang S. A wave structure based method for recognition of marine acoustic target signals. *J Acoust Soc America* (2015) 137(4):2242. doi:10.1121/1.4920186

10. Tian S, Chen D, Wang H, Liu J. Deep convolution stack for waveform in underwater acoustic target recognition. *Sci Rep* (2021) 11(1):9614. Cited in: Pubmed; PMID WOS:000656457900011. doi:10.1038/s41598-021-88799-z

11. Wang J, Chen Z. Feature extraction of ship-radiated noise based on intrinsic time-scale decomposition and a statistical complexity measure. *Entropy* (2019) 21(11):1079. Cited in: Pubmed; PMID WOS:000502145000052. doi:10.3390/e21111079

12. Xu Y, Cai Z, Kong X. Classification of ship radiated noise based on Bi-logarithmic scale spectrum and convolutional network. *J Electro Inf Tech* (2022) 44:1947–55. doi:10.11999/JEIT211407

13. Nan L, Han S, Liu W, Xu J. Non cooperative detection method of underwater acoustic DSSS signal under disturbed condition. *Ship Electron Eng* (2017) 37:46–8+58. doi:10.3969/j.issn.1672-9730.2017.09.010

14. Wang B. Spectrum control algorithm in acoustic field. *Mine Warfare & Ship Self-Defence* (2015) 23:54–7.

15. Rao B. *Feature extraction method for weak modulation of ship radiated noise*. (China: Southeast University) (2020). Thesis.

16. Shen L, Gong K, Fan L, Pan Y. MFSK signal recognition method based on the feature of local density and distance. *J Signal Process* (2016) 32(12):1478–88. Cited in: Pubmed; PMID CSCD:5885455. doi:10.16798/j.issn.1003-0530.2016.12.013

17. Sheng C, HongHua Z. Detection of underwater acoustic signal from ship noise based on WPT method. In: Proceedings of the Fourth International Workshop on Chaos-Fractals Theories and Applications; 2011 19-21 Oct; IWCFTA (2011). p. 324–7. Citedin: Pubmed; PMID INSPEC:12407766. doi:10.1109/iwcfta.2011.27

18. Wu C, Wang B, Xu Q, Zhu Y. Ship radiated noise recognition technology based on wavelet packet decomposition and PCA-Attention-LSTM. *Tech Acoust* (2022) 41:264–73. doi:10.16300/j.cnki.1000-3630

19. Li Y, Chen X, Yu J. A hybrid energy feature extraction approach for ship-radiated noise based on CEEMDAN combined with energy difference and energy entropy. *Processes* (2019) 7(2):69. Cited in: Pubmed; PMID WOS:000460800900015. doi:10.3390/pr7020069

20. Yang H, Li L-l, Li G-h, Guan Q-r. A novel feature extraction method for ship-radiated noise. *Defence Tech* (2022) 18(4):604–17. Cited in: Pubmed; PMID WOS:000793693500007. doi:10.1016/j.dt.2021.03.012

21. Niu F, Hui J, Zhao A, Cheng Y, Chen Y. Application of SN-emd in mode feature extraction of ship radiated noise. *Math Probl Eng* (2018) 2018:1–16. in: Pubmed; PMID WOS:000453782500001. doi:10.1155/2018/2184612

22. Xie D, Sun H, Qi J. A new feature extraction method based on improved variational mode decomposition, normalized maximal information coefficient and permutation entropy for ship-radiated noise. *Entropy* (2020) 22(6):620. Cited in: Pubmed; PMID WOS:000551064200001. doi:10.3390/e22060620

23. Guo Z, Zhao M, Hu C, Ni J. A study on feature extraction and application for ship radiated noise's generalized multiscale mathematical morphology feature. *J Vibration Shock* (2022) 41:21–8+100. doi:10.13465/j.cnki.jvs.2022.04.004

24. Gaunaurd GC, Brill D, Huang H, Moore PWB, Strifors HC. Signal processing of the echo signatures returned by submerged shells insonified by dolphin "clicks": Active classification. *J Acoust Soc Am* (1998) 103(3):1547–57. in: Pubmed; PMID WOS:000072522900036. doi:10.1121/1.421302

25. Hui J, Wang Y, Liang G, Li C. Research on measurement and simulation of low noise pass-through characteristics. *Appl Acoust* (2000) 2000:29–34.

26. Li Y, Geng B, Jiao S. Dispersion entropy-based lempel-ziv complexity: A new metric for signal analysis. *Chaos, Solitons & Fractals* (2022) 161:112400. Cited in: Pubmed; PMID INSPEC:21959212. doi:10.1016/j.chaos.2022.112400

27. Li Y, Mu L, Gao P. Particle swarm optimization fractional slope entropy: A new time series complexity indicator for bearing fault diagnosis. *Fractal Fract* (2022) 6(7):345. in: Pubmed; PMID WOS:000832093000001. doi:10.3390/fractalfract6070345

28. Li Y, Tang B, Yi Y. A novel complexity-based mode feature representation for feature extraction of ship-radiated noise using VMD and slope entropy. *Appl Acoust* (2022) 196:108899. Cited in: Pubmed; PMID WOS:000853020600014. doi:10.1016/j.apacoust.2022.108899

29. Meng Q, Yang S, Yu S. Recognition of marine acoustic target signals based on wave structure and support vector machine. *J Electro Inf Tech* (2015) 37(9):2117–23. Cited in: Pubmed; PMID CSCD:5505564.

30. Li W. Support vector machine and ship radiation noise classification. *Ship Sci Tech* (2017) 39:19–21. doi:10.3404/j.issn.1672–7619.2017.6A.006

31. Ke X, Yuan F, Cheng E. Integrated optimization of underwater acoustic ship-radiated noise recognition based on two-dimensional feature fusion. *Appl Acoust* (2020) 159:107057. Cited in: Pubmed; PMID WOS:000502894900008. doi:10.1016/j.apacoust.2019.107057

32. Jiang H. Research on target recognition method based on spectrum analysis. China: Zhejiang Ocean University (2020). Thesis.

33. Wang B, Wu C, Zhu Y, Zhang M, Li H, Zhang W. Ship radiated noise recognition technology based on ML-DS decision fusion. *Comput Intelligence Neurosci* (2021) 2021:2021–14. in: Pubmed; PMID WOS:000756171100004. doi:10.1155/2021/8901565

34. Yang H, Gao L, Li G. Underwater acoustic signal prediction based on MVMD and optimized kernel Extreme learning machine. *Complexity* (2020) 2020:1–17. in: Pubmed; PMID WOS:000533315200005. doi:10.1155/2020/6947059

35. Li Y, Jiao S, Geng B, Zhou Y. Research on feature extraction of ship-radiated noise based on multi-scale reverse dispersion entropy. *Appl Acoust* (2021) 173:107737. Cited in: Pubmed; PMID WOS:000595628100043. doi:10.1016/j.apacoust.2020.107737

36. Yue Z, Wei K, Qing X. A novel modeling and recognition method for underwater sound based on HMT in wavelet domain. *Ai 2004: Adv Artif IntelligenceProceedings* (2004) 3339:332–43. Cited in: Pubmed; PMID WOS:000226133600030. doi:10.1007/978-3-540-30549-1_30

37. Luo X, Feng Y. An underwater acoustic target recognition method based on restricted Boltzmann machine. *Sensors* (2020) 20(18):5399. Cited in: Pubmed; PMID WOS:000580193400001. doi:10.3390/s20185399

38. Luo X, Feng Y, Zhang M. An underwater acoustic target recognition method based on combined feature with automatic coding and reconstruction. *Ieee Access* (2021) 9:63841–54. . Cited in: Pubmed; PMID WOS:000645842000001. doi:10.1109/access.2021.3075344

39. Luo X, Shen Z. A space-frequency joint detection and tracking method for line-spectrum components of underwater acoustic signals. *Appl Acoust* (2021) 172:107609. Cited in: Pubmed; PMID WOS:000590401800007. doi:10.1016/j.apacoust.2020.107609

40. Yang H, Xu G, Yi S, Li Y. Ieee. A new cooperative deep learning method for underwater acoustic target recognition. In: Oceans 2019 - Marseille; 17-20 June 2019; Marseille, France (2019). Cited in: Pubmed; PMID WOS:000591652100423.

41. Chandran SC, Kamal S, Mujeeb A, Supriya MH. Generative adversarial learning for improved data efficiency in underwater target classification. *Eng Sci Tech Int J* (2022) 30:101043. Cited in: Pubmed; PMID WOS:000807389200005. doi:10.1016/j.jestch.2021.07.006

42. Cao X, Zhang X, Yu Y, Niu L. Deep learning-based recognition of underwater target. In: 2016 IEEE International Conference on Digital Signal Processing (DSP); 16-18 Oct. 2016; China (2016). p. 89–93.

43. Cai L, Luo P, Zhou G. Multistage analysis of abnormal human behavior in complex scenes. *J Sensors* (2019) 2019:1–10. in: Pubmed; PMID WOS:000499158000002. doi:10.1155/2019/1276438

44. Cai L, Luo P, Zhou G, Chen Z. Maneuvering target recognition method based on multi-perspective light field reconstruction. *Int J Distrib Sens Netw* (2019) 15(8):155014771987065–12. in: Pubmed; PMID WOS:000482086100001. doi:10.1177/1550147719870657

45. Cai L, Luo P, Zhou G, Xu T, Chen Z. Multiperspective light field reconstruction method via transfer reinforcement learning. *Comput Intelligence Neurosci* (2020) 2020:1–14. in: Pubmed; PMID WOS:000514358700001. doi:10.1155/2020/8989752

46. Cai L, Sun Q. Multiautonomous underwater vehicle consistent collaborative hunting method based on generative adversarial network. *Int J Adv Robotic Syst* (2020) 17(3):172988142092523. Cited in: Pubmed; PMID WOS:000546901500001. doi:10.1177/1729881420925233

47. Feng H, Chengwei L, Lijuan G, Feng C, Haihong F. Underwater acoustic target recognition with ResNet18 on ShipsEar dataset. In: 2021 IEEE 4th International Conference on Electronics Technology (ICET); 7th to 10th May 2021; Chengdu, China (2021). p. 1240–4. doi:10.1109/icet51757.2021.9451099in: Pubmed; PMID INSPEC:20843152

48. Liu D, Zhao X, Cao W, Wang W, Lu Y. Design and performance evaluation of a deep neural network for spectrum recognition of underwater targets. *Comput Intelligence Neurosci* (2020) 2020:1–11. in: Pubmed; PMID WOS:000561340500001. doi:10.1155/2020/8848507

49. Yu Y, Cao X, Zhang X. Ieee. Underwater target classification using deep neural network. In: 2018 Oceans - Mts/Ieee Kobe Techno-Oceans (Oto); 28-31 May 2018; Kobe, Japan (2018). . Cited in: Pubmed; PMID WOS:000465206800134.

50. Wu Y, Wang Y. A research on underwater target recognition neural network for small samples. *J Northwest Polytechnical Univ* (2022) 40(1):40–6. Cited in: Pubmed; PMID CSCD:7180236. doi:10.1051/jnwpu/20224010040

frontiers | Frontiers in Physics

TYPE Original Research
PUBLISHED 25 October 2022
DOI 10.3389/fphy.2022.1058474

OPEN ACCESS

EDITED BY
Yuxing Li,
Xi'an University of Technology, China

REVIEWED BY
Zhenyi Ou,
Guangdong Ocean University, China
Xiao Chen,
Shaanxi University of Science and Technology, China
Xiaohui Yang,
Inner Mongolia University of Science and Technology, China

*CORRESPONDENCE
Yu Lei,
leiyu@xupt.edu.cn

SPECIALTY SECTION
This article was submitted to Physical Acoustics and Ultrasonics, a section of the journal Frontiers in Physics

RECEIVED 30 September 2022
ACCEPTED 11 October 2022
PUBLISHED 25 October 2022

CITATION
Zhao D, Lei Y, Xu J and Cai H (2022), A comparative study of four types of multi-scale entropies in feature extraction of underwater acoustic signals for potential GNSS positioning applications. *Front. Phys.* 10:1058474. doi: 10.3389/fphy.2022.1058474

A comparative study of four types of multi-scale entropies in feature extraction of underwater acoustic signals for potential GNSS positioning applications

Danning Zhao[1,2,3], Yu Lei[4]*, Jinsong Xu[5] and Hongbing Cai[5]

[1]National Time Service Center, Chinese Academy of Sciences, Xi'an, China, [2]University of Chinese Academy of Sciences, Beijing, China, [3]School of Electronic and Electrical Engineering, Baoji University of Arts and Sciences, Baoji, China, [4]School of Computer Sciences and Technologies, Xi'an University of Posts and Telecommunications, Xi'an, China, [5]JSNU SPBPU Institute of Engineering, Jiangsu Normal University, Xuzhou, China

The combination of underwater acoustic processing and the Global Navigation Satellite System (GNSS) has achieved remarkable economic benefits in offshore operations. As the key technology of GNNS positioning, feature extraction of underwater acoustic signals is affected by the complex marine environment. To extract more effective information from underwater acoustic signals, we use four types of multi-scale entropies, including multi-scale sample entropy (MSE), multi-scale fuzzy entropy (MFE), multi-scale permutation entropy (MPE), and multi-scale dispersion entropy (MDE), to analyze and distinguish underwater acoustic signals. In this study, two groups of real-word underwater acoustic signal experiments were performed for feature extraction of ship-radiated noises (SRNs) and ambient noises (ANs). The results indicated that the performance of the MFE-based feature extraction method is superior to that of feature extraction methods based on the other three entropies under the same number of features, and the highest average recognition rate (ARR) of the MFE-based feature extraction method for SRNs reaches 100% when the number of features is 3.

KEYWORDS

multi-scale fuzzy entropy, multi-scale dispersion entropy, multi-scale permutation entropy, multi-scale sample entropy, marine ambient noise, ship-radiated noise, feature extraction

1 Introduction

The Global Navigation Satellite System (GNSS) plays an indispensable role in offshore operations and coastal defense; the positioning of marine targets depends heavily on accurate feature extraction. However, the extremely complex marine environment may seriously interfere with receiving underwater acoustic signals [1–4]. Therefore, it poses challenges to feature extraction of underwater acoustic signals and GNSS positioning [5, 6].

Traditional feature extraction methods include time domain, frequency domain, and time–frequency domain methods, which are not suitable for processing nonlinear and non-stationary signals [7–9]. With the continuous development of entropy theory, entropy-based feature extraction methods are used to analyze underwater acoustic signals [10–13], which is also effective in the analysis of nonlinear and non-stationary signals. The common entropies include sample entropy (SE), fuzzy entropy (FE), permutation entropy (PE), and dispersion entropy (DE).

SE and FE are acclaimed tools for quantifying the regularity and unpredictability of time series [14–16]. Richman and Moorman first proposed the concept of SE, which overcomes the defect that approximate entropy is restricted by the data record length [17]. As an improved algorithm of SE, the FE was put forward by Chen et al. which not only has the advantages of SE that is effective on short time series but also gives the definition of entropy in the case of small parameters by introducing the concept of fuzzy sets [18].

Both PE and DE are complexity metrics based on Shannon entropy, which can represent the complexity of the signal [19–21]. A new PE is proposed by Bandt and Pompe [22], which measures the chaos degree of the time series through employing the permutation pattern and has stronger anti-noise ability. However, PE considers only the order of the time series, and hence, some information of amplitudes may be not regarded. To deal with the problem, DE is introduced in [23] as a new complexity index, which considers the magnitude relationship of amplitude, and it is superior to PE in calculation speed as well as the ability to describe the valuable information of a signal.

Since these entropies mentioned above cannot reflect the useful information of the signal from the multi-scale, many scholars at home and abroad introduced the coarse-grained operation to generate multi-scale improved algorithm based on entropy [24], including multi-scale sample entropy (MSE), multi-scale fuzzy entropy (MFE), multi-scale permutation entropy (MPE), and multi-scale dispersion entropy (MDE). Among them, MSE successfully tracked the change of drug concentration during sevoflurane anesthesia [25]; MFE and MDE can accurately diagnose the fault types and fault severities [26, 27]; MPE was applied to feature extraction of ship-radiated noise and showed excellent performance [28].

In order to illustrate the feasibility of multi-scale entropy in feature extraction of underwater acoustic signals, we performed two comparative experiments for ambient noises (Ans) and ship-radiated noises (SRNs) by using feature extraction methods based on MSE, MFE, MPE, and MDE, respectively. The general structure of this paper is as follows: Section 2 introduces the basic theories of MSE, MFE, MPE, and MDE; Section 3 and Section 4 carry out the experiments of feature extraction and classification for six Ans and six SRNs separately; finally, and Section 5 is the conclusion of this article.

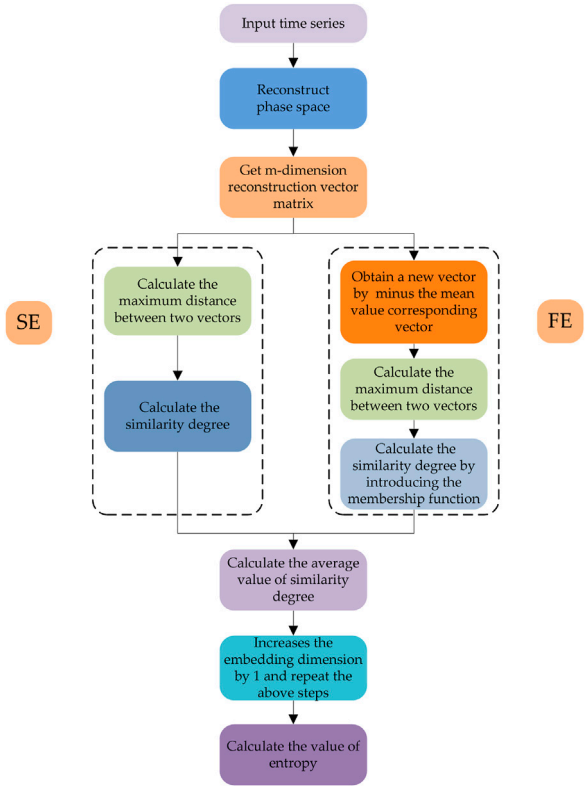

FIGURE 1
Flow chart of SE and FE.

2 Theory

2.1 Sample entropy and fuzzy entropy

Fuzzy entropy is an improved algorithm of sample entropy; SE and FE can be used to characterize the complexity of time series. Figure 1 shows the flow chart of SE and FE. In the flow of SE, the phase space of time series is reconstructed, next the maximum distance between two vectors is calculated to obtain the similarity degree and average value of similarity degree, and then, the embedding dimension is added to 1. By repeating the abovementioned steps, the value of SE can be calculated as follows:

$$En = ln\,\varphi^{m} - ln\,\varphi^{m+1}, \tag{1}$$

where m is the embedding dimension, φ^{m} is the average value of the similarity degree under the embedding dimension m, and φ^{m+1} is the average value of the similarity degree under the embedding dimension $m + 1$.

Compared with SE, in the flow of FE, after phase space reconstruction of time series, all elements of each vector are subtracted from the mean value of the corresponding vector, the maximum distance between two vectors is calculated, and the membership function is introduced to calculate the similarity; in

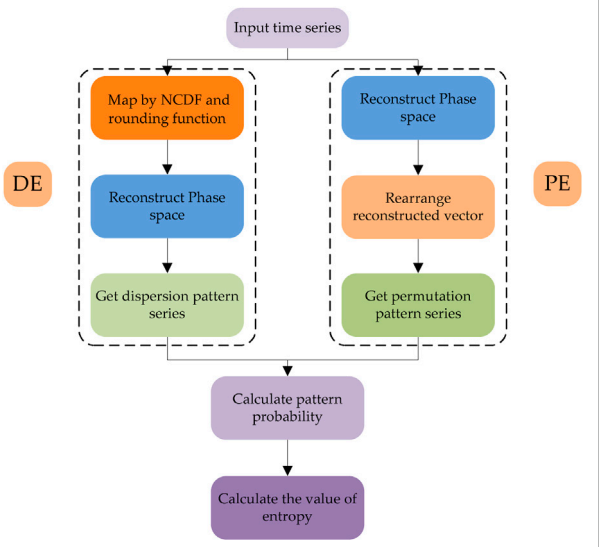

FIGURE 2
Flow chart of PE and DE.

addition, other steps are the same as in SE, and the value calculation formula is shown as Eqn. 1. The work in [14, 15] shows the specific steps of SE and DE, respectively.

2.2 Permutation entropy and dispersion entropy

PE and DE are algorithms based on the Shannon entropy theorem. Figure 2 depicts the flow chart of PE and DE, and their differences are shown in the dotted box. For DE, the time series is mapped to a new series by the normal cumulative distribution function (NCDF) and rounding function, and then we reconstruct the phase space of this new time series to obtain a dispersion pattern series, then we calculate pattern probability, and the value of entropy is defined as follows:

$$H_{En} = -\sum_{i=1}^{n} p(i) \cdot ln(p(i)), \tag{2}$$

where n is the number of pattern series and $p(i)$ is the probability of a corresponding pattern series.

For PE, the phase space of the time series is reconstructed directly, and then, we rearrange the reconstructed vectors to obtain a new array pattern sequence; then, we calculate pattern probability, and the value of PE is calculated by using Eqn. 2. The specific steps of PE and DE are shown in [22, 23], respectively.

2.3 Multi-scale method

The four types of entropy mentioned above can only measure the time series on a single scale, which often leads to a lack of series information. In order to solve this problem, the multi-scale method is adopted, the specific steps are as follows:

The coarse graining operation is introduced to a time series $X = \{x(i), i = 1, 2, \ldots, N\}$, the total length of the series is N, and the results of coarse graining can be defined as

$$y_j(g) = \frac{1}{g} \sum_{i=(j-1)g+1}^{jg} x(i), j = 1, 2, \cdots, \left[\frac{N}{g}\right], \tag{3}$$

where g represents the scale factor, $g = 1 \ldots ...$, and $[N/g]$ is the integer part of N/g, indicating the length of the coarse graining series. When g is 1, the coarse-grained series is the same as the original series. Next, the entropy of the time series at each scale is calculated to obtain multi-scale entropy.

3 Feature extraction of ANs

3.1 Ambient noise

Six distinct types of ANs are selected for complexity, feature extraction and recognition, which came from the National Park Service [29]. These ANs are labeled HRS, LRS, LWS, MWS, SS, and WSS, respectively. 400,000 sampling points are taken for each AN, and Figure 3 shows the time domain waveform of six ANs.

3.2 Single feature extraction and classification

In order to compare the feature extraction effects of four kinds of entropy for each AN. For each group of feature extraction experiments, we take 100 samples for each AN without repeating sampling points, and each sample is composed of 4000 sampling points. The MSE, MPE, MDE, and MFE of the six ANs are extracted from SF1 (SF1 means the scale factor 1, SF2 means the scale factor 2, and so on) to SF10. For comparison and analysis, Table 1 shows the parameter settings of four kinds of entropy.

It can be seen from Figure 4 that the MSE of HRS, LWS, SS, and WSS are mixed together; compared with MPE and MDE, MSE and MFE are better at distinguishing MWB; the discrimination effect of MPE on HRS and SS is better than the other three entropies; and each entropy of ANs has a large amount of aliasing. It concluded that the discrimination effect of four kinds of entropy four marine environmental noise is poor.

In order to compare the recognition effects of each entropy for six ANs more conveniently, we calculated the highest ARR of each AN under four kinds of entropy by the K-nearest neighbor (KNN) algorithm [30]. Table 2 shows the highest ARR of a single feature for six ANs.

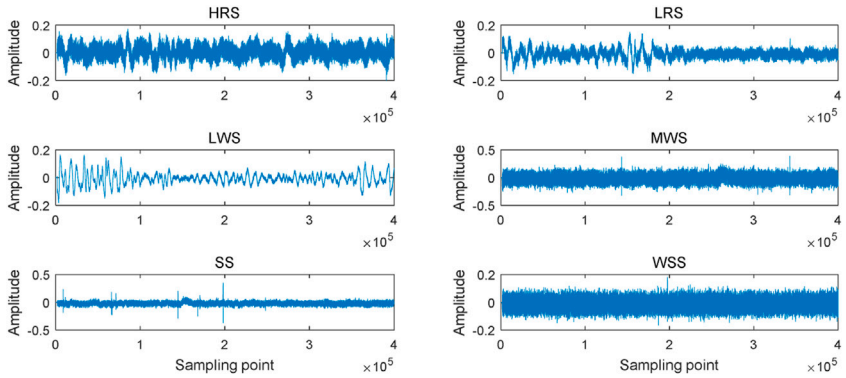

FIGURE 3
Time domain waveform of six ANs.

TABLE 1 Parameter settings of four kinds of entropy.

Entropy	Embedding dimension	Time delay	Category number	Threshold	Fuzzy power
MSE	5	1	-	0.15	-
MPE	5	1	-	-	-
MDE	5	1	5	-	-
MFE	5	1	-	0.15	2

As can be seen from Table 1, the embedding dimension and time delay of the four entropies are set to 5 and 1, respectively; the category number of MDE is 5; for MDE, the threshold c of both MSE and MFE is 0.15; the fuzzy power of MFE is 2. Figure 4 shows the single-feature distributions corresponding to the highest ARRs for six ANs.

It can be observed from Table 2 that the ARR of the four feature extraction methods for the six ANs is lower than 77.0% the recognition rate of the four feature extraction methods for HRS is higher than 60%; the recognition rates of the MSE-based feature extraction method for LRS and MWS is 100%; the ARR of the MSE-based feature extraction method for six ANs is the lowest, the ARR of the MFE-based feature extraction method for six ANs is the highest; it can be concluded that it is difficult to accurately distinguish six ANs by the single-feature extraction method.

3.3 Multi-feature extraction and classification

In order to further improve the recognition rate of the six ANs, the multi-feature extraction method based on four kinds of entropy is used to extract and classify the six ANs. Figure 5 indicates that the multi-feature distribution results correspond to the highest ARR for six ANs.

From the Figure 5, we can find that compared with the single-feature extraction method, the multi-feature extraction method has a better discrimination effect on six ANs; multi-feature extraction methods based on MSE and MFE have a better ability to distinguish MWS than MPE and MDE; compared with the other three feature extraction methods, the multi-feature extraction method based on MSE has the worst effect on SS; multi-feature extraction methods based on MFE are better at distinguishing WSS. Results show that compared with the other three feature extraction methods, the multi-feature extraction method based on MFE can better distinguish six ANs.

We calculate the highest average recognition rates of multi-features for six ANs by the KNN algorithm, in which (1, 3) represents double features of complexity parameter under SF1, and SF3 (1, 3, 5) represents triple features of complexity parameter under SF1, SF3, and SF5, and so on. Table 3 shows the highest ARR of four types of entropies for six ANs under different numbers of features. Figure 6 shows the highest ARR of four types of entropies for six ANs.

It can be seen from Table 3 and Figure 6 that with the increase of the number of features, the recognition of feature extraction methods based on the four entropy increases first rapidly and then decreases slowly; under the same number of features, the multi-feature extraction method based on MSE has the lowest recognition rate; the recognition rate of the multi-feature extraction method based on MFE is the highest, and reaches 98.7% when the number of extracted features is 3, which is at least 2.6% higher than the other three multi-feature

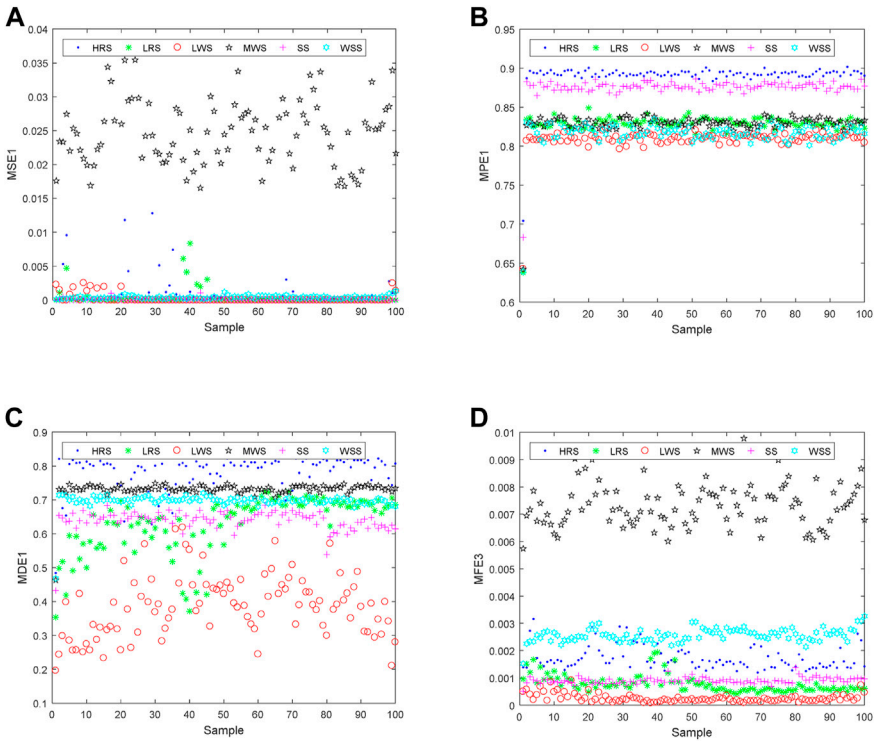

FIGURE 4
Single-feature distribution correspond to the highest ARR for six ANs. **(A)** is MSE, **(B)** is MPE, **(C)** is MDE, **(D)** is MFE.

TABLE 2 The highest ARR of a single feature for six ANs.

Entropy	SF	Recognition rate						ARR (%)
		HRS (%)	LRS (%)	LWS (%)	MWS (%)	SS (%)	WSS (%)	
MSE	1	62.0	100.0	6.0	100.0	16.0	70.0	59.0
MPE	1	94.0	46.0	64.0	34.0	100.0	30.0	61.3
MDE	1	94.0	6.0	72.0	90.0	56.0	86.0	67.3
MFE	3	74.0	50.0	98.0	100.0	68.0	68.0	76.3

extraction methods. The results show that the multi-feature extraction method can better identify six ANs, compared with the other three multi-feature extraction methods, MFE can better distinguish six ANs.

4 Feature extraction of SRNs

4.1 Ship-radiated noise signals

Six different types of SRNs are chosen for feature extraction and classification, which are called ship1, ship2, ship3, ship4, ship5 and ship6 respectively. The six types of SRNs are all from the National Park Service [29]. The number of sampling points of each type of SRN is 4×10^5 and the sampling frequency is 44.1 kHz. Figure 7 indicates the time domain waveform of six SRNs.

4.2 Single-feature extraction and classification

100 samples are selected for each type of S-Ss, and the sampling points of each sample is 4000. MSE, MPE, MDE, and

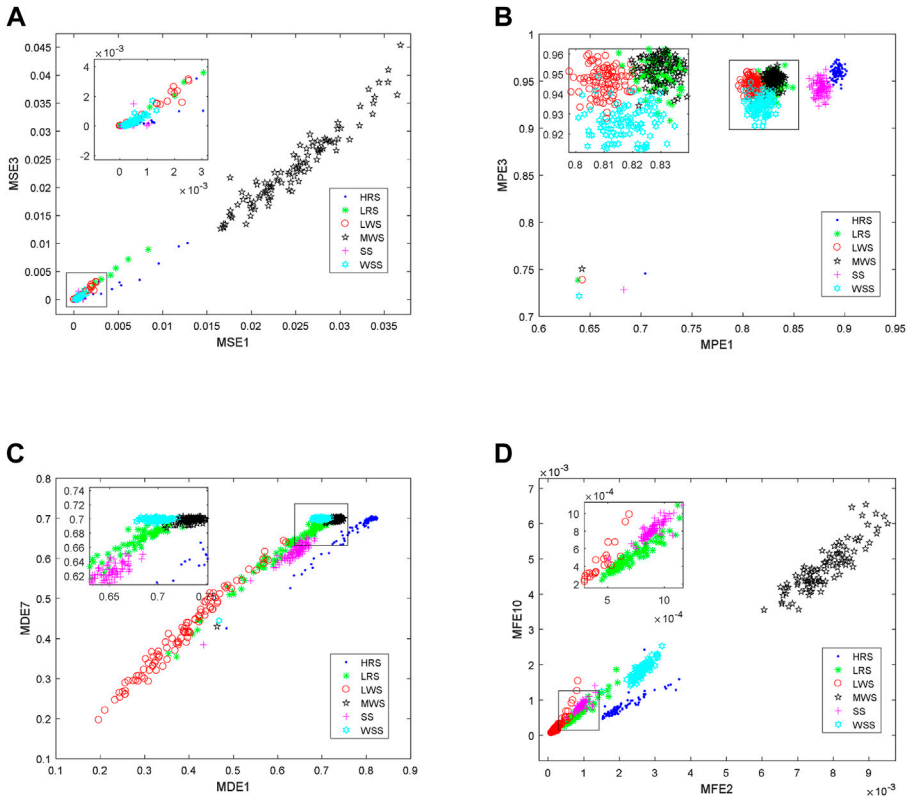

FIGURE 5
Multi-feature distribution results correspond to the highest ARR for six ANs. **(A)** is MSE, **(B)** is MPE, **(C)** is MDE, **(D)** is MFE.

TABLE 3 Highest ARR of four types of entropies for six ANs under different number of features.

Entropy	Parameters	Number of extracted features		
		2	3	4
MPE	ARR	80.0%	82.0%	82.7%
	SF combination	(1, 3)	(1, 3, 5)	(1, 3, 5, 7)
MDE	ARR	90.3%	92.3%	92.7%
	SF combination	(1,7)	(1, 3, 7)	(1, 3, 7, 9)
MFE	ARR	97.3%	98.7%	98.3%
	SF combination	(2, 10)	(1, 2, 10)	(1, 2, 3, 10)
MSE	ARR	66.3%	67.3%	68.0%
	SF combination	(1, 3)	(1, 3, 6)	(1, 2, 3, 6)

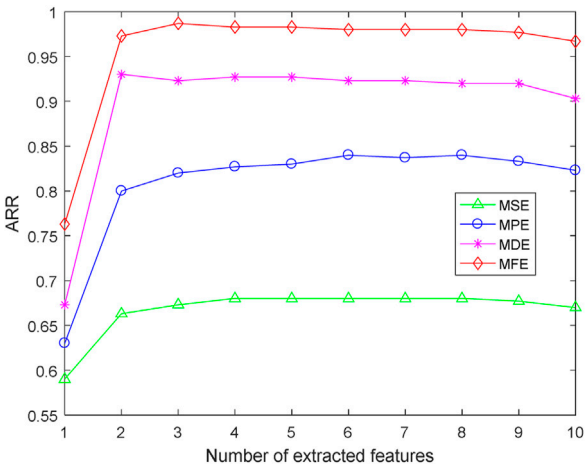

FIGURE 6
Highest ARR of four types of entropies for six ANs.

MFE of the six SRNs are extracted from SF1 to SF10. The parameters of the four kinds of entropy are consistent with those mentioned in Section 2; Figure 9 demonstrates the single-feature distributions corresponding to the highest ARR for six SRNs.

Figure 8 shows that for the four kinds of entropies, the feature distributions of six SRNs all have aliasing in general, especially ship3 and ship5; for MSE, the scattered points representing

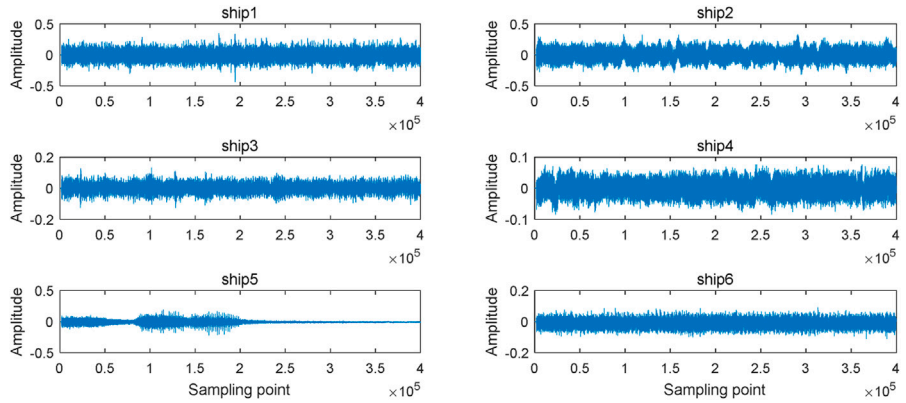

FIGURE 7
Time domain waveform of six SRNs.

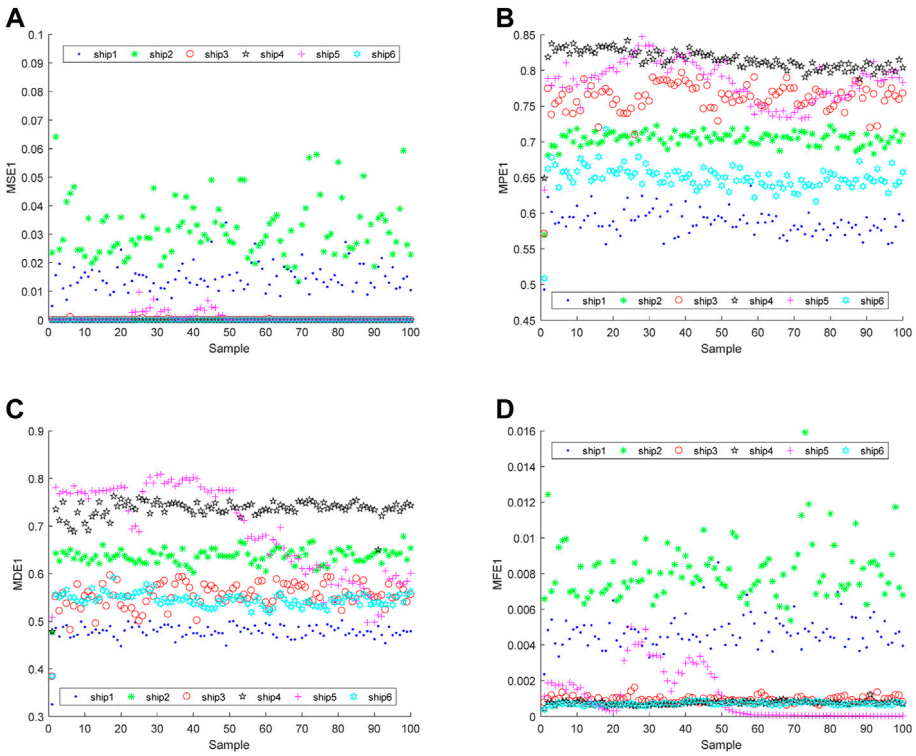

FIGURE 8
Single-feature distributions correspond to the highest ARR for six SRNs. **(A)** is MSE, **(B)** is MPE, **(C)** is MDE, **(D)** is MFE.

ship3 to ship6 are distributed almost in the same straight line; compared with MSE and MFE, the feature distributions of MPE and MDE have fewer overlapping areas; for MFE, the feature distributions of ship2 fluctuate in a larger area compared with that of other SRNs. In summary, only the single feature is adopted, which makes it difficult to distinguish the six S-Ss, and the MSE has the worst separability for six SRNs.

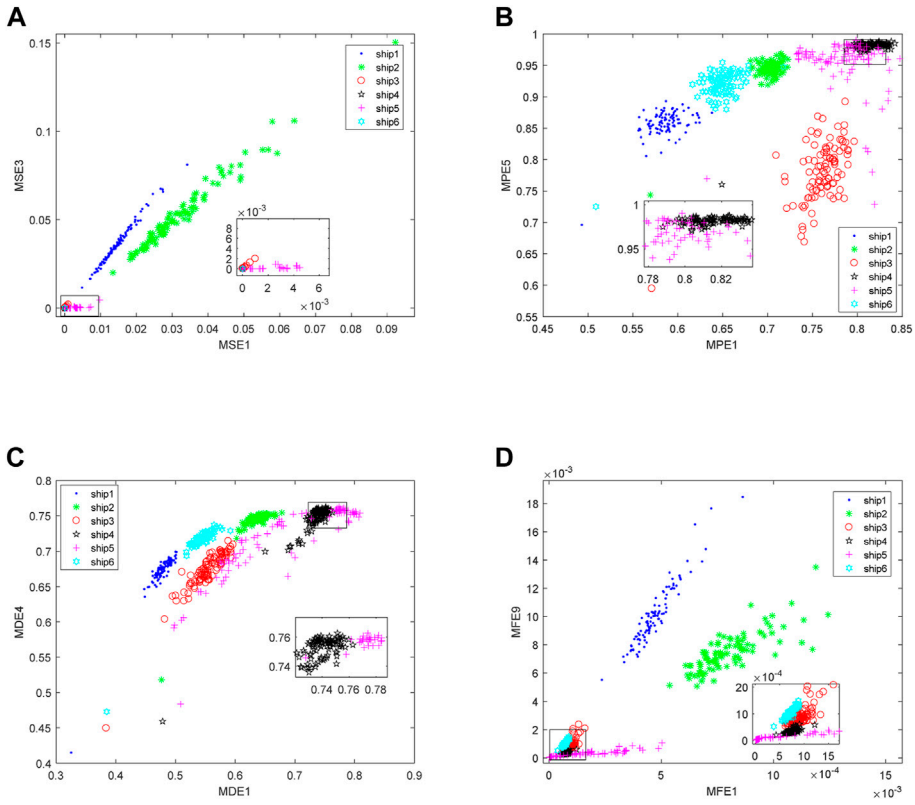

FIGURE 9
Multi-feature distributions correspond to the highest ARR for six SRNs. **(A)** is MSE, **(B)** is MPE, **(C)** is MDE, **(D)** is MFE.

TABLE 4 Highest ARR of a single feature.

Entropy	SF	Recognition rate						ARR (%)
		Ship1 (%)	Ship2 (%)	Ship3 (%)	Ship4 (%)	Ship5 (%)	Ship6 (%)	
MSE	1	86.0	86.0	78.0	0.0	0.0	4.0	42.3
MPE	1	86.0	96.0	90.0	26.0	26.0	92.0	69.3
MDE	1	96.0	98.0	44.0	98.0	12.0	60.0	68.0
MFE	1	86.0	98.0	54.0	40.0	100	52.0	71.7

In order to more obviously compare the average recognition rates of six SRNs, the KNN classifier was introduced to classify six different SRNs. 100 samples of each SRN are selected, of which 50 samples are used as training samples and the other 50 samples are test samples. Table 4 shows the highest ARR of a single feature.

From Table4, it can be concluded that, for the MSE-based feature extraction method, the ARR is the lowest, the recognition rates of ship4 and ship5 are 0%, and the recognition rate of ship6 only reaches 4%; compared with the feature extraction methods based on MSE, MPE, and MDE, the MFE-based feature extraction method has the highest ARR; for the feature extraction methods based on these four entropies, the highest ARRs are lower than 75%. It can be concluded that it is difficult to accurately distinguish six SRNs by the single-feature extraction method.

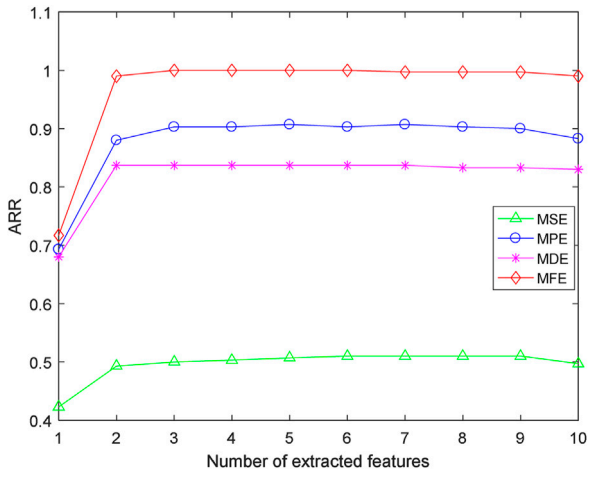

FIGURE 10
Highest ARR of four types of entropies for six SRNs.

TABLE 5 Highest ARR of four types of entropies for six SRNs under different number of features.

Entropy	Parameters	Number of features		
		2	3	4
MSE	ARR	49.3%	50.0%	50.3%
	SF combination	(1, 3)	(1, 2, 3)	(1, 2, 3, 4)
MPE	ARR	88.0%	90.3%	90.3%
	SF combination	(1, 5)	(1, 5, 10)	(1, 5, 7, 9)
MDE	ARR	83.7%	83.7%	83.7%
	SF combination	(1, 4)	(1, 2, 4)	(1, 2, 3, 5)
MFE	ARR	99.0%	100.0%	100.0%
	SF combination	(1, 9)	(1, 6, 8)	(1, 6, 7, 8)

4.3 Multi-feature extraction and classification

To more clearly compare the feature extraction effects of four kinds of entropies on six SRNs, we adopted the multi-feature extraction methods based on MSE, MPE, MDE, and MFE separately. Figure 9 shows the multi-feature distributions corresponding to the highest ARR for six SRNs.

It can be observed from Figure 9 that the aliasing of multi-feature distribution of MSE for six SRNs is the most serious, and the multi-feature distribution of MFE has the least overlapping part; for the four multi-feature extraction methods based on MSE, MPE, MDE, and MFE, respectively, they can accurately distinguish ship1 and ship2; compared with the other three multi-feature extraction methods, the MFE-based multi-feature extraction method has excellent performance in the recognition of ship5. In summary, the MFE-based multi-feature extraction method has the best separability for six kinds of ships.

In order to further compare the discrimination abilities of the four entropies for six SRNs, we calculated the highest average recognition rates of multi-features for six SRNs. Figure 10 is the highest ARR of four types of entropies for six SRNs, Table 5 shows the highest ARR of four types of entropies for six SRNs under different numbers of features.

As can be indicted from Figure 10 and Table 5, for the feature extraction methods based on the four types of entropy, the recognition rate for six SRNs increased with the increase of the number of features; under the same number of features, the highest ARR of the MSE-based feature extraction method is the lowest; the highest ARR of the MFE-based feature extraction method is higher than these of which based on the other types of entropy; the highest ARR of the MFE-based feature extraction method reaches 100% when the number of features is 3. In conclusion, compared with the extraction methods based on MSE, MPE, and MDE, the MFE-based feature extraction method has the highest recognition rate.

5 Conclusion

To effectively extract the features of the underwater acoustic signal, two comparative experiments were performed for the real-world underwater acoustic signal by using feature extraction methods on MSE, MPE, MDE, and MFE. The following conclusions are obtained:

1) Through the feature extraction and classification recognition of ANs, it is concluded that with the increase of the number of features, the recognition of the feature extraction method based on four entropies first increases rapidly and then decreases slowly. The multi-feature extraction method based on MFE has the best feature extraction effect and the highest ARR for six ANs with the same number of features.
2) In the feature extraction of SRNs, compared with feature extraction methods based on the other types of entropies, the highest ARR of MFE-based feature extraction method are the highest under the same number of features; the average recognition rate of MFE-based feature extraction method reaches 100% when the number of features is 3; the application of MFE in feature extraction can effectively

improve the performance of GNNS in positioning for marine target.

Data availability statement

The datasets presented in this study can be found in online repositories. The names of the repository/repositories and accession number(s) can be found in the article/supplementary material.

Author contributions

All authors listed have made a substantial, direct, and intellectual contribution to the work and approved it for publication.

Conflict of interest

The authors declare that the research was conducted in the absence of any commercial or financial relationships that could be construed as a potential conflict of interest.

Publisher's note

All claims expressed in this article are solely those of the authors and do not necessarily represent those of their affiliated organizations, or those of the publisher, the editors, and the reviewers. Any product that may be evaluated in this article, or claim that may be made by its manufacturer, is not guaranteed or endorsed by the publisher.

References

1. Li Q. Advances of research work in some areas of underwater acoustics signal processing. *Appl Acoust* (2001) 20(1):1–5. doi:10.15949/j.cnki.0371-0025.2001.04.002

2. Vaccaro R. J. The past, present, and the future of underwater acoustic signal processing. *IEEE Signal Process Mag* (1998) 15(4):21–51. doi:10.1109/79.689583

3. Wang Q., Zeng X., Wang L., Wang H., Cai H. Passive moving target classification via spectra multiplication method. *IEEE Signal Process Lett* (2017) 24(4):451–5. doi:10.1109/lsp.2017.2672601

4. Yang H., Li L., Li G. A new denoising method for underwater acoustic signal. *IEEE Access* (2020) 8:201874–88. doi:10.1109/access.2020.3035403

5. Li G., Chang W., Yang H. A new hybrid model for underwater acoustic signal prediction. *Complexity* (2020) 2020:1–19. doi:10.1155/2020/5167469

6. Jiang J., Shi T., Huang M., Xiao Z. Multi-scale spectral feature extraction for underwater acoustic target recognition. *Measurement* (2020) 166(15):108227. doi:10.1016/j.measurement.2020.108227

7. Banazadeh A., Seif M., Khodaei M., Rezaie M. Identification of the equivalent linear dynamics and controller design for an unmanned underwater vehicle. *Ocean Eng* (2017) 139:152–68. doi:10.1016/j.oceaneng.2017.04.048

8. Feng Z., Zuo M., Jian Q., Tian T., Liu Z. Joint amplitude and frequency demodulation analysis based on local mean decomposition for fault diagnosis of planetary gearboxes. *Mech Syst Signal Process* (2013) 40(1):56–75. doi:10.1016/j.ymssp.2013.05.016

9. Wang S., Zeng X. Robust underwater noise targets classification using auditory inspired time-frequency analysis. *Appl Acoust* (2014) 78:68–76. doi:10.1016/j.apacoust.2013.11.003

10. Li Y., Xiao C., Jing Y., Yang X. A fusion frequency feature extraction method for underwater acoustic signal based on variational mode decomposition, duffing chaotic oscillator and a kind of permutation entropy. *Electronics* (2019) 8(1):61. doi:10.3390/electronics8010061

11. Yang X., Wang L., Li X. A novel linear spectrum frequency feature extraction technique for warship radio noise based on complete ensemble empirical mode decomposition with adaptive noise, duffing chaotic oscillator, and weighted-permutation entropy. *Entropy* (2019) 21:507. doi:10.3390/e21050507

12. Li Y., Tang B., Yi Y. A novel complexity-based mode feature representation for feature extraction of ship-radiated noise using VMD and slope entropy. *Appl Acoust* (2022) 196:108899. doi:10.1016/j.apacoust.2022.108899

13. Chen Z., Li Y., Liang H., Yu J. Hierarchical cosine similarity entropy for feature extraction of ship-radiated noise. *Entropy* (2018) 20(6):425. doi:10.3390/e20060425

14. Li M., Liu H., Zhu W., Yang L. Applying improved multiscale fuzzy entropy for feature extraction of MI-EEG. *Appl Sci* (2017) 7(1):92. doi:10.3390/app7010092

15. Manis G., Aktaruzzaman M., Sassi R. Low computational cost for sample entropy. *Entropy* (2018) 20(1):61. doi:10.3390/e20010061

16. Cuesta-Frau D., Miró-Martínez P., Oltra-Crespo S., Molina-Picó A., Dakappa P. H., Mahabala C., et al. Classification of fever patterns using a single extracted entropy feature: A feasibility study based on sample entropy. *Math Biosciences Eng* (2020) 17(1):239–49. doi:10.3934/mbe.2020013

17. Richman J., Moorman J. Physiological time-series analysis using approximate entropy and sample entropy. *Am J Physiology-Heart Circulatory Physiol* (2000) 278:H2039–49. doi:10.1152/ajpheart.2000.278.6.h2039

18. Chen W., Wang Z., Xie H., Yu W. Characterization of surface EMG signal based on fuzzy entropy. *IEEE Trans Neural Syst Rehabil Eng* (2007) 15(2):266–72. doi:10.1109/tnsre.2007.897025

19. Zanin M., Zunino L., Rosso O., Papo D. Permutation entropy and its main biomedical and econophysics applications: A review. *Entropy* (2012) 14(8):1553–77. doi:10.3390/e14081553

20. Li Y., Li Y., Chen Z., Chen X. Feature extraction of ship-radiated noise based on permutation entropy of the intrinsic mode function with the highest energy. *Entropy* (2016) 18(11):393. doi:10.3390/e18110393

21. Li Y., Geng B., Jiao S. Dispersion entropy-based lempel-ziv complexity: A new metric for signal analysis. *Chaos Solitons Fractals* (2022) 161:112400. doi:10.1016/j.chaos.2022.112400

22. Bandt C., Pompe B. Permutation entropy: A natural complexity measure for time series. *Phys Rev Lett* (2002) 88:174102. doi:10.1103/physrevlett.88.174102

23. Rostaghi M., Azami H. Dispersion entropy: A measure for time series analysis. *IEEE Signal Process Lett* (2016) 23:610–4. doi:10.1109/lsp.2016.2542881

24. Anne H. Multiscale entropy approaches and their applications. *Entropy* (2020) 22(6):644. doi:10.3390/e22060644

25. Wang Y., Liang Z., Voss L. J., Sleigh J. W., Li X. Multi-scale sample entropy of electroencephalography during sevoflurane anesthesia. *J Clin Monit Comput* (2014) 28:409–17. doi:10.1007/s10877-014-9550-1

26. Lebreton C., Kbidi F., Graillet A., Jegado T., Alicalapa F., Benne M., et al. PV System failures diagnosis based on multiscale dispersion entropy. *Entropy* (2022) 24(9):1311. doi:10.3390/e24091311

27. Zhao H., Sun M., Deng W., Yang X. A new feature extraction method based on EEMD and multi-scale fuzzy entropy for motor bearing. *Entropy* (2017) 19(1):14. doi:10.3390/e19010014

28. Li Y., Li Y., Yu J. A novel feature extraction method for ship-radiated noise based on variational mode decomposition and multi-scale permutation entropy. *Entropy* (2017) 19(7):342. doi:10.3390/e19070342

29. National Park Service. Soundclips (2022). Available At: https://www.nps.gov/glba/learn/nature/soundclips.

30. Venkatesan C., Karthigaikumar P., Varatharajan R. A novel LMS algorithm for ECG signal preprocessing and KNN classifier based abnormality detection. *Multimed Tools Appl* (2018) 77:10365–74. doi:10.1007/s11042-018-5762-6

frontiers | Frontiers in Physics

TYPE Original Research
PUBLISHED 11 November 2022
DOI 10.3389/fphy.2022.1070920

OPEN ACCESS

EDITED BY
Govind Vashishtha,
Sant Longowal Institute of Engineering and Technology, India

REVIEWED BY
Vikrant Guleria,
Sant Longowal Institute of Engineering and Technology, India
Sumika Chauhan,
National Institute of Technology Delhi, India

*CORRESPONDENCE
Jianbo Zhou,
jbzhou@nwpu.edu.cn

SPECIALTY SECTION
This article was submitted to Physical Acoustics and Ultrasonics, a section of the journal Frontiers in Physics

RECEIVED 15 October 2022
ACCEPTED 31 October 2022
PUBLISHED 11 November 2022

CITATION
Liang N, Zhou J and Yang Y (2022), Revising the application of cross-spectrum processing in motion parameter estimation for harmonic sources.
Front. Phys. 10:1070920.
doi: 10.3389/fphy.2022.1070920

Revising the application of cross-spectrum processing in motion parameter estimation for harmonic sources

Ningning Liang[1,2], Jianbo Zhou[1,2]* and Yixin Yang[1,2]

[1]School of Marine Science and Technology, Northwestern Polytechnical University, Xi'an, China, [2]Shaanxi Key Laboratory of Underwater Information Technology, Northwestern Polytechnical University, Xi'an, China

Single-receiver motion parameter estimation is an effective and economical technology for passive source localization and train-bearing fault diagnosis, in which time-consuming time-frequency analysis (TFA) methods are widely used to suppress noise when extracting the continuous Doppler shift of the overhead pass. Cross-spectrum processing is a potential way to improve the computational efficiency of TFA methods, but its application is overshadowed by the phenomena of unknown Doppler shift offset and power spectrum estimation error. In this paper, conventional cross-spectrum processing is proven to be an approximation trick for power spectrum estimation in a small frequency interval, and the two phenomena are fully explained by the frequency aliasing of bandpass sampling and the approximation error. On this basis, an revised framework for applying the cross-spectrum processing is provided. Processing results of the SWellEx-96 experiment data demonstrate that the computational efficiencies of spectrogram and a parameterized TFA method could be improved up to 85% and 88.2%, respectively, without a noticeable impact on the accuracy of parameter estimates.

KEYWORDS

Doppler shift, motion parameter estimation, time-frequency analysis, single receiver, cross-spectrum processing, computational efficiency

1 Introduction

Received single-frequency noise, which frequency changes with time dramatically during the overhead pass, contains lots of information about the moving target. By fitting the observed time-varying instantaneous frequency (IF) curve of these tones with the model of Doppler shift under the nonlinear least squares criterion, the Doppler-related parameters, e.g., the radiated frequency, the moving speed, and the shortest distance between the receiver and the target, can be estimated easily and economically with only a single receiver. The conventional application of this single-receiver parameter estimation method are source recognition, classification and localization [1]. In addition, this method is also able to be jointed with the bearing fault identification methods [2, 3] and serves for

train-bearing fault diagnosis [4, 5] through an non-contact way in wayside during the running of a train.

Many studies have addressed the estimation of Doppler-related parameters from the line spectrum with a single receiver, where the key point of these studies is how to extract the IF curve from the received tones. The earliest approach may be the phase interpolation method, Ferguson [6] used it to observe and compare the variation with time of the aircraft's blade rate from the received tones of a microphone on land and a hydrophone beneath the sea. Then Ferguson and Quinn [1] introduced time-frequency analysis (TFA) methods to obtain an more accurate estimation for the aircraft's blade rate. Because the parameter estimation precision is primarily determined by the accuracy of the extracted IF curve, many of the advanced TFA methods [7–11] have been investigated to suppress noise and concentrate energies for IF contents. Nevertheless, against the classical short-time Fourier transform (STFT, also called a spectrogram), these more effective TFA methods are highly inefficient in computation [10, 11].

Cross-spectrum processing is a potential way to improve the computational efficiency of TFA methods. Rakotonarivo and Kuperman [12] have shown that the radial velocity feature between a moving tone source and a fixed receiver can be quickly ascertained from the cross-spectrum of sound pressures. Yang et al. [13] derived the same results in a different way. Build on this knowledge cross-spectrum processing has been extended to scenarios of a single vector hydrophone [14] and a multi-tone source [15]. However, this method requires precise knowledge regarding the frequency of radiated tones to determine the time interval of the cross-spectrum processing, which should be strictly an integer multiple of the period of the tone signal. If a time interval of a non-integral multiple of the period of the tone signal is utilized, an unknown offset, which has been confirmed by Wang et al. [16], will be brought into the estimates of the radial velocity and will prevent the motion parameter estimation. In addition, it is found that false IF curves of Doppler shift exist occasionally and can not be predicted by the cross-spectrum theory. Apparently these two phenomena leads to the inability of this cross-spectrum method to general applications.

This paper analyzes reasons behind the two unwelcome phenomena and tries to perfect the way of applying cross-spectrum processing in parameter estimations. The main content is organized as follows. Section 2 discusses reasons behind the two unwelcome phenomena. Section 3 outlines the revised framework of applying the cross-spectrum processing for the fast parameter estimation and explains its details for implementation. Section 4 verifies the computational efficiency of the revised framework with the received tones in the event S5 of the SWellEx-96 experiment. Finally, Section 5 draws some conclusion.

2 A deep understanding about the cross-spectrum method

2.1 Conventional cross-spectrum method

Conventional cross-spectrum method [12] is proposed in the community of underwater acoustics. According to the normal mode theory [17], the expression of sound pressures in ocean waveguide under general conditions is:

$$p(r,z) = \sum_{m=1}^{M} A_m \exp(jk_{rm}r), \tag{1}$$

where

$$A_m = Q\frac{\psi_m(0,z_s)\psi_m(r,z)}{\sqrt{k_{rm}r}}, \tag{2}$$

Q is a constant, r is the horizontal distance between the receiver and the point source, z is the receiver depth, z_s is the source depth, M is the number of propagating modes, and ψ_m and k_{rm} are the modal depth function and the horizontal wavenumber of the mth mode, respectively.

Assume that r is the distance between a moving source and a receiver at time t, and the corresponding radial velocity is v_r, which satisfies $\Delta r = v_r\Delta t$ in a small time interval. Then, sound pressures at $t + \frac{\Delta t}{2}$ and $t - \frac{\Delta t}{2}$ can be expressed as:

$$\begin{aligned} p\left(t+\frac{\Delta t}{2}\right) &= p\left(r+\frac{\Delta r}{2}\right) = \sum_m A_m \exp\left(jk_{rm}\left(r+\frac{\Delta r}{2}\right)\right) \\ p\left(t-\frac{\Delta t}{2}\right) &= p\left(r-\frac{\Delta r}{2}\right) = \sum_m A_m \exp\left(jk_{rm}\left(r-\frac{\Delta r}{2}\right)\right) \end{aligned}. \tag{3}$$

The cross spectrum of these two sound pressures $p(t + \frac{\Delta t}{2})$ and $p(t - \frac{\Delta t}{2})$ is [12]:

$$\begin{aligned} I_c(t,f_0,\Delta t) &= p\left(t-\frac{\Delta t}{2}\right)p^*\left(t+\frac{\Delta t}{2}\right) \\ &\approx \exp(-j\bar{k}_r\Delta r)\sum_{m,n} A_m A_n^* \exp(j\Delta k_{mn}r) \end{aligned}, \tag{4}$$

where $\bar{k}_r = 2\pi f_0/c_p$ at frequency f_0, c_p is the average modal phase speed and can be approximated by the (average) sound speed of water $c_p \approx c$ in practical applications, and $\Delta k_{mn} = k_{rm} - k_{rn}$ is the difference between the horizontal wavenumber of the nth mode and that of the mth mode.

Because the oscillations of $\exp(-j\Delta k_{mn}r)$ exhibit a much longer period than those of $\exp(-j\bar{k}_r\Delta r)$, $I_c(t, f_0, \Delta t)$ should be dominated by the latter term, i.e.,

$$I_c(t,f_0,\Delta t) \propto \exp(-j\bar{k}_r\Delta r) = \exp\left(-j2\pi\frac{f_0 v_r}{c}\Delta t\right). \tag{5}$$

In cross-spectrum method, the sound pressures of a given frequency f_0 at different times are extracted from the spectrogram of the received time series. Then, oscillation frequency $\frac{f_0 v_r}{c}$ at time t can be determined simply by the Fourier spectrum of cross-spectrum series $I_c(t, f, n\Delta)$, where n is the positive integer and Δ

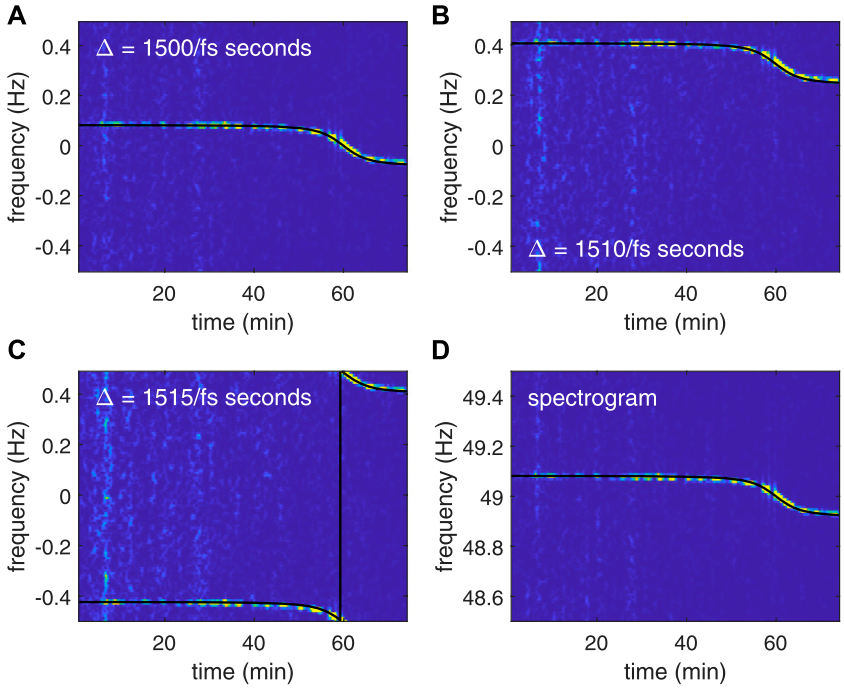

FIGURE 1
The SWellEx-96 signal used in Section 4 is employed to illustrate the phenomenon of Doppler shift offset. The sampling rate of the signal is f_s = 1,500 Hz. **(A–C)** illustrate, respectively, the TFDs produced by the conventional cross-spectrum method (i.e., the step R2.3 of F-STFT without compensation) with different lengths of the spectral window N_{w1} = [1,500, 1,510, 1,515] in sound pressures extraction. Black curves represent the IF curves of each TFD predicted by the bandpass sampling theorem. Frequency axes of these TFDs represent oscillation frequency $\frac{f_0 v_r}{c}$. For a comparison, **(D)** shows the TFD produced by STFT and the theoretical IF curve given by Eq. A7. It can be seen that a slight increase of N_{w1} brings a significant offset for the aliased IF trajectories.

is the time difference between two adjacent segments in the spectrogram. Since f_0 and c are known, one gets the value of radial velocity v_r at time t. Finally, Doppler-related parameters can be obtained by fitting the observed time-varying v_r curve with its mathematical model under the nonlinear least squares criterion.

2.2 Phenomenon of Doppler shift offset and its interpretation

A problem in applications of the conventional cross-spectrum method is that the method requires precise knowledge regarding the frequency of the tone signal, i.e., f_0, to determine the time difference Δ between two adjacent segments in the spectrogram, where Δ should be a strict integer multiple of the period of f_0. However, in general applications, f_0 is often not accurately known and the sampling frequency f_s may be a non-integral multiple of f_0. As a result, an appropriate Δ is hard to be determined and f_0 will not appear in the frequency axis of the spectrogram, one can only extract sound pressures from the closest frequency point to f_0. In such a case, as shown in Figure 1, slight changes of Δ produce an remarkable offset to the oscillation frequency $\frac{f_0 v_r}{c}$. Because the quantity of offset cannot be predicted by the theory of cross-spectrum processing, further processing for parameter estimation is prevented.

Loosely, the procedure of extracting sound pressures from the spectrogram can be regarded as a procedure of resampling to the received time series with sampling rate $f_s = 1/\Delta$. Bandpass sampling theorem [18] shows that, if a tone is sampled at a frequency that less than the Nyquist sampling rate, its real frequency f_0 will be misrepresented by an aliased frequency $f' = f_0 - \text{round}(f_0/f_s) \times f_s$ that do lie within the range $[-f_s/2, f_s/2)$ because

$$\begin{aligned}\exp(j2\pi f_0 t) &= \exp(j2\pi(f' + \text{round}(f_0/f_s) \times f_s)t) \\ &= \exp(j2\pi f' t + 2\pi \text{round}(f_0/f_s) \times f_s t) \\ &= \exp(j2\pi f' t)\end{aligned} \quad (6)$$

at any sampling time $t = n\Delta$, where n is the positive integer and the function round(x) rounds x to its nearest integer. Therefore, for the received IF curve of Doppler shift $f = f_0(1 - v_r/c)$ (i.e., Eq. A7 in Appendix), if the time difference Δ between two adjacent segments in the spectrogram is a strict integer multiple of the period of f_0, i.e., $f_0/f_s = \text{round}(f_0/f_s)$, we have the aliased frequency $f' = \frac{f_0 v_r}{c}$. On the other hand, if Δ is not an

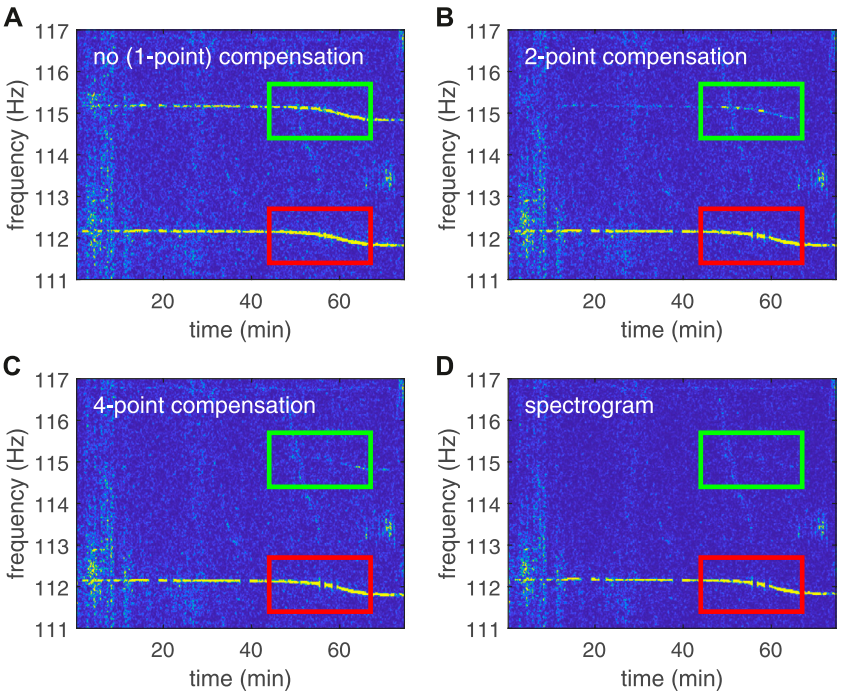

FIGURE 2
The SWellEx-96 signal used in Section 4 is employed to illustrate the phenomenon of power spectrum error. **(A–C)** illustrate, respectively, the TFDs produced by Eq. 9 (i.e., the step R2.4 of F-STFT) with different compensations, where the length of the spectral window $N_{w1} = 500$. The aliased IF trajectories has been mapped into the real frequency band by a contrary procedure of aliasing. **(D)** Shows the TFD produced by STFT. The green rectangles show the changes of an aliased IF trajectory with the increase of compensation points, and the red rectangles show the changes of the target IF trajectory with the increase of compensation points. It can be seen that a few compensation points are able to give a good approximation for the spectrogram if the phenomenon of power spectrum error occurs.

integer multiple of the period of f_0, i.e., $f_0/f_s \neq \text{round}(f_0/f_s)$, we have the aliased frequency $f' = \frac{f_0 v_r}{c} + f_{\text{offset}}$, where $f_{\text{offset}} = f_0 - \text{round}(f_0/f_s) \times f_s$ denotes the quantity of offset.

The black curves in the Figures 1A–C represent the aliased IF trajectories predicted by the bandpass sampling theorem. One can see that these curves are consistent well with the IF trajectories of each TFD.

2.3 Phenomenon of power spectrum error and its interpretation

As shown in Figures 2A,D, the TFD of the cross-spectrum method and that of the spectrogram may be different sometimes. Although bandpass sampling theory provides a well interpretation for the offset phenomenon, the theory can not interpret such a difference because power spectrum of the real frequency and the aliased frequency should be equal according to Eq. 6. Therefore, technically the procedure of extracting sound pressures from the spectrogram is not a procedure of bandpass sampling.

In the cross-spectrum method, the radial velocity is estimated from the cross-spectrum of pressures (i.e., $p(t + \Delta)p^*(t)$, $p(t + 2\Delta)p^*(t)$, $\cdots$). According to the linearity property of Fourier transform, the Fourier spectrum of $p(t + \Delta)p^*(t)$, $p(t + 2\Delta)p^*(t)$, $\cdots$ equals the weighted (by $p^*(t)$) Fourier spectrum of $p(t + \Delta)$, $p(t + 2\Delta)$, $\cdots$. Because multiplying a constant $p^*(t)$ does not induce useful information of radial velocity, the information of radial velocity should be included in the Fourier spectrum of $p(t + \Delta)$, $p(t + 2\Delta)$, $\cdots$. Therefore, the cross-spectrum processing (i.e., multiplying the $p^*(t)$) is unnecessary and can be omitted to simplify processing steps. In addition, note that the pressures $p(t + \Delta)$, $p(t + 2\Delta)$, $\cdots$ are extracted from the spectrogram of the received time series in practice but are not directly time-sampled from the received signals as a conventional manner of sampling does, these two sampling manners are not of equivalence as analyzed below.

Suppose that $x(q)$ is a discrete signal and $q = 0, 1, \ldots, NM - 1$, where N and M are two positive integers. Its discrete Fourier transform (DFT) at frequency $\frac{k}{NM}$ is given as:

$$Y(k) = \sum_{q=0}^{NM-1} x(q) e^{-j2\pi \frac{k}{NM} q}, \tag{7}$$

where $k = 0, 1, \ldots, NM - 1$.

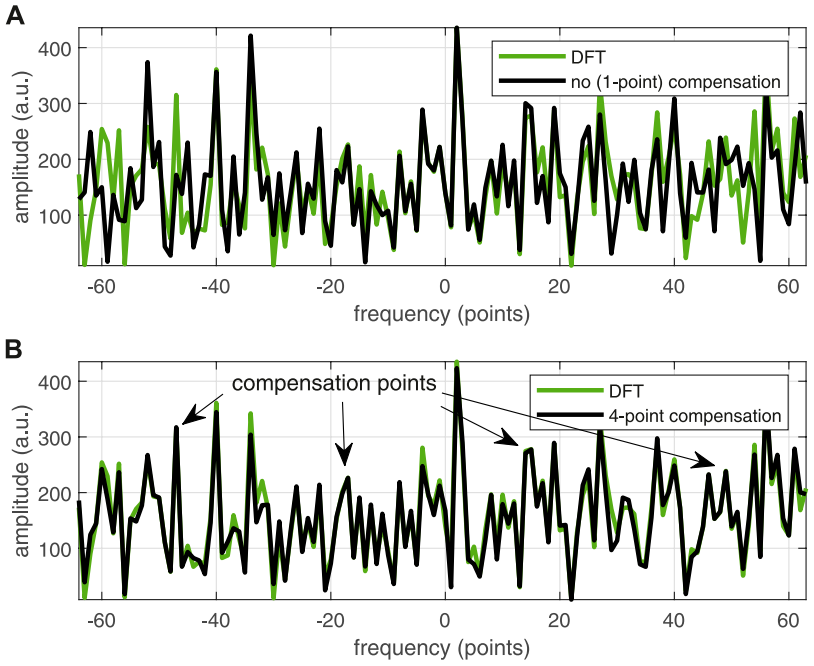

FIGURE 3
Power spectrum of an random sequence given by Eq. 7 (green curves) and Eq. 9 (black curves) with $N = 64$, $M = 128$. **(A)** No compensation, default $k_2 = 0$. **(B)** Four-point compensation, $k_2 = -48, -16, 15, 47$. Note that the horizontal axis, i.e., k_2, is limited to $[-M/2, M/2-1]$ rather than $[0, M-1]$ to shift zero-frequency component to the center of spectrum with the purpose of fitting the axis of green curves.

Defining $X(n,m) = x(n+Nm)$, i.e., we reshape the discrete signal $x(q)$ to an $N \times M$ matrix. Then, the DFT of column m of X at frequency $\frac{k_1}{N}$ is given as:

$$Y_1(k_1, m) = \sum_{n=0}^{N-1} X(n,m) e^{-j2\pi \frac{k_1}{N} n}, \tag{8}$$

where $k_1 = 0, 1, \ldots, N-1$. If $f_0 \approx \frac{k_1}{N}$, then the row k_1 of Y_1 represents the pressures $p(t+\Delta)$, $p(t+2\Delta)$, $\cdots$ according to the cross-spectrum processing.

Further, the DFT of row k_1 of Y_1 at frequency $\frac{k_2}{M}$ is given as:

$$\begin{aligned} Y_2(k_2) &= \sum_{m=0}^{M-1} Y_1(k_1, m) e^{-j2\pi \frac{k_2}{M} m} \\ &= \sum_{m=0}^{M-1} \sum_{n=0}^{N-1} X(n,m) e^{-j2\pi \frac{k_1}{N} n} e^{-j2\pi \frac{k_2}{M} m} \\ &= \sum_{m=0}^{M-1} \sum_{n=0}^{N-1} X(n,m) e^{-j2\pi \frac{(n+Nm)(Mk_1+k_2)}{NM}} e^{j2\pi \frac{nk_2}{NM}} e^{j2\pi m k_1} \\ &= \sum_{m=0}^{M-1} \sum_{n=0}^{N-1} X(n,m) e^{-j2\pi \frac{(n+Nm)(Mk_1+k_2)}{NM}} e^{j2\pi \frac{nk_2}{NM}} \\ &= \sum_{m=0}^{M-1} \sum_{n=0}^{N-1} x(n+Nm) e^{-j2\pi \frac{(n+Nm)(Mk_1+k_2)}{NM}} e^{j2\pi \frac{nk_2}{NM}} \\ &= \sum_{q=0}^{NM-1} \left[x(q) e^{j2\pi \frac{k_2}{NM} \bmod (q,N)} \right] e^{-j2\pi \frac{(Mk_1+k_2)}{NM} q}, \end{aligned} \tag{9}$$

where the function $\bmod(q, N)$ denotes the remainder after the division of q by N. Due to the presence of the term $e^{j2\pi \frac{k_2}{NM} \bmod (q,N)}$, $Y_2(k_2)$ equals to $Y(Mk_1 + k_2)$ only when $k_2 = 0$. However, $e^{j2\pi \frac{k_2}{NM} \bmod (q,N)} \approx 1$ when k_2 approaches 0, considering the periodicity of the term we have

$$Y_2(k_2) \approx \begin{cases} Y(Mk_1 + k_2), & 0 \le k_2 < (M-1)/2 \\ Y(Mk_1 + k_2 - M), & (M-1)/2 \le k_2 \le M-1 \end{cases}. \tag{10}$$

Eq. 10 shows that the Fourier spectrum of pressures $p(t+\Delta)$, $p(t+2\Delta)$, $\cdots$ can be regarded as only an approximation for that of the received time series in a narrow frequency band, where the frequency band corresponds with that indicated by the bandpass sampling theory (i.e., Eq. 6). Therefore, one can safely map the aliased IF trajectories into the real frequency band by a contrary procedure of aliasing. Obviously, this approximation allows for the improvement of the computational efficiency by using shorter N-point DFT and M-point DFT to substitute a longer NM-point DFT.

As is shown in Figure 3A, because $Y_2 = Y$ holds true only when $k_2 = 0$ and the effect of the term $e^{j2\pi \frac{k_2}{NM} \bmod (q,N)}$ increases with the growth of values of k_2, directly applying Eq. 9 gives good approximations around zero-frequency, and relatively bad approximations far from zero-frequency. To

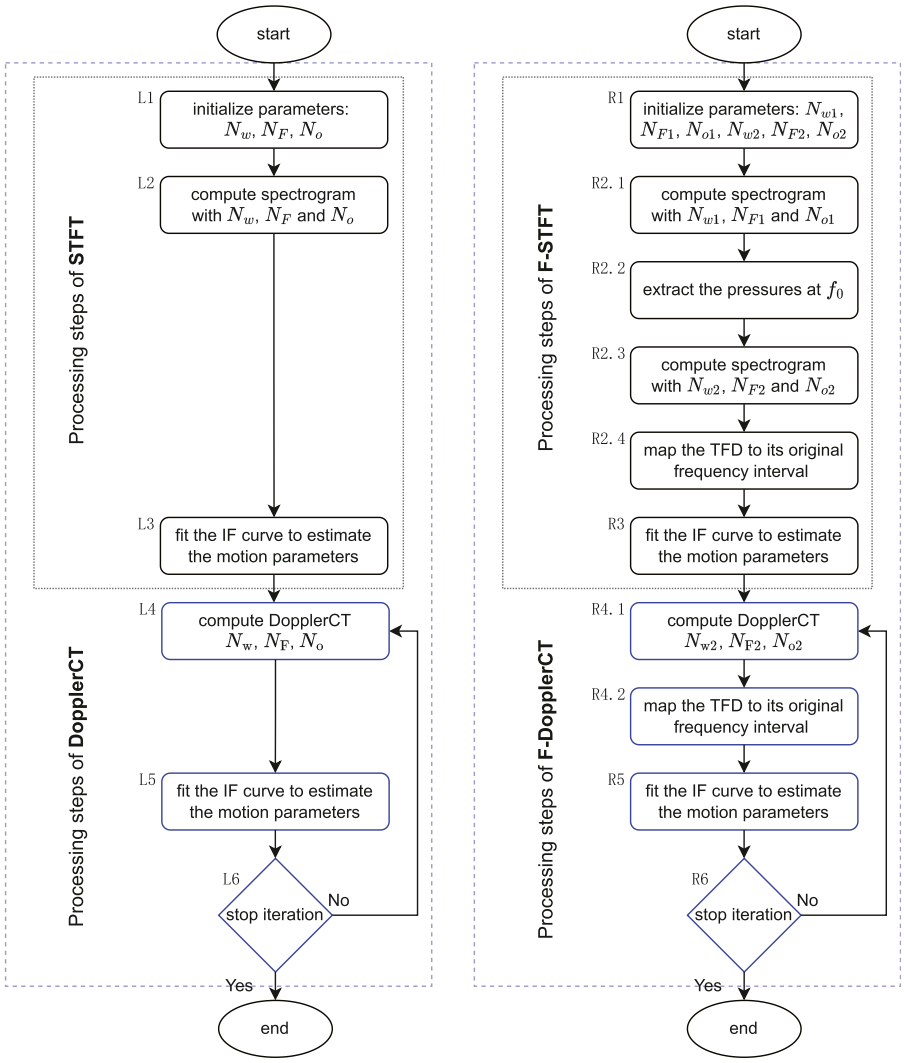

FIGURE 4
Flowcharts to illustrate the conventional framework (the left flowchart) and the suggested framework for fast parameter estimations (the right flowchart). The tags R1-R5 and L1-L5 indicate each step of the two flowcharts.

improve the degree of accuracy, one can multiply $x(q)$ by the complex conjugation of the term $e^{j2\pi\frac{k_2}{NM} \bmod (q,N)}$ in advance to compensate its effect. When each of the points of k_2 are well-compensated, the results of Y_2 (Eq. 9) will be exactly equal to the results of Y (Eq. 7). However, because the spectrum of the adjacent points in a small interval of k_2 can be well-approximated by the spectrum of the centre point, compensating for all of the points of k_2 is not very necessary. As shown in Figure 3B, compensating a few points of k_2 is sufficient to approximate the real spectrum. In practice, sharing the same compensation in adjacent points is a useful trick for maintaining high computational efficiency. One can balance the demand for computational efficiency and the demand for the degree of accuracy by simply adjusting the number of compensation points from 1 to M.

Figures 2B,C depict the TFDs computed by Eq. 9 with 2-point compensation and 4-point compensation, respectively. As the green rectangles and the red rectangles show, a few compensation points are able to significantly reduce the TFD difference between the approximate method and the spectrogram.

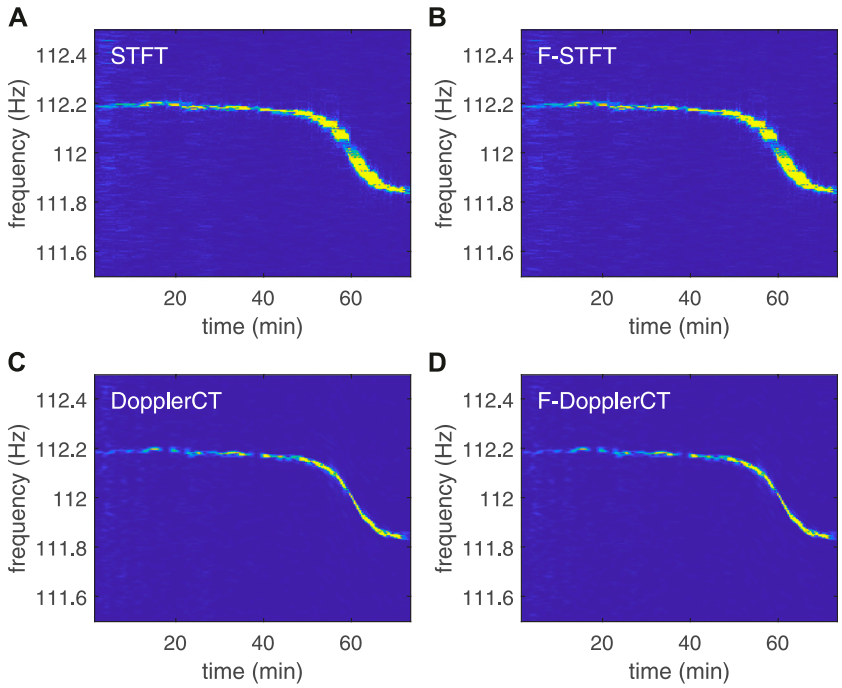

FIGURE 5
TFDs of the 112Hz tone that given by different methods : **(A)** STFT, **(B)** F-STFT, **(C)** DopplerCT, **(D)** F-DopplerCT. It is clearly shown that the two fast methods is able to generate almost the same TFDs as STFT and DopplerCT.

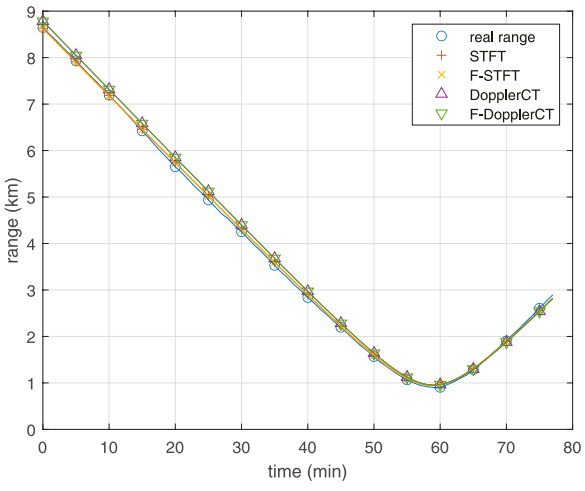

FIGURE 6
Comparison of the source range given by GPS records and that estimated from the IF curves depicted in Figure 5.

3 An revised parameter estimation framework of applying cross-spectrum processing

The processing framework for fast parameter estimations based on Eq. 9, together with the conventional framework of motion parameter estimations, are shown in Figure 4, where STFT and Doppler chirplet transform (DopplerCT) [10] are employed as the representatives of the conventional and the advanced TFA methods, respectively. For ease of description, these two TFA methods implemented based on Eq. 9 are denoted below as F-STFT and F-DopplerCT. Note that the first iteration of parameterized TFA methods (DopplerCT and F-DopplerCT) needs some configuration parameters, these parameters are initialized by the estimates of the conventional non-parameterized methods (STFT and F-STFT) in Figure 4. Therefore, STFT can be regarded as the 0th iteration of DopplerCT, and consequently, the processing with STFT is always faster than the processing with DopplerCT. Same goes for the relationship of F-STFT and F-DopplerCT.

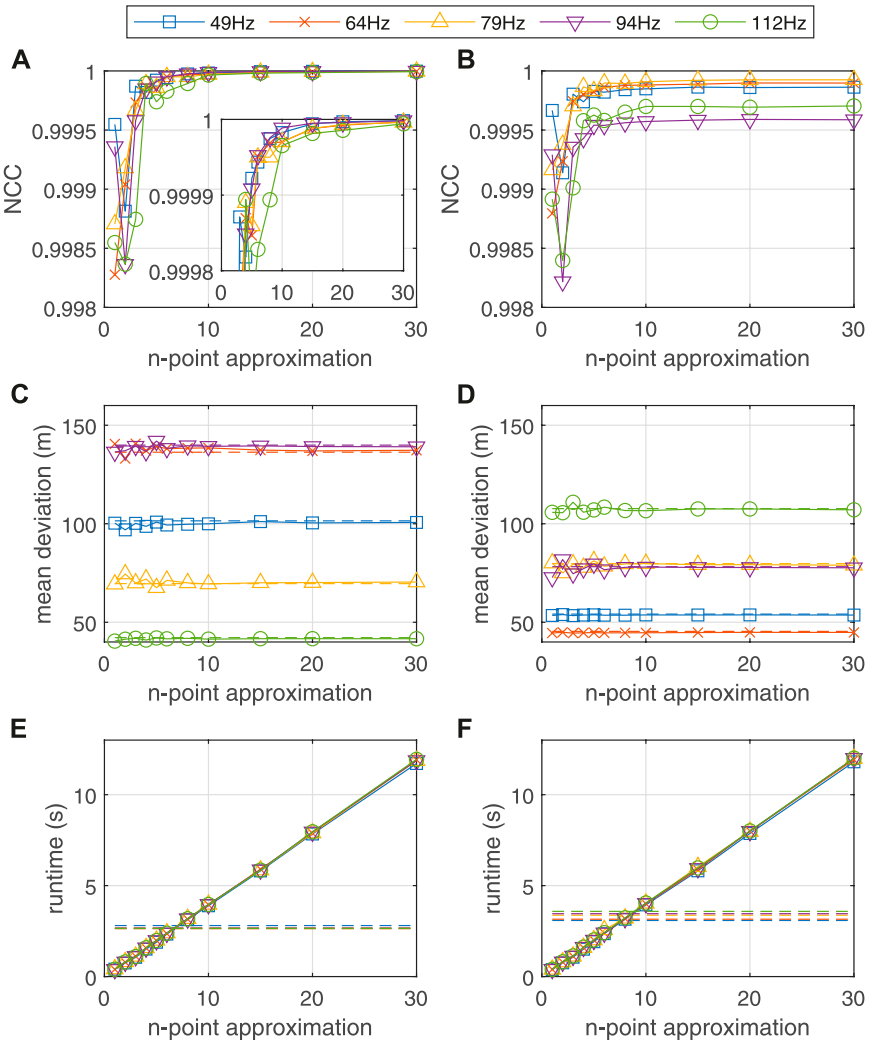

FIGURE 7
Changes of the NCC coefficient **(A,B)**, the mean deviation between source range estimates and GPS records **(C,D)**, and the runtime of computing a TFD **(E,F)** with the increase of the number of compensation points. Results of F-STFT are shown in the left three panels **(A,C,E)**, while that of F-DopplerCT are shown in the right three panels **(B,D,F)**. Dash lines in **(C–F)** represents the corresponding results of STFT and DopplerCT.

Figure 4 shows clearly that the main difference of the proposed framework to the conventional framework is the way of computing the TFD, where only the spectrum on a narrow band around f_0 is computed (in an approximate manner) through the steps R2 and R4, instead of computing the Fourier spectrum in the whole frequency band of Nyquist ($\pm f_s/2$) through the steps L2 and L4. The main parameters involved in the two frameworks are the length of the spectral window, the number of overlapped samples, and the number of DFT points to compute the TFD, they are denoted as $\{N_w, N_o, N_F\}$, $\{N_{w1}, N_{o1}, N_{F1}\}$, and $\{N_{w2}, N_{o2}, N_{F2}\}$ in different steps. Without a loss of generality, the number N_F is assumed that can be resolved (strictly or just approximately) into two factors N_{F1} and N_{F2}, i.e., $N_F = N_{F1}N_{F2}$, so that the conventional and proposed frameworks perform with the same time-frequency resolution and are comparable. N_{F1} determines the bandwidth of a TFD (e.g., the bandwidth in Figure 5 is $f_s/N_{F1} = 1$ Hz). To hold true for Eq. 9, N_{w1} should be equal to N_{F1} and N_{o1} to 0, i.e., no zero padding and overlapping in step R2.1. N_{F2} determines the frequency resolution of a TFD, which are $\frac{f_s}{N_{F1}N_{F2}}$. Zero padding and overlapping are allowed for the steps R2.3 and R4.1, where $N_{F2} \geq N_{w2} > N_{o2} \geq 0$.

4 Experimental example

The SWellEx-96 experiment [19] was conducted in 1996 in the littoral waters outside the port of San Diego. The

TABLE 1 Average run time of computing TFDs of the five tones. The percentage of run time of F-STFT and F-DopplerCT are computed referring to the average run time of conventional methods STFT and DopplerCT. As the two bold numbers indicate, the average run time of conventional methods STFT and DopplerCT is able to be dropped to 15% and 11.8% by applying the framework shown in Figure 4, respectively.

Run time	STFT	F-STFT with n-point compensation										
		1	2	3	4	5	6	8	10	15	20	30
Average (s)	2.68	0.40	0.79	1.10	1.56	1.96	2.37	3.16	3.95	5.86	7.90	11.86
Percentage (%)	100	**15.0**	29.5	40.8	58.2	73.1	88.4	117.9	147.0	218.2	294.4	441.9
Run time	**STFT**	**F-DopplerCT with n-point compensation**										
		1	**2**	**3**	**4**	**5**	**6**	**8**	**10**	**15**	**20**	**30**
Average (s)	3.33	0.40	0.79	1.11	1.58	1.99	2.43	3.19	4.01	5.93	7.97	11.94
Percentage (%)	100	**11.8**	23.8	33.4	47.5	59.8	72.8	95.8	120.3	178.0	239.2	358.7

experimental data of event S5 are used to validate the effectiveness of the proposed framework. In S5, a source was towed at a constant speed of five knots (2.5 m/s) along a linear track. It transmitted numerous tonals of various source levels between 49 Hz and 400 Hz. The first five tones of the "High Tonal Set" (49 Hz, 64 Hz, 79 Hz, 94 Hz, and 112 Hz), which were projected at maximum level of approximately 158 dB and received by the shallowest element (at a depth of 94.125 m) of a vertical line array, are analyzed below. The sampling rate of the signal is f_s = 1,500 Hz.

Figure 5 illustrates, respectively, the TFDs of the 112 Hz tone produced by STFT, F-STFT, DopplerCT, and F-DopplerCT. The parameters used for computing these TFDs are $N_{w1} = N_{F1}$ = 1,500, $N_{o1} = 0$, $N_{w2} = N_{F2} = 200$, $N_{o2} = 180$, $N_w = N_F = N_{w1}N_{w2}$, and $N_o = N_{w1}N_{o2}$. Note that only one iteration is performed to render a high energy concentration by DopplerCT and F-DopplerCT because in this example the signal-to-noise rate is very high. It is obvious that F-STFT and F-DopplerCT generate TFDs that are almost the same as STFT and DopplerCT. Following the frameworks shown in Figure 4, the source ranges estimated from the IF trajectories depicted in Figure 5, together with the GPS records, are shown in Figure 6. It can be seen that these estimated source ranges are in good agreement with the GPS records.

Figure 7 depicts the processing results for all five tones. In Figures 7A,B, normalized cross correlation (NCC) is used to quantify the similarity between two TFDs,

$$\mathrm{NCC} = \frac{\frac{1}{MN}\sum_{m=1}^{M}\sum_{n=1}^{N}\left(S_1(m,n)-\bar{S}_1\right)\left(S_2(m,n)-\bar{S}_2\right)}{\sqrt{\frac{1}{MN}\sum_{m=1}^{M}\sum_{n=1}^{N}\left(S_1(m,n)-\bar{S}_1\right)^2}\sqrt{\frac{1}{MN}\sum_{m=1}^{M}\sum_{n=1}^{N}\left(S_2(m,n)-\bar{S}_2\right)^2}}, \tag{11}$$

where $\bar{S}$ represents the mean value of a TFD S. Figure 7A shows that, with the increase of the number of compensation points, the NCC coefficient between the TFDs of F-STFT and STFT quickly approaches 1, i.e., the TFD of STFT can be well approximated by the TFD of F-STFT. Same goes for the circumstance of F-DopplerCT and DopplerCT as Figure 7B shown, where, affected by the complexity of computing the advanced TFA method, the NCC coefficient finally approaches a number very close to 1 but not exactly 1. In Figures 7C,D, mean deviation is used to quantify the difference between the estimated source range and the GPS recording. F-DopplerCT has less deviation than F-STFT in the mass. In addition, the mean deviation of F-STFT and F-DopplerCT is very close to that of STFT and DopplerCT (dash lines), indicating that power spectrum approximation hardly affects the accuracy of estimates in practice. Figures 7E,F show the run time of computing the TFD. It can be seen that the run time of F-STFT and F-DopplerCT increases linearly with the number of compensation points. When the number is small enough, power spectrum approximation significantly improves the computational efficiency of TFD. The average run time of computing TFDs of the five tones are tabulated in Table 1. Obviously, the average run time of DopplerCT is longer than that of STFT due to the complicated computation of the advanced TFA method. But the average run time of F-DopplerCT (one iteration) is only slightly longer than that of F-STFT. Comparing with the two conventional methods STFT and DopplerCT, the run time can be saved up to 85% and 88.2% by the approximation processing, respectively. The high performance of computational efficiency of the suggested framework is confirmed in this example.

5 Conclusion

This paper perfects the application of cross-spectrum processing in accelerating Doppler-related parameter

estimation for a tone source that travels past a single receiver in a straight line at constant speed, where time-consuming advanced TFA methods are widely used to suppress noise when extracting the continuous Doppler shift of a overhead pass. The conventional way of applying cross-spectrum processing is overshadowed by the phenomena of unknown Doppler shift offset and power spectrum estimation error. In this paper, the conventional cross-spectrum processing is proven to be an approximated estimation of the power spectrum in a small frequency interval, instead of exactly computing power spectrum over the total Nyquist frequency interval. This fact not only interprets why the method is highly computational efficiency but also reveals that reasons behind the two phenomena are the frequency aliasing and the approximation error, respectively. Based on these understandings, an revised framework of applying the cross-spectrum processing to accelerate the computation of TFDs is provided especially for TFDs of advanced TFA methods. Processing to the SWellEx-96 experiment data supports the above explanations for the two phenomena and demonstrates that the computational efficiencies of STFT and DopplerCT could be improved up to 85% and 88.2%, respectively, without a noticeable impact on the accuracy of parameter estimates. The feature of this proposed framework is apparent: a similar function of bandpass filtering is achieved with only FFT operations. This framework can be applied to accelerate the computations of most TFA methods. In addition, due to the feasibility of parallel computing in precision compensation, this framework is very meaningful in practical applications where the execution time is an important performance index. For future work, as this study focuses on only the narrowband case of applying cross-spectrum technique [12], relationships and applicability of the proposed framework to the broadband case is worth examining.

Data availability statement

Publicly available datasets were analyzed in this study. This data can be found here: Booth, Newell O; Hodgkiss, William S; Ensberg, David E (2015): SWellEx-96 Experiment Acoustic Data. UC San Diego Library Digital Collections. http://dx.doi.org/10.6075/J0MW2F21.

Author contributions

NL: Designed the study, performed the data analysis, and wrote the first draft of the manuscript. JZ and YY: Supervised the study, funding acquisition. All authors contributed to manuscript revision and approved the submitted version.

Funding

This research was supported by the National Natural Science Foundation of China (grant numbers 11974286, 11904290), China Association for Science and Technology Youth Talent Promotion Project (grant number 2020QNRC002), and Central University Operating Expenses Project (grant number W022005).

Conflict of interest

The authors declare that the research was conducted in the absence of any commercial or financial relationships that could be construed as a potential conflict of interest.

Publisher's note

All claims expressed in this article are solely those of the authors and do not necessarily represent those of their affiliated organizations, or those of the publisher, the editors and the reviewers. Any product that may be evaluated in this article, or claim that may be made by its manufacturer, is not guaranteed or endorsed by the publisher.

References

1. Ferguson BG, Quinn BG. Application of the short-time Fourier transform and the Wigner–Ville distribution to the acoustic localization of aircraft. *The J Acoust Soc America* (1994) 96:821–7. doi:10.1121/1.410320

2. Vashishtha G, Chauhan S, Kumar A, Kumar R. An ameliorated African vulture optimization algorithm to diagnose the rolling bearing defects. *Meas Sci Tech* (2022) 33:075013. doi:10.1088/1361-6501/ac656a

3. Vashishtha G, Chauhan S, Yadav N, Kumar A, Kumar R. A two-level adaptive chirp mode decomposition and tangent entropy in estimation of single-valued neutrosophic cross-entropy for detecting impeller defects in centrifugal pump. *Appl Acoust* (2022) 197:108905. doi:10.1016/j.apacoust.2022.108905

4. Zhang D, Entezami M, Stewart E, Roberts C, Yu D. A novel Doppler effect reduction method for wayside acoustic train bearing fault detection systems. *Appl Acoust* (2019) 145:112–24. doi:10.1016/j.apacoust.2018.09.017

5. Zhang D, Entezami M, Stewart E, Roberts C, Yu D, Lei Y. Wayside acoustic detection of train bearings based on an enhanced spline-kernelled chirplet transform. *J Sound Vibration* (2020) 480:115401. doi:10.1016/j.jsv.2020.115401

6. Ferguson BG. Doppler effect for sound emitted by a moving airborne source and received by acoustic sensors located above and below the sea surface. *J Acoust Soc America* (1993) 94:3244–7. doi:10.1121/1.407230

7. Reid DC, Zoubir AM, Boashash B. Aircraft flight parameter estimation based on passive acoustic techniques using the polynomial wigner–ville distribution. *J Acoust Soc America* (1997) 102:207–23. doi:10.1121/1.419803

8. Xu L, Yang Y, Yu S. Analysis of moving source characteristics using polynomial chirplet transform. *J Acoust Soc America* (2015) 137:EL320–6. doi:10.1121/1.4916796

9. Xu L, Yang Y. Parameter estimation of underwater moving sources by using matched wigner transform. *Appl Acoust* (2016) 101:5–14. doi:10.1016/j.apacoust.2015.07.020

10. Liang N, Yang Y, Guo X. Doppler chirplet transform for the velocity estimation of a fast moving acoustic source of discrete tones. *J Acoust Soc America* (2019) 145:EL34–8. doi:10.1121/1.5087496

11. Zhang B, Yang Y, Guo X. Cross-term rejection in the wigner-ville distribution for velocity estimation of a narrowband sound source. *ACTA Acustica* (2021) 46: 973–82. doi:10.15949/j.cnki.0371-0025.2021.06.018

12. Rakotonarivo ST, Kuperman WA. Model-independent range localization of a moving source in shallow water. *J Acoust Soc America* (2012) 132:2218–23. doi:10.1121/1.4748795

13. Yang K, Li H, Duan R, Yang Q. Analysis on the characteristic of cross-correlated field and its potential application on source localization in deep water. *J Comp Acous* (2017) 25:1750001. doi:10.1142/S0218396X17500011

14. Yu C, Zhou M, Shuqing M, Changchun B. Range passive localization of the moving source with a single vector hydrophone. In: 2016 IEEE/OES China Ocean Acoustics (COA) (2016). p. 1–5.

15. Zhao A, Song P, Hui J, Li J, Tang K. Passive estimation of target velocity based on cross-spectrum histogram. *J Acoust Soc America* (2022) 151:2967–74. doi:10.1121/10.0010367

16. Wang C, Wang J, Du P. Estimation of moving target speed using weak line spectrum of single-hydrophon. In: 2017 IEEE International Conference on Signal Processing, Communications and Computing (ICSPCC) (2017). p. 1–5.

17. Jensen FB, Kuperman WA, Porter MB, Schmidt H. *Computational ocean acoustics*. 2 edn. New York: Springer (2011).

18. Vaughan R, Scott N, White D. The theory of bandpass sampling. *IEEE Trans Signal Process* (1991) 39:1973. doi:10.1109/78.134430

19. Booth NO, Hodgkiss WS, Ensberg DE. *Swellex-96 experiment acoustic data*. San Diego, CA: UC San Diego Library Digital Collections (2015).

20. Lo KW, 141. Flight parameter estimation usinginstantaneous frequency and direction of arrival measurements from a single acoustic sensor node. *J Acoust Soc America* (2017). p. 1332–48. doi:10.1121/1.4976091

6 Appendix Doppler frequency shift

Consider an ideal case where a pure-tone source travels along a straight line at a constant speed v and passes by a fixed receiver, as shown in Figure A1. The sound speed is given by a constant c (the average sound speed of a propagation medium in practice). The time when the source passes through CPA is denoted by τ_c, and at the very moment, the distance between the source and the receiver is represented by d_c.

Due to the propagation delay, the acoustic signal emitted by the source at time τ (source time) arrives at the receiver node at a later time t (receiver time), given by:

$$t = \tau + R(\tau)/c, \tag{A1}$$

where $R(\tau)$ represents the slant range between the source and the receiver at time τ. According to the geometry relationship shown in Figure A1, $R(\tau)$ can be derived as:

$$R(\tau) = \sqrt{v^2(\tau - \tau_c)^2 + d_c^2}. \tag{A2}$$

Combining Eqs A1, A2, we obtain:

$$\tau = \frac{c^2 t - v^2\tau_c - \sqrt{v^2c^2(t-\tau_c)^2 + d_c^2(c^2 - v^2)}}{c^2 - v^2}. \tag{A3}$$

Especially, when $\tau = \tau_c$, we have:

$$\begin{aligned} t_c &= \tau_c + R(\tau_c)/c \\ &= \tau_c + d_c/c \end{aligned}, \tag{A4}$$

where t_c denotes the moment that sounds emitted at τ_c have propagated to the receiver.

Suppose that the phase of a tone signal with a frequency f_0 emitted at time τ is:

$$\phi(\tau) = 2\pi f_0\tau + \phi_0, \tag{A5}$$

where ϕ_0 denotes a constant initial phase. Then, after the propagation over the slant range $R(\tau)$, $\phi(\tau)$ will be sampled by the receiver at time t. Combining Eq. A3, the phase of the received signal at time t can be expressed as

$$\begin{aligned} \psi(t) &= \phi(\tau) = 2\pi f_0\tau + \phi_0 \\ &= 2\pi f_0 \frac{c^2 t - \sqrt{v^2c^2(t-\tau_c)^2 + d_c^2(c^2 - v^2)}}{c^2 - v^2} + \psi_0 \end{aligned}, \tag{A6}$$

where $\psi_0 = -2\pi f_0 \frac{v^2\tau_c}{c^2 - v^2} + \phi_0$ is a constant.

Further, the IF of this tone signal received at time t is given by [20]:

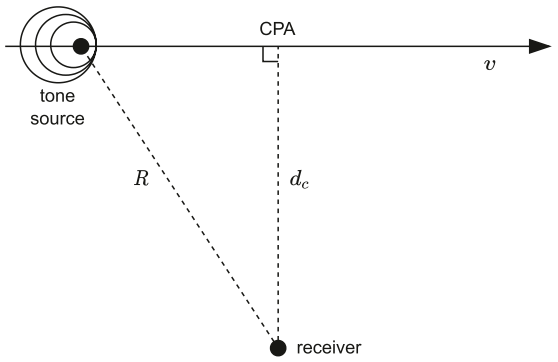

FIGURE A1
The trajectory of a tone source as it travels past the receiver node in a straight line at constant velocity v. R gives the slant range between the receiver and the source. The distance from the receiver to the CPA is denoted by d_c.

$$\begin{aligned} f(t) &= \frac{1}{2\pi}\frac{\partial\psi(t)}{\partial t} = f_0\frac{\partial\tau(t)}{\partial t} \\ &= f_0\frac{c^2}{c^2 - v^2}\left[1 - \frac{v^2(t-\tau_c)}{\sqrt{v^2c^2(t-\tau_c)^2 + d_c^2(c^2 - v^2)}}\right]. \end{aligned} \tag{A7}$$

Eq. A7 represents the regular of the Doppler frequency shift. By fitting the extracted IF curve of the received tone signal with Eq. A7, one can thus obtain the estimates of the Doppler-related parameters, i.e., f_0, v, c, τ_c and d_c. Note that if we denote the radial velocity of the source that is observed at the receiver as

$$\begin{aligned} v_r(t) &= \frac{\partial R(t)}{\partial t} = \frac{\partial R(\tau)}{\partial\tau}\frac{\partial\tau(t)}{\partial t} \\ &= -\frac{v^2 c}{c^2 - v^2}\left[1 - \frac{c^2(t-\tau_c)}{\sqrt{v^2c^2(t-\tau_c)^2 + d_c{}^2(c^2 - v^2)}}\right], \end{aligned} \tag{A8}$$

then Eq. A7 can be reformulated as:

$$f(t) = f_0(1 - v_r/c), \tag{A9}$$

where the term of the Doppler frequency shift $f_0 v_r/c$ appears with an expression that is the same as the expression of the oscillation frequency in the cross-spectrum processing (Eq. 5).

frontiers | Frontiers in Physics

TYPE Original Research
PUBLISHED 02 December 2022
DOI 10.3389/fphy.2022.1053353

OPEN ACCESS

EDITED BY
Yuxing Li,
Xi'an University of Technology, China

REVIEWED BY
Dezhou Kong,
Shandong Agricultural University, China
Ge Tian,
Xi'an University of Technology, China

*CORRESPONDENCE
Kaiping Liu,
kaipliu@163.com

SPECIALTY SECTION
This article was submitted to Physical Acoustics and Ultrasonics, a section of the journal Frontiers in Physics

RECEIVED 25 September 2022
ACCEPTED 02 November 2022
PUBLISHED 02 December 2022

CITATION
Huang P and Liu K (2022), A new conjugate gradient algorithm for noise reduction in signal processing and image restoration.
Front. Phys. 10:1053353.
doi: 10.3389/fphy.2022.1053353

A new conjugate gradient algorithm for noise reduction in signal processing and image restoration

Pan Huang[1] and Kaiping Liu[2]*

[1]School of Mathematics and Information Science, Weifang University, Weifang, Shandong, China, [2]School of Management Science, Qufu Normal University, Rizhao, Shandong, China

Noise-reduction methods are an area of intensive research in signal processing. In this article, a new conjugate gradient method is proposed for noise reduction in signal processing and image restoration. The superiority of this method lies in its employment of the ideas of accelerated conjugate gradient methods in conjunction with a new adaptive method for choosing the step size. In this work, using some assumptions, the weak convergence of the designed method was established. As example applications, we implemented our method to solve signal-processing and image-restoration problems. The results of our numerical simulations demonstrate the effectiveness and superiority of the new approach.

KEYWORDS

signal processing, image restoration, weak convergence, noise reduction, conjugate gradient method

1 Introduction

Noise reduction is an important step in signal pre-processing; it is widely applied in many fields, including underwater acoustic imaging [1, 2], pattern recognition [3], and target detection and feature extraction [4], among others [5]. In this article, a new approach based on a conjugate gradient method is derived from mathematical principles.

We consider the degradation model of signal or image such as:

$$y = \mathcal{A}\omega + \varepsilon, \tag{1}$$

where $\omega \in \mathbb{R}^N$ is an original signal or image, $\mathcal{A}$ is the degradation operator, ε is the noise, $y \in \mathbb{R}^M$ is the observed data. The essence of noise reduction is solving Eq. 1 to obtain ω. The solving of Eq. 1 can be considered as the following problem [6]:

$$\min_{\omega \in \mathbb{R}^N} \frac{1}{2}\|y - \mathcal{A}\omega\|^2 \text{ s.t. } \|\omega\|_1 \leq r, \tag{2}$$

where $r > 0$ and $\|\cdot\|_1$ is the ℓ_1 norm. Let $C = \{\omega \in \mathbb{R}^N : \|\omega\|_1 \leq r\}$ and $Q = \{y\}$, then Eq. 2 can be seen as a split feasibility problem (SFP) [7–10]. Thus, we translate the problem of noise reduction to SFP, which can be described as:

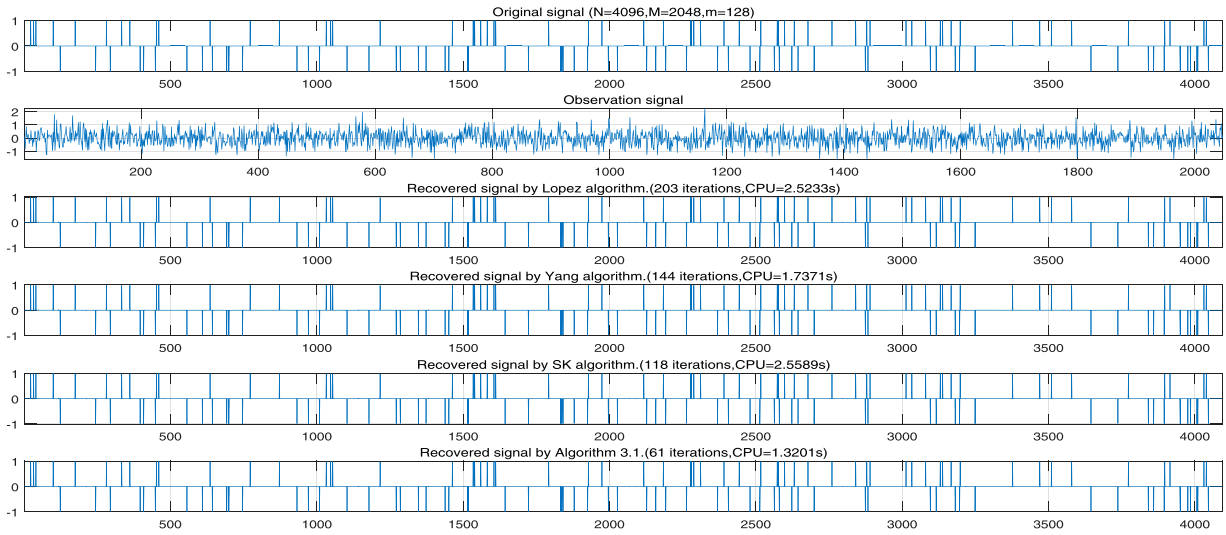

FIGURE 1
From top to bottom: original signal, observed signal, and signals recovered by López's algorithm, Yang's algorithm, Sakurai and Iiduka's algorithm, and Algorithm 1.

$$\text{find } \omega \in C \text{ such that } \mathcal{A}\omega \in Q, \tag{3}$$

where H_1 and H_2 are real Hilbert spaces, $\mathcal{A}$: $H_1 \to H_2$ is a bounded linear operator, the closed and convex set $C \subset H_1$ ($C \neq \varnothing$), and $Q \subset H_2$ ($Q \neq \varnothing$). In order to solve the SFP, Byrne [11, 12] presented the *CQ* algorithm, which creates a sequence $\{\omega_i\}$:

$$\omega_{i+1} = P_C\left(\omega_i - \tau_i \mathcal{A}^*\left(I - P_Q\right)\mathcal{A}\omega_i\right), \tag{4}$$

where P_C is the projection to C, P_Q is the projection to Q, $\tau_i \in (0, \frac{2}{\|\mathcal{A}\|^2})$, and $\mathcal{A}^*$ is the adjoint operator of $\mathcal{A}$. For convex functions c and q, the definitions of C and Q are

$$C = \{\omega \in H_1 \colon c(\omega) \leq 0\} \text{ and } Q = \{u \in H_2 \colon q(u) \leq 0\}.$$

There have been some research works devoted to solving Eq. 3. In 2004, Yang [13] presented a relaxed *CQ* algorithm using P_{C_i} and P_{Q_i} to replace P_C and P_Q. Here, we define two sets at point ω_i by

$$C_i = \{\omega \in H_1 \colon c(\omega_i) \leq \langle \zeta_i, \omega_i - \omega \rangle\}, \tag{5}$$

where $\zeta_i \in \partial c(\omega_i)$, and

$$Q_i = \{u \in H_2 \colon q(\mathcal{A}\omega_i) \leq \langle \vartheta_i, \mathcal{A}\omega_i - u \rangle\}, \tag{6}$$

where $\vartheta_i \in \partial q(\mathcal{A}\omega_i)$. For all $i > 1$, clearly, $C \subseteq C_i$ and $Q \subseteq Q_i$. In addition, C_i and Q_i are half-spaces. Furthermore, referring to [14], we define

$$f_i(\omega) = \frac{1}{2}\|\left(I - P_{C_i}\right)\omega\|^2 + \frac{1}{2}\|\left(I - P_{Q_i}\right)\mathcal{A}\omega\|^2, \tag{7}$$

where C_i and Q_i are given as in Eqs. 5, 6. In this specific case, their gradient is

$$\nabla f_i(\omega) = \left(I - P_{C_i}\right)\omega + \mathcal{A}^*\left(I - P_{Q_i}\right)\mathcal{A}\omega. \tag{8}$$

Yang [13] presented a relaxed *CQ* algorithm in a finite-dimensional Hilbert space:

$$\omega_{i+1} = P_C\left(\omega_i - \tau_i \nabla f_i(\omega_i)\right), \tag{9}$$

where $\tau_i \in (0, \frac{2}{\|\mathcal{A}\|^2})$. Notice that calculating $\|\mathcal{A}\|$ is complex and costly when $\mathcal{A}$ is a high-dimensional dense matrix. In 2005, Yang [15] presented a new adaptive step size τ_i, which is defined as:

$$\tau_i = \frac{\rho_i}{\|\nabla f_i(x)\|}, \tag{10}$$

where

$$\sum_{i=1}^{\infty} \rho_i = \infty, \quad \sum_{i=1}^{\infty} \rho_i^2 < +\infty .$$

However, Yang's step size (Eq. 10) requires that Q_i is bounded and the matrix $\mathcal{A}$ is full rank. Recently, Wang [16] absolutely eliminated these problems. Considering the *CQ* algorithm, López [17] introduced a novel step size to overcome these problems; this is defined as:

$$\tau_i = \frac{\rho_i f_i(x_i)}{\|\nabla f_i(x_i)\|^2}, \tag{11}$$

where $\rho_i \in (0, 4)$. With Lopez's step size (Eq. 11), it was proved that $\{\omega_i\}$ in Eq. 9 weakly converges to the solution of the SFP.

In 2005, Qu and Xiu [18] introduced a relaxed *CQ* algorithm that is improved by using an Armijo line search in Euclidian space. In 2017, on the basis of the above application, Gibali [19] extended this to Hilbert spaces, which proved that $\{\omega_i\}$ weakly converges to a solution of the SFP as follows:

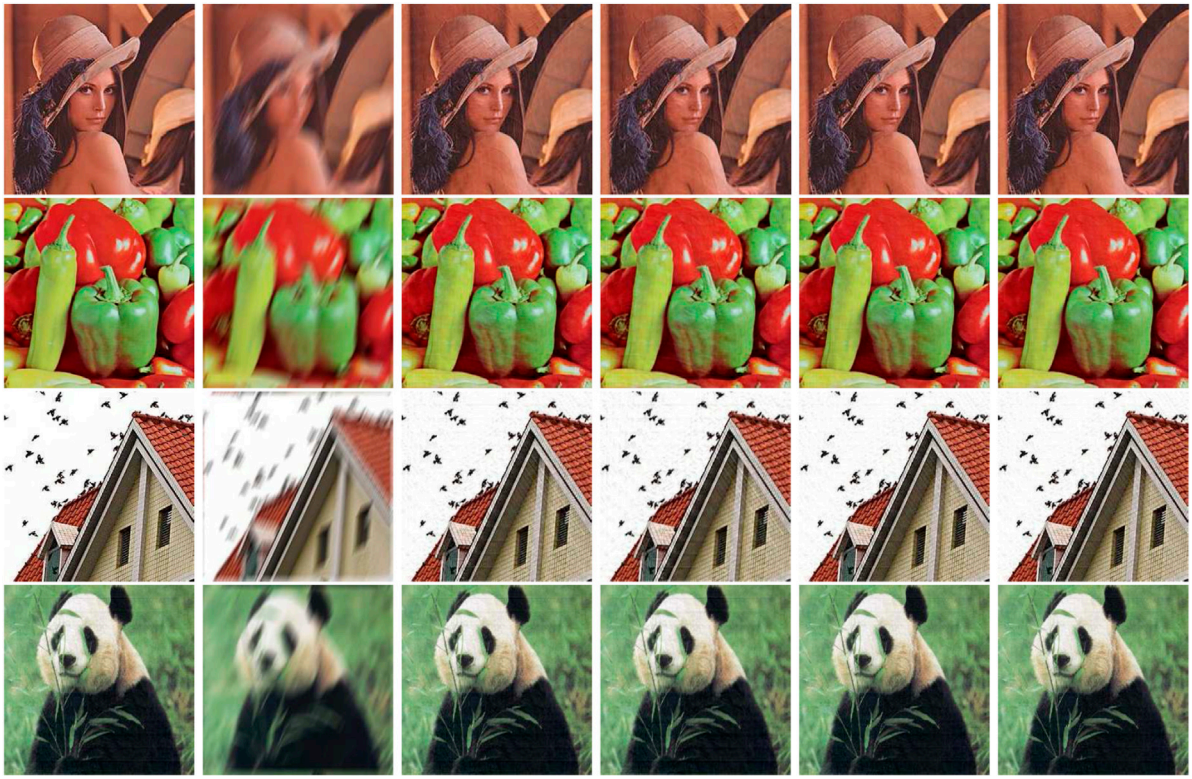

FIGURE 2
Comparison of recovered color images of Lena, peppers, house, panda using different algorithms with 1,000 iterations. From left to right: original image, noised image, López's algorithm, Yang's algorithm, Sakurai and Iiduka's algorithm, and Algorithm 1.

$$\begin{aligned} y_i &= P_{C_i}(\omega_i - \tau_i \nabla f_i(\omega_i)), \\ \omega_{i+1} &= P_{C_i}(\omega_i - \tau_i \nabla f_i(y_i)), \end{aligned} \tag{12}$$

where $\tau_i = \gamma \ell^{l_i}$, $\gamma > 0$, $\ell \in (0, 1)$, l_i is the smallest nonnegative integer, and $\nu \in (0, 1)$ satisfies:

$$\tau_i \|\nabla f_i(\omega_i) - \nabla f_i(y_i)\| \leq \nu \|\omega_i - y_i\|.$$

In 2020, Kesornprom et al. [20] introduced a gradient-*CQ* algorithm that derived a weak-convergence theorem for solving the SFP in the framework of Hilbert spaces. This is described as:

$$\begin{aligned} y_i &= \omega_i - \tau_i \nabla f_i(\omega_i), \\ \omega_{i+1} &= P_{C_i}(y_i - \varphi_i \nabla f_i(y_i)), \end{aligned}$$

where C_i, f_i, and ∇f_i are given in Eqs 5, 7, 8, respectively, and

$$\tau_i = \frac{\rho_i f_i(\omega_i)}{\|\nabla f_i(\omega_i)\|^2 + \theta_i}, \text{ and}$$
$$\varphi_i = \frac{\rho_i f_i(y_i)}{\|\nabla f_i(y_i)\|^2 + \theta_i}, \ 0 < \rho_i < 4, \ 0 < \theta_i < 1.$$

The conjugate gradient method [21] is a commonly used acceleration scheme in the steepest descent method. The conjugate gradient direction of f at ω_i is

$$d_{i+1} = -\nabla f_i(\omega_i) + \beta_i d_i,$$

where $d_0 = -\nabla f(\omega_0)$ and $\beta_i \in (0, \infty)$. In this article, motivated by previous works [22–24], a new viscosity approximation method based on the conjugate gradient method is introduced. Many other iterative methods of solving the SFP have been proposed [25–29].

Herein, combining the relaxed *CQ* algorithm with a new step size and the conjugate gradient method, we find the solution of noise reduction problem in Eq. 1 by solving the SFP in Hilbert spaces with a novel approach. Section 2 gives some basic definitions and lemmas. In Section 3, the theorem for proving the weak convergence of our method is presented. In Section 4, we present experimental results and compare them with the relaxed *CQ* algorithms of López [17], Yang [15], and Sakurai and Iiduka [20]. Finally, conclusions are given in Section 5.

2 Preliminaries

Throughout this article, to obtain our results, some technical lemmas are used.

Lemma 2.1 [30]. *Suppose the nonempty set $C \subset H_1$ is closed and convex. Thus, for all h_1, $h_2 \in H_1$ and $c \in C$,*

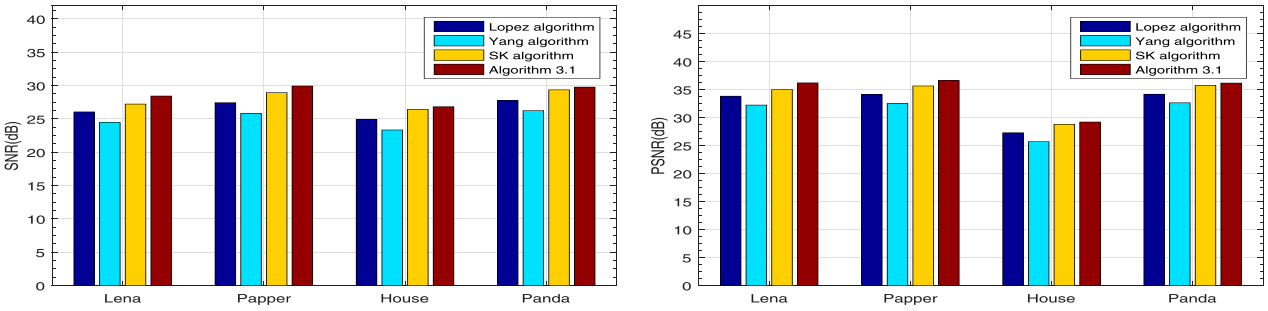

FIGURE 3
Comparison of SNR (left) and PSNR (right) values resulting from image recovery using the four algorithms with 1,000 iterations.

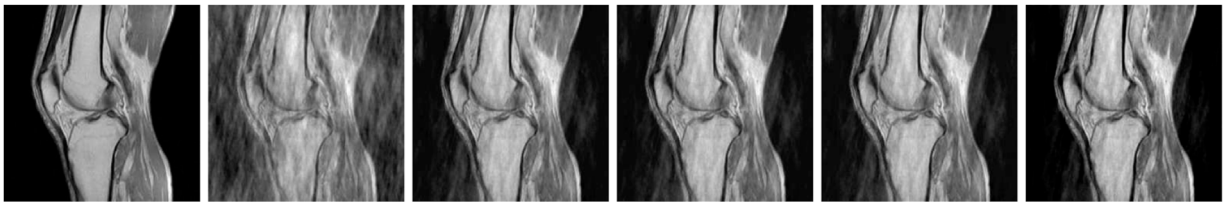

FIGURE 4
Comparison of CT images of a knee joint recovered using different algorithms with 500 iterations. From left to right: original image, noised image, López's algorithm, Yang's algorithm, Sakurai and Iiduka's algorithm, and Algorithm 1.

(i) $\langle h_1 - P_C h_1, c - P_C h_1\rangle \le 0$;
(ii) $\|P_C h_1 - P_C h_2\|^2 \le \langle P_C h_1 - P_C h_2, h_1 - h_2\rangle$;
(iii) $\|P_C h_1 - c\|^2 \le \|h_1 - c\|^2 - \|P_C h_1 - h_1\|^2$.

From Lemma 2.1(ii), let I express the identity operator; then, $I - P_C$ is a firmly nonexpansive operator, i.e.,

$$\|(I - P_C)h_1 - (I - P_C)h_2\|^2 \le \langle (I - P_C)h_1 - (I - P_C)h_2, h_1 - h_2\rangle,\ \forall h_1, h_2 \in H_1.$$

Definition 1. *Suppose* $\mathbb{R}$ *is a set of real numbers,* G: $H \to \mathbb{R}$ *is convex; the definition of its subdifferential at* w *is then*

$$\partial G(w) = \{\zeta \in H | G(z) \ge G(w) + \langle \zeta, z - w\rangle,\ \forall z \in H\}.$$

To obtain our results, we prove the following lemma.

Lemma 2.2. *Let* $f_i(\omega)$ *be defined in Eq. 7; then* ∇f_i *is Lipschitz continuous with Lipschitz constant* $1 + \|\mathcal{A}\|^2$

Proof. For any $p, q \in H$,

$$\begin{aligned}\|\nabla f_i(p) - \nabla f_i(q)\| &= \|(I - P_{C_i})p - (I - P_{C_i})q + \mathcal{A}^*(I - P_{Q_i})\mathcal{A}p - \mathcal{A}^*(I - P_{Q_i})\mathcal{A}q\| \\ &\le \|p - P_{C_i}p + P_{C_i}q - q\| + \|\mathcal{A}^*(I - P_{Q_i})\mathcal{A}p - \mathcal{A}^*(I - P_{Q_i})\mathcal{A}q)\| \\ &\le \|p - q\| + \|\mathcal{A}\|\|(I - P_{Q_i})\mathcal{A}p - (I - P_{Q_i})\mathcal{A}q)\| \\ &\le \|p - q\| + \|\mathcal{A}\|\|\mathcal{A}p - \mathcal{A}q\| \\ &\le \|p - q\| + \|\mathcal{A}\|^2\|p - q\| \\ &= (1 + \|\mathcal{A}\|^2)\|p - q\|.\end{aligned}$$

So, ∇f_i is $1 + \|\mathcal{A}\|^2$-Lipschitz continuous.

3 Algorithm and convergence

A novel gradient-*CQ* algorithm is established in this section. Furthermore, we prove that the sequence created by our approach is convergent.

Algorithm 1. *Let* $\alpha_1, \alpha_2, \beta_i, \hat{\beta}_i \in (0, 1)$, *and the sequences* $\{d_i\}$, $\{\omega_i\}$, $\{y_i\}$, $\{\hat{d}_i\}$, *and* $\{z_i\}$ *be denoted as:*

$$\begin{aligned} d_{i+1} &= -\tau_i \nabla f_i(\omega_i) + \alpha_1 \beta_i d_i, \\ y_i &= \omega_i + d_{i+1}, \\ \hat{d}_{i+1} &= -\varphi_i \nabla f_i(y_i) + \alpha_2 \hat{\beta}_i \hat{d}_i, \\ z_i &= y_i + \hat{d}_{i+1}, \\ \omega_{i+1} &= P_{C_i}(z_i), \end{aligned}$$

where $\tau_i = \frac{\rho_i f_i(\omega_i)}{\|\nabla f_i(\omega_i)\|^2 + \theta_i}$, $\varphi_i = \frac{\rho_i f_i(y_i)}{\|\nabla f_i(y_i)\|^2 + \theta_i}$, *and* $0 < \rho_i < 4$, $0 < \theta_i < 1$.

We next state our weak-convergence theorem.

Theorem 3.1. *The following assumptions hold:*

(C1) $\inf_i \rho_i(4 - \rho_i) > 0$;
(C2) $\lim_{i\to\infty} \theta_i = 0$;
(C3) $\lim_{i\to\infty} \beta_i = 0$, $\lim_{i\to\infty} \hat{\beta}_i = 0$
(C4) $\{(I - P_{C_i})\omega_i\}$ and $\{(I - P_{Q_i})A\omega_i\}$ are bounded.
So, $\{\omega_i\}$ *in Algorithm 1 converges weakly to* $\omega^* \in \Omega$, *which is the nonempty solution set of the SFP.*

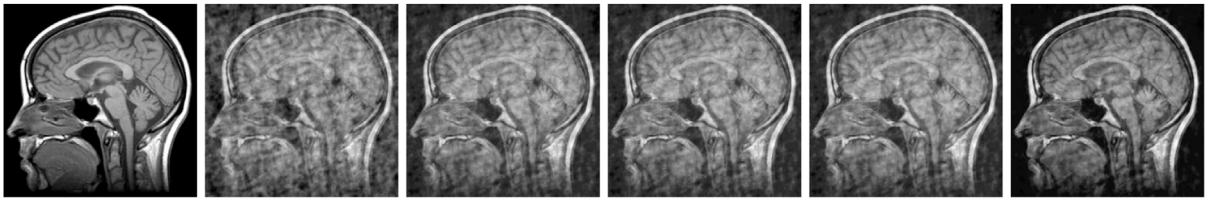

FIGURE 5
Comparison of CT images of a head recovered using different algorithms with 500 iterations. From left to right: original image, noised image, López's algorithm, Yang's algorithm, Sakurai and Iiduka's algorithm, and Algorithm 1.

Proof. First, by using mathematical induction, we show that $\{d_i\}$ and $\{\hat{d}_i\}$ are bounded. Assume that $\|d_i\| \le M$ holds, for some $i \ge i_0$. Assumption C3 implies that there exists $i_0 \in \mathbb{N}$ such that $\beta_i \le \frac{1}{2}, \forall\, i \ge i_0$. Let $M = \max\{\|d_{i_0}\|,\ 2\sup_{i\ge 1}\|\tau_i[(I-P_{C_i})\omega_i + \mathcal{A}^*(I-P_{Q_i})\mathcal{A}\omega_i]\|\} < \infty$. From Algorithm 1, the triangle inequality guarantees that

$$\begin{aligned}\|d_{i+1}\| &= \|-\tau_i[(I-P_{C_i})\omega_i + \mathcal{A}^*(I-P_{Q_i})\mathcal{A}\omega_i] + \alpha_1\beta_i d_i\| \\ &\le \|\tau_i[(I-P_{C_i})\omega_i + \mathcal{A}^*(I-P_{Q_i})\mathcal{A}\omega_i]\| + \alpha_1\beta_i\|d_i\| \\ &\le M,\end{aligned}$$

which means that $\|d_i\| \le M$ for all $i \ge i_0$, so $\{d_i\}$ is bounded.

Assume that $\|\hat{d}_i\| \le \hat{M}$ is true for some $i \ge i_0$ and let $\hat{M} = \max\{\|\hat{d}_{i_0}\|, 2\sup_{i\ge 1}\|\varphi_i[(I-P_{C_i})x_i + \mathcal{A}^*(I-P_{Q_i})\mathcal{A}x_i]\|\} < \infty$. As with the proof that $\|d_i\|$ is bounded, we deduce

$$\begin{aligned}\|\hat{d}_{i+1}\| &= \|-\varphi_i[(I-P_{C_i})y_i + \mathcal{A}^*(I-P_{Q_i})\mathcal{A}y_i] + \alpha_2\hat{\beta}_i\hat{d}_i\| \\ &\le \|\varphi_i[(I-P_{C_i})y_i + \mathcal{A}^*(I-P_{Q_i})\mathcal{A}y_i]\| + \alpha_2\hat{\beta}_i\hat{d}_i\| \\ &\le \hat{M}.\end{aligned}$$

Let $z \in \Omega$. Since $Q \subseteq Q_i$ and $C \subseteq C_i$, we obtain $Az = P_{Q_i}(\mathcal{A}z) = P_Q(\mathcal{A}z)$ and $z = P_{C_i}(z) = P_C(z)$. We have $\nabla f_i(z) = 0$. From Lemma 2.1(iii),

$$\begin{aligned}\|\omega_{i+1} - z\|^2 &= \|P_{C_i}(z_i) - z\|^2 \\ &\le \|z_i - z\|^2 - \|P_{C_i}(z_i) - z_i\|^2 \\ &= \|z_i - z\|^2 - \|\omega_{i+1} - z_i\|^2.\end{aligned} \tag{13}$$

Combining Lemma 2.1(ii), Eq. 7, and Eq. 8, we obtain

$$\begin{aligned}\langle \nabla f_i(y_i), y_i - z\rangle &= \langle (I-P_{C_i})y_i, y_i - z\rangle + \langle \mathcal{A}^*(I-P_{Q_i})\mathcal{A}y_i, y_i - z\rangle \\ &= \langle (I-P_{C_i})y_i, y_i - z\rangle + \langle (I-P_{Q_i})\mathcal{A}y_i, \mathcal{A}y_i - \mathcal{A}z\rangle \\ &\ge \|(I-P_{C_i})y_i\|^2 + \|(I-P_{Q_i})\mathcal{A}y_i\|^2 \\ &= 2f_i(y_i).\end{aligned} \tag{14}$$

as with Eq. 14, it follows that

$$\langle \nabla f_i(\omega_i), \omega_i - z\rangle \ge 2f_i(\omega_i).$$

notice that

$$\begin{aligned}\|y_i - z - \varphi_i\nabla f_i(y_i)\|^2 &= \|y_i - z\|^2 + \varphi_i^2\|\nabla f_i(y_i)\|^2 - 2\varphi_i\langle \nabla f_i(y_i), y_i - z\rangle \\ &\le \|y_i - z\|^2 + \varphi_i^2\|\nabla f_i(y_i)\|^2 - 4\varphi_i f_{(y_i)} \\ &= \|y_i - z\|^2 + \rho_i^2\frac{f_i^2(y_i)}{(\|\nabla f_i(y_i)\|^2 + \theta_i)^2}\|\nabla f_i(y_i)\|^2 \\ &\quad -4\rho_i\frac{f_i^2(y_i)}{\|\nabla f_i(y_i)\|^2 + \theta_i} \\ &\le \|y_i - z\|^2 + \rho_i^2\frac{f_i^2(y_i)}{(\|\nabla f_i(y_i)\|^2 + \theta_i)^2}(\|\nabla f_i(y_i)\|^2 + \theta_i) \\ &\quad -4\rho_i\frac{f_i^2(y_i)}{\|\nabla f_i(y_i)\|^2 + \theta_i} \\ &= \|y_i - z\|^2 - \rho_i(4-\rho_i)\frac{f_i^2(y_i)}{\|\nabla f_i(y_i)\|^2 + \theta_i}.\end{aligned} \tag{15}$$

similar to Eq. 15, we deduce

$$\begin{aligned}\|\omega_i - z - \tau_i\nabla f_i(\omega_i)\|^2 &= \|\omega_i - z\|^2 + \tau_i^2\|\nabla f_i(\omega_i)\|^2 - 2\tau_i\langle \nabla f_i(\omega_i), \omega_i - z\rangle \\ &\le \|\omega_i - z\|^2 + \tau_i^2\|\nabla f_i(\omega_i)\|^2 - 4\tau_i f_i(\omega_i) \\ &= \|\omega_i - z\|^2 + \rho_i^2\frac{f_i^2(\omega_i)}{(\|\nabla f_i(\omega_i)\|^2 + \theta_i)^2}\|\nabla f_i(\omega_i)\|^2 \\ &\quad -4\rho_i\frac{f_i^2(\omega_i)}{\|\nabla f_i(\omega_i)\|^2 + \theta_i} \\ &\le \|\omega_i - z\|^2 + \rho_i^2\frac{f_i^2(\omega_i)}{(\|\nabla f_i(\omega_i)\|^2 + \theta_i)^2}(\|\nabla f_i(\omega_i)\|^2 + \theta_i) \\ &\quad -4\rho_i\frac{f_i^2(\omega_i)}{\|\nabla f_i(\omega_i)\|^2 + \theta_i} \\ &= \|\omega_i - z\|^2 - \rho_i(4-\rho_i)\frac{f_i^2(\omega_i)}{\|\nabla f_i(\omega_i)\|^2 + \theta_i}.\end{aligned} \tag{16}$$

Furthermore, combining Algorithm 1, and Eq. 15, we have

$$\begin{aligned}\|z_i - z\|^2 &= \|y_i - z - \varphi_i\nabla f_i(y_i) + \alpha_2\hat{\beta}_i\hat{d}_i\|^2 \\ &= \|y_i - z - \varphi_i\nabla f_i(y_i)\|^2 + \|\alpha_2\hat{\beta}_i\hat{d}_i\|^2 \\ &\quad + 2\langle y_i - z - \varphi_i\nabla f_i(y_i), \alpha_2\hat{\beta}_i\hat{d}_i\rangle \\ &\le \|y_i - z - \varphi_i\nabla f_i(y_i)\|^2 \\ &\quad + 2\langle y_i - z - \varphi_i\nabla f_i(y_i) + \alpha_2\hat{\beta}_i\hat{d}_i, \alpha_2\hat{\beta}_i\hat{d}_i\rangle \\ &\le \|y_i - z - \varphi_i\nabla f_i(y_i)\|^2 + 2\alpha_2\hat{\beta}_i\langle z_i - z, \hat{d}_i\rangle \\ &\le \|y_i - z\|^2 - \rho_i(4-\rho_i)\frac{f_i^2(y_i)}{\|\nabla f_i(y_i)\|^2 + \theta_i} + \hat{\beta}_i\hat{M},\end{aligned} \tag{17}$$

where $\hat{M} = \sup_{i\in N} 2\alpha_2\langle z_i - z, \hat{d}_i\rangle$. As with Eq. 17, we deduce

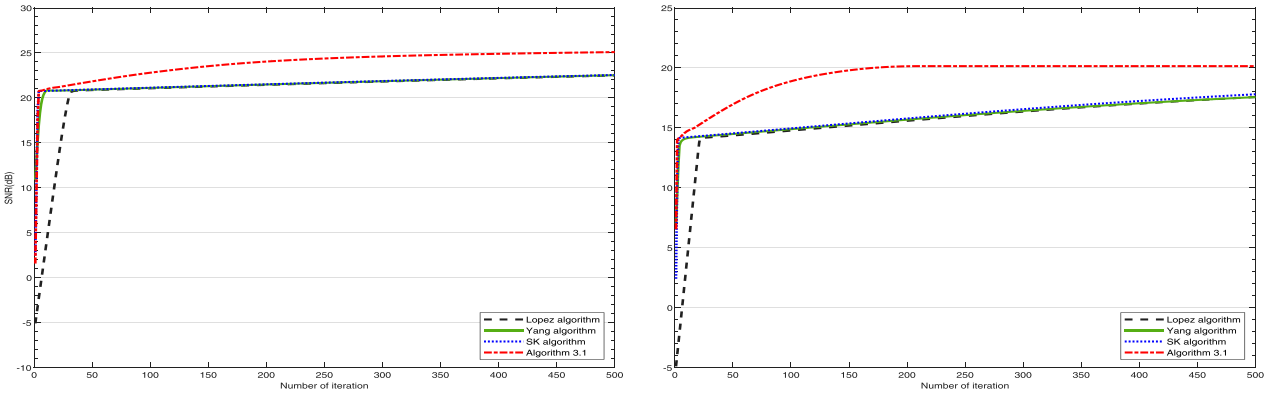

FIGURE 6
Comparison of SNR values of the knee joint (left) and head (right) images resulting from image recovery using the four algorithms with 500 iterations.

$$\begin{aligned}\|y_i - z\|^2 &= \|\omega_i - z - \tau_i \nabla f_i(\omega_i) + \alpha_1 \beta_i d_i\|^2 \\ &\le \|\omega_i - z - \tau_i \nabla f_i(\omega_i)\|^2 + 2\alpha_1 \beta_i \langle y_i - z, d_i \rangle \\ &\le \|\omega_i - z\|^2 - \rho_i(4-\rho_i)\frac{f_i^2(\omega_i)}{\|\nabla f_i(\omega_i)\|^2 + \theta_i} + \beta_i M,\end{aligned} \tag{18}$$

where $M = \sup_{i \in N} 2\alpha_1 \langle y_i - z, d_i \rangle$. Thus, from Eqs 13, 17, 18, it holds that

$$\begin{aligned}\|\omega_{i+1} - z\|^2 \le{}& \|y_i - z\|^2 - \rho_i(4-\rho_i)\frac{f_i^2(y_i)}{\|\nabla f_i(y_i)\|^2 + \theta_i} + \hat{\beta}_i \hat{M} \\ &- \|\omega_{i+1} - y_i + \varphi_i \nabla f_i(y_i) - \alpha_2 \hat{\beta}_i \hat{d}_i\|^2 \\ \le{}& \|\omega_i - z\|^2 - \rho_i(4-\rho_i)\left(\frac{f_i^2(\omega_i)}{\|\nabla f_i(\omega_i)\|^2 + \theta_i} + \frac{f_i^2(y_i)}{\|\nabla f_i(y_i)\|^2 + \theta_i}\right) \\ &+ \left(\beta_i M + \hat{\beta}_i \hat{M}\right) - \|\omega_{i+1} - y_i + \varphi_i \nabla f_i(y_i) - \alpha_2 \hat{\beta}_i \hat{d}_i\|^2.\end{aligned} \tag{19}$$

from Theorem 3.1(C3) and $0 < \rho_i < 4$, we deduce

$$\|\omega_{i+1} - z\| \le \|\omega_i - z\|.$$

Therefore, $\lim_{n \to \infty} \|\omega_i - z\|$ exists; hence $\{\omega_i\}$ is bounded. Consequently, $\{y_i\}$ and $\{z_i\}$ are bounded. Back to the previous step (Eq. 19), we obtain

$$\liminf_{i \to \infty} \rho_i(4-\rho_i)\left(\frac{f_i^2(\omega_i)}{\|\nabla f_i(\omega_i)\|^2 + \theta_i} + \frac{f_i^2(y_i)}{\|\nabla f_i(y_i)\|^2 + \theta_i}\right) = 0,$$

which implies by (C2) and (C3) of Theorem 3.1 that

$$\lim_{i \to \infty} \frac{f_i^2(\omega_i)}{\|\nabla f_i(\omega_i)\|^2} = \lim_{i \to \infty} \frac{f_i^2(y_i)}{\|\nabla f_i(y_i)\|^2} = 0. \tag{20}$$

furthermore, it yields

$$\begin{aligned}\|\nabla f_i(\omega_i)\| &= \|\nabla f_i(\omega_i) - \nabla f_i(z)\| \le L\|\omega_i - z\|, \\ \|\nabla f_i(y_i)\| &= \|\nabla f_i(y_i) - \nabla f_i(z)\| \le L\|y_i - z\|,\end{aligned} \tag{21}$$

where $L = 1 + \|\mathcal{A}\|^2$. This implies that $\|\nabla f_i(\omega_i)\|$ and $\|\nabla f_i(y_i)\|$ are bounded. From Eqs 20, 21, we have

$$\lim_{i \to \infty} f_i(\omega_i) = \lim_{i \to \infty} f_i(y_i) = 0,$$

which implies

FIGURE 7
Original image.

$$\begin{aligned}&\lim_{i \to \infty} \left(\|(I - P_{C_i})\omega_i\| + \|(I - P_{Q_i})\mathcal{A}\omega_i\|\right) \\ &= \lim_{i \to \infty} \left(\|(I - P_{C_i})y_i\| + \|(I - P_{Q_i})\mathcal{A}y_i\|\right) = 0.\end{aligned}$$

Moreover, from Eq. 19, we have

$$\lim_{i \to \infty} \|\omega_{i+1} - y_i + \varphi_i \nabla f_i(y_i) - \alpha_2 \hat{\beta}_i \hat{d}_i\| = 0. \tag{22}$$

We notice that

$$\lim_{i \to \infty} \varphi_i \|\nabla f_i(y_i)\| = \lim_{i \to \infty}\left(\frac{\rho_i f_i(y_i)}{\|\nabla f_i(y_i)\|^2 + \theta_i}\|\nabla f_i(y_i)\|\right) = 0. \tag{23}$$

Therefore, combining Eqs. 22, 23 and $\lim_{i \to \infty} \hat{\beta}_i = 0$, we have

$$\lim_{i \to \infty} \|\omega_{i+1} - y_i\| = 0.$$

In addition, from Algorithm 1 and Theorem 3.1(C3), we obtain

$$\lim_{i \to \infty} \|y_i - \omega_i\| = \lim_{i \to \infty} (\tau_i \|\nabla f_i(\omega_i)\|) = 0.$$

Then, we deduce

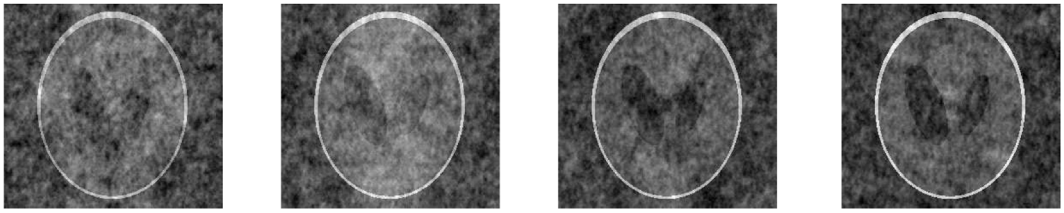

FIGURE 8
Versions of the image in Figure 7 with sampling rates of 30%, 40%, 50%, and 60% from left to right.

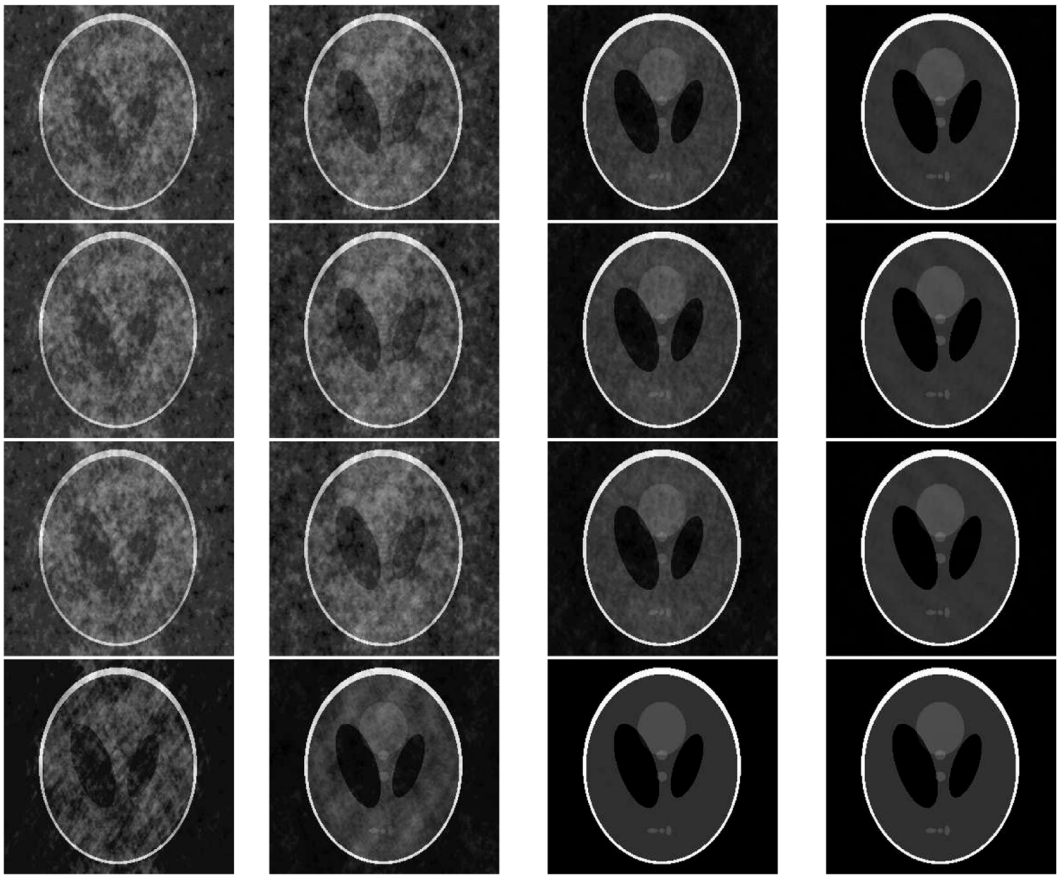

FIGURE 9
Comparison of images recovered using the four algorithms. From top to bottom: López's algorithm, Yang's algorithm, Sakurai and Iiduka's algorithm, and Algorithm 1; from left to right: sampling rates of 30%, 40%, 50%, and 60%.

$$\lim_{i\to\infty} \|\omega_{i+1} - \omega_i\| = 0,$$

considering $\{\omega_i\}$ is bounded. Consequently, we can find a subsequence $\{\omega_{i_k}\} \to \omega^\star$ and $\omega^\star \in H_1$. Subsequently, we prove $\omega^\star \in \Omega$. Using Eq. 5, and the fact that $\omega_{k+1} \in C_{i_k}$, we have

$$c(\omega_{i_k}) \le \langle \zeta_{i_k}, \omega_{i_k} - \omega_{i_k+1} \rangle,$$

where $\zeta_{i_k} \in \partial c(\omega_{i_k})$. Applying the boundedness of ∂c, it follows that

$$c(\omega_{i_k}) \le \|\zeta_{i_k}\| \|\omega_{i_k} - \omega_{i_k+1}\| \to 0, k \to \infty . \tag{24}$$

From $\omega_{i_k} \rightharpoonup \omega^\star$ and Eq. 24, we deduce

$$c(\omega^\star) \le \lim_{k\to\infty} \inf c(\omega_{i_k}) \le 0.$$

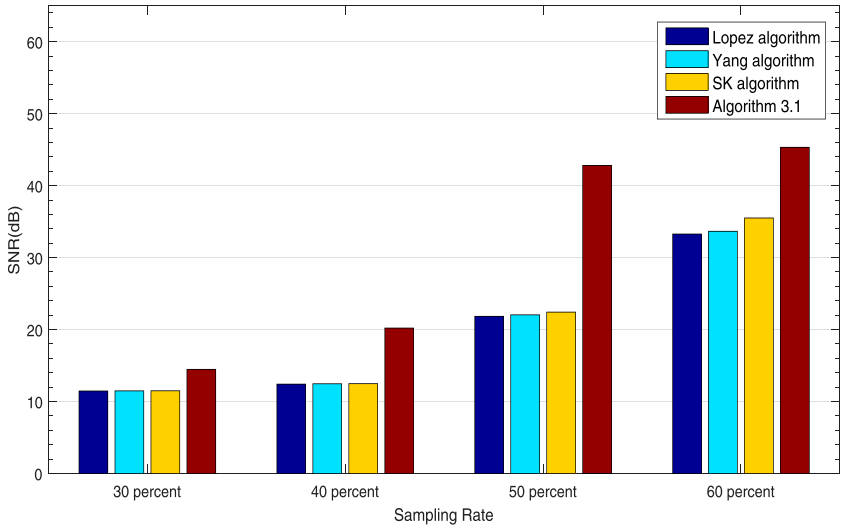

FIGURE 10
Comparison of the SNR values of the images in Figure 9.

Hence, $\omega^* \in C$. Then, we show that $\mathcal{A}x^* \in Q$. The fact that $P_{Q_{i_k}}(\mathcal{A}\omega_{i_k}) \in Q_{i_k}$ implies

$$q(\mathcal{A}\omega_{i_k}) \leq \langle \vartheta_{i_k}, \mathcal{A}\omega_{i_k} - P_{Q_{i_k}}(\mathcal{A}\omega_{i_k})\rangle, \tag{25}$$

where $\vartheta_{i_k} \in \partial q(\mathcal{A}\omega_{i_k})$. Then, we get

$$q(\mathcal{A}\omega_{i_k}) \leq \|\omega_{i_k}\|\|\mathcal{A}\omega_{i_k} - P_{Q_{i_k}}(\mathcal{A}\omega_{i_k})\| \to 0, k \to \infty .$$

Moreover, according to Eq. 25, we deduce

$$q(\mathcal{A}\omega^*) \leq \lim_{k\to\infty} \inf q(\mathcal{A}\omega_{i_k}) \leq 0.$$

Therefore, $\mathcal{A}\omega^* \in Q$. We can thus draw the conclusion that the sequence $\{\omega_i\} \to \Omega$.

4 Experimental results

In this section, we describe numerical simulations to demonstrate the applications of Yang's algorithm [15], López's algorithm [17], Sakurai and Iiduka's algorithm [20], and the proposed algorithm (Algorithm 1) in signal processing and image recovery. The results of our simulations show that the proposed method has higher efficiency than the well-known methods in the literature. The experiments were carried out in the environment of Matlab2016 and the CPU is Intel(R) Core(TM) i5-8265U with @1.60GHz 1.80 GHz.

4.1 Signal processing

In the test, let original signal has m nonzero components, we choose $N = 4{,}096$, $M = 2048$, and $m = 128$ according to Eq. 1 . The mean value and variance of Gaussian noise are 0 and 10^{-4}, respectively. The initial point $\omega_1 = (1,1,\ldots,1)^{\mathrm{T}}$, $\omega_0 = (0,0,\ldots,0)^{\mathrm{T}}$, $\alpha_1 = 0.8$, $\alpha_2 = 0.9$, $\rho_i = 1.1$, $\theta_i = \frac{1}{i^3}$ and $r = m$. The mean squared error (MSE) can be chosen as the evaluation criterion, which is defined as:

$$\mathrm{MSE} = \frac{1}{N}\|\omega^* - \omega\|^2,$$

where ω is the original signal, ω^* is the recovered signal. We set the stopping criteria MSE $\leq 10^{-5}$. Figure 1 shows the results of this experiment. These indicate that the number of iterations and CPU time required by our approach are the best of the four methods.

4.2 Image recovery

The value of each pixel in a grayscale image is in the range [0.255]. The image restoration can be described as the minimizer:

$$\min_{\bar{s}\in C} \|\mathcal{A}\bar{s} - y\|_2,$$

where $\|\cdot\|_2$ is the standard Euclidean norm, y is the observed image, $\bar{s}$ is the approximation of the original image, and $\mathcal{A}$ is a blurring operator. When a color image is processed, we divide it into three channels: red, green, and blue. Supposing the size of the image in each channel is $M \times N$, we have the formula for the MSE:

$$\mathrm{MSE} = \frac{1}{MN}\sum_{i=0}^{M-1}\sum_{j=0}^{N-1}\|\bar{s}(i,j) - s(i,j)\|^2,$$

where $\bar{s}$ and s are the restored and original images, respectively.

Seeking to illustrate the effects of image recovery, we use the signal-to-noise ratio (SNR) and peak SNR (PSNR), which are defined:

$$\mathrm{SNR} := 20\log_{10}\frac{\|\bar{s}\|_2}{\|s-\bar{s}\|_2},\ \mathrm{PSNR} := 20\log_{10}\frac{255}{\sqrt{\mathrm{MSE}}}.$$

In short, larger SNR and PSNR values indicate better restoration of the image. Figure 2 show the results of different color images recovery. Figure 3 shows a comparison of the SNR and PSNR values for images recovered using the four algorithms. The experimental results show that the proposed algorithm always has the largest SNR and PSNR values for different images, which clearly indicates that the proposed algorithm is more effective in recovery than other algorithms.We next applied our method to medical images. Figures 4, 5 show computed tomography (CT) images of a knee joint and a head, and Figure 6 shows a comparison of the SNR values resulting from recovery using each algorithm for these images. From Figure 6, it can be seen clearly that the SNR of our method(the red line) is significantly higher than other methods.

Figure 7 shows an original grayscale image. In Figure 8, we investigate the use of our method on this image with different sampling rates. In Figure 9, we show the image recovered by the four algorithms with different sampling rates. Figure 10 shows a comparison of the SNR values of these images. It can clearly be seen that the performance of our method is the best.Finally, it can clearly be seen that our method provides higher SNR and PSNR values than López's algorithm, Yang's algorithm, or Sakurai and Iiduka's algorithm.

5 Conclusion

In this article, we propose a new conjugate gradient method for signal recovery. The superiority of our method lies in its employment of the ideas of accelerated conjugate gradient methods with a new adaptive way of choosing the step size. Under some assumptions, the weak convergence of the designed method was established. As application demonstrations, we implemented our method to solve signal-processing and image-restoration problems. The results of our numerical simulations verify the effectiveness and superiority of the new approach. However, in the numerical experiments in this paper, we always assume that the noise is known. In the future work, we will devote to signal and image recovery research without prior knowledge of noise by optimization method.

Data availability statement

The raw data supporting the conclusion of this article will be made available by the authors, without undue reservation.

Author contributions

PH and KL designed the work, wrote the manuscript, and managed communication among all the authors. PH and KL analyzed the data. All authors contributed to the article and approved the submitted version.

Funding

This project is supported by the Shandong Provincial Natural Science Foundation (Grant No. ZR2019MA022).

Acknowledgments

The authors would like to thank the reviewers and editors for their useful comments, which have helped to improve this article.

Conflict of interest

The authors declare that the research was conducted in the absence of any commercial or financial relationships that could be construed as a potential conflict of interest.

Publisher's note

All claims expressed in this article are solely those of the authors and do not necessarily represent those of their affiliated organizations, or those of the publisher, the editors and the reviewers. Any product that may be evaluated in this article, or claim that may be made by its manufacturer, is not guaranteed or endorsed by the publisher.

References

1. Zhang X, Wu H, Sun H, Ying W. Multireceiver SAS imagery based on monostatic conversion. *IEEE J Sel Top Appl Earth Obs Remote Sens* (2021) 14: 10835–53. doi:10.1109/jstars.2021.3121405

2. Zhang X, Ying W, Yang P, Sun M. Parameter estimation of underwater impulsive noise with the Class B model. *IET Radar Sonar & Navigation* (2020) 14:1055–60. doi:10.1049/iet-rsn.2019.0477

3. Li Y, Geng B, Jiao S. Dispersion entropy-based lempel–ziv complexity: A new metric for signal analysis. *Chaos Solitons Fractals* (2022) 161:112400. doi:10.1016/j.chaos.2022.112400

4. Li Y, Tang B, Yi Y. A novel complexity-based mode feature representation for feature extraction of ship-radiated noise using VMD and slope entropy. *Appl Acoust* (2022) 196:108899. doi:10.1016/j.apacoust.2022.108899

5. Li Y, Mu L, Gao P. Particle swarm optimization fractional slope entropy: A new time series complexity indicator for bearing fault diagnosis. *Fractal Fract* (2022) 6: 345. doi:10.3390/fractalfract6070345

6. Cai T, Xu G, Zhang J. On recovery of sparse signals via l_1 minimization. *IEEE Trans Inf Theor* (2009) 55:3388–97. doi:10.1109/tit.2009.2021377

7. Censor Y, Elfving T. A multiprojection algorithm using Bregman projections in a product space. *Numer Algorithms* (1994) 8:221–39. doi:10.1007/bf02142692

8. Xu H. Iterative methods for the split feasibility problem in infinite-dimensional Hilbert spaces. *Inverse Probl* (2010) 26:105018. doi:10.1088/0266-5611/26/10/105018

9. Moudafi A, Gibali A. l_1-l_2 regularization of split feasibility problems. *Numer Algorithms* (2017) 78:739–57. doi:10.1007/s11075-017-0398-6

10. Bauschke H, Combettes P. A weak-to-strong convergence principle for Fejér-monotone methods in Hilbert spaces. *Mathematics OR* (2001) 26:248–64. doi:10.1287/moor.26.2.248.10558

11. Byrne C. Iterative oblique projection onto convex sets and the split feasibility problem. *Inverse Probl* (2002) 18:441–53. doi:10.1088/0266-5611/18/2/310

12. Byrne C. A unified treatment of some iterative algorithms in signal processing and image reconstruction. *Inverse Probl* (2004) 20:103–20. doi:10.1088/0266-5611/20/1/006

13. Yang Q. The relaxed CQ algorithm solving the split feasibility problem. *Inverse Probl* (2004) 20:1261–6. doi:10.1088/0266-5611/20/4/014

14. Wang F. Polyak's gradient method for split feasibility problem constrained by level sets. *Numer Algorithms* (2017) 77:925–38. doi:10.1007/s11075-017-0347-4

15. Yang Q. On variable-step relaxed projection algorithm for variational inequalities. *J Math Anal Appl* (2005) 302:166–79. doi:10.1016/j.jmaa.2004.07.048

16. Wang F. On the convergence of CQ algorithm with variable steps for the split equality problem. *Numer Algorithms* (2017) 74:927–35. doi:10.1007/s11075-016-0177-9

17. Lopez G, Martin-Marquez V, Wang F, Xu HK. Solving the split feasibility problem without prior knowledge of matrix norms. *Inverse Probl* (2012) 28:085004. doi:10.1088/0266-5611/28/8/085004

18. Qu B, Xiu N. A note on the CQ algorithm for the split feasibility problem. *Inverse Probl* (2005) 21:1655–65. doi:10.1088/0266-5611/21/5/009

19. Gibali A, Liu LW, Tang YC. Note on the modified relaxation CQ algorithm for the split feasibility problem. *Optim Lett* (2017) 12:817–30. doi:10.1007/s11590-017-1148-3

20. Kesornprom S, Pholasa N, Cholamjiak P. On the convergence analysis of the gradient-CQ algorithms for the split feasibility problem. *Numer Algorithms* (2020) 84:997–1017. doi:10.1007/s11075-019-00790-y

21. Nocedal J, Wright SJ. *Numerical optimization*. New York: Springer (2006).

22. Hideaki I. Iterative algorithm for solving triple-hierarchical constrained optimization problem. *J Optim Theor Appl* (2011) 148:580–92. doi:10.1007/s10957-010-9769-z

23. Nocedal J. *Numerical optimization: Springer series in operations research and financial engineering*. New York: Springer (2006).

24. Sakurai K, Iiduka H. Acceleration of the Halpern algorithm to search for a fixed point of a nonexpansive mapping. *Fixed Point Theor Appl* (2014) 2014:202. doi:10.1186/1687-1812-2014-202

25. Dang Y, Gao Y. The strong convergence of a KM-CQ-like algorithm for a split feasibility problem. *Inverse Probl* (2011) 27:015007. doi:10.1088/0266-5611/27/1/015007

26. Suantai S, Pholasa N, Cholamjiak P. Relaxed CQ algorithms involving the inertial technique for multiple-sets split feasibility problems. *Rev Real Acad Cienc Exactas* (2019) 13:1081–99. doi:10.1007/s13398-018-0535-7

27. Wang F, Xu HK. Approximating curve and strong convergence of the CQ algorithm for the split feasibility problem. *J Inequal Appl* (2010) 2010:1–13. doi:10.1155/2010/102085

28. Xu H. Iterative methods for the split feasibility problem in infinite-dimensional Hilbert spaces. *Inverse Probl* (2010) 26:105018. doi:10.1088/0266-5611/26/10/105018

29. Zhao J, Zhang Y, Yang Q. Modified projection methods for the split feasibility problem and the multiple-sets split feasibility problem. *Appl Math Comput* (2012) 219:1644–53. doi:10.1016/j.amc.2012.08.005

30. Goebel K, Reich S. *Uniform convexity*. New York: Marcel Dekker (1984).

frontiers | Frontiers in Physics

TYPE Original Research
PUBLISHED 05 January 2023
DOI 10.3389/fphy.2022.1113330

OPEN ACCESS

EDITED BY
Yuxing Li,
Xi'an University of Technology, China

REVIEWED BY
Dan Liu,
Institute of Acoustics (CAS), China
Xianghao Hou,
Northwestern Polytechnical University, China

*CORRESPONDENCE
Xin Huang,
shaoshanhx@126.com

SPECIALTY SECTION
This article was submitted to Physical Acoustics and Ultrasonics, a section of the journal Frontiers in Physics

RECEIVED 01 December 2022
ACCEPTED 19 December 2022
PUBLISHED 05 January 2023

CITATION
Qu K, Ou Z, Huang X and Liu L (2023), A simplified model for acoustic focalization in environments with seabed uncertainties. *Front. Phys.* 10:1113330. doi: 10.3389/fphy.2022.1113330

A simplified model for acoustic focalization in environments with seabed uncertainties

Ke Qu[1], Zhenyi Ou[1], Xin Huang[2]* and Liwen Liu[3,4]

[1]College of Electronics and Information Engineering, Guangdong Ocean University, Zhanjiang, China, [2]Laboratory of Coastal Ocean Variation and Disaster Prediction, Guangdong Ocean University, Zhanjiang, China, [3]School of Marine Science and Technology, Northwestern Polytechnical University, Xi'an, China, [4]Xi'an Institute of Precision Mechanics, Xi'an, China

Introduction: Parameter mismatch poses a challenge to source localization in cases involving environments with seabed uncertainties. By including environmental parameters in the search space, focalization can be used to estimate the location of the source using environmental information that is limited *a priori*. **Methods:** To reduce the number of parameters, a simplified seabed model is proposed here for such focalization. Only two geoacoustic parameters—the amplitude F and phase c_F of reflection—are used to describe the seabed. Focalization is generally tested using genetic algorithms for the colored noise case (COLNOISE) benchmark problem. **Results:** The proposed simplified model can obtain the location of the source more easily than a layered model. Due to its advantage in terms of parameter sensitivity and inter-coupling, the simplified model can ensure the robustness of the results of inversion. The proposed method was tested on a broadband signal in the Asian Seas International Acoustics Experiment (ASIAEX2001), where both the location and the geoacoustic parameters were easily inverted. **Discussion:** The simplified model provides a sufficiently high acoustic resolution for focalization, and its reduction of the geoacoustic parameters helps solve the problem of inversion.

KEYWORDS

focalization, matched field processing, geoacoustic parameter, genetic algorithm, geoacoustic model

1 Introduction

Matched field processing (MFP) is a well-known technology for solving inversion problems by comparing acoustic data with solutions to wave equations [1]. Depending on the unknown quantity, MFP can be divided into source localization [2], tomography [3], and geoacoustic inversion [4, 5]. Owing to the temporal and spatial variations in environmental parameters in the ocean and difficulties of marine measurement, there is a mismatch between the ocean and its environmental model, which is a challenge for MFP. To overcome the mismatch and accurately estimate the location of the source with limited *a priori* environmental information, focalization has generally been used [6]. By including the environment in the parameter search space, focalization circumvents stringent requirements pertaining to accurate knowledge of the environment.

Because focalization involves more unknown parameters than traditional localization, it leads to a more complex optimization problem. In practical application, it becomes necessary to use a dimension reduction algorithm to parameterize the environment. The dimension reduction problem was solved by means of feature extraction [7–9]. A typical example is the empirical orthogonal function (EOF) [10, 11]. Using principal component extraction, the sound speed profile can be described by three to five parameters. However, environmental

parameterization is often more complicated in case of the seabed. As the direct measurement of the bottom is difficult and expensive, it is more challenging to obtain parameters of the seabed than the sound speed profile. Actual structure of the bottom of the sea is generally too complex to mathematically represent. Therefore, it is usually described by an effect-equivalent description. The most common method in this vein involves describing a certain number of bottom layers using the sound speed, density, and attenuation. When the half-space model is used, the seabed is represented by three parameters. The number of geoacoustic parameters increases rapidly with the number of layers in the seabed, where this complicates focalization owing to sensitivity- and coupling-related problems. Qu and Hu proposed a single-parameter seabed model and designed a relevant method of geoacoustic inversion [12, 13]. As this single-parameter seabed model can calculate only an incoherent sound field, it is inapplicable to MFP. Shang developed a method called the rapid bottom characteristic using two parameters, P and Q, to analyze acoustic problems in shallow water [14, 15]. They were able to describe different types of regions of propagation, Green's function, and the waveguide invariant [16–18]. Similarly, reflection loss was introduced by Harrison to explain reverberation [19]. The simplified seabed model with one or two parameters has been applied to geoacoustic inversion in several previous studies, but whether it can be used as an effective acoustic lens for source focalization remains to be studied.

This paper proposes a simplified seabed model with two parameters for the reflection of sound from the bottom, and examines focalization by using a small number of geoacoustic parameters. Section 2 discusses general aspects of the simplified geoacoustic model. In Section 3, focalization based on the simplified model is tested on the colored noise case (COLNOISE) benchmark problem. Compared with the layered model, some characteristics of the simplified model are discussed by using the objective function and marginal probability density. The linear relation between a new geoacoustic parameter and acoustic quantities is presented to help solve the inversion problem. In Section 4, the broadband focalization of data from the Asian Seas International Acoustics Experiment (ASISEX) in the East China Sea is analyzed, and the result shows that the search for the focalization parameter converges to the correct location of the source and the geoacoustic parameters. The conclusions and directions for future work are summarized in Section 5.

2 Simplified geoacoustic model for focalization

When sound interacts with the seabed, the result of acoustic reflection can be summarized in terms of amplitude and phase change. To simplify the geoacoustic model, the natural choice is to describe the seabed based on the amplitude and phase parameters of reflection. Past studies in the area have used parameters that are similar in physical significance, where some of them can be converted into one another under certain conditions. For compatibility with past work, this paper uses Jones's mathematical expression F for the amplitude of reflection. The bottom loss BL can be expressed as [20]

$$BL = F \cdot \varphi. \tag{1}$$

Based on a large amount of historical data and theoretical derivation, it is well known that BL for a high-speed seabed whose sound speed is higher than the sound speed of sea water is always proportional to the grazing angle φ for a small value of the latter. Considering long-distance propagation, a large grazing angle yields is a large value of BL and a large number of reflections from the seabed. The resulting acoustic energy is almost completely consumed by reflection from the seabed. On the contrary, the value of BL for a small grazing angle is smaller, and there are fewer reflections off the seabed. The acoustic energy for a small grazing angle is still effective at long distances and becomes the dominant component in the far field. Therefore, the slope of the bottom loss F (dB/rad) can be used to describe the change in amplitude in the far field.

For representative phase calculations, which are necessary for MFP, the phase parameter must be given at the same time as the amplitude parameter. Based on the half-space model, the phase change θ can be calculated as

$$\theta = -2\ \tan^{-1}\frac{\left(\cos^2\varphi - n^2\right)^{1/2}}{m\sin\varphi}, \tag{2}$$

where n is the ratio of the sound speed in water to that on the seabed, and m is the ratio of the density of the seabed to that of water. For a small grazing angle,

$$\lim_{\varphi \longrightarrow 0}\frac{\left(\cos^2\varphi - n^2\right)^{1/2}}{m\sin\varphi} = +\infty\ . \tag{3}$$

Let $Y = \frac{(\cos^2\varphi - n^2)^{1/2}}{m\sin\varphi}$, then

$$\tan^{-1} Y(\varphi) = \frac{\pi}{2} - \frac{1}{Y}\cdots\frac{(-1)^{n+1}}{2n+1}Y^{-2n-1} \approx \frac{\pi}{2} - \frac{1}{Y}. \tag{4}$$

By substituting (4) into (2), the expression for the phase change θ in the limit of a small grazing angle is

$$\theta \approx -\pi + \frac{2m}{\sqrt{(1-n^2)}}\varphi \approx -\pi + \frac{\pi}{\varphi_c}\varphi. \tag{5}$$

Hence, the phase change increases approximately linearly with the grazing angle. The reflection phase varies from -π to 0 while the grazing angle increases from zero to the critical angle φ_c. We define a parameter of the reflection phase c_F. The phase change is then given by

$$\theta = -\pi + \frac{\pi}{\cos^{-1}(c_w/c_F)}\varphi. \tag{6}$$

where the critical angle of total reflection, $\varphi_c = \cos^{-1}(c_w/c_F)$, c_w is the sound speed of sea water near the bottom, and c_F is the equivalent speed on the seabed. Compared with the layered model, c_F is not the sound speed at a specific depth. c_F is an effect-equivalent description of sound speed in reflection phase change. Based on Eq. 1–6, the amplitude parameter F and phase parameter c_F can be used to describe the acoustic properties of the seabed. The coherent sound field for MFP and other applications can then be calculated. This simplified model, which can calculate the coherent sound field using few parameters, is applicable to the sound field beyond the short range where acoustic energy is dominated by interactions with the seabed at a small grazing angle. To verify the validity of the approximation in the simplified model, a section test has been carried out on a multi-layer seabed.

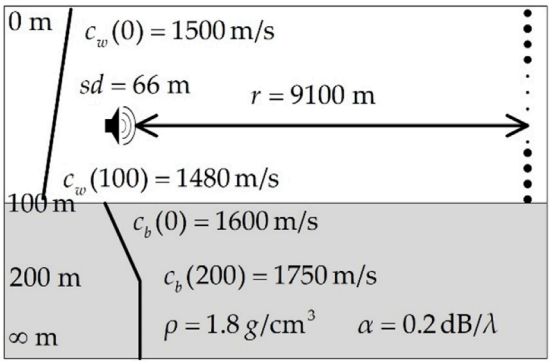

FIGURE 1
Schematic of environment for the COLNOISE case.

3 Testing on benchmark problem of matched field processing

3.1 COLNOISE benchmark problem

To get a sense of the relative merits of different schemes, the Naval Research Laboratory has provided a set of simulated data for MFP testing called the benchmark problem [21, 22]. According to the research objectives of this paper, the COLNOISE case was selected for a focalization test. The test environment is shown in Figure 1. The COLNOISE case is a range-independent waveguide with a depth of 100 m. The 250 Hz source depth *sd* is 66 m at a range r = 9.1 km. A vertical line array (VLA) of 20 hydrophones spanning the water column receives the signal, which is affected by color noise with a signal-to-noise ratio (SNR) of 40 dB. The color noise is design to describe the construction of a cross spectral density for noise due to breaking waves. The sound speed on the surface of the ocean is $c_w(0)$ = 1500 m/s and that at the bottom is $c_w(200)$ = 1750 m/s, the density of the seabed is ρ = 1.8 g/cm^3, and the attenuation coefficient is α = 0.2 dB/λ. To study the performance of the simplified model in terms of focalization, the geoacoustic and localization parameters were inverted, and the sound speed profile in seawater was set to a known value.

3.2 Focalization based on genetic algorithms

A classic method of inversion based on the genetic algorithm has been used to test the geoacoustic model, as shown in Figure 2. The initial population was randomly generated according to the search space, and the copy field was calculated by the normal mode program KRAKENC (https://oalib-acoustics.org) to match with signals of the vertical array. An objective function was used to determine an individual's fitness, and offspring replaced part of the population to approach the fittest population. Following this, *a posteriori* probability estimation was carried out on samples of the optimization process to obtain the complete results. The process is as shown below.

The first step of focalization is environmental parameterization, which helps set the search space for the geoacoustic and location-related parameters. In focalization according to the simplified model, four parameters were used: the source depth *sd*, range *r*, amplitude *F*, and phase c_F. In focalization using the layered model, seven parameters were used: the source depth *sd*, range *r*, sound speed on the surface of the seabed $c_b(0)$, base speed of sound $c_b(d)$, depth of the sediment layer *d*, density of the seabed ρ, and attenuation coefficient α. Bounds of the parameters for these two environments are given in Table. 1. To investigate whether the geoacoustic model can guarantee accurate results of location without prior information, the parameters of the two environments were set with a wide search interval that could cover different types of seabeds.

The genetic algorithm, which is based on an analogy with biological evolution, was used to find the global optimum without performing an exhaustive search [23]. According the results of environmental parameterization, an initial population was randomly generated. Then, based on the individual's fitness of matching, the population moved to the fittest model vector through evolutionary steps consisting of selection, crossover, and mutation. Parameters of the optimization were set as follows: the population size was 100, reproduction rate was 0.5, crossover rate was 0.8 and mutation rate was 0.08. To collect samples to estimate the *a posteriori* probability distributions, 20 independent runs were executed in parallel.

To suppress ambiguous solutions, a high-resolution objective function is necessary for focalization. The Bartlett processor was used to match the "measured" sound field and the copy field. The objective function $\psi(m)$ is

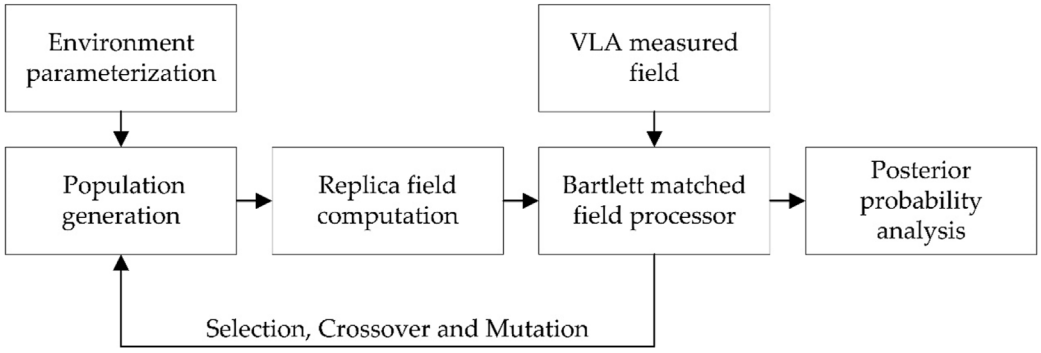

FIGURE 2
Flowchart of focalization.

TABLE 1 Environmental parameters for two types of environments considered.

Parameters	Bounds		Grid
	Environment 1	Environment 2	
sd (m)	[1 100]	−	1
r (m)	[5000 10,000]	−	100
F (dB/rad)	[0.50 3.50]	−	0.01
c_e (m/s)	[1550 1800]	−	1
$c_b(0)$ (m/s)	−	[1550 1800]	1
d (m)	−	[100,300]	1
$c_b(d)$ (m/s)	−	[1550 1800]	1
ρ (g/cm^3)	−	[1.00 2.00]	0.01
α (db/λ)	−	[0.01 1]	0.01

$$\psi(m) = 1 - \frac{\left|\sum_{i=1}^{N} Q_i P_i(m)^*\right|}{\left[\sum_{i=1}^{N}|Q_i|^2\right]\left[\sum_{i=1}^{N}|p_i(m)|^2\right]}^2, \tag{7}$$

where Q is the "measured" pressure, P is the replica pressure, m is the vector in the search space, i is the number of hydrophones, and N is the total number of hydrophones. The fitness of each individual is evaluated by the objective function and the final result of the evolution approaches the optimum value of zero for a perfect match.

The complete solution to the focalization problem should involve a measure of uncertainty for the model parameters. The obtained samples of the search space can be used to estimate the *a posteriori* probabilities. Gerstoft offered a semi-empirical method based on the sampling procedure of the genetic algorithm. The probability σ of the k-th vector m^k is given by [24].

$$\sigma\left(m^k\right) = \frac{\exp\left[-\psi\left(m^k\right)/T\right]}{\sum_{j=1}^{N_{obs}} \exp\left[-\psi\left(m^j\right)/T\right]}, \tag{8}$$

where N_{obs} is the number of observed model vectors, and T is temperature, which is equal to the average value of objective function of the 50 best samples. The marginal probability distribution of the l-th parameter obtaining a particular value κ can be calculated by:

$$\sigma(m_l = \kappa) = \frac{\sum_{j=1}^{N_{obs}} \exp\left[-\psi\left(m^j\right)/T\right]\delta\left(m_l^j = \kappa\right)}{\sum_{j=1}^{N_{obs}} \exp\left[-\psi\left(m^j\right)/T\right]}, \tag{9}$$

where δ is the Dirac function. Based on the marginal probability distribution of $\sigma(m_l)$, the robustness of the results can be analyzed. As theoretical solutions in the normal mode are efficient and appropriate for inversion problems, forward solutions of the acoustic equation were calculated by the normal mode model KRAKENC. By describing reflection off the seabed, parameters of the simplified model can also be entered into the KRAKENC programs to calculate the sound field.

3.3 Analysis of results

In the benchmark problem test, all parallel runs converged to the same optimal vector. The depth of the source sd was 66 m, range r was 9.1 km, amplitude F was 1.9 dB/rad, and phase parameter c_F was 1628 m/s. The results of the location parameter show that the simplified model performs focalization as a layered model if a large number of configurations of the receive array were used.

The most appealing characteristics of the simplified model when applied to focalization are intuitively illustrated in Figure 3. The process of evolution of the first 200 generations for the two environments is shown in the figure, and values of the objective function for all parameters of the randomly selected runs of focalization are given. Even though the evolution in different runs has random characteristics, a sense of how well each parameter has been estimated can be obtained from the scatter plot of the objective function for the two environments. The optimal value of the layered model (0.003) is significantly lower than that of the simplified model (0.963). This shows that more parameters can better describe the details of the seabed. However, the simplified model provides a sufficiently high acoustic resolution for focalization. In the parallel runs, almost all the inversion based on the simplified model converged to the global optimum earlier than that based on the layered model. At the same time, the optimal value of the geoacoustic parameters was obtained in the first 200 generations, whereas the geoacoustic parameters of the layered model could not be determined in the first few hundred generations. Because the two environments have the same conditions except for the geoacoustic model, it can be inferred that the simplified model can reduce the complexity of the inversion optimization.

The scatter plots that appear as an arch (e.g., $c(0)$, F; c_F, and location-related parameters) that indicate that the parameters had been well estimated. Plots that appear nearly flat at the base (e.g., d, $c_b(d)$ and α) had been estimated less well. Parameter sensitivity is an important factor. Some geoacoustic parameters of the layered model—for example, density ρ—could not significantly affect the sound field. In the optimization, the insensitive parameters will make focalization over parameterize with meaningless values of some vector m. Another important factor is the correlation between the geoacoustic parameters. The limitation of the layered model in terms of correlation and sensitivity has been exhaustively studied [25]. A well-know example is the correlation between d and $c_b(d)$ that is related through the reflection properties. For the layered model assumption, the combinations of d and $c_b(d)$ with different values can provide almost the same bottom reflection effect. These combinations will obtain similar values of the objective function and appear as local optimums in the focalization. The uncertainty in these correlated parameters generates errors in the estimation of all other parameters. The advantages of the simplified model have been analyzed through the ambiguous surface, as shown in Figure 4. There are clear changes in the objective function in the search space, which means that the two parameters of the simplified model are relatively sensitive and contained useful information on the sound field. No local optimum occurs on the ambiguous surface, the influence of F and c_F on the sound field is independent, and the correlation between the parameters of the simplified model was weak. In the ambiguous surface of the two geoacoustic parameters of the simplified model, as shown in Figure 4, the geoacoustic parameters are well estimated without any local optimum. The values of the cost

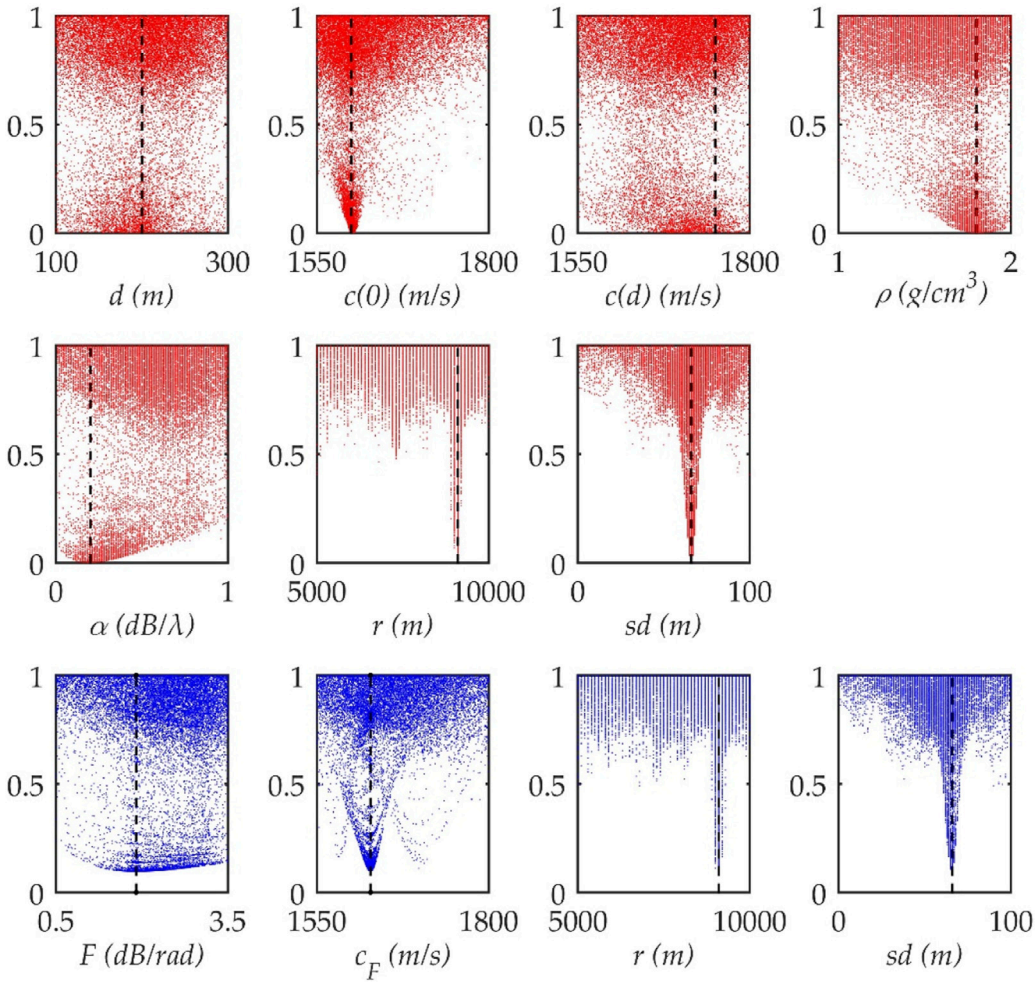

FIGURE 3
Values of the cost function obtained using optimization inversion. The dash lines represent the optimal values. Red represents the layered model. Blue represents the simplified model.

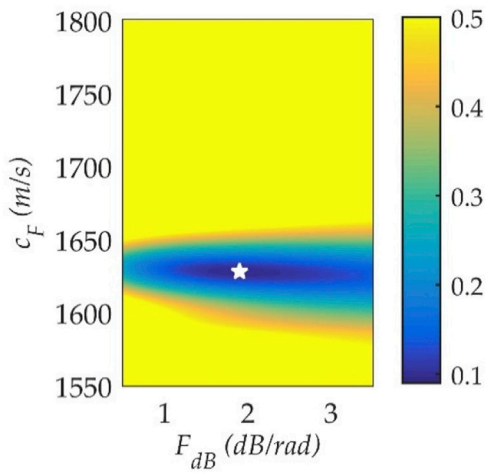

FIGURE 4
Ambiguous surface for geoacoustic parameters of the simplified model. The pentagram represents the optimal value.

function of the simplified model are shown in Figure 5. When another parameter in the simplified is the optimal value, the objective function increases monotonically with distance from the optimal value. By virtue of this monotonic characteristic, the optimization of the focalization is more efficient in the simplified model than the layered model.

$$I = \frac{\lambda I_0}{H^2 r}\sum_l \exp(-2\beta_l r), \tag{10}$$

where I_0 is the intensity at the source, H is the depth of water, λ is wavelength, and β_l is the attenuation of the l-th normal mode, and can be expressed as

$$\beta_l = -\frac{\ln|V|}{S_l}, \tag{11}$$

where V is the reflection coefficient and S_l the span of the l-th normal mode. The grazing angle of the l-th normal mode is

$$\varphi_l = \frac{l\lambda}{2H}, \tag{12}$$

The span of the l-th normal mode is

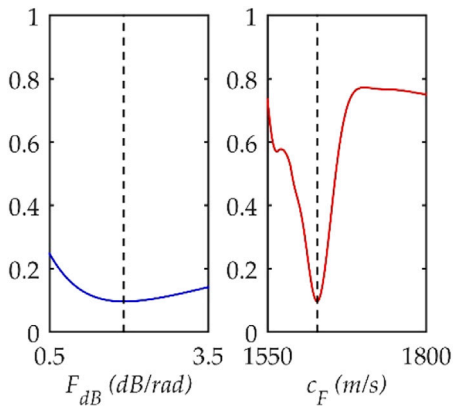

FIGURE 5
Values of the cost function for the geoacoustic parameter of the simplified model. The vertical lines represent the optimal value. Note also that the linear property of F is also an advantage for inversion. The change in F is linearly related to changes in the other quantities, which are derived from the measured pressure. Based on normal mode theory, the intensity I is given by.

$$S_l = \frac{4H^2}{l\lambda}, \tag{13}$$

It is easy to find the relation between parameters of the amplitude V and F as

$$F\varphi = 20\ \log_{10} V. \tag{14}$$

Combining the equations above, the intensity I over a range r can be rewritten as a function of F:

$$I = \frac{\lambda I_0}{H^2 r}\sum_{l=1}^{N}\exp\left(-\frac{l^2\lambda^2 rF}{80H^3\ \log_{10} e}\right). \tag{15}$$

In application, the part in the parentheses is significantly smaller than one. Replacing the summation with the quadrature, the intensity is given by

$$I = \int_0^N \frac{\lambda I_0}{H^2 r}\exp\left(-\frac{l^2\lambda^2 rF}{80H^3\ \log_{10} e}\right)dl. \tag{16}$$

The number of effective modes is $N = 2H/\lambda$. By including the Gaussian error function $erf\,(x) = (2/\sqrt{\pi})\int_0^x e^{-\eta^2}d\eta$, intensity can be expressed as

$$I = \sqrt{\frac{20\pi\log_{10} e}{FHr^3}}I_0 erf\left(\sqrt{\frac{Fr}{20H\log_{10} e}}\right) \tag{17}$$

For the far field, assuming $Fr \gg 20H\log_{10} e$, the simple linear relation between F and I can be expressed as

$$I = \sqrt{20\pi\log_{10} e/FHr^3}\,I_0. \tag{18}$$

In addition to the intensity of sound, there is a linear relationship for the time domain quantity. The number of interactions of sound with the seabed in the l-th normal mode can be calculated by

$$n = \frac{r\varphi_l}{2H}. \tag{19}$$

The loss in intensity is

$$E = \frac{I}{I_0} = 10\exp\left(-\frac{Fr}{20H}\ \varphi_l^2\right). \tag{20}$$

Based on the geometry of the reflection off the seabed, the time delay τ after direct arrival can be calculated by

$$\tau = \frac{r\sec\varphi_l - r}{c_w} \approx \frac{r\varphi_l^2}{2c_w}, \tag{21}$$

where c_w is the mean sound speed in seawater. The loss in intensity can then be rewritten as

$$Ed\tau = 10\sqrt{\frac{c_w}{2r\tau}}\exp\left(-\frac{Fc_w\tau}{10H}\right)d\tau, \tag{22}$$

Based on 18 and 22, F can be directly calculated from two acoustic measurement. The computationally fast linear relation ensures a change in the arch of the objective function that helps avoid the local optimum, which in turn helps reduce the complexity of numerical optimization [12, 13].

The complete solution of the inversion problem involves providing the estimated probability for a measure of the uncertainty of the result of inversion. The marginal probability density of the simplified model environment is shown in Figure 6. All parameters peak within the given bound, indicating that they are sensitive and well estimated. As all parameters converge to the global optimal value with the highest probability, the results of focalization are highly reliable.

The results of tests on the benchmark problem show that the simplified model is feasible and effective for focalization. As an environmental lens, it has sufficiently high acoustic resolution to focus on the correct positional parameters. With a decrease in the number of parameters to be solved, the amount of calculation needed for optimization is reduced. This also reduces the number of known conditions required, which simplifies marine measurement in applications. The relatively sensitive parameters and the lack of coupling between them are conducive to inversion.

4 Broadband focalization based on experimental data

The Asia Sea International Acoustic Experiment 2001 (ASIAEX2001) was conducted in the East China Sea. Owing to the good quality of data and thorough investigation of the environment, these data have been widely used to test various inversion problems. They were used to test the simplified model proposed here.

Two ships were used in the propagation experiment. The receiving ship anchored and hung a 32-elements vertical array for receiving signals, where the upper 16 elements were 2 m apart and the lower 16 were 4 m apart, and they covered a range of depth from 4.6 to 90.5 m. The launching ship moved away from the receiving ship in a straight line, throwing 38 g TNT wideband sources (WBS) at a fixed depth of 50 m. The depth of water can be roughly considered range independent at a depth of 105 m. Figure 7 shows the sound speed profile measured by the CTD

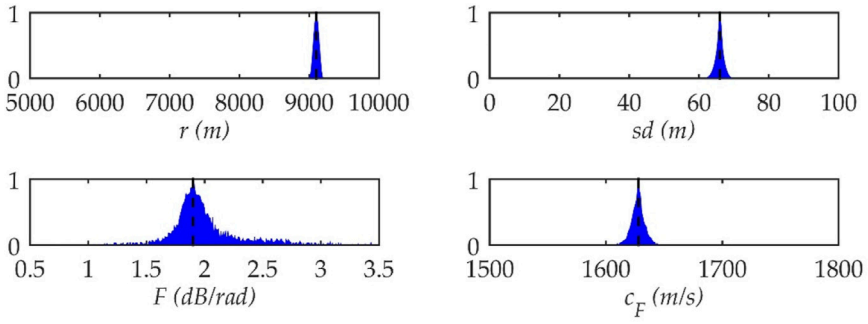

FIGURE 6
Normalized marginal probability density for the simplified model environment. The vertical lines represent the optimal values.

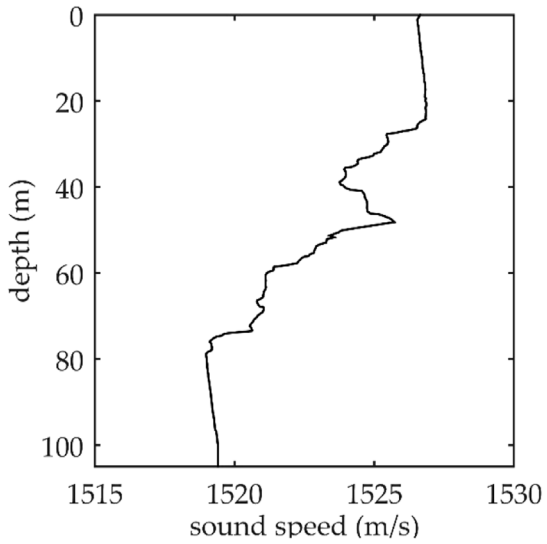

FIGURE 7
Sound speed profile.

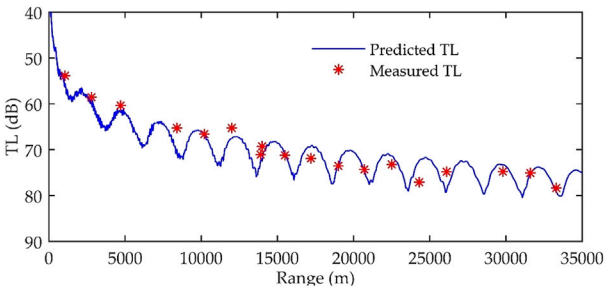

FIGURE 8
The predicted and the measured TL. The source depth is 50 m and the receiver depth is 60.5 m.

TABLE 2 Inversion result.

Source	Results
Focalization using the first WBS	$sd = 48m\ r = 10.2km\ F = \frac{2.91dB}{rad}\ c_F = 1616m/s$
Focalization using the second WBS	$sd = 49m\ r = 10.2km\ F = \frac{2.89dB}{rad}\ c_F = 1628m/s$
Linear geoacoustic inversion [12]	$F = \frac{3.01dB}{rad}\ c_F = 1618m/s$
Geoacoustic inversion by MFP [26]	$c_F = 1610 \pm 12m/s$

in the experiment. In the MFP, the sound speed profile was used as known condition.

Focalization has been carried out using the same method as in the previous section, by using 35 frequency points in the 99–201 Hz frequency band. Two WBS at 10.2 km were selected for testing, and the results are shown in Table 2. The focalization of two sources yielded reliable location-related parameters, which verified the feasibility of the simplified model for broadband focalization. In the linear geoacoustic inversion [12], F is the single parameter to model the seabed. Due to reducing the number of parameters to one, F can be obtained using a least-squares fitting to transmission loss of different ranges. The critical angle is deduced from the variation of transmission loss, and then the equivalent speed c_F can be calculated. In different inversion schemes, the inversion results of geoacoustic parameters of the simplified model are similar.

Note that the hierarchy of the parameters is the foundation of focalization. Because the sound field tended to be more sensitive to variation in the location-related parameters. In the benchmark problem, even if the layered model did not yield the correct value, the inversion still yielded the correct location-related parameters. However, the localization of the source is still influenced by the geoacoustic parameters. As shown in the focalization of the layered environment, the uncertainty in the geoacoustic parameters has a negative impact on the efficiency and accuracy of localization. Although obtaining the geoacoustic parameters is not the primary goal of focalization, it is important for it. Correct geoacoustic inversion not only improves our understanding of the ocean waveguide, but also helps obtain the location-related parameters more efficiently and accurately. A comparison between the measured transmission loss (TL) and the predicted TL based on the inverted geoacoustic parameters is shown in Figure 8. Even if errors have originated

from the source depth, the TLs are in good agreement with each other. In the focalization, the simplified model also obtains accurate acoustic characteristics of the seabed while the complexity of inversion is reduced by reducing the number of parameters.

5 Conclusion

In this paper, a simplified model of the seabed that uses only two parameters has been applied for focalization. As the complexity of inversion increases with the number of parameters, it is valuable to reduce the dimensionality of the inversion problem.

Based on the genetic algorithm, focalization was tested on a benchmark problem using the simplified model and a layered model. In the COLNOISE case, the simplified model with only two parameters satisfied the requirements of MFP and obtained accurate results in terms of location. An analysis of the objective function led the amplitude F and phase c_F to be more sensitive than some parameters of the layered model, and no clear coupling was noted between the parameters. This accelerated the convergence to the optimal solution and ensured the robustness of the results. In addition, some characteristic quantities of the sound field that can be used for matching in MFP are related linearly to F. These linear relations, manifests as an arched curve for changes to the objective function, render the optimization simple and reliable. When used on experimental data from ASIAEX on the East China Sea, the simplified model was found to be suitable for broadband focalization, and both the location-related and the geoacoustic parameters were obtained quickly and accurately.

In order to provide constraints to the dimensionality of inversion problem, the simplified model presents a very compact expression of the acoustic properties of seabed. It can accelerate the convergence to the optimal solution and ensure the robustness of the results. However, it also has limitations. For example, it can be used only in the far field. As the reduction in the number of parameters reduces the acoustic resolution, applications of the proposed model to low-SNR environments or single-hydrophone inversion need to be explored in future research.

Data availability statement

The raw data supporting the conclusion of this article will be made available by the authors, without undue reservation.

Author contributions

ZO completed the literature research, analysis, and manuscript writing. KQ completed the Conceptualization, methodology and funding acquisition. LL completed the validation, visualization and project administration.

Funding

This research was funded by the Natural Science Foundation of Guangdong Province grant number [2022A1515011519].

Conflict of interest

The authors declare that the research was conducted in the absence of any commercial or financial relationships that could be construed as a potential conflict of interest.

Publisher's note

References

1. Baggeroer AB, Kuperman WA, Mikhalevsky PN. An overview of matched field methods in ocean acoustics. *IEEE J.Ocean.Eng.* (1993) 18(4):401–24. doi:10.1109/48.262292

2. Zhang B, Hou X, Yang Y. Robust underwater direction-of-arrival tracking with uncertain environmental disturbances using a uniform circular hydrophone array. *J.Acoust.Soc.Am.* (2022) 151(6):4101–13. doi:10.1121/10.0011730

3. Zhao X, Wang D. Ocean acoustic tomography from different receiver geometries using the adjoint method. *J.Acoust.Soc.Am.* (2015) 138(6):3733–41. doi:10.1121/1.4938232

4. Zheng Z, Yang TC, Pan X. Geoacoustic inversion using an autonomous underwater vehicle in conjunction with distributed sensors. *IEEE J.Ocean.Eng.* (2020) 45(1):319–41. doi:10.1109/joe.2018.2869481

5. Chapman NR, Shang E. Review of geoacoustic inversion in underwater acoustics. *J.Theor.Comput.Acous.* (2021) 29(3):2021. doi:10.1142/s259172852130004x

6. Collins MD, Kuperman WA. Focalization: Environmental focusing and source localization. *J.Acoust.Soc.Am.* (1991) 98(3):1410–22. doi:10.1121/1.401933

7. Li Y, Geng B, Jiao S. Dispersion entropy-based lempel-ziv complexity: A new metric for signal analysis. *Chaos.soliton.fract.* (2022) 161:112400. doi:10.1016/j.chaos.2022.112400

8. Li Y, Gao P, Tang B, Yi Y, Zhang J. Double feature extraction method of ship-radiated noise signal based on slope entropy and permutation entropy. *Entropy* (2021) 24(1):22. doi:10.3390/e24010022

9. Li Y, Tang B, Yi Y. A novel complexity-based mode feature representation for feature extraction of ship-radiated noise using VMD and slope entropy. *Appl.Acoust.* (2022) 196:1088992022. doi:10.1016/j.apacoust.2022.108899

10. Bianco MJ, Gerstoft P. Dictionary learning of sound speed profiles. *J.Acoust.Soc.Am.* (2017) 141(3):1749–58. doi:10.1121/1.4977926

11. Cheng L, Zhao H, Li J, Xu W. Tensor-based basis function learning for three-dimensional sound speed fields. *J.Acoust.Soc.Am.* (2022) 151(1):269–85. doi:10.1121/10.0009280

12. Qu K, Zhao M, Hu C. Single parameter inversion using transmission loss in shallow water. *Acta Acoust* (2013) 38(4):472. doi:10.15949/j.cnki.0371-0025.2013.04.017

13. Qu K, Hu C, Zhao MChina Shanghai Acoustic Laboratory, Institute of Acoustics, Chinese Academy of Sciences, Shanghai 200032, China;; University of Chinese Academy of Sciences, Beijing 100190, China. A rapid inversion scheme for seabed single parameter using time-domain impulse response. *Acta Phys.Sin.* (2013) 62(22):224303. doi:10.7498/aps.62.224303

14. Ge H, Zhao H, Gong X, Shang E. Bottom-reflection phase-shift estimation from ASIAEX data. *IEEE J.Ocean.Eng.* (2004) 29(4):1045–9. doi:10.1109/joe.2004.834180

15. Shang E, Gao T, Wu J. A shallow-water reverberation model based on perturbation theory. *IEEE J.Ocean.Eng.* (2008) 33(4):451–61. doi:10.1109/joe.2008.2001686

16. Shang E, Wu J, Zhao Z. Relating waveguide invariant and bottom reflection phase-shift parameter *P* in a Pekeris waveguide. *J.Acoust.Soc.Am.* (34512012) 131(4):3691–7. doi:10.1121/1.3699242

17. Zhao Z, Shang E, Rouseff D. The comparison of bottom parameter inversion in geoacoustic space and in (P, Q) space. *J.Comput.Acoust.* (2017) 25(2):1750011–23, Apr. doi:10.1142/s0218396x17500114

18. Zhang C, Wu J, Mo Y, Sun B, Ma L. The same reflective characteristics for different effective geoacoustic parameters in different models. *IEEE J.Ocean.Eng.* (2020) 1. doi:10.1109/JOE.2020.2984295

19. Harrison CH, Simons DG. Geoacoustic inversion of ambient noise: A simple method. *J.Acoust.Soc.Am.* (2002) 112(4):1377–89. doi:10.1121/1.1506365

20. Jones AD, Graham JD, Clarke PA. Single parameter description of seafloors for shallow oceans. *J.Acoust.Soc.Am.* (2008) 123(5):3214. doi:10.1121/1.2933399

21. Porter MB, Tolstoy A. The matched field processing benchmark problems. *J.Comput.Acoust.* (1994) 2(3):161–85. doi:10.1142/s0218396x94000129

22. Bonnel J, Pecknold SP, Hines PC, Chapman NR. An experimental benchmark for geoacoustic inversion methods. *IEEE J.Ocean.Eng.* (2020) 1558. doi:10.1109/JOE.2019.2960879

23. Gerstoft P, Rogers LT, Krolik JL, Hodgkiss WS. Inversion for refractivity parameters from radar sea clutter. *Radio.sci.* (80532003) 38(3). doi:10.1029/2002rs002640

24. Gerstoft P. Inversion of seismoacoustic data using genetic algorithms and a posteriori probability distributions. *J.Acoust.Soc.Am.* (1994) 95(2):770–82. doi:10.1121/1.408387

25. Chapman NR. A critical review of geoacoustic inversion: What does it really tell us about the ocean bottom. *J.Acoust.Soc.Am.* (30232016) 140(4):3023. doi:10.1121/1.4969376

26. li Z, Zhang R, Yan J, Li F, Liu J. Geoacoustic inversion by matchedfield processing combined with vertical reflection coefficients and vertical correlation. *IEEE J.Ocean.Eng.* (2004) 29(4):973–9. doi:10.1109/joe.2004.834172

frontiers | Frontiers in Physics

TYPE Mini Review
PUBLISHED 21 February 2023
DOI 10.3389/fphy.2023.1146493

OPEN ACCESS

EDITED BY
Yuxing Li,
Xi'an University of Technology, China

REVIEWED BY
Xiaoman Li,
Jiangsu University of Science and Technology, China
Ke Qu,
Guangdong Ocean University, China
Zhenyi Ou,
Guangdong Ocean University Zhanjiang, China, in collaboration with reviewer KQ

*CORRESPONDENCE
Guanni Ji,
jiguanni@xjy.edu.cn

SPECIALTY SECTION
This article was submitted to Physical Acoustics and Ultrasonics, a section of the journal Frontiers in Physics

RECEIVED 17 January 2023
ACCEPTED 09 February 2023
PUBLISHED 21 February 2023

CITATION
Ji G (2023), Feature extraction method of ship-radiated noise based on dispersion entropy: A review.
Front. Phys. 11:1146493.
doi: 10.3389/fphy.2023.1146493

Feature extraction method of ship-radiated noise based on dispersion entropy: A review

Guanni Ji*

Xi'an Traffic Engineering Institute, Xi'an, China

There is abundant ship information in ship-radiated noise, which is helpful for ship target recognition, classification and tracking. However, owing to the increasing complexity of the marine environment, it makes difficult to extract S-RN features. Dispersion entropy has been proven to be an excellent method to extract the features of S-RN by analyzing the complexity of S-RN, and has been widely used in feature extraction of S-RN. This paper summarizes the research progress of DE in the feature extraction of S-RN in recent years, and provides a comprehensive reference for researchers related to this topic. First, DE and its improved algorithm are described. Then the traditional and DE-based S-RN feature extraction methods are summarized, and the application of DE in S-RN feature extraction methods is concluded from two aspects: methods that apply DE algorithms only and methods that combine DE with mode decomposition algorithms. Finally, the research prospects of DE and the summary of this paper are given.

KEYWORDS

ship-radiated noise, feature extraction, dispersion entropy, mode decomposition, entropy

1 Introduction

In the ocean, sound waves are an effective way to transmit information over long distances. Ship-radiated noise (S-RN) is a good marine sound source, which is of great significance to ship navigation safety and marine exploration [1, 2]. However, the ocean is always accompanied by a large amount of environmental noise, which is a huge interference to the reception and recognition of S-RN. How to effectively extract the features of S-RN has become a hot issue [3, 4].

The traditional feature extraction method for S-RN mainly has two types: 1) feature extraction method based on spectrum analysis. The S-RN is analyzed by the spectrum, and the line spectrum feature and shape feature of power spectrum in S-RN are extracted [5]. 2) Feature extraction method based on time-frequency domain analysis. The features of the S-RN are extracted by Fourier transform [6], wavelet transform [7] and Hilbert-Huang transform [8], and so on. Although these methods achieved some results, the identification of S-RN in practical applications still cannot meet the expected requirements.

Recently, some nonlinear dynamical methods have achieved better results in feature extraction, such as Lempel-Ziv complexity (LZC) [9], fractal dimension [10], entropy [11]. LZC has been successfully applied to feature extraction of S-RN, such as permutation LZC (PLZC) [12], dispersion LZC (DLZC) [13, 14] and DE-based LZC (DELZC) [15], but it has high requirements for the length of time series, and its over-dependence on pattern conversion also limits the ability of LZC to characterize signals. Compared with LZC, the fractal dimension is suitable for processing various types of nonlinear and nonstationary

signals like S-RN [16], but this excellent effect costs a lot of time; in addition, there are only a few types of fractal dimensions, such as box dimension [9, 17], so the application of fractal method to extract discriminant features has not been thoroughly studied. Last but not least, for entropy, the development in feature extraction of S-RN is more comprehensive and faster than LZC and fractal dimension, and recently proposed entropy in common use are PE [18–20], DE [21–23] and slope entropy [24–26]. However, the PE cannot reflect the amplitude change information of S-RN, and slope entropy is seriously affected by threshold setting, and the characteristic value is sufficiently enough. DE is the most widely used in S-RN feature extraction because of the absence of these defects. In general, compared with other entropies, LZC and fractal dimension, DE has higher computational efficiency and deeper stability, and there are richer research results of DE in feature extraction of S-RN.

The DE-based method has been widely used in feature extraction of S-RN and has shown superior performance. In this paper, we will give a comprehensive review of the DE-based methods and divide them into two types: methods that apply DE algorithms only [27, 28] and methods that combine DE with mode decomposition algorithms [23, 29]; then we introduce two aspects of DE in and its application for S-RN. The rest of this review is structured as follows. Section 2 introduces the DE and its improved algorithm. Section 3 describes the traditional S-RN feature extraction methods and the S-RN feature extraction method based on DE, and summarizes the relevant applications. The prospects of DE in the feature extraction method for S-RN are presented in Section 4. Section 5 gives the conclusion of this review.

2 Theory of dispersion entropy

2.1 DE algorithm

DE [30] is one of the important indexes to evaluate the complexity of time series, which considers the relationship between amplitudes, and has strong robustness and fast operability. The specific calculation steps are as follows:

Step 1: For a given time series $X = \{x(j), j = 1, 2, ..., N\}$, it is mapped to series $Y = \{y(j), j = 1, 2, ..., N\}$ by the normal cumulative distribution function (NCDF), and the element $y(j)$ is obtained as follows:

$$y(j) = \frac{1}{\sigma\sqrt{2\pi}}\int_{-\infty}^{x(j)} e^{\frac{-(t-\mu)^2}{2\sigma^2}} dt, j = 1, 2, \cdots, N \tag{1}$$

where μ and σ represent the mean and standard deviation of sequence X respectively, and each element $y(j) \epsilon (0, 1)$.

Step 2: The series Y is converted to a new series $Z^c = \{z_j^c, j = 1, 2, ..., N\}$, and the conversion formula is as follows:

$$z_j^c = R(c \cdot y(j) + 0.5) \tag{2}$$

where z_j^c is an integer within $[1, 2, ..., c]$, R a is rounding function and c indicates the category.

Step 3: The sequence Z^c is transformed into $l = N - (m-1)d$ components $z_i^{m,c}$, each component is defined as:

$$z_i^{m,c} = \{z_i^c, z_{i+d}^c, ..., z_{i+(m-1)d}^c\}, i = 1, 2, ..., N - (m-1)d \tag{3}$$

where m is the embedding dimension, and d represents a time delay. Step 4: Each component is labeled as a dispersion pattern $\pi_{v_0 v_1 v_{m-1}}$ with $z_i^c = v_0, z_{i+d}^c = v_1, \cdots, z_{i+(m-1)d}^c = v_{m-1}$. According to step 2, each element in the component has c values, therefore, there are c^m dispersion patterns corresponding to $z_i^{m,c}$ in total. The probability of each dispersion pattern can be expressed as:

$$p(\pi_{v_0 v_1 v_{m-1}}) = \frac{Num(\pi_{v_0 v_1 v_{m-1}})}{N - (m-1)d} \tag{4}$$

where $Num(\pi_{v_0 v_1 v_{m-1}})$ indicates the number of dispersion patterns $\pi_{v_0 v_1 v_{m-1}}$ of series X.

Step 6: The value of DE can be calculated according to the formula of Shannon entropy:

$$DE(X, m, c, d) = -\sum_{\pi=1}^{c^m} p(\pi_{v_0 v_1 v_{m-1}}) \cdot ln(p(\pi_{v_0 v_1 v_{m-1}})) \tag{5}$$

and the normalized DE (NDE) can be defined as:

$$NDE(X, m, c, d) = \frac{DE(X, m, c, d)}{\ln c^m} \tag{6}$$

2.2 Improved DE algorithm

Since DE has excellent ability to represent signal complexity, many scholars have improved DE to improve the performance of DE, such as reverse DE (RDE), multiscale DE (MDE), and so on. According to the different ways of DE improvement, the improved dispersion entropy is mainly divided into two categories: 1) the improvement of DE steps; and 2) the preprocessing of DE.

To enhance the capacity of DE to characterize the complexity of signals, some scholars are committed to optimizing the calculation steps of DE, and various upgraded versions of DE have been advanced. Azami et al. [31] developed the fluctuation-based DE (FDE) by considering the fluctuation of signals, which provides a powerful tool for analyzing fluctuating signals. Li et al. [21] introduced distance information to DE, the reverse DE (RDE) is raised and demonstrates high stability when analyzing various sensor signals. To address the problem that DE is insensitive to information perception between adjacent elements of time series [32], proposed the fine-sorted DE (FSDE) by adding an additional factor to fine sort the normalized elements. Inspired by FDE and RDE, Jiao et al. [22] combined the advantages of FDE and RDE to propose fluctuation-based reverse DE (FRDE), and this operation further improved the stability and separability of DE. In 2021, the weighted multivariate DE (WMDE) was proposed [33] by integrating multivariate analysis and weighted calculation, which is more sensitive to signal changes and stable. In view of the problem of DE instability due to amplitude variation, Rostagh et al. [34] introduced a fuzzy membership function into DE and developed fuzzy DE (FuzzDE), which improves the performance of DE in detecting frequency changes and periodic changes. Influenced by fractional order calculation [35,36] proposed fractional extended DE (FrEDE) and fractional order fuzzy DE (FuzzDEα) respectively. In addition, Wang et al. [11] advanced a normalized cumulative residual function (NCRF) to magnify the difference between dispersion patterns, and give the give the definition of cumulative residual symbolic DE (CRSDE), which

TABLE 1 The overview of improved DE algorithms based on DE steps.

References	Improved DE	Improvement	Main advantages
[30]	FDE	Fluctuation information	Broadly used for the characterization of real signals
[20]	RDE	Distance information	High distinguishing ability for sensor signals
[31]	FSDE	Fine-sorted dispersion pattern	Provide a powerful aid to feature extraction for fault diagnosis
[21]	FRDE	Distance information and fluctuation information	Facilitates the distinction of ship signals and gear fault signals
[32]	WMDE	Weight information	Reveal the ordinal structure of stock market indices
[33]	FuzzDE	Fuzzy membership functions	Better performance in distinguishing various signlas
[34]	FrEDE	Fractional calculus	Accurately distinguish different faulty states
[35]	FuzzDEα	Fractional order calculation	Detect dynamics changes of signals sensitively
[49]	CRSDE	Normalized cumulative residual function	Excellent performance in detecting dynamics of sleep stages

realizes the representation of more effective pattern information. In summary, these improved algorithms can represent more abundant feature information and have higher anti-noise ability. The overview of improved DE algorithms based on DE steps are shown in Table 1.

Several improved DE algorithms have been proposed by preprocessing the signals to enhance the performance of DE. Zhang et al. [37] proposed MDE by introducing coarse-graining on the basis of DE to retain information on the potential characteristics of faults at different scales. Azami et al. [38] and Li et al. [27] also introduced coarse graining to RDE and FDE, and proposed multiscale FDE (MRDE) and multiscale FDE (MFDE), respectively, which describe the complexity of signals from different scales. In addition [39,40] introduced hierarchical information and proposed hierarchical DE (HDE) and hierarchical FDE (HFDE) respectively to characterize the complexity of all band signals. Xing et al. [41] combined the concepts of hierarchy and multiscale to propose the hierarchical multiscale RDE (HMRDE), which reflects the effective information of the bearing signal from both hierarchical and scaling perspectives. To represent the comprehensive information on signals, Azami et al. [42] proposed refined composite MDE (RCMDE), which is a refined composite multiscale processing based on DE. The proposed RCMDE not only solves the single-scale problem of DE, but also improves the stability of traditional coarse graining. Inspired by RCMDE, some scholars immediately proposed refined composite MFDE (RCMFDE) [43], refined composite RDE (RCMRDE) [44], and refined composite multiscale FRDE (RCMFRDE) [28], respectively. Referring to the experience that fine composite processing can effectively represent signal complexity, some scholars introduced multivariate theory based on refined composite multiscale processing, and proposed refined composite multiscale multivariate MDE (RCMMDE) [45] and refined composite multiscale multivariate FDE (RCMMFDE) [46], which have low sensitivity to signal length and high noise resistance. As the advantages of fine composite multiscale processing and hierarchical analysis have been recognized, refined composite HFDE (RCHFDE) [47] and hierarchical refined composite MFDE (HRCMFDE) [48] have been proposed respectively, which solve the problem of high frequency signal loss in coarse-graining process. Last but not least, some scholars have also proposed some other improved algorithms, such as time-shift multiscale cumulative residual symbolic (DE) TCRSDE [49], refined time-shift multiscale normalised DE (RTSMNDE) [11], time-shift MDE (TSMDE) [50], and generalized RCMFDE (GRCMFDE) [51], which all further improve the performance of dispersion entropy. The overview of improved DE algorithms based on preprocessing is listed in Table 2.

Whether the improvement of the DE step or the preprocessing of the DE further improves the performance of the scattering entropy and effectively represents the complexity of the signal. In order to show the development of DE more intuitively, we employ the Figure 1 to show all the improved DE algorithms.

3 Feature extraction methods for S-RN

The feature extraction of S-RN has been a difficult problem in the field of underwater acoustic signal processing due to the complexity of marine environmental noise. To solve this challenge, some S-RN feature extraction methods have been developed, mainly including two types: 1) traditional methods, such as those based on spectrum analysis, or time-frequency domain analysis; and 2) nonlinear dynamic methods, such as those based on fractal, Lempel-Ziv complexity (LZC), or entropy. The overall framework of feature extraction method for S-RN is displayed in Figure 2.

Traditional feature extraction methods have certain limitations when analyzing non-stationary S-RN, and the feature extraction results cannot well reflect the true characteristics of the target signal. While Entropy, LZC and fractal dimension are the mainstream nonlinear dynamic indexes applied to feature extraction of S-RN. However, LZC is limited by the length of time series and binary conversion, and it often needs to be combined with entropy theory to meet the demand of feature extraction, current research includes PLZC, DLZC, and DELZC, which have shown excellent performance in feature extraction. Although the fractal dimension can effectively analyze nonlinear signals such as S-RN, it will consume consumes considerable time, and the feature based on fractal dimension are not sufficiently stable. With the development of entropy theory, the ability of entropy to represent signals has also been improved, which can show more feature information of S-RN. From recent research, it can be seen that PE, DE, and slope entropy are the three main entropies used in feature extraction of S-RN, these

TABLE 2 The overview of improved DE algorithms based on preprocessing.

References	Improved DE	Improvement	Main advantages
[36]	MDE	Coarse-graining	Retain information on the potential characteristics of faults at different scales
[37]	MFDE	Coarse-graining	Further understand the dynamics of neurological disease records
[25]	MRDE	Coarse-graining	Describe the complexity of ship signals from different scales
[38]	HDE	Hierarchical information	Characterize the complexity of all band fault signals
[39]	HFDE	Hierarchical information	Compensate for the shortcomings of MFDE in ignoring high frequency component information
[40]	HMRDE	Hierarchical coarse-graining	Effectively reflect the difference characteristics in different frequency domains
[41]	RCMDE	Refined composite coarse-graining	Fully min the information of biomedical signals
[42]	RCMRDE	Refined composite coarse-graining	Min the comprehensive information on rolling bearing failures
[43]	RCMFDE	Refined composite coarse-graining	Further enhance the stability of MFDE
[26]	RCMFRDE	Refined composite coarse-graining	Reduce damage caused by misidentification of ships
[44]	RCMMDE	Refined composite multivariate coarse-graining	Has certain advantages in robustness compare to MDE
[45]	RCMMFDE	Refined composite multivariate coarse-graining	Low sensitivity to signal length and high noise resistance
[46]	RCHFDE	Refined composite hierarchical	Has the better stability and robustness than HFDE
[47]	HRCMFDE	Hierarchical Refined composite coarse-graining	Solve the problem of high frequency signal loss in coarse grain process
[48]	TCRSDE	Time-shift coarse-graining	Obtain comprehensive Neurodynamics characteristics
[49]	RTSMNDE	Refined time-shif coarse-graining normalised	Diagnose the locations and degrees of rolling bearing failures effectively
[50]	TSMDE	Time-shift coarse-graining	Achieve outstanding diagnosis performance for rolling bearing
[51]	GRCMFDE	Generalized refined composite coarse-graining	Provide a highly separable feature for diagnosing the fault of rolling bearings

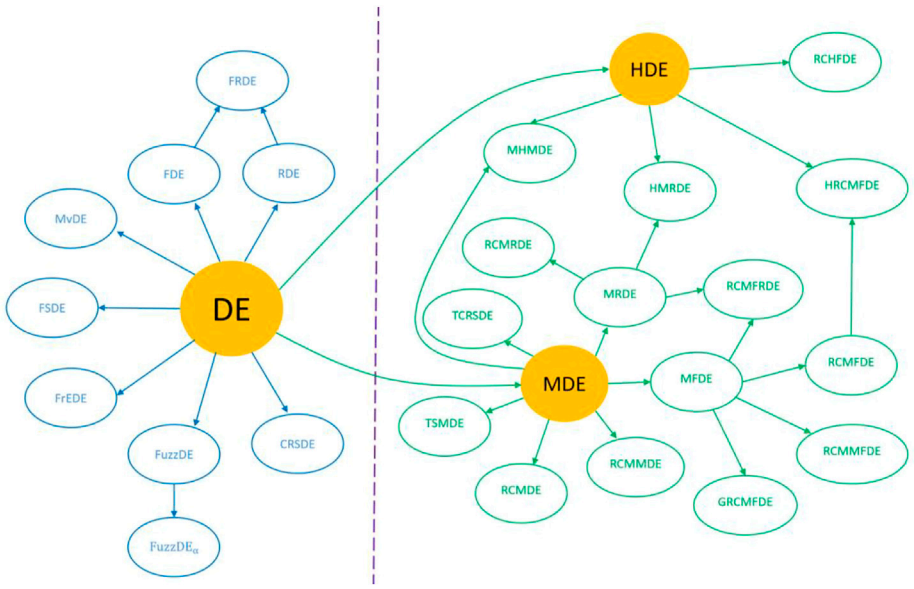

FIGURE 1
Improved DE algorithms.

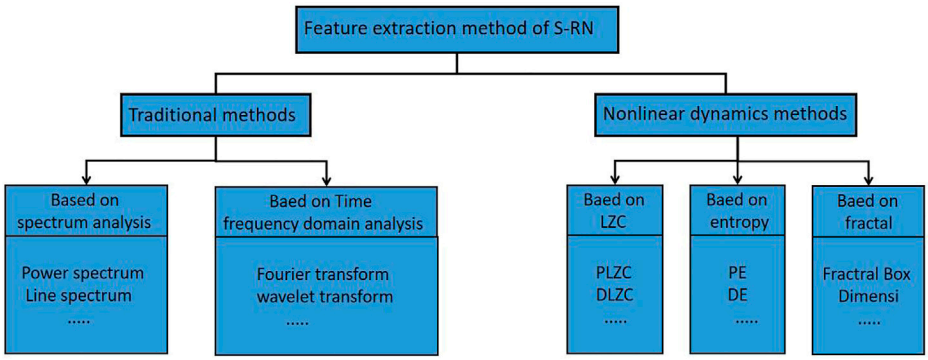

FIGURE 2
Overall framework of feature extraction method for S-RN.

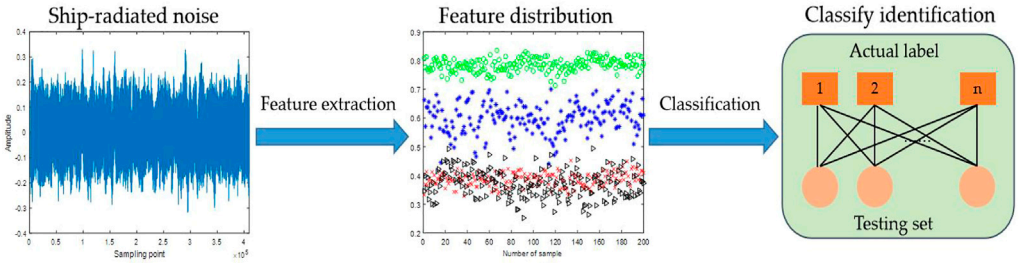

FIGURE 3
The main steps of feature extraction for S-RN using only DE.

entropies get rid of over-dependence on time series length and are more computationally efficient. Among them, DE is particularly convenient and effective, because it overcomes the defect that PE ignores amplitude information and is not limited by threshold parameters like slope entropy. Therefore, we review and summarize the DE-based feature extraction methods in this section.

In this section, the references on feature extraction of S-RN based on DE are listed and summarized as the following two subsections: methods that apply DE algorithms only, and methods that combine DE with mode decomposition algorithms, including empirical wavelet transform (EWT), intrinsic time-scale decomposition (ITD), and variational mode decomposition (VMD). Table 1 provides a brief summary of research articles on applications of DE combined mode decomposition in feature extraction of S-RN, which were published after 2015 to cover the latest contributions since the existing review.

3.1 Feature extraction using only DE algorithm

Due to the high computational efficiency, strong robustness and separability of DE, it has been introduced into the field of feature extraction of S-RN. The main steps of feature extraction for S-RN using only DE are illustrated in Figure 3.

Due to the high computational efficiency, strong robustness and separability of DE, it has been introduced into the field of feature extraction of S-RN in recent years. Li et al. [21] first defined the concept of RDE and take it as a new feature of S-RN, the utilization of RDE realized the accurate classification of three ship signals. In 2020, Li et al. [27] successively proposed MRDE-based feature extraction method and feature extraction method based on MRDE combined with the gray correlation degree (GRD) [52], the studies indicated that MRDE performs better than MDE, MPE and other entropy indexes in characterizing ship feature. In addition, RCMDE-KNN-based classification method of S-RN was raised [53], this method enhances the stability and anti-noise ability of the extracted ship features, and the recognition rate for four types of ships reaches 100%. Jiao et al. [22] presented FRDE and applied it to feature extraction of S-RN, the experimental results show that FRDE feature extraction is more prominent than PE and DE. Based on FRDE and RCMDE [28], proposed a novel feature extraction method of S-RN based on RCMFRDE, the experiments show that the excellent performance for feature extraction and classification of S-RN. Xiao [54] introduced hierarchical DE (HDE) into the underwater acoustic field for the first time, which mines the information hidden in the high frequency band of ship radiated noise. Table 3 reveals the applications of DE in feature extraction of S-RN, in which Rr means recognition rate, MRDE + GRD means MRDE and GRD.

TABLE 3 Applications of DE in feature extraction of S-RN.

References	Method	Database	Metric	Main conclusion
[20]	RDE	Unkonwn	99% Rr	Provide an effective complexity metric to analyze S-RN
[25]	MRDE	National Park Service	100% Rr	Accurate recognition of four types of S-RN is realized from different scales
[52]	MRDE + GRD	National Park Service	97.75% Rr	Effectiveness and practicability for feature extraction of S-RN
[53]	RCMDE	National Park Service	100% Rr	More suitable and stable for feature extraction of S-RN
[21]	FRDE	National Park Service	99.11% Rr	The most outstanding recognition effect in four S-RN
[26]	RCMFRDE	Unkonwn	100% Rt	Improve the feature extraction and classification performance of S-RN
[54]	HDE	Unkonwn	100% Rr	Show the different frequency bands feature of signals S-RN

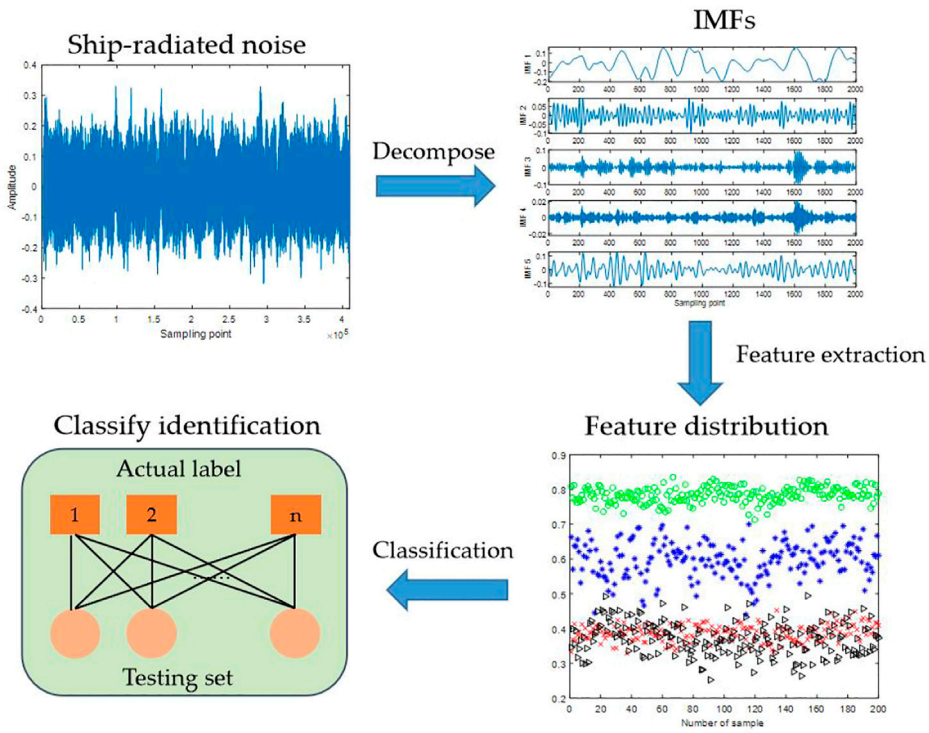

FIGURE 4
The main steps of ship-radiation noise method using DE and mode decomposition.

3.2 Feature extraction combining DE with mode decomposition algorithms

The feature extraction methods based on mode decomposition and DE have been widely used in the underwater acoustic field and show excellent performance. Figure 4 displays the main steps of S-RN feature method using DE and mode decomposition.

In recent years, some scholars have proposed many S-RN feature extraction methods based on DE and mode decomposition and achieve better results. Li et al. [29] combined ITD with FDE, and proposed a new S-RN feature extraction method, which achieves more than 95% classification accuracy for ten types of S-RN, realizing effective recognition of S-RN [55]. Improved the ITD and proposed a S-RN feature extraction method combining improved ITD (IITD) with MDE, which further enhanced the effect of feature extraction. Yang et al. [23] presented a novel a S-RN feature extraction technology using VMD and FDE, and the results presented that the presented technique has better separation effect and higher discrimination. Li et al [56]. Applied extreme-point symmetric mode decomposition (ESMD) to decompose the S-RN, extracted the DE of intrinsic mode functions (IMFs), and effectively distinguished different types of S-RN. [57] developed a S-RN feature extraction method based on EWT and RDE, and the results reveled that EWT not only has better decomposition performance than empirical mode decomposition (EMD), ensemble empirical mode decomposition (EEMD), and VMD, but also RDE has better separability than PE, RPE and DE; in addition, the recognition rate of the proposed method is higher than 95% for four kinds of

TABLE 4 Applications of DE combined mode decomposition in feature extraction of S-RN.

References	Method	Database	Metric	Main conclusion
[27]	ITD + FDE	Unkonwn	95.8% Rr	Effectively achieve the classification of S-RN
[55]	Improved ITD + MDE	Unkonwn	86% Rr	Provide a new scheme for accurate identification of different types of ship signals
[28]	VMD + FDE	Unkonwn	97.5% Rr	More precise for S-RN feature extraction
[56]	ESMD + DE	Unkonwn	99.5% Rr	Assist the feature extraction and classification recognition for S-RN
[57]	EWT + RDE	National Park Service	99.5% Rr	Improve the S-RN separability and stability
[58]	CEEMDASN + RCMFDE	National Park Service	98.5%Rr	Effectively solves the problem of information loss in feature extraction of ship signals
[59]	VMD + MDE	Unkonwn	100% Rr	Extract the line spectrum frequency feature of S-RN
[60]	VMD + WFDE	National Park Service	>90% Rr	Accurately and efficiently extract the features of ship signals

S-RN. Yang et al. [58] put forward a S-RN feature method based on complete ensemble empirical mode decomposition with adaptive selective noise (CEEMDANSN) and RCMFDE, which effectively solves the problem of information loss in feature extraction of ship signals. Li et al. [59] and Liu et al [60] used VMD to decompose the S-RN, and extracted the MDE and WFDE of IMFs respectively, which effectively extract the features of S-RN, and the recognition rate is higher than 90%. Table 4 exhibits the applications of DE combined mode decomposition in feature extraction of S-RN, in which Rr means recognition rate, ITD + FDE means ITD and FDE, VMD + FDE means VMD and FDE.

4 Prospects of DE in feature extraction method for S-RN

Based on the above research, we can find that traditional feature extraction methods for S-RN have great limitations, and cannot effectively reflect the real characteristics of S-RN; moreover, compared with other nonlinear dynamic indexes such as LZC and fractal dimension, DE can better represent the complexity of the signal, and effectively distinguish different types of S-RN. However, the feature extraction of S-RN has always been the focus of the research on the development of marine economy and coastal defense, and the huge development needs promote the output of more relevant research results. At present, it is hard to meet the growing demand by relying solely on DE-based indexes. So combining with multiple features and further upgrade DE with multiple improvement methods is an important development direction in the future.

(1) Combined with other categories of feature indicators.

Different types of features have their own advantages and disadvantages, they are applicable to different ship signals. Combining DE with other types of features for feature extraction, such as entropy index and LZC-based index, can make full use of the complementarity between different features. Therefore, DE combined with other class features is suitable for more complex environments and unknown ship signals, which can further improve the feature extraction performance and recognition effect of S-RN.

(2) Upgrade DE with multiple improvement methods.

Different improvements measures of DE have solved different problems encountered in signal analysis. For the complex and changeable S-RN, the improvement for a specific problem has difficulty reflecting the comprehensive characteristic information. For this reason, integration of multiple improvement methods, including different computational steps and ship signal preprocessing, will be one of the future focuses on upgrading the feature extraction method based on DE.

5 Conclusion

This paper is intended to review the application of DE in feature extraction of ship-radiated noise, and divides it into two categories: Only DE theory and the combination of DE and mode decomposition algorithm. The main conclusions of the review are as follows

(1) Both DE and its improved version improve the feature extraction effect of S-RN from different aspects, and previous studies also show that the feature extraction method based on DE is superior to other entropy measures.
(2) The mode decomposition algorithm is used in feature extraction to reduce the aliasing effect between feature information, combined with DE theory, the anti-noise and stability of the extracted S-RN features are further improved.
(3) Through the review and analysis of the previous DE in the feature extraction of S-RN, the shortcomings and improvements of the current method are illuminated, and the future prospects and work directions are summarized.

Author contributions

The conception, and writing of this review are all completed by GJ.

Conflict of interest

The authors declare that the research was conducted in the absence of any commercial or financial relationships that could be construed as a potential conflict of interest.

Publisher's note

References

1. Yuan F, Ke X, Cheng E. Joint representation and recognition for ship-radiated noise based on multimodal deep learning. *J Mar Sci Eng* (2019) 7(11):380. doi:10.3390/jmse7110380

2. Wang S, Zeng X. Robust underwater noise targets classification using auditory inspired time–frequency analysis. *Appl Acoust* (2014) 78(4):68–76. doi:10.1016/j.apacoust.2013.11.003

3. Gassmann M, Wiggins SM, Hildebrand JA. Deep-water measurements of container ship radiated noise signatures and directionality. *The J Acoust Soc America* (2017) 142:1563–74. doi:10.1121/1.5001063

4. Yan J, Sun H, Chen H, Junejo NUR, Cheng E. Resonance-based time-frequency manifold for feature extraction of ship-radiated noise. *Sensors* (2018) 18(4):936. doi:10.3390/s18040936

5. Ha D, Nguyen V, Quoc K. Modeling of Doppler power spectrum for underwater acoustic channels. *J Commun Networks* (2017) 19(3):270–81. doi:10.1109/jcn.2017.000044

6. Wang Q. Underwater bottom still mine classification using robust time-frequency feature and relevance vector machine. *Int J Comput Math* (2009) 86:794–806. doi:10.1080/00207160701704572

7. Rioul O, Vetterli M. Wavelets and signal processing. *IEEE Signal Process. Mag* (1991) 8(4):14–38. doi:10.1109/79.91217

8. Lin L, Chu F. Feature extraction of AE characteristics in offshore structure model using Hilbert–Huang transform. *Measurement* (2011) 44:46–54. doi:10.1016/j.measurement.2010.09.002

9. Giorgilli A, CasatiSironi DL, Galgani L. An efficient procedure to compute fractal dimensions by box counting. *Phys Lett A* (1986) 115(5):202–6. doi:10.1016/0375-9601(86)90465-2

10. Hu J, Gao JJC, Principe J. Analysis of biomedical signals by the lempel-ziv complexity: The effect of finite data size. *IEEE Trans Biomed Eng* (2006) 53(12):2606–9. doi:10.1109/tbme.2006.883825

11. Zheng J, Pan H, Liu Q, Ding K. Refined time-shift multiscale normalised dispersion entropy and its application to fault diagnosis of rolling bearing. *Physica A: Stat Mech its Appl* (2019) 545:123641. doi:10.1016/j.physa.2019.123641

12. Yi Y, Li Y, Wu J. Multi-scale permutation Lempel-Ziv complexity and its application in feature extraction for Ship-radiated noise. *Front Mar Sci* (2022) 9:1047332. doi:10.3389/fmars.2022.1047332

13. Li Y, Jiao S, Geng B. Refined composite multiscale fluctuation-based dispersion Lempel–Ziv complexity for signal analysis. *ISA Trans* (2022). in press. doi:10.1016/j.isatra.2022.06.040

14. Li Y, Jiang X, Tang B, Ning F, Lou Y. Feature extraction methods of ship-radiated noise: From single feature of multi-scale dispersion Lempel-Ziv complexity to mixed double features. *Appl Acoust* (2022) 199:109032. doi:10.1016/j.apacoust.2022.109032

15. Li Y, Geng B, Jiao S. Dispersion entropy-based lempel-ziv complexity: A new metric for signal analysis. *Chaos, Solitons & Fractals* (2022) 161:112400. doi:10.1016/j.chaos.2022.112400

16. Su Y, Li Z, Wang X. Ship recognition via its radiated sound: The fractal based approaches. *J Acoust Soc America* (2002) 1(112):172–7. doi:10.1121/1.1487840

17. Shi C. Signal pattern recognition based on fractal features and machine learning. *Appl Sci* (2018) 8(8):1327. doi:10.3390/app8081327

18. Li Y, Li Y, Chen X. Feature extraction of ship-radiated noise based on permutation entropy of the intrinsic mode function with the highest energy. *Entropy* (2016) 18(11):393. doi:10.3390/e18110393

19. Xie D, Hong S, Yao C. Optimized variational mode decomposition and permutation entropy with their application in feature extraction of ship-radiated noise. *Entropy* (2021) 23(5):503. doi:10.3390/e23050503

20. Li Y, Li Y, Yu J. A novel feature extraction method for ship-radiated noise based on variational mode decomposition and multi-scale permutation entropy. *Entropy* (2017) 19(7):342. doi:10.3390/e19070342

21. Li Y, Gao X, Wang L. Reverse dispersion entropy: A new complexity measure for sensor signal. *Sensors* (2019) 19(23):5203. doi:10.3390/s19235203

22. Jiao S, Geng B, Li Y, Zhang Q, Wang Q. Fluctuation-based reverse dispersion entropy and its applications to signal classification. *Appl Acoust* (2021) 175:107857. doi:10.1016/j.apacoust.2020.107857

23. Yang H, Zhao K, Li G. A new ship-radiated noise feature extraction technique based on variational mode decomposition and fluctuation-based dispersion entropy. *Entropy* (2019) 21(3):235. doi:10.3390/e21030235

24. Li Y, Gao P, Tang B, Yi Y, Zhang J. Double feature extraction method of ship-radiated noise signal based on slope entropy and permutation entropy. *Entropy* (2022) 24(1):22. doi:10.3390/e24010022

25. Li Y, Tang B, Jiao S. Optimized ship-radiated noise feature extraction approaches based on CEEMDAN and slope entropy. *Entropy* (2022) 24(9):1265. doi:10.3390/e24091265

26. Li Y, Tang B, Yi Y. A novel complexity-based mode feature representation for feature extraction of ship-radiated noise using VMD and slope entropy. *Appl Acoust* (2022) 196:108899. doi:10.1016/j.apacoust.2022.108899

27. Li Y, Jiao S, Geng B, Zhou Y. Research on feature extraction of ship-radiated noise based on multi-scale reverse dispersion entropy. *Appl Acoust* (2021) 173:107737. doi:10.1016/j.apacoust.2020.107737

28. Li Y, Jiao S, Geng B, Jiang X. Rcmfrde: Refined composite multiscale fluctuation-based reverse dispersion entropy for feature extraction of ship-radiated noise. *Math Probl Eng* (2021) 2021:7150921–18. doi:10.1155/2021/7150921

29. Li Z, Li Y, Zhang K. A feature extraction method of ship-radiated noise based on fluctuation-based dispersion entropy and intrinsic time-scale decomposition. *Entropy* (2019) 21(7):693. doi:10.3390/e21070693

30. Rostaghi M, Azami H. Dispersion entropy: A measure for time series analysis. *IEEE Signal Process Lett* (2016) 23(5):610–4. doi:10.1109/lsp.2016.2542881

31. Azami H. Amplitude- and fluctuation-based dispersion entropy. *Entropy* (2018) 20(3):210. doi:10.3390/e20030210

32. Fu W, Tan J, Xu Y, Wang K, Chen T. Fault diagnosis for rolling bearings based on fine-sorted dispersion entropy and SVM optimized with mutation SCA-PSO. *Entropy* (2019) 21(4):404. doi:10.3390/e21040404

33. Wang Z, Shang P. Generalized entropy plane based on multiscale weighted multivariate dispersion entropy for financial time series. *Chaos, Solitons & Fractals* (2021) 142:110473. doi:10.1016/j.chaos.2020.110473

34. Rostaghi M, Khatibi MM, Ashory MR, Azami H. Fuzzy dispersion entropy: A nonlinear measure for signal analysis. *IEEE Trans Fuzzy Syst* (2022) 30(9):3785–96. doi:10.1109/tfuzz.2021.3128957

35. Shao K, He Y, Liu X, Xing Z, Du B. Fault detection for wind turbine system using fractional extended dispersion entropy and cumulative sum control chart. *IEEE Trans Instrumentation Meas* (2022) 71:1–9. doi:10.1109/tim.2022.3198479

36. Li Y, Tang B, Geng B, Jiao S. Fractional order fuzzy dispersion entropy and its application in bearing fault diagnosis. *Fractal and Fractional* (2022) 6(10):544. doi:10.3390/fractalfract6100544

37. Zhang Y, Tong S, Cong F, Xu J. Research of feature extraction method based on sparse reconstruction and multiscale dispersion entropy. *Appl Sci* (2018) 8(6):888. doi:10.3390/app8060888

38. Azami H, Arnold SE, Sanei S, Chang Z, Sapiro G, Escudero J, et al. Multiscale fluctuation-based dispersion entropy and its applications to neurological diseases. *IEEE Access* (2019) 7:68718–33. doi:10.1109/access.2019.2918560

39. Song E, Ke Y, Yao C, Dong Q, Yang L. Fault diagnosis method for high-pressure common rail injector based on IFOA-VMD and hierarchical dispersion entropy. *Entropy* (2019) 21(10):923. doi:10.3390/e21100923

40. Ke Y, Yao C, Song E, Dong Q, Yang L. An early fault diagnosis method of common-rail injector based on improved CYCBD and hierarchical fluctuation dispersion entropy. *Digit Signal Process* (2021) 114:103049. doi:10.1016/j.dsp.2021.103049

41. Xing J, Xu J. An improved incipient fault diagnosis method of bearing damage based on hierarchical multi-scale reverse dispersion entropy. *Entropy* (2022) 24(6):770. doi:10.3390/e24060770

42. Azami H, Rostaghi M, Abásolo D, Escudero J. Refined composite multiscale dispersion entropy and its application to biomedical signals. *IEEE Trans Biomed Eng* (2017) 64(12):2872–9. doi:10.1109/TBME.2017.2679136

43. Liu A, Yang Z, Li H, Wang C, Liu X. Intelligent diagnosis of rolling element bearing based on refined composite multiscale reverse dispersion entropy and random forest. *Sensors* (2022) 22(5):2046. doi:10.3390/s22052046

44. Zhou F, Yang X, Shen J, Liu W. Fault diagnosis of hydraulic pumps using PSO-VMD and refined composite multiscale fluctuation dispersion entropy. *Shock and Vibration* (2020) 2020:8840676.

45. Li C, Zheng J, Pan H, Tong J, Zhang Y. Refined composite multivariate multiscale dispersion entropy and its application to fault diagnosis of rolling bearing. *IEEE Access* (2019) 7:47663–73. doi:10.1109/access.2019.2907997

46. Xi C, Yang G, Liu L, Jiang H, Chen X. A refined composite multivariate multiscale fluctuation dispersion entropy and its application to multivariate signal of rotating machinery. *Entropy* (2021) 23(1):128. doi:10.3390/e23010128

47. Zhou F, Gong J, Yang X, Han T, Yu Z. A new gear intelligent fault diagnosis method based on refined composite hierarchical fluctuation dispersion entropy and manifold learning. *Measurement* (2021) 186:110136. doi:10.1016/j.measurement.2021.110136

48. Chen Y, Yuan Z, Chen J, Sun K. A novel fault diagnosis method for rolling bearing based on hierarchical refined composite multiscale fluctuation-based dispersion entropy and PSO-elm. *Entropy* (2022) 24(11):1517. doi:10.3390/e24111517

49. Wang Y, Xu Y, Liu M, Guo Y, Wu Y, Chen C, et al. Cumulative residual symbolic dispersion entropy and its multiscale version: Methodology, verification, and application. *Chaos, Solitons & Fractals* (2022) 160:112266. doi:10.1016/j.chaos.2022.112266

50. Shao K, Fu W, Tan J, Wang K. Coordinated approach fusing time-shift multiscale dispersion entropy and vibrational harris hawks optimization-based SVM for fault diagnosis of rolling bearing. *Measurement* (2021) 173:108580. doi:10.1016/j.measurement.2020.108580

51. Zheng J, Pan H. Use of generalized refined composite multiscale fractional dispersion entropy to diagnose the faults of rolling bearing. *Nonlinear Dyn* (2020) 101:1417–40. doi:10.1007/s11071-020-05821-1

52. Li Y, Jiao S, Geng B. A comparative study of four multi-scale entropies combined with grey relational degree in classification of ship-radiated noise. *Appl Acoust* (2021) 176:107865. doi:10.1016/j.apacoust.2020.107865

53. Li Y, Jiao S, Geng B, Zhang Q, Zhang Y. A comparative study of four nonlinear dynamic methods and their applications in classification of ship-radiated noise. *Defence Tech* (2022) 18(2):183–93. doi:10.1016/j.dt.2020.11.011

54. Xiao L. Feature extraction of ship-radiated noise based on hierarchical dispersion entropy. *Shock and Vibration* (2022) 2022:3238461–10. doi:10.1155/2022/3238461

55. Li Z, Li Y, Zhang K, Guo J. A novel improved feature extraction technique for ship-radiated noise based on IITD and MDE. *Entropy* (2019) 21(12):1215. doi:10.3390/e21121215

56. Li G, Zhao K, Yang H. Feature extraction method for ship-radiated noise based on extreme-point symmetric mode decomposition and dispersion entropy. *Indian J Geo-Marine Sci* (2020) 49(02):175–83.

57. Li Y, Jiao S, Gao X. A novel signal feature extraction technology based on empirical wavelet transform and reverse dispersion entropy. *Defence Tech* (2021) 17(5):1625–35. doi:10.1016/j.dt.2020.09.001

58. Yang H, Li L, Li G, Guan Q. A novel feature extraction method for ship-radiated noise. *Defence Tech* (2022) 18(4):604–17. doi:10.1016/j.dt.2021.03.012

59. Li G, Hou Y, Yang H. A novel method for frequency feature extraction of ship radiated noise based on variational mode decomposition, double coupled Duffing chaotic oscillator and multivariate multiscale dispersion entropy. *Alexandria Eng J* (2022) 61(8):6329–47. doi:10.1016/j.aej.2021.11.059

60. Liu F, Li G, Yang H. A new feature extraction method of ship radiated noise based on variational mode decomposition, weighted fluctuation-based dispersion entropy and relevance vector machine. *Ocean Eng* (2022) 266:113143. doi:10.1016/j.oceaneng.2022.113143

frontiers | Frontiers in Physics

TYPE Original Research
PUBLISHED 28 February 2023
DOI 10.3389/fphy.2023.1142400

OPEN ACCESS

EDITED BY
Yuxing Li,
Xi'an University of Technology, China

REVIEWED BY
Baichun Gong,
Nanjing University of Aeronautics and Astronautics, China
Xin Qing,
Harbin Engineering University, China

*CORRESPONDENCE
Xianghao Hou,
houxianghao1990@nwpu.edu.cn

SPECIALTY SECTION
This article was submitted to Physical Acoustics and Ultrasonics, a section of the journal Frontiers in Physics

RECEIVED 11 January 2023
ACCEPTED 06 February 2023
PUBLISHED 28 February 2023

CITATION
Zhang B, Hou X, Yang Y, Zhou J and Xu S (2023), Variational Bayesian cardinalized probability hypothesis density filter for robust underwater multi-target direction-of-arrival tracking with uncertain measurement noise.
Front. Phys. 11:1142400.
doi: 10.3389/fphy.2023.1142400

Variational Bayesian cardinalized probability hypothesis density filter for robust underwater multi-target direction-of-arrival tracking with uncertain measurement noise

Boxuan Zhang[1,2], Xianghao Hou[1,2]*, Yixin Yang[1,2], Jianbo Zhou[1,2] and Shengli Xu[3,4]

[1]School of Marine Science and Technology, Northwestern Polytechnical University, Xi'an, China, [2]Shaanxi Key Laboratory of Underwater Information Technology, Xi'an, China, [3]Shanghai Electro-Mechanical Engineering Institute, Shanghai, China, [4]Unmanned System Research Institute, Northwestern Polytechnical University, Xi'an, China

The direction-of-arrival (DOA) tracking of underwater targets is an important research topic in sonar signal processing. Considering that the underwater DOA tracking is a typical multi-target problem under unknown underwater environment with missing detection, false alarm, and uncertain measurement noise, a robust underwater multi-target DOA tracking method for uncertain measurement noise is proposed. First, a kinematic model of the multiple underwater targets and bearing angle measurement model with missing detection and false alarms are established. Then, the multi-target DOA tracking algorithm is derived by using the cardinalized probability hypothesis density (CPHD) filter, the performance of which largely depends on the accuracy of the parameter of measurement noise variance. In addition, the variational Bayesian approach is used to adaptively estimate the uncertain measurement of noise variance for each measurement of target in the real time of tracking. Thus, the robust underwater multi-target DOA tracking is carried out. Finally, comprehensive experimental validations and discussions are made to prove that the proposed algorithm can provide robust DOA tracking in the multi-target tracking scenario with uncertain measurement noise.

KEYWORDS

underwater multi-target direction-of-arrival tracking, cardinalized probability hypothesis density filter, uncertain measurement noise, variational Bayesian approach, adaptive tracking

1 Introduction

The direction-of-arrival (DOA) estimation and tracking is an important research topic in sonar signal processing [1–5]. For the scenario of moving targets, the traditional DOA estimation methods cut the measurement of the output of sonar array signal into small periods in time to process, which ignores the kinematic characteristics of the targets [6–8]. The DOA tracking methods not only use the measurement information but also rely on the kinematic characteristics of the underwater targets [9–18]. Therefore, by not only depending

on the current measurements but also utilizing the prior kinematic information of an unknown underwater target, the DOA tracking methods can provide more robust and accurate results than the traditional DOA estimation methods.

In view of the advantages of the DOA tracking methods, researchers have carried out a lot of work around DOA tracking. The DOA tracking methods first take the outputs of the sonar array signals or results of the traditional DOA estimation methods as the measurements. Then, considering the typical kinematics of the underwater targets, the kinematic model by the bearing angle is established. Then, based on the framework of the Bayesian filter theory [19], the bearing angle of the target can be recursively estimated from the current measurements. Depending on the bearing angle measurements obtained by the traditional DOA estimation methods, the Kalman filter (KF) is always utilized as the DOA tracking algorithm [9, 10] for the linear relationship between the measurement and bearing angle of the target. Besides utilizing the bearing angle measurements, some research take the outputs of sonar array signals as measurements. However, under such a circumstance, the mathematical relationship between the bearing angle of the target and the measurement is non-linear. For such non-linear problems, many tracking algorithms based on the non-linear Bayesian filter have proposed the extended Kalman filter (EKF) [11, 12].The first-order Taylor series expansion of the measurement model was used to approximate the non-linear model to a linear model. The unscented Kalman filter (UKF) [20, 21] uses a group of determined sigma points to linearize the non-linear model. The particle filter (PF) [22] generates and transforms a large number of arbitrary particles to represent the distribution of the target state. Thus, the PF can theoretically achieve accurate tracking in any non-linear tracking system with any distribution of the uncertainties, while the computational complexity of the PF stays significant.

Although the tracking techniques are widely utilized in the scenario of underwater target tracking, most of them are only applicable to the single-target tracking scenario [9–12, 20–22]. However, the underwater DOA tracking issue is a typical multi-target tracking scenario where the multi-target tracking techniques should be considered and proposed. The methods for multi-target tracking problem can be divided into two categories: the traditional data association methods and random finite set (RFS)–based multi-target tracking methods. The data association methods establish the association between measurements and targets, so as to transform the multi-target tracking problem into a single-target tracking problem to use the abovementioned single-target tracking methods. However, these data association techniques have to match every measurement with its target which can make computation highly complex with large number of targets or false alarms caused by uncertain measurement noise [23, 24]. From the beginning of this century, the RFS-based multi-target tracking methods have developed rapidly to overcome the drawbacks caused by the data association techniques. The RFS can be defined by a set with elements along with the number of the elements which are subjected to random distributions. The RFS-based multi-target tracking methods define the states and measurements of targets as RFSs such that the data association procedure can be avoided. As a result, by utilizing the RFS technique, the computational complexity of multi-target tracking can be hugely reduced, especially when the number of targets and false alarms is large. For the RFS-based multi-target tracking, Mahler first proposed the concept of "first-order moment filter," also known as probability hypothesis density (PHD) filter [25]. Since, the PHD filter has no closed-form solution in general, Vo et al. [26] proposed sequential Monte Carlo solution for the PHD filter (SMC-PHD), and Clark et al. [27] proposed the Gaussian mixture model implementation of the PHD filter (GM-PHD), which push the PHD filter from theory to application. The GM-PHD filter requires both the kinematic model of targets and the measurement model to be linear. The SMC-HD filter represents the distribution of the states of the targets by generating and transferring many of the particles, which is suitable for non-linear models. However, the calculation of the particles leads to high computation overload. Subsequently, Mahler [28, 29] introduced the cardinality distribution to describe the number of targets on the basis of the PHD filter to make a more accurate estimation of the number of targets and proposed the CPHD filter. Similar to the PHD filter, the CPHD filter also has no closed-form solution in general and has to be implemented on the basis of the SMC or GM model [30]. Considering that the computational complexity of the RFS-based method is lower than that of the data association method, researchers have proposed many multi-target DOA tracking methods based on the PHD and CPHD filters [13–16]. These methods use the output of the array signal as measurements with the non-linear measurement model, thus implementing them based on SMC.

Due to high-dimension array signal–based measurements and the large number of particles for the SMC method, the existing RFS-based multi-target DOA tracking methods get a large computation overload. Moreover, in the real scenario of underwater tracking, the unknown ocean environment always results in uncertain measurement noise. Thus, besides considering the computational complexity, accomplishing robust and accurate tracking when the measurements are in a low SNR scenario is also important, especially in the underwater target tracking case. However, most of the existing DOA tracking methods assume the measurement noise to be a certain stochastic process which leads to the degradation of the tracking performance in the real scenario of uncertain measurement noise. To deal with the uncertain measurement noise, Zhang et al. [12] derived a robust single-target DOA tracking method based on the EKF by estimating the measurement noise covariance matrix (MNCM) by using the improved Sage-Husa algorithm. By estimating the MNCM in a maximum-likelihood (ML) framework, the expectation-maximum adaptive Kalman filter (EM-AKF) was proposed [31, 32]. Sarkka and Hartikainen [33, 34] assumed the MNCM to be subject to an inverse Wishart distribution and iteratively estimated the MNCM by using variational Bayesian approach, namely, the variational Bayesian adaptive Kalman filter (VB-AKF). Huang et al. [37] assumed the mean square error matrix (MSEM) to also be subjected to an inverse Wishart distribution and jointly estimated it along with the MNCM to improve the performance of VB-AKF. In the existing works, the superior accuracy and stability of the VB-AKF has been demonstrated [33–37]. However, the MNCM estimation method has not been applied to robust multi-target DOA tracking yet. Thus, considering the uncertain underwater environment and its influences on the underwater target tracking missions, adopting variational Bayesian online estimation technique into the multitarget tracking scenario is inspiring and necessary.

In this article, the bearing angle estimates obtained by using the traditional DOA estimation method are regarded as the measurements, and the multi-target DOA tracking algorithm is derived by using the GM-CPHD filter. Different from most of the existing tracking algorithms, we considered the uncertain measurement noise caused by the unknown underwater environment, which always makes a

certain tracking algorithm diverge. Thus, the variational Bayesian approach is utilized to estimate the covariance matrix of the measurement noise along with the states of targets in the framework of the GM-CPHD filter. In this way, the variational Bayesian GM-CPHD filter (VB-GMCPHD) for robust underwater multi-target DOA tracking is proposed for the scenario of robust tracking under uncertain measurement noise. Finally, the results of the experiment show the robustness and accuracy of the proposed method in real underwater multi-target DOA tracking scenario. The contributions of this article are summarized as follows:

First, the multi-target DOA tracking algorithm is derived by using the GM-CPHD filter for the real underwater tracking scenario with missing detection and false alarm.

Second, the issue of uncertain measurement noise is addressed by using the variational Bayesian approach to estimate the measurement noise variance. Thus, the VB-GMCPHD for robust underwater multi-target DOA tracking is proposed.

Finally, the real experimental data is utilized to verify the superior accuracy and robustness of the proposed method in real underwater DOA tracking scenario.

The rest of this article is organized as follows: in Section 2, the problem of underwater multi-target DOA tracking with missing detection and false alarm is formulated. In Section 3, the GM-CPHD filter for DOA tracking is described. In Section 4, based on the variational Bayesian approach, an innovative multi-target DOA tracking method for uncertain measurement noise scenario, namely the VB-GMCPHD, is proposed. In Section 5, experimental validations are made and the results are proved, demonstrating the superior performance of the proposed VB-GMCPHD. Finally, the conclusions are drawn in Section 6.

2 Multi-target tracking models

The sets of the states of the targets and the measurements are assumed to be RFSs. Assuming that n_k targets exist within the detection range of the sonar at time step k and the state of the i_n-th target is $\boldsymbol{x}_k^{i_n}$, the set of the states of targets at time step k is expressed as $\boldsymbol{X}_k = \left\{\boldsymbol{x}_k^1, \boldsymbol{x}_k^2, ..., \boldsymbol{x}_k^{n_k}\right\}$. Let θ_k denote the bearing angle of the i_n-th target ($\theta_k^{i_n}$ is the angle between the target and positive x-axis with respect to the positive counterclockwise.) and $\dot{\theta}_k^{i_n}$ denote the change rate of $\theta_k^{i_n}$, then the state of the i_n-th target is expressed as $\boldsymbol{x}_k^{i_n} = (\theta_k^{i_n}, \dot{\theta}_k^{i_n})^{\mathrm{T}}$, where $(\cdot)^{\mathrm{T}}$ denotes the matrix transposition. Since the underwater targets are usually not maneuvering to save energy and keep concealed, the bearing angles of the targets are assumed to be subject to the constant velocity (CV) model. The CV model of the state of the i_n-th target is expressed as

$$\begin{cases} \boldsymbol{x}_k^{i_n} = \boldsymbol{F}_{k|k-1}\boldsymbol{x}_{k-1}^{i_n} + \boldsymbol{G}_k w_k \\ \boldsymbol{F}_{k|k-1} = \begin{bmatrix} 1 & T \\ 0 & 1 \end{bmatrix}, \boldsymbol{G}_k = \begin{bmatrix} T^2/2 \\ T \end{bmatrix}, \end{cases} \tag{1}$$

where $\boldsymbol{F}_{k|k-1}$ and $\boldsymbol{G}_k$ are the state transition matrix and the noise driving matrix, w_k denotes the zero-mean Gaussian process noise with the covariance matrix Q_k caused by the unknown underwater environment, and T is the interval between the adjacent time steps.

The estimates of the bearing angles of the targets with error obtained by the traditional DOA estimation methods are taken as measurements. Considering the probability of missing detection and false alarm, the number of measurements and the states of the targets are always different in a multi-target tracking problem. It is assumed that m_k^d targets are detected and m_k^f false alarms exist, i.e., $m_k = m_k^d + m_k^f$ measurements are obtained at time step k. The set of measurements at time step k are expressed as $\boldsymbol{Z}_k = \left\{\boldsymbol{z}_k^1, \boldsymbol{z}_k^2, ..., \boldsymbol{z}_k^{m_k}\right\}$. Then the measurement of the i_m^d-th detected target $\boldsymbol{z}_k^{i_m^d}$ at time step k can be expressed as

$$\boldsymbol{z}_k^{i_m^d} = \boldsymbol{H}_k \boldsymbol{x}_k^{i_m^d} + v_k, \tag{2}$$

where $\boldsymbol{H}_k$ denotes the measurement matrix and $\boldsymbol{H}_k = [1, 0]$, v_k is the error of the bearing angle estimate obtained by using traditional DOA estimation, which is subject to Gaussian distribution with zero mean and variance of $\sigma_{r,k}^2$. The false alarms $\boldsymbol{z}_k^1, \boldsymbol{z}_k^2, ..., \boldsymbol{z}_k^{m_k^f}$ are assumed to be subject to Poisson distribution with intensity of κ_k.

3 GM-CPHD filter for multi-target DOA tracking

The CPHD filter performs multi-target tracking by recursively calculating the PHD and the cardinality distribution to represent the distribution of the states and the number of the targets, respectively. The closed-form solution of the CPHD filter is given in the assumption of the linear Gaussian mixture (GM) model, which is called the GM-CPHD filter. Each component of the Gaussian mixture model represents the respective states of the targets [30].

The cardinality distribution $p_{k-1}(n)$ and the PHD $v_{k-1}(x)$ are assumed to be known, and $v_{k-1}(x)$ is subject to the Gaussian mixture model as

$$v_{k-1}(x) = \sum_{i=1}^{J_{k-1}} w_{k-1}^{(i)} N\left(\boldsymbol{x}_k; \boldsymbol{m}_{k-1}^{(i)}, \boldsymbol{P}_{k-1}^{(i)}\right), \tag{3}$$

where $w_{k-1}^{(i)}$ denotes the weight, $N(\cdot; \boldsymbol{m}, \boldsymbol{P})$ denotes the Gaussian distribution with the mean of $\boldsymbol{m}$ and covariance matrix of $\boldsymbol{P}$, and $\boldsymbol{m}_{k-1}^{(i)}$ and $\boldsymbol{P}_{k-1}^{(i)}$ denote the estimate of the state of the target and the mean square error matrix (MSEM), respectively. Then, the process of the GM-CPHD filter at time step k is divided into prediction and update as follows:

(1) Prediction

Once the cardinality distribution $p_{k-1}(n)$ at time step $k-1$ is given, the predicted cardinality distribution is expressed as

$$p_{k|k-1}(n) = \sum_{j=0}^{n} p_{\Gamma,k}(n-j) \sum_{l=j}^{\infty} C_l^j p_{k-1}(l) p_{s,k}^j (1-p_{s,k})^{l-j}, \tag{4}$$

where $C_l^j = l!/(j!(l-j)!)$, $p_{\Gamma,k}(\cdot)$ is the cardinality distribution of birth targets, and $p_{s,k}$ is the probability of targets surviving.

Once the PHD $v_{k-1}(x)$ at time step $k-1$ is given, the predicted PHD is expressed as

$$v_{k|k-1}(x) = v_{s,k|k-1}(x) + \gamma_k(x), \tag{5}$$

where $v_{s,k|k-1}(x)$ and $\gamma_k(x)$ denote the PHD of surviving targets and birth targets, respectively. $v_{s,k|k-1}(x)$ is expressed as

$$v_{s,k|k-1}(x) = p_{s,k}\sum_{j=1}^{J_{k-1}} w_{k-1}^{(j)} N\left(x; \boldsymbol{m}_{s,k|k-1}^{(j)}, \boldsymbol{P}_{s,k|k-1}^{(j)}\right), \tag{6}$$

where the predicted state $\boldsymbol{m}_{s,k|k-1}^{(j)}$ and predicted MSEM $\boldsymbol{P}_{s,k|k-1}^{(j)}$ of the j-th surviving target is given as follows:

$$\boldsymbol{m}_{s,k|k-1}^{(j)} = \boldsymbol{F}_{k-1}\boldsymbol{m}_{k-1}^{(j)}, \tag{7}$$

$$\boldsymbol{P}_{s,k|k-1}^{(j)} = \boldsymbol{G}_k\sigma_q^2\boldsymbol{G}_k^T + \boldsymbol{F}_{k-1}\boldsymbol{P}_{k-1}^{(j)}\boldsymbol{F}_{k-1}^T. \tag{8}$$

The PHD of birth targets $\gamma_k(x)$ is also subject to the Gaussian mixture model as follows:

$$\gamma_k(x) = \sum_{i=1}^{J_{\gamma,k}} w_{\gamma,k}^{(i)} N\left(x; \boldsymbol{m}_{\gamma,k}^{(i)}, \boldsymbol{P}_{\gamma,k}^{(i)}\right). \tag{9}$$

where $J_{\gamma,k}$ denotes the number of components of the Gaussian mixture model for $\gamma_k(x)$, and $w_{\gamma,k}^{(i)}$, $\boldsymbol{m}_{\gamma,k}^{(i)}$, and $\boldsymbol{P}_{\gamma,k}^{(i)}$ denote the weight, state, and MSEM of the i-th birth target, respectively.

According to Equations 5, 6, and 9, the predicted PHD can be expressed as follows:

$$v_{k|k-1}(x) = \sum_{i=1}^{J_{k|k-1}} w_{k|k-1}^{(i)} N\left(x; \boldsymbol{m}_{k|k-1}^{(i)}, \boldsymbol{P}_{k|k-1}^{(i)}\right), \tag{10}$$

where $w_{k|k-1}^{(i)}$, $\boldsymbol{m}_{k|k-1}^{(i)}$, and $\boldsymbol{P}_{k|k-1}^{(i)}$ denote the weight, predicted estimate of the state, and predicted MSEM of the i-th target, respectively.

(2) Update

The cardinality distribution $p_k(n)$ and PHD $v_k(x)$ at time step k are obtained by using the measurement set $\boldsymbol{Z}_k$ to update $p_{k|k-1}(n)$ and $v_{k|k-1}(x)$ as follows:

$$p_k(n) = \frac{\Psi_k^0[\boldsymbol{w}_{k|k-1}, \boldsymbol{Z}_k](n)p_{k|k-1}(n)}{\langle \Psi_k^0[\boldsymbol{w}_{k|k-1}, \boldsymbol{Z}_k], p_{k|k-1}\rangle}, \tag{11}$$

$$v_k(x) = \frac{\langle \Psi_k^1[\boldsymbol{w}_{k|k-1}, \boldsymbol{Z}_k], \boldsymbol{p}_{k|k-1}\rangle}{\langle \Psi_k^0[\boldsymbol{w}_{k|k-1}, \boldsymbol{Z}_k], \boldsymbol{p}_{k|k-1}\rangle}(1 - p_{D,k})v_{k|k-1}(x) + \sum_{z\in Z_k}\sum_{j=1}^{J_{k|k-1}} w_k^{(j)}(z)N\left(\boldsymbol{x}; \boldsymbol{m}_k^{(j)}, \boldsymbol{P}_k^{(j)}\right), \tag{12}$$

where $\langle \boldsymbol{\alpha}, \boldsymbol{\beta}\rangle$ denotes the inner product of $\boldsymbol{\alpha}$ and $\boldsymbol{\beta}$, i.e., $\langle \boldsymbol{\alpha}, \boldsymbol{\beta}\rangle = \sum_{l=1}^{L}\alpha_l\beta_l$ ($\boldsymbol{\alpha} = [\alpha_1, \alpha_2, ..., \alpha_L]$, $\boldsymbol{\beta} = [\beta_1, \beta_2, ..., \beta_L]$), and $p_{D,k}$ denotes the detection probability, and

$$\Psi_k^u[\boldsymbol{w}, \boldsymbol{Z}](n) = \sum_{j=0}^{\min(|\boldsymbol{Z}|,n)} (|\boldsymbol{Z}| - j)p_{K,k}(|\boldsymbol{Z}| - j) A_n^{j+u}\frac{(1 - p_{D,k})^{n-(j+u)}}{\langle 1, \boldsymbol{w}\rangle^{j+u}}e_j(\Lambda_k(\boldsymbol{w}, \boldsymbol{Z})), \tag{13}$$

$$\Lambda_{k,z}(x) = \left\{\frac{\langle 1, \kappa_k\rangle}{\kappa_k(z)}p_{D,k}\boldsymbol{w}^T\boldsymbol{q}_k(z): z \in Z\right\}, \tag{14}$$

$$\boldsymbol{w}_{k|k-1} = \left[w_{k|k-1}^{(1)}, \ldots, w_{k|k-1}^{(J_{k|k-1})}\right]^T, \tag{15}$$

$$\boldsymbol{q}_k(z) = \left[q_k^{(1)}(z), \ldots, q_k^{(J_{k|k-1})}(z)\right]^T, \tag{16}$$

$$q_k^{(j)}(\boldsymbol{z}) = N\left(\boldsymbol{z}; \boldsymbol{\eta}_{k|k-1}^{(j)}, \boldsymbol{S}_{k|k-1}^{(j)}\right), \tag{17}$$

$$\boldsymbol{\eta}_{k|k-1}^{(j)} = \boldsymbol{H}_k\boldsymbol{m}_{k|k-1}^{(j)}, \tag{18}$$

$$\boldsymbol{S}_{k|k-1}^{(j)} = \boldsymbol{H}_k\boldsymbol{P}_{k|k-1}^{(j)}\boldsymbol{H}_k^T + \sigma_{r,k}^2, \tag{19}$$

$$w_k^{(j)}(\boldsymbol{z}) = p_{D,k}w_{k|k-1}^{(j)}q_k^{(j)}(\boldsymbol{z})\frac{\langle \Psi_k^1[w_{k|k-1}, \boldsymbol{Z}_k\backslash\{\boldsymbol{z}\}], p_{k|k-1}\rangle}{\langle \Psi_k^0[w_{k|k-1}, \boldsymbol{Z}_k], p_{k|k-1}\rangle}\frac{\langle 1, \kappa_k\rangle}{\kappa_k(\boldsymbol{z})}, \tag{20}$$

$$\boldsymbol{m}_k^{(j)}(\boldsymbol{z}) = \boldsymbol{m}_{k|k-1}^{(j)} + \boldsymbol{K}_k^{(j)}\left(\boldsymbol{z} - \boldsymbol{\eta}_{k|k-1}^{(j)}\right), \tag{21}$$

$$\boldsymbol{P}_k^{(j)} = \left[\boldsymbol{I} - \boldsymbol{K}_k^{(j)}\boldsymbol{H}_k\right]\boldsymbol{P}_{k|k-1}^{(j)}, \tag{22}$$

$$\boldsymbol{K}_k^{(j)} = \boldsymbol{P}_{k|k-1}^{(j)}\boldsymbol{H}_k^T\left[\boldsymbol{S}_{k|k-1}^{(j)}\right]^{-1}, \tag{23}$$

where $|\boldsymbol{Z}|$ denotes the number of the elements of the set $\boldsymbol{Z}$, $p_{K,k}$ denotes the cardinality distribution of false alarm at time step k, $e_j(\cdot)$ denotes elementary symmetric function of order j, and $e_j(Z) = \sum_{S\subseteq Z, |S|=j}\left(\prod_{\zeta\in S}\zeta\right)$, $e_0(Z) = 1$, $A_l^j = l!/(l-j)!$, and $\boldsymbol{Z}_k\backslash\{\boldsymbol{z}\}$ denotes the set $\boldsymbol{Z}_k$ without element $\boldsymbol{z}$.

At last, the components with tiny weight are pruned away, the components with uniform distribution are combined, and the maximum number of components is limited [27]. Then, the updated PHD at time step k is expressed in the Gaussian mixture model as follows:

$$v_k(x) = \sum_{i=1}^{J_k} w_k^{(i)} N\left(x; \boldsymbol{m}_k^{(i)}, \boldsymbol{P}_k^{(i)}\right), \tag{24}$$

where $w_k^{(i)}$, $\boldsymbol{m}_k^{(i)}$, and $\boldsymbol{P}_k^{(i)}$ denote the weight, estimate of the state, and MSEM of the i-th target at time step k, respectively.

The n corresponding to the maximum value of the cardinality distribution $p_k(n)$ is the estimate of the number of targets. The $\boldsymbol{m}_k^{(i)}$ corresponding to the components with the $\hat{N}_k$ largest weight in the PHD $v_k(x)$ is the estimate of the target states. The first element of the estimated state vector is the estimate of the bearing angle of the target. By substituting $p_k(n)$ and $v_k(x)$ into the next time step, the GM-CPHD filter can be used to recursively estimate the state of the target to carry out DOA tracking.

4 VB-GMPHD filter for robust multi-target DOA tracking with uncertain measurement noise

The existing DOA tracking techniques usually assume that the measurement noise is a certain stochastic process, which means the MNCM is constant. However, in the real scenario of underwater tracking, the unknown underwater environment always results in uncertain measurement noise, which means the MNCM is time varying. Thus, the assumption of the existing DOA tracking technology on constant MNCM is inconsistent with the real scenario, which results in the decline of tracking performance. In order to improve the robustness of multi-target DOA tracking, variational Bayesian approach is used to estimate the MNCM in the real time of tracking. In this article, the measurement is a number instead of a vector, thus the MNCM reduces to the measurement noise variance.

4.1 Choice of prior distribution

In the multi-target DOA tracking scenario, when using the i_m-th measurement to estimate the corresponding i_n-th target, the one-

step predicted probability density distribution (PDF) $p(\boldsymbol{x}_k^{i_n}|\boldsymbol{z}_{1:\,k-1}^{i_m})$ and the likelihood PDF $p(\boldsymbol{z}_k^{i_m}|\boldsymbol{x}_k^{i_n})$ are assumed to be subject to Gaussian distributions in the framework of the KF [35] as follows:

$$p\left(\boldsymbol{x}_k^{i_n}\middle|\boldsymbol{z}_{1:k-1}^{i_m},\boldsymbol{P}_{k|k-1}\right)=\mathrm{N}\left(\boldsymbol{x}_k^{i_n};\hat{\boldsymbol{x}}_{k|k-1}^{i_n},\boldsymbol{P}_{k|k-1}^{i_n}\right),\tag{25}$$

$$p\left(\boldsymbol{z}_k^{i_m}\middle|\boldsymbol{x}_k^{i_n},\sigma_{r,k}^2\right)=\mathrm{N}\left(\boldsymbol{z}_k^{i_m};\boldsymbol{H}_k\boldsymbol{x}_k^{i_n},\sigma_{r,k}^2\right),\tag{26}$$

where $\mathrm{N}(\cdot;\mu,\boldsymbol{\Sigma})$ denotes the PDF of the Gaussian distribution with mean μ and covariance matrix $\boldsymbol{\Sigma}$, $\boldsymbol{H}_k$ is the measurement matrix given in Equation 2, and $\sigma_{r,k}^2$ denotes the measurement noise variance. $\hat{\boldsymbol{x}}_{k|k-1}^{i_n}$ and $\boldsymbol{P}_{k|k-1}^{i_n}$ denote the predicted state and predicted MSEM of the i_n-th target, respectively, which are expressed as

$$\hat{\boldsymbol{x}}_{k|k-1}^{i_n}=\boldsymbol{F}_{k|k-1}\hat{\boldsymbol{x}}_{k-1|k-1}^{i_n},\tag{27}$$

$$\boldsymbol{P}_{k|k-1}^{i_n}=\boldsymbol{F}_{k|k-1}\boldsymbol{P}_{k-1|k-1}^{i_n}\boldsymbol{F}_{k|k-1}^{\mathrm{T}}+\boldsymbol{Q}_{k-1},\tag{28}$$

where $\hat{\boldsymbol{x}}_{k-1|k-1}^{i_n}$ and $\boldsymbol{P}_{k-1|k-1}^{i_n}$ are the estimates of the state and MSEM of the i_n-th target at time step k-1, respectively.

In order to infer $\boldsymbol{x}_k^{i_n}$ along with $\sigma_{r,k}^2$, a conjugate prior distribution has to be selected for the fluctuant $\sigma_{r,k}^2$, since a conjugate distribution can guarantee the same functional forms of the prior distribution and posterior distribution. In the Bayesian theory, the inverse Wishart distribution is usually used as the conjugate prior for the covariance matrix of a Gaussian distribution with known mean [36]. Since $\sigma_{r,k}^2$ is the variance of the Gaussian distribution, the prior distribution $p(\sigma_{r,k}^2|\boldsymbol{z}_{1:\,k-1}^{i_m})$ is selected as the inverse Wishart distribution, given by

$$p\left(\sigma_{r,k}^2\middle|\boldsymbol{z}_{1:\,k-1}^{i_m}\right)=\mathrm{IW}\left(\sigma_{r,k}^2;\hat{u}_{k|k-1},\hat{\boldsymbol{U}}_{k|k-1}\right),\tag{29}$$

where $\mathrm{IW}(\cdot;\lambda,\boldsymbol{\Psi})$ denotes the PDF of the inverse Wishart distribution with degree of freedom (dof) λ and inverse scale matrix $\boldsymbol{\Psi}$ [37], $\hat{u}_{k|k-1}$ and $\hat{\boldsymbol{U}}_{k|k-1}$ are the dof and inverse scale matrix of $p(\sigma_{r,k}^2|\boldsymbol{z}_{1:\,k-1}^{i_m})$, respectively.

The posterior distribution $p(\sigma_{r,k-1}^2|\boldsymbol{z}_{1:\,k-1}^{i_m})$ is also subject to an inverse Wishart distribution as follows:

$$p\left(\sigma_{r,k-1}^2\middle|\boldsymbol{z}_{1:\,k-1}^{i_m}\right)=\mathrm{IW}\left(\sigma_{r,k-1}^2;\hat{u}_{k-1|k-1},\hat{\boldsymbol{U}}_{k-1|k-1}\right).\tag{30}$$

To guarantee that $p(\sigma_{r,k-1}^2|\boldsymbol{z}_{1:\,k-1}^{i_m})$ is the inverse Wishart distribution given by Equation 29, the previous approximate posterior distribution is spread through a forgetting factor $\rho\in(0,1]$, which indicates the extent of time fluctuations of the MNCM. Then, the prior dof $\hat{u}_{k|k-1}$ and prior inverse scale matrix $\hat{\boldsymbol{U}}_{k|k-1}$ are given as follows [34]:

$$\hat{u}_{k|k-1}=\rho\left(\hat{u}_{k-1|k-1}-r-1\right)+r+1,\tag{31}$$

$$\hat{\boldsymbol{U}}_{k|k-1}=\rho\hat{\boldsymbol{U}}_{k-1|k-1}.\tag{32}$$

where r denotes the order of the MNCM $\sigma_{r,k}^2$.

4.2 Variational approximations of posterior PDFs

According to the variational Bayesian approximation, the joint posterior PDF of the state of the i_n-th target $\boldsymbol{x}_k^{i_n}$ and MNCM $\sigma_{r,k}^2$ is approximated to

$$p\left(\boldsymbol{x}_k^{i_n},\sigma_{r,k}^2\mid\boldsymbol{z}_{1:\,k}^{i_m}\right)\approx q\left(\boldsymbol{x}_k^{i_n}\right)q\left(\sigma_{r,k}^2\right),\tag{33}$$

where $q(\boldsymbol{x}_k^{i_n})$ and $q(\sigma_{r,k}^2)$ are the approximate posterior PDFs of $\boldsymbol{x}_k^{i_n}$ and $\sigma_{r,k}^2$, respectively [38, 39]. The variational Bayesian approximation is formed by minimizing the Kullback–Leibler divergence (KLD) between the true joint distribution $p(\boldsymbol{x}_k^{i_n},\sigma_{r,k}^2\mid\boldsymbol{z}_{1:\,k}^{i_m})$ and the approximate distribution $q(\boldsymbol{x}_k^{i_n})q(\sigma_{r,k}^2)$, i.e.,

$$\left\{q\left(\boldsymbol{x}_k^{i_n}\right),q\left(\sigma_{r,k}^2\right)\right\}=\arg\min\mathrm{KLD}\left(q\left(\boldsymbol{x}_k^{i_n}\right)q\left(\sigma_{r,k}^2\right)\parallel p\left(\boldsymbol{x}_k^{i_n},\sigma_{r,k}^2\mid\boldsymbol{z}_{1:\,k}^{i_m}\right)\right),\tag{34}$$

where $\mathrm{KLD}(q(x)\parallel p(x))$ denotes the KLD between $q(x)$ and $p(x)$ [38, 39], and

$$\mathrm{KLD}\left(q(x)\parallel p(x)\right)=\int q(x)\log\frac{q(x)}{p(x)}dx.\tag{35}$$

The optimal solution of Equation 34 satisfies the following equations [39]:

$$\log q\left(\boldsymbol{x}_k^{i_n}\right)=\mathrm{E}_{\sigma_{r,k}^2}\left[\log p\left(\boldsymbol{x}_k^{i_n},\sigma_{r,k}^2,\boldsymbol{z}_{1:\,k}^{i_m}\right)\right]+c_{\boldsymbol{x}},\tag{36}$$

$$\log q\left(\sigma_{r,k}^2\right)=\mathrm{E}_{\boldsymbol{x}_k^{i_n}}\left[\log p\left(\boldsymbol{x}_k^{i_n},\sigma_{r,k}^2,\boldsymbol{z}_{1:\,k}^{i_m}\right)\right]+c_{\boldsymbol{R}},\tag{37}$$

where $\mathrm{E}_{\boldsymbol{x}_k^{i_n}}[\cdot]$ and $\mathrm{E}_{\sigma_{r,k}^2}[\cdot]$ denote the expectation with regard to $\boldsymbol{x}_k^{i_n}$ and $\sigma_{r,k}^2$, respectively, and $c_{\boldsymbol{x}}$ and $c_{\boldsymbol{R}}$ denote the constants with respect to $\boldsymbol{x}_k^{i_n}$ and $\sigma_{r,k}^2$, respectively. Since the variational parameters of $q(\boldsymbol{x}_k^{i_n})$ and $q(\sigma_{r,k}^2)$ are coupled, a fixed point iteration process is applied to solve Equations 36, 37, i.e., the approximate posterior PDF $q(\boldsymbol{x}_k^{i_n})$ is updated to $q^{(n+1)}(\boldsymbol{x}_k^{i_n})$ at the $n+1$-th iteration using the posterior PDF $q^{(n)}(\sigma_{r,k}^2)$, and $q(\sigma_{r,k}^2)$ is updated to $q^{(n+1)}(\sigma_{r,k}^2)$ using the posterior $q^{(n)}(\boldsymbol{x}_k^{i_n})$.

According to Equations 25, 26, 29, the joint PDF is expressed as

$$\begin{aligned}p\left(\boldsymbol{x}_k^{i_n},\sigma_{r,k}^2,\boldsymbol{z}_{1:\,k}^{i_m}\right)&=p\left(\boldsymbol{z}_k^{i_m}\middle|\boldsymbol{x}_k^{i_n},\sigma_{r,k}^2\right)p\left(\boldsymbol{x}_k^{i_n}\middle|\boldsymbol{z}_{1:\,k-1}^{i_m}\right)p\left(\sigma_{r,k}^2\middle|\boldsymbol{z}_{1:\,k-1}^{i_m}\right)p\left(\boldsymbol{z}_{1:\,k-1}^{i_m}\right)\\&=\mathrm{N}\left(\boldsymbol{z}_k^{i_m};h\left(\boldsymbol{x}_k^{i_n}\right),\sigma_{r,k}^2\right)\mathrm{N}\left(\boldsymbol{x}_k^{i_n};\hat{\boldsymbol{x}}_{k|k-1}^{i_n},\boldsymbol{P}_{k|k-1}^{i_n}\right)\\&\quad\times\mathrm{IW}\left(\sigma_{r,k}^2;\hat{u}_{k|k-1},\hat{\boldsymbol{U}}_{k|k-1}\right)p\left(\boldsymbol{z}_{1:\,k-1}^{i_m}\right)\end{aligned}\tag{38}$$

(1) Update of $\boldsymbol{x}_k^{i_n}$

The posterior $q^{(n+1)}(\boldsymbol{x}_k^{i_n}|\boldsymbol{z}_{1:\,k-1}^{i_m})$ is updated according to the extended Kalman filter equations as

$$q^{(n+1)}\left(\boldsymbol{x}_k^{i_n}\middle|\boldsymbol{z}_{1:\,k-1}^{i_m}\right)=\mathrm{N}\left(\boldsymbol{x}_k^{i_n};\hat{\boldsymbol{x}}_{k|k}^{(n+1)},\hat{\boldsymbol{P}}_{k|k}^{(n+1)}\right),\tag{39}$$

where the mean vector $\hat{\boldsymbol{x}}_{k|k}^{(n+1)}$ and the covariance matrix $\hat{\boldsymbol{P}}_{k|k}^{(n+1)}$ are given as follows:

$$\boldsymbol{K}_k^{(n+1)}=\boldsymbol{P}_{k|k-1}^{i_n}\left(\boldsymbol{H}_k\right)^{\mathrm{T}}\left(\boldsymbol{H}_k\boldsymbol{P}_{k|k-1}^{i_n}\left(\boldsymbol{H}_k\right)^{\mathrm{T}}+\left(\sigma_{r,k}^{(n)}\right)^2\right)^{-1},\tag{40}$$

$$\hat{\boldsymbol{x}}_{k|k}^{(n+1)}=\hat{\boldsymbol{x}}_{k|k-1}^{i_n}+\boldsymbol{K}_k^{(n+1)}\left(\boldsymbol{z}_k^{i_m}-\boldsymbol{H}_k\hat{\boldsymbol{x}}_{k|k-1}\right),\tag{41}$$

$$\boldsymbol{P}_{k|k}^{(n+1)}=\boldsymbol{P}_{k|k-1}^{i_n}-\boldsymbol{K}_k^{(n+1)}\boldsymbol{H}_k^{(n)}\boldsymbol{P}_{k|k-1}^{i_n}.\tag{42}$$

(2) Update of $\sigma_{r,k}^2$

According to Equation 38, $\log q^{(n)}(\sigma_{r,k}^2)$ is given by

$$
\begin{aligned}
&\log q^{(n+1)}\left(\sigma_{r,k}^2\right)\\
&= -0.5\left(r+\hat{u}_{k|k-1}+2\right)\log\left|\sigma_{r,k}^2\right| - 0.5\mathrm{tr}\left(\hat{\boldsymbol{U}}_{k|k-1}\left(\sigma_{r,k}^2\right)^{-1}\right)\\
&\quad - 0.5\left(\boldsymbol{z}_k^{i_m}-\boldsymbol{H}_k\boldsymbol{x}_k^{i_n}\right)^{\mathrm{T}}\left(\sigma_{r,k}^2\right)^{-1}\left(\boldsymbol{z}_k^{i_m}-\boldsymbol{H}_k\boldsymbol{x}_k^{i_n}\right)+c_{\boldsymbol{R}}\\
&= -0.5\left(r+\hat{u}_{k|k-1}+2\right)\log\left|\sigma_{r,k}^2\right| - 0.5\mathrm{tr}\left(\left(\boldsymbol{B}_k^{(n)}+\hat{\boldsymbol{U}}_{k|k-1}\right)\left(\sigma_{r,k}^2\right)^{-1}\right)+c_{\boldsymbol{R}}
\end{aligned}
\tag{43}
$$

where

$$
\begin{aligned}
\boldsymbol{B}_k^{(n)} &= \mathrm{E}^{(n)}\left[\left(\boldsymbol{z}_k^{i_m}-\boldsymbol{H}_k\boldsymbol{x}_k^{i_n}\right)\left(\boldsymbol{z}_k^{i_m}-\boldsymbol{H}_k\boldsymbol{x}_k^{i_n}\right)^{\mathrm{T}}\right]\\
&= \mathrm{E}^{(n)}\left[\left(\boldsymbol{z}_k^{i_m}-\boldsymbol{H}_k\hat{\boldsymbol{x}}_{k|k}^{(n)}+\boldsymbol{H}_k\hat{\boldsymbol{x}}_{k|k}^{(n)}-\boldsymbol{H}_k\boldsymbol{x}_k^{i_n}\right)\left(\boldsymbol{z}_k^{i_m}-\boldsymbol{H}_k\hat{\boldsymbol{x}}_{k|k}^{(n)}+\boldsymbol{H}_k\hat{\boldsymbol{x}}_{k|k}^{(n)}-\boldsymbol{H}_k\boldsymbol{x}_k^{i_n}\right)^{\mathrm{T}}\right]\\
&= \left(\boldsymbol{z}_k^{i_m}-\boldsymbol{H}_k\hat{\boldsymbol{x}}_{k|k}^{(n)}\right)\left(\boldsymbol{z}_k^{i_m}-\boldsymbol{H}_k\hat{\boldsymbol{x}}_{k|k}^{(n)}\right)^{\mathrm{T}}+\boldsymbol{H}_k\mathrm{E}^{(n)}\left[\left(\boldsymbol{x}_k^{i_n}-\hat{\boldsymbol{x}}_{k|k}^{(n)}\right)\left(\boldsymbol{x}_k^{i_n}-\hat{\boldsymbol{x}}_{k|k}^{(n)}\right)^{\mathrm{T}}\right]\boldsymbol{H}_k^{\mathrm{T}}\\
&= \left(\boldsymbol{z}_k^{i_m}-\boldsymbol{H}_k\hat{\boldsymbol{x}}_{k|k}^{(n)}\right)\left(\boldsymbol{z}_k^{i_m}-\boldsymbol{H}_k\hat{\boldsymbol{x}}_{k|k}^{(n)}\right)^{\mathrm{T}}+\boldsymbol{H}_k\boldsymbol{P}_{k|k}^{(n)}\boldsymbol{H}_k^{\mathrm{T}}.
\end{aligned}
\tag{44}
$$

From Equation 43, $q^{(n+1)}(\sigma_{r,k}^2)$ is updated as

$$
q^{(n+1)}\left(\sigma_{r,k}^2\right)=\mathrm{IW}\left(\sigma_{r,k}^2;\hat{u}_k^{(n+1)},\hat{\boldsymbol{U}}_k^{(n+1)}\right),
\tag{45}
$$

where the dof $\hat{u}_k^{(n+1)}$ and the inverse scale matrix $\hat{\boldsymbol{U}}_k^{(n+1)}$ are given as follows:

$$
\hat{u}_k^{(n+1)}=\hat{u}_{k|k-1}+1,
\tag{46}
$$

$$
\hat{\boldsymbol{U}}_k^{(n+1)}=\boldsymbol{B}_k^{(n)}+\hat{\boldsymbol{U}}_{k|k-1}.
\tag{47}
$$

Then, according to Equation 38, $\log q^{(n)}(\boldsymbol{x}_k^{i_n})$ is given by

$$
\begin{aligned}
\log q^{(n+1)}(\boldsymbol{x}_k) = &-0.5\left(\boldsymbol{z}_k^{i_m}-\boldsymbol{H}_k\boldsymbol{x}_k^{i_n}\right)^{\mathrm{T}}\mathrm{E}^{(n+1)}\left[\left(\sigma_{r,k}^2\right)^{-1}\right]\left(\boldsymbol{z}_k^{i_m}-\boldsymbol{H}_k\boldsymbol{x}_k^{i_n}\right)\\
&-0.5\left(\boldsymbol{x}_k^{i_n}-\hat{\boldsymbol{x}}_{k|k-1}^{i_n}\right)^{\mathrm{T}}\boldsymbol{P}_{k|k-1}^{-1}\left(\boldsymbol{x}_k^{i_n}-\hat{\boldsymbol{x}}_{k|k-1}^{i_n}\right)+c_{\boldsymbol{x}}
\end{aligned}
\tag{48}
$$

where $\mathrm{E}^{(n+1)}[(\sigma_{r,k}^2)^{-1}]$ is given by

$$
\mathrm{E}^{(n+1)}\left[\left(\sigma_{r,k}^2\right)^{-1}\right]=\left(\hat{u}_k^{(n+1)}-m-1\right)\left(\hat{\boldsymbol{U}}_k^{(n+1)}\right)^{-1}.
\tag{49}
$$

The modified one-step predicted PDF $p^{(n+1)}(\boldsymbol{z}_k|\boldsymbol{x}_k)$ at the $n+1$-th iteration is defined as

$$
p^{(n+1)}\left(\boldsymbol{z}_k^{i_m}|\boldsymbol{x}_k^{i_n}\right)=\mathrm{N}\left(\boldsymbol{z}_k^{i_m};\boldsymbol{H}_k\boldsymbol{x}_k^{i_n},\left(\hat{\sigma}_{r,k}^{(n+1)}\right)^2\right),
\tag{50}
$$

where the modified MNCM $(\hat{\sigma}_{r,k}^{(n+1)})^2$ is formulated as

$$
\left(\hat{\sigma}_{r,k}^{(n+1)}\right)^2=\left\{\mathrm{E}^{(n+1)}\left[\left(\sigma_{r,k}^2\right)^{-1}\right]\right\}^{-1}=\hat{\boldsymbol{U}}_k^{(n+1)}/\left(\hat{u}_k^{(n+1)}-m-1\right).
\tag{51}
$$

Finally, after N fixed-point iterations, the variational approximations of the posterior PDFs for the i_n-th target are given as follows:

$$
q\left(\boldsymbol{x}_k^{i_n}\right)\approx q^{(N)}\left(\boldsymbol{x}_k^{i_n}\right)=\mathrm{N}\left(\boldsymbol{x}_k^{i_n};\hat{\boldsymbol{x}}_{k|k}^{(N)},\boldsymbol{P}_{k|k}^{(N)}\right)=\mathrm{N}\left(\boldsymbol{x}_k^{i_n};\hat{\boldsymbol{x}}_{k|k}^{i_n},\boldsymbol{P}_{k|k}^{i_n}\right),
\tag{52}
$$

$$
q\left(\sigma_{r,k}^2\right)\approx q^{(N)}\left(\sigma_{r,k}^2\right)=\mathrm{IW}\left(\sigma_{r,k}^2;\hat{u}_k^{(N)},\hat{\boldsymbol{U}}_k^{(N)}\right)=\mathrm{IW}\left(\sigma_{r,k}^2;\hat{u}_{k|k},\hat{\boldsymbol{U}}_{k|k}\right).
\tag{53}
$$

4.3 Algorithm of VB-GMCPHD filter

According to the above derivation, the pseudo-code of the variational Bayesian GM-CPHD filter (VB-GMCPHD) for DOA tracking at one time step is given in Algorithm 1.

1. Initialize GM components $\{w_0^{(i)},\boldsymbol{m}_0^{(i)},\boldsymbol{P}_0^{(i)}\}_{i=1}^{J_0}$ and cardinality distribution $p_0(n)$;
For $k=1{:}\,K$
Prediction:
2. Predict the cardinality distribution $p_{k|k-1}(n)$ by using Equation 4;
3. Calculate the components of survive targets:
  For $i=1{:}\,J_{k-1}$
    $w_{s,k|k-1}^{(i)}=p_{s,k}w_{k-1}^{(i)}$, $\boldsymbol{m}_{s,k|k-1}^{(i)}=\boldsymbol{F}_{k-1}\boldsymbol{m}_{k-1}^{(i)}$,
    $\boldsymbol{P}_{s,k|k-1}^{(i)}=\boldsymbol{G}_k\sigma_q^2\boldsymbol{G}_k^T+\boldsymbol{F}_{k-1}\boldsymbol{P}_{k-1}^{(i)}\boldsymbol{F}_{k-1}^T$;
    $\hat{u}_{k|k-1}^{(i)}=\rho(\hat{u}_{k-1}^{(i)}-r-1)+r+1$, $\hat{\boldsymbol{U}}_{k|k-1}^{(i)}=\rho\hat{\boldsymbol{U}}_{k-1}^{(i)}$.
  End
4. Add the components of birth targets $\left\{w_{\gamma,k}^{(i)},\boldsymbol{m}_{\gamma,k}^{(i)},\boldsymbol{P}_{\gamma,k}^{(i)}\right\}_{i=J_{k-1}+1}^{i=J_{k-1}+J_{\gamma,k}}$;
5. Express the predicted GM components as $\{w_{k|k-1}^{(i)},\boldsymbol{m}_{k|k-1}^{(i)},\boldsymbol{P}_{k|k-1}^{(i)}\}_{i=1}^{i=J_{k|k-1}}$, where $J_{k|k-1}=J_{k-1}+J_{\gamma,k}$;
Update:
6. Update the cardinality distribution $p_k(n)$ by using Equation 11;
7. Update GM components of targets:
  For $i=1{:}\,J_{k|k-1}$
    $w_k^{(i)}=\frac{\langle\Psi_k^1[\boldsymbol{w}_{k|k-1},\boldsymbol{Z}_k],p_{k|k-1}\rangle}{\langle\Psi_k^0[\boldsymbol{w}_{k|k-1},\boldsymbol{Z}_k],p_{k|k-1}\rangle}(1-p_{D,k})w_{k-1}^{(i)}$, $\boldsymbol{m}_k^{(i)}=\boldsymbol{m}_{k|k-1}^{(i)}$,
    $\boldsymbol{P}_k^{(i)}=\boldsymbol{P}_{k|k-1}^{(i)}$;
  End
  For $m=1{:}\,m_k$
    For $i=1{:}\,J_{k|k-1}$
8. Estimate $\sigma_{r,k}^2$ along with states of targets by using VB iterations
Initialization: $\hat{\boldsymbol{m}}_{k|k}^{(0)}=\boldsymbol{m}_{k|k-1}^{(i)}$, $(\hat{\sigma}_{r,k}^{(0)})^2=\hat{\boldsymbol{U}}_{k|k-1}/\hat{u}_{k|k-1}$.
  For $n=0{:}\,N-1$
    $\boldsymbol{S}_{k|k-1}^{(n)}=\boldsymbol{H}_k\boldsymbol{P}_{k|k-1}^{i}\boldsymbol{H}_k^T+(\hat{\sigma}_{r,k}^{(n)})^2$
    $\boldsymbol{K}_k^{(n+1)}=\boldsymbol{P}_{k|k-1}^{(i)}(\boldsymbol{H}_k)^{\top}(\boldsymbol{S}_{k|k-1}^{(n)})^{-1}$, $\hat{\boldsymbol{m}}_{k|k}^{(n+1)}=\hat{\boldsymbol{m}}_{k|k-1}+\boldsymbol{K}_k^{(n+1)}(z_m-\boldsymbol{H}_k\hat{\boldsymbol{m}}_{k|k}^{(n)})$,
    $\boldsymbol{P}_{k|k}^{(n+1)}=\boldsymbol{P}_{k|k-1}^{(i)}-\boldsymbol{K}_k^{(n+1)}\boldsymbol{H}_k\boldsymbol{P}_{k|k-1}^{(i)}$.
    $\boldsymbol{B}_k^{(n+1)}=(z_m-\boldsymbol{H}_k\hat{\boldsymbol{m}}_{k|k}^{(n+1)})(z_m-\boldsymbol{H}_k\hat{\boldsymbol{m}}_{k|k}^{(n+1)})^{\top}+\boldsymbol{H}_k\boldsymbol{P}_{k|k}^{(n+1)}(\boldsymbol{H}_k)^{\top}$,
    $\hat{\boldsymbol{U}}_{k|k}^{(n+1)}=\hat{\boldsymbol{U}}_{k|k-1}+\boldsymbol{B}_k^{(n+1)}$, $\hat{u}_{k|k}^{(n+1)}=\hat{u}_{k|k-1}+1$,
    $(\hat{\sigma}_{r,k}^{(n+1)})^2=\hat{\boldsymbol{U}}_{k|k}^{(n+1)}/\hat{u}_{k|k}^{(n+1)}$.
  End
  $\boldsymbol{S}_{k|k-1}=\boldsymbol{S}_{k|k-1}^{(N)}$
  $\boldsymbol{m}_k^{(J_{k|k-1}+(m-1)m_k+i)}=\hat{\boldsymbol{m}}_{k|k}^{(N)}$,
  $\boldsymbol{P}_k^{(J_{k|k-1}+(m-1)m_k+i)}=\boldsymbol{P}_{k|k}^{(N)}$;
  $w_k^{(J_{k|k-1}+(m-1)m_k+i)}=p_{D,k}w_{k|k-1}^{(i)}q_k^{(i)}(\boldsymbol{z}_m)\frac{\langle\Psi_k^1[w_{k|k-1},\boldsymbol{Z}_k\backslash\{\boldsymbol{z}_m\}],p_{k|k-1}\rangle}{\langle\Psi_k^0[w_{k|k-1},\boldsymbol{Z}_k],p_{k|k-1}\rangle}\frac{\langle 1,\kappa_k\rangle}{\kappa_k(\boldsymbol{z}_m)}$
    End
  End
9. $J_{k|k}=J_{k|k-1}+J_{k|k-1}m_k$, Prune, merge, and limit the $J_{k|k}$ components, and new J_k components are obtained;
10. Express the updated GM components as $\{w_k^{(i)},\boldsymbol{m}_k^{(i)},\boldsymbol{P}_k^{(i)}\}_{i=1}^{i=J_k}$;
11. The n corresponding to the peak of $p_k(n)$ is the estimate of the target number;
12. The $\boldsymbol{m}_k^{(i)}$ corresponding to the $\hat{N}_k$ components with the largest weight is the estimate of target states.
End

Algorithm 1. VB-CPHD filter for Robust multi-target DOA tracking

5 Results and discussion

5.1 Experimental setup

The open experimental data set SWellEx-96 [40] is used to verify the tracking performance of the proposed VB-GMCPHD filter for robust DOA tracking. The experiment was performed at the United States Marine Physical Laboratory from 10 to 18 May 1996, approximately 12 km from the tip of Point Loma near San Diego, California. The data of the north horizontal linear array of the S59 event of the experiment is used in this section. 900 s of experimental data is used to test the proposed method in this section. Before the experiment, a CTD is used to obtain the sound velocity in the experimental area. The experimental ship tows a continuous sound source at a depth of 54 m at a speed of 5 knots and sails north, which is named target 1 in this article. In addition, an uncooperative ship sails from northwest to southeast with continuous radiating noise, which is named target 2 in this article. The radar system of an experimental ship records the distance and bearing of the uncooperative ship and derives the latitude and longitude of the uncooperative ship. The horizontal linear array is placed on the seafloor at a depth of 213 m and continuously records the received acoustic signal at a sampling frequency of 3,276.8 Hz. The horizontal array consists of 32 elements, among which 27 elements provide effective data. The positions of the effective elements are shown in Figure 1, where the position of the first element is taken as the origin of coordinates. Figure 1 shows that the elements are actually not arranged in a straight line but in a slight curve. Therefore, the port and starboard ambiguity problem of a linear array is avoided.

To evaluate the difference between the real set and estimated set of the states of the targets, an evaluation has to be chosen. Because the number of elements of the real set and estimated set of the states of the targets is different, the root-mean-square type of evaluation (such as the root mean square error) is not usable. In this article, optimal sub-pattern assignment (OSPA) error is selected to evaluate the multi-target tracking performance, which is defined as follows [41]:

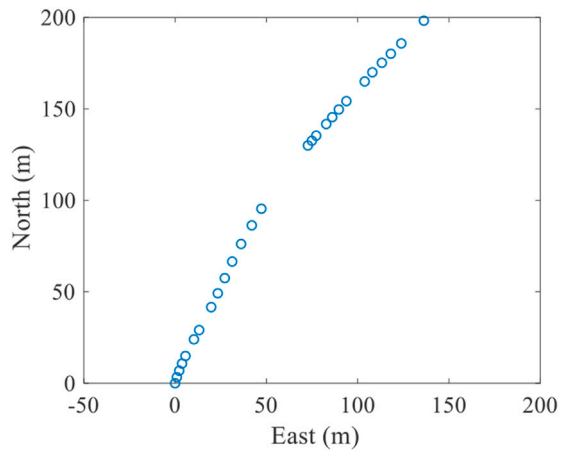

FIGURE 1
Position of the horizontal linear array.

$$\begin{cases} d_p^{(c)}(\boldsymbol{X},\boldsymbol{Y}) = \left(\frac{1}{n}\min_{\pi\in\Pi}\sum_{i=1}^{m} d^{(c)}(x_i, y_{\pi(i)})^p + c^p(n-m)\right)^{1/p}, & m \le n \\ d_p^{(c)}(\boldsymbol{X},\boldsymbol{Y}) = d_p^{(c)}(\boldsymbol{Y},\boldsymbol{X}), & m > n \end{cases} \tag{54}$$

where $d_p^{(c)}(\boldsymbol{X},\boldsymbol{Y})$ is the OSPA error, $\boldsymbol{X} = \{x_1, x_2, ..., x_m\}$ and $\boldsymbol{Y} = \{y_1, y_2, ..., y_n\}$ are RFSs, Π denotes the set made up with m elements from $\{1, 2, ..., n\}$, and $d^{(c)}(x,y) = \min\{d(x,y), c\}$, $d(x,y)$ is the Euclidean distance between x and y, while c and p denote the truncation parameter and order, and are set to 5 and 1, respectively. The smaller the OSPA error means the higher the precision.

5.2 Experimental results

The minimum variance distortionless response (MVDR) was used to obtain the measurement of the bearing angles of the targets at 48 Hz–52 Hz every 10 s, and the bearing angle scans from 0 to 360° every 1°. According to the CTD data, the sound velocity was set to 1,493 m/s. The bearing time recording (BTR) obtained by the MVDR is given by the background 3D color diagram of Figure 2A. The true bearing angles of the two targets are given by the black line. The bearing angles corresponding to the peaks of the spectrum are extracted at each moment, and the obtained measurements of bearing angles of targets are shown by red dots in Figure 2A. Figure 2A shows trajectories of three targets. The bearing angle of target 1 moves from 135° to 50°, the bearing angle of target 2 moves from 285° to 275°, and the bearing angle of an unknown uncooperative target stays near 320°, which is named target 3 in this article. Figure 2A also shows some error, missing detection, and false alarm in the measurements.

The proposed robust multi-target DOA tracking method is used to process the bearing angle measurements, and the results of KF-JPDA [42], GM-PHD filter [27], and GM-CPHD filter [30] are also given for comparison. The process noise variance of the CV model is set to 2.5×10^{-4}. The detection probability and false alarm probability are set to 0.9 and 0.1, respectively. The measurement noise variance $\sigma_{r,k}^2$ of KF-JPDA, GM-PHD filter, and GM-CPHD filter is set to 25. The parameters $\hat{u}_0$, $\hat{U}_0$, and ρ of the VB- GMCPHD are set to 12, 12 $\sigma_{r,k}^2$, and 0.95, respectively, and the number of VB iterations N is set to 5.

The tracking results of KF-JPDA, GM-PHD filter, GM-CPHD filter, and VB-GMCPHD filter are shown in Figures 2B–E, and the OSPA errors are shown in Figure 2F. The average OSPA errors tracking step are shown in Table 1; Figures 2B–E show that all multi-target DOA tracking methods carried out stable tracking of the three targets, and the tracking trajectories are consistent with the real trajectories. Figure 2F and Table 1 show that KF-JPDA, GM-PHD filter, GM-CPHD filter, and the proposed VB-GMCPHD filter significantly reduce OSPA errors on the basis of measurements, and the OSPA errors of the VB-GMCPHD filter are slightly smaller than those of the KF-JPDA, GM-PHD filter, and GM-CPHD filter.

Since the power of measurement noise hardly varies in the experiment, the performance of the proposed VB-GMCPHD filter for the robust multi-target DOA tracking improves slightly when compared to the other methods. In order to further test the robustness of the proposed robust underwater multi-target DOA tracking method in the scenario of uncertain measurement noise, a period of high-power noise was added to the experimental data from

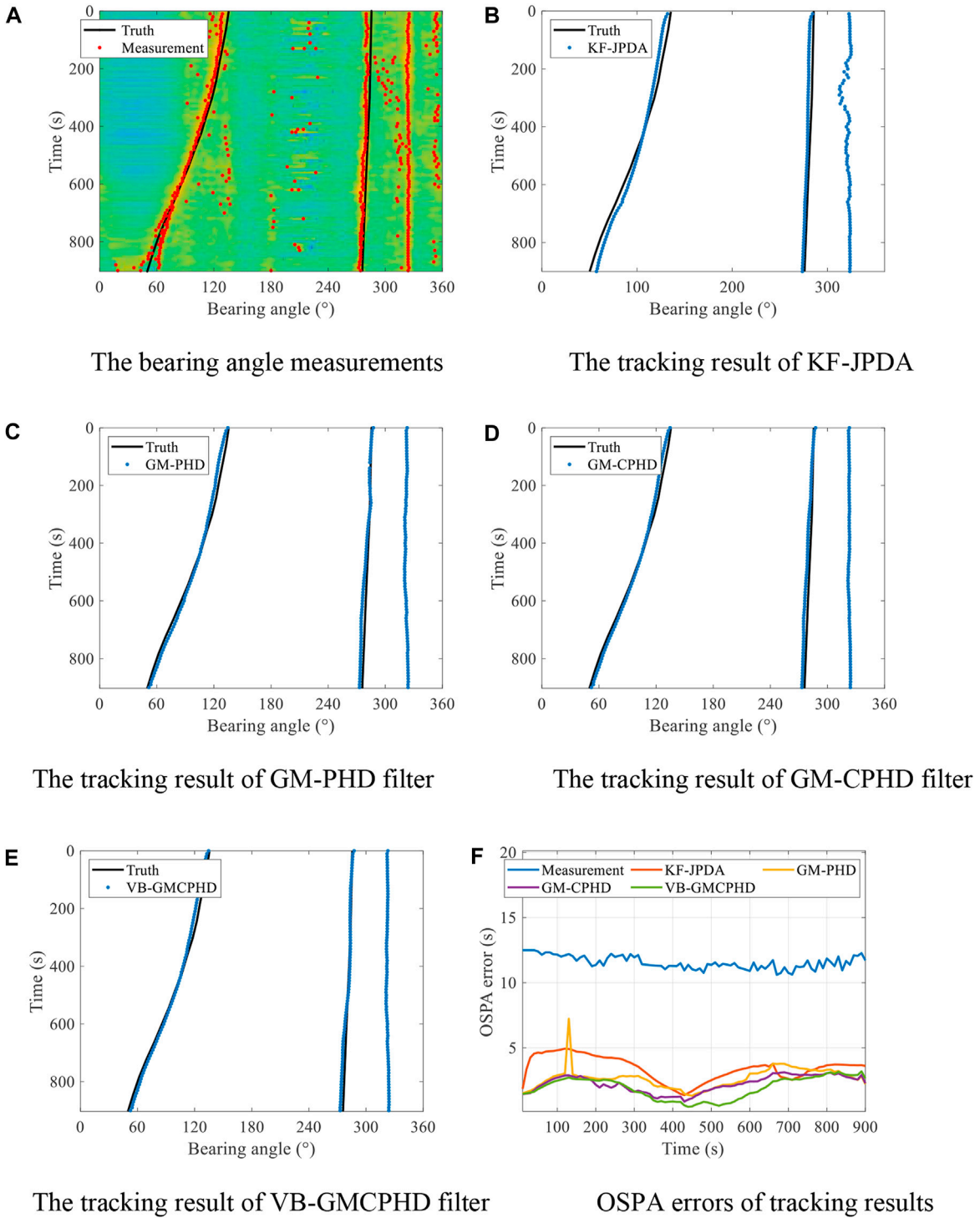

FIGURE 2
Bearing angle measurements, tracking results, and the OSPA errors of KF-JPDA, GM-PHD filter, GM-CPHD filter, and VB-GMCPHD filter. **(A)** Bearing angle measurements. **(B)** Tracking result of KF-JPDA. **(C)** The tracking result of GM-PHD filter. **(D)** The tracking result of GM-CPHD filter. **(E)** The tracking result of VB-GMCPHD filter. **(F)** OSPA errors of tracking results.

500 s to 600 s. Then, the abovementioned process was repeated for the data with added noise.

The BTR and bearing angle measurements obtained by MVDR are shown in Figure 3A. The tracking results of KF-JPDA, GM-PHD filter, GM-CPHD filter, and VB-GMCPHD filter are shown in Figures 3B–E, respectively. The OSPA errors of the tracking results are shown in Figure 3F, and the average OSPA errors per tracking step are shown in Table 2.

Figure 3 shows that KF-JPDA, GM-PHD filter, and GM-CPHD filter provide stable tracking of the bearing angles of the three targets

TABLE 1 The average OSPA errors of the tracking results of KF-JPDA, GM-PHD filter, GM-CPHD filter, and VB- GMCPHD filter in one tracking step.

	KF-JPDA	GM-PHD	GM-CPHD	VB- GMCPHD
Average OSPA error (°)	3.42	2.67	2.24	1.93

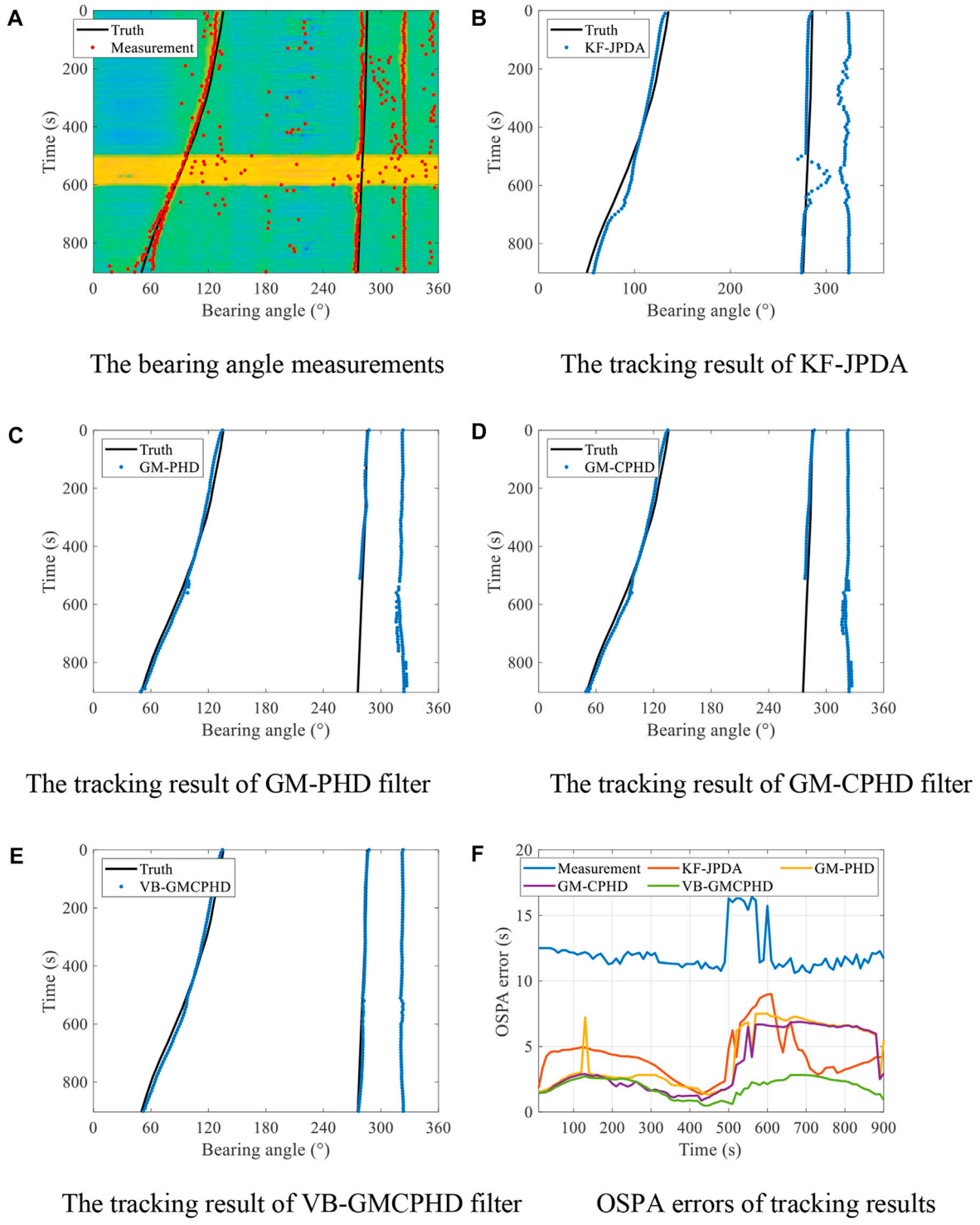

FIGURE 3
Bearing angle measurements, tracking results, and OSPA errors of KF-JPDA, GM-PHD filter, GM-CPHD filter, and VB-GMCPHD filter when processing the experimental data with added noise. **(A)** Bearing angle measurements. **(B)** Tracking result of KF-JPDA. **(C)** Tracking result of GM-PHD filter. **(D)** Tracking result of GM-CPHD filter. **(E)** Tracking result of VB-GMCPHD filter. **(F)** OSPA errors of tracking results.

TABLE 2 The average OSPA errors of the tracking results of KF-JPDA, GM-PHD filter, GM-CPHD filter, and VB-GMCPHD filter in one tracking step when processing the experimental data with added noise.

	KF-JPDA	GM-PHD	GM-CPHD	VB-GMCPHD
Average OSPA error (°)	4.26	4.22	3.71	1.97

when the measurement noise variance is stationary from 0 to 500 s. However, when the measurement noise variance increases from 500 s to 600 s, the assumption of fixed measurement noise variance of KF-JPDA, GM-PHD filter, and GM-CPHD filter becomes inconsistent with the real increasing measurement noise variance, which results in inaccurate Kalman filter gain. Therefore, the KF-JPDA, GM-PHD filter, and GM-CPHD filter carry out fluctuating tracking trajectory or even miss tracking, which results in an increasing of the OSPA error. The OSPA error of the proposed VB-GMCPHD filter for robust multi-target DOA tracking is significantly less than that of the KF-JPDA, GM-PHD filter, and GM-CPHD filter. The reason is that the VB-GMCPHD filter estimates the measurement noise variance in the real time of tracking so the Kalman filter gain calculated by using the estimate of measurement noise variance is more accurate. Therefore, the increasing measurement noise variance hardly affects the performance of the VB-GMCPHD filter, and the robust DOA tracking with uncertain measurement noise is carried out. Table 2 proves the superiority of the proposed VB-GMCPHD filter in robustness again.

6 Conclusion

The robust multi-target underwater DOA tracking problem in uncertain measurement noise scenario is studied in this article. In order to solve the underwater multi-target DOA tracking problem, a multi-target DOA tracking technique is derived on the basis of the GM-CPHD filter, which is combined the kinematics of the target, the bearing angle measurements, and the multi-target tracking scheme at the same time. Then, considering the uncertain measurement noise results from unknown underwater environment, the online measurement estimator is designed on the basis of the variational Bayesian approach to estimate the measurement noise variance along with the states of the targets as an integrated part during the multi-target DOA tracking procedure. Thus, a robust underwater multi-target DOA tracking method with uncertain measurement noise, named VB-GMCPHD filter, is proposed. From the experiment results validated by real sea trial data, the accuracy and robustness of the proposed VB-GMCPHD is verified and comprehensive discussions are made. From the experimental results and discussions, the proposed VB-GMCPHD can be regarded as an alternative method to accomplish DOA tracking missions, especially when the underwater environment is uncertain.

Data availability statement

Publicly available data sets were analyzed in this study. These data can be found at http://swellex96.ucsd.edu/.

Author contributions

BZ, XH, and YY contributed to the conception and design of the study. XH, YY, JZ, and SX contributed to the investigation of the study. BZ performed the experimental data analysis and wrote the first draft of the manuscript. XH wrote sections of the manuscript. All authors contributed to manuscript revision, and read and approved the submitted version.

Funding

This work was supported by the National Natural Science Foundation of China (Grant No. 12104113), the Shanghai Aerospace Science and Technology Innovation Foundation (Grant No. SAST2022-011), the foundation of Central University Operating Expenses Project (Grant No. G2022KY05102), and the Natural Science Basic Research Program of Shaanxi (Grant No. 2023-JC-JQ-07).

Conflict of interest

The authors declare that the research was conducted in the absence of any commercial or financial relationships that could be construed as a potential conflict of interest.

Publisher's note

All claims expressed in this article are solely those of the authors and do not necessarily represent those of their affiliated organizations, or those of the publisher, editors, and reviewers. Any product that may be evaluated in this article, or claim that may be made by its manufacturer, is not guaranteed or endorsed by the publisher.

References

1. Hou X, Yang L, Yang Y, Zhou J, Qiao G. Bearing-only underwater uncooperative target tracking for non-Gaussian environment using fast particle filter. *IET Radar Sonar Nav* (2022) 16:501–14. doi:10.1049/rsn2.12198

2. Hou X, Zhou J, Yang Y, Yang L, Qiao G. 3D underwater uncooperative target tracking for a time-varying non-Gaussian environment by distributed passive underwater buoys. *Entropy* (2021) 23:902. doi:10.3390/e23070902

3. Li Y, Tang B, Yi Y. A novel complexity-based mode feature representation for feature extraction of ship-radiated noise using VMD and slope entropy. *Appl Acoust* (2022) 196:108899. doi:10.1016/j.apacoust.2022.108899

4. Li Y, Geng B, Jiao S. Dispersion entropy-based lempel-ziv complexity: A new metric for signal analysis. *Chaos solitons fractals* (2022) 161:112400. doi:10.1016/j.chaos.2022.112400

5. Li Y, Jiao S, Geng B. Refined composite multiscale fluctuation-based dispersion Lempel–Ziv complexity for signal analysis. *ISA Trans* (2022). in press. doi:10.1016/j.isatra.2022.06.040

6. Yang Y, Zhang Y, Yang L. Wideband sparse spatial spectrum estimation using matrix filter with nulling in a strong interference environment. *J Acoust Soc Am* (2018) 143:3891–8. doi:10.1121/1.5042406

7. Yan F, Jin M, Qiao X. Low-complexity DOA estimation based on compressed MUSIC and its performance analysis. *IEEE Trans Signal Process* (2013) 61:1915–30. doi:10.1109/TSP.2013.2243442

8. Cao R, Liu B, Gao F, Zhang X. A low-complex one-snapshot DOA estimation algorithm with massive ULA. *IEEE Commun Lett* (2017) 21:1071–4. doi:10.1109/LCOMM.2017.2652442

9. Yan H, Fan HH. Signal-selective DOA tracking for wideband cyclostationary sources. *IEEE Trans Signal Process* (2007) 55:2007–15. doi:10.1109/TSP.2007.893204

10. Chen W, Zhang W, Wu Y, Chen T, Hu Z. Joint algorithm based on interference suppression and Kalman filter for bearing-only weak target robust tracking. *IEEE Access* (2019) 7:131653–62. doi:10.1109/ACCESS.2019.2940956

11. Kong D, Chun J. A fast DOA tracking algorithm based on the extended Kalman filter. In: Proceedings of the IEEE 2000 National Aerospace and Electronics Conference (NAECON); October 2000; Dayton, OH, USA. IEEE (2000). p. 235–8. doi:10.1109/NAECON.2000.894916

12. Zhang B, Hou X, Yang Y. Robust underwater direction-of-arrival tracking with uncertain environmental disturbances using a uniform circular hydrophone array. *J Acoust Soc Am* (2022) 151:4101–13. doi:10.1121/10.0011730

13. Saucan AA, Chonavel T, Sintes C, Le Caillec JM. Marked Poisson point process PHD filter for DOA tracking. In: Proceedings of the 2015 23rd European Signal Processing Conference (EUSIPCO); September 2015; Nice, France. IEEE (2015). p. 2621–5. doi:10.1109/EUSIPCO.2015.7362859

14. Saucan AA, Chonavel T, Sintes C, Le Caillec JM. Track before detect DOA tracking of extended targets with marked Poisson point processes. In: Proceedings of the 2015 18th International Conference on Information Fusion (Fusion); July 2015; Washington, DC. IEEE (2015). p. 754–60.

15. Saucan AA, Chonavel T, Sintes C, Le Caillec JM. CPHD-DOA tracking of multiple extended sonar targets in impulsive environments. *IEEE Trans Signal Process* (2016) 64:1147–60. doi:10.1109/TSP.2015.2504349

16. Masnadi-Shirazi A, Rao BD. A covariance-based superpositional CPHD filter for multisource DOA tracking. *IEEE Trans Signal Process* (2018) 66:309–23. doi:10.1109/TSP.2017.2768025

17. Li G, Wei P, Li Y, Chen Y. A labeled multi-Bernoulli filter for multisource DOA tracking. In: Proceedings of the 2019 International Conference on Control, Automation and Information Sciences (ICCAIS); October 2019; Chengdu, China. IEEE (2019). p. 1–6. doi:10.1109/ICCAIS46528.2019.9074552

18. Zhao J, Gui R, Dong X. A new measurement association mapping strategy for DOA tracking. *Digit Signal Process* (2021) 118:103228. doi:10.1016/j.dsp.2021.103228

19. Yardim C, Michalopoulou ZH, Gerstoft P. An overview of sequential Bayesian filtering in ocean acoustics. *IEEE J Ocean Eng* (2011) 36:71–89. doi:10.1109/JOE.2010.2098810

20. Koteswara Rao S, Raja Rajeswari K, Lingamurty KS. Unscented Kalman filter with application to bearings-only target tracking. *IETE J Res* (2009) 55:63–7. doi:10.4103/0377-2063.53236

21. Leong PH, Arulampalam S, Lamahewa TA, Abhayapala TD. A Gaussian-sum based cubature Kalman filter for bearings-only tracking. *IEEE T Aero Elec Sys* (2013) 49:1161–76. doi:10.1109/TAES.2013.6494405

22. Orton M, Fitzgerald W. A Bayesian approach to tracking multiple targets using sensor arrays and particle filters. *IEEE Trans Signal Process* (2002) 50:216–23. doi:10.1109/78.978377

23. Qiu W, Li L, Lei P, Wang Z. Multiple targets tracking by using probability data association and cubature Kalman filter. In: Proceedings of the 2018 10th International Conference on Wireless Communications and Signal Processing (WCSP); October 2018; Hangzhou, China. IEEE (2018). p. 1–5. doi:10.1109/WCSP.2018.8555720

24. Li X, Willett P, Baum M, Baum M, Li Y. PMHT approach for underwater bearing-only multisensor–multitarget tracking in clutter. *IEEE J Oceanic Eng* (2016) 41:831–9. doi:10.1109/JOE.2015.2506220

25. Mahler RPS. Multitarget Bayes filtering via first-order multitarget moments. *IEEE T Aero Elec Sys* (2003) 39:1152–78. doi:10.1109/TAES.2003.1261119

26. Vo BN, Singh S, Doucet A. Sequential Monte Carlo methods for multitarget filtering with random finite sets. *IEEE T Aero Elec Sys* (2005) 41:1224–45. doi:10.1109/TAES.2005.1561884

27. Clark DE, Panta K, Vo BN. The GM-PHD filter multiple target tracker. In: Proceedings of the 2006 9th International Conference on Information Fusion; July 2006; Florence, Italy. IEEE (2006). p. 1–8. doi:10.1109/ICIF.2006.301809

28. Mahler R. A theory of PHD filters of higher order in target number. In: *Signal processing, sensor fusion, and target recognition XV. SPIE*, 6235. Orlando (Kissimmee) Florida, United States (2006). p. 193–204. doi:10.1117/12.667083

29. Mahler R. PHD filters of higher order in target number. *IEEE T Aero Elec Sys* (2007) 43:1523–43. doi:10.1109/TAES.2007.4441756

30. Vo BT, Vo BN, Cantoni A. Analytic implementations of the cardinalized probability hypothesis density filter. *IEEE T Signal Proces* (2007) 55:3553–67. doi:10.1109/TSP.2007.894241

31. Huang D, Leung H, Naser ES. Expectation maximization based GPS/INS integration for land-vehicle navigation. *IEEE Trans Aerosp Electron Syst* (2007) 43:1168–77. doi:10.1109/TAES.2007.4383607

32. Huang Y, Zhang Y, Xu B, Wu Z, Chambers JA. A new adaptive extended Kalman filter for cooperative localization. *IEEE Trans Aerosp Electron Syst* (2017) 54:353–68. doi:10.1109/TAES.2017.2756763

33. Sarkka S, Nummenmaa A. Recursive noise adaptive Kalman filtering by variational Bayesian approximations. *IEEE Trans Autom Control* (2009) 54:596–600. doi:10.1109/TAC.2008.2008348

34. Hartikainen SSJ. *Variational Bayesian adaptation of noise covariances in non-linear Kalman filtering* (2013). *arXiv* (2013). preprint arXiv:1302.0681. doi:10.48550/arXiv.1302.0681

35. Mohinder SG. *Kalman filtering: Theory and practice using MATLAB*. Hoboken, NJ: Wiley (2001).

36. O'Hagan A, Forster JJ. *Kendall's advanced theory of statistics: Bayesian inference*. London, U.K.: Edward Arnold (2004).

37. Huang Y, Zhang Y, Wu Z, Li N, Chambers J. A novel adaptive Kalman filter with inaccurate process and measurement noise covariance matrices. *IEEE Trans Autom Control* (2017) 63:594–601. doi:10.1109/TAC.2017.2730480

38. Bishop CM. *Pattern recognition and machine learning*. Berlin, Germany: Springer (2007).

39. Tzikas DG, Likas AC, Galatsanos NP. The variational approximation for Bayesian inference. *IEEE Signal Proc Mag* (2008) 25:131–46. doi:10.1109/MSP.2008.929620

40. Booth NO, Hodgkiss WS, Ensberg DE. *SWellEx-96 experiment acoustic data*. San Diego. UC San Diego Library Digital Collections (2015). doi:10.6075/J0MW2F21

41. Song Y, Hu Z, Li T, Fan H. Performance evaluation metrics and approaches for target tracking: A survey. *Sensors* (2022) 22:793. doi:10.3390/s22030793

42. Fortmann T, Bar-Shalom Y, Scheffe M. Sonar tracking of multiple targets using joint probabilistic data association. *IEEE J Oceanic Eng* (1983) 8:173–84. doi:10.1109/JOE.1983.1145560

frontiers | Frontiers in Physics

TYPE Original Research
PUBLISHED 13 March 2023
DOI 10.3389/fphy.2023.1109220

OPEN ACCESS

EDITED BY
Yuxing Li,
Xi'an University of Technology, China

REVIEWED BY
Adriano Todorovic Fabro,
Universidade de Brasilia, Brazil
Xing Chuanxi,
Yunnan Minzu University, China

*CORRESPONDENCE
Yaxiao Mo,
✉ moyaxiao1987@126.com

SPECIALTY SECTION
This article was submitted to Physical Acoustics and Ultrasonics, a section of the journal Frontiers in Physics

RECEIVED 27 November 2022
ACCEPTED 18 January 2023
PUBLISHED 13 March 2023

CITATION
Li X, Chen H, Lu H, Bi X and Mo Y (2023), A method of underwater sound source range estimation without prior knowledge based on single sensor in shallow water. *Front. Phys.* 11:1109220. doi: 10.3389/fphy.2023.1109220

A method of underwater sound source range estimation without prior knowledge based on single sensor in shallow water

Xiaoman Li[1], Hongyun Chen[1], Hongyu Lu[1], Xuejie Bi[1] and Yaxiao Mo[2]*

[1]Ocean College, Jiangsu University of Science and Technology, Zhenjiang, China, [2]Key Laboratory of Underwater Acoustic Environment, Institute of Acoustics, Chinese Academy of Sciences, Beijing, China

Introduction: The lack of prior knowledge of the marine environment increases the difficulty of passive ranging of underwater sound sources by using a single hydrophone. The dispersion curve of the normal mode contains extensive marine environmental information, which can be extracted without prior knowledge, but the characteristics of dispersion curves of different modes vary, and the mode order cannot be determined from the received data.

Methods: Herein, a method based on a single hydrophone that can jointly identify the mode order and estimate the propagation range in unknown marine environment is proposed. The method uses Bayesian theory as the main methodology and is applicable to broadband pulse sound sources in shallow seas with long-range propagation. The dispersion curves extracted from the data and those calculated by the dispersion formula are the input signal and the replica of the methods, respectively. Accurate identification of the normal mode order and estimation of the propagation range can be achieved by establishing the joint cost function.

Results: In the case of unknown *a priori* knowledge of the marine environment, the method enables rapid inversion, is tolerant to environmental parameter mismatch, and is low cost and practical.

Discussion: The simulation and measured data analysis results demonstrate the accuracy and validity of the method. The measured data contains linear frequency modulation impulse source signal and explosion sound source signals, and the mean relative error of range estimation is less than 5%.

KEYWORDS

shallow water waveguide, normal mode order identification, range estimation, Bayesian inversion theory, without prior knowledge

1 Introduction

Multipath and dispersion are important characteristics of shallow water waveguides, and the study of dispersion characteristics is very important in the field of underwater acoustics. The received signal is a superposition of multiple-order normal modes when a broadband pulsed sound propagates in a shallow sea, and the amplitude and phase of the signal also change, thus increasing the difficulty of signal processing [1].

The passive ranging of underwater sound sources is aimed at estimating the propagation range on the basis of extracted environmental information by processing the received signal when the location of the source is unknown. This research is of great importance in national

defense applications and in marine biolocation. However, most existing methods rely on sensor arrays [2, 3], which are not only costly but also yield ranging results with high uncertainty, because the arrays are susceptible to the influence of the water environment. Ranging methods based on a single hydrophone have been proposed to address the shortcomings of array-based ranging methods [4–7]. The feature extraction of underwater acoustic signal mostly depends on ship radiated noise [8–10]. However, the close association of dispersion characteristics and the characteristics of each mode with the marine environment provides possibilities for analyzing the structure and extracting the environmental parameters [7]. The dispersion curves are widely used in the passive ranging of single hydrophones for broadband pulsed sources. After analyzing the received signals, the information on the ocean environment, source location, and Eigen functions contained in the dispersion characteristics are effectively used to achieve the inversion of the ocean environmental parameters in shallow waveguides [11–13]; the estimation of the speed of sound profile (SSP) in water [14]; as well as the passive localization of a variety of broadband impulse sources, such as light bulb sources [15], dolphin calls [16], and explosion sources [17, 18]. However, all of the above methods require some or all of the *a priori* knowledge of the marine environment to obtain accurate ranging results, which is very difficult for a practical application.

Combining the extracted dispersion curves and Bayesian estimation theory to achieve sound source ranging can reduce the reliance on *a priori* knowledge of the marine environment [19–21], However, the method based on the dispersion characteristics has two conditions for application: *a priori* knowledge of the marine environment and the determined order of the normal modes. The characteristics of dispersion curves of different modes vary. Mode order identification is the basis for underwater engineering applications using dispersion curves. Factors such as the SSP (the sound speed profile) in water, the geoacoustic structure, and the location of the source/receiver can affect the propagation of the sound signal and consequently lead to some normal modes being missed in the received signal. Separating the modes from measured data can be accomplished through a warping transform [11], and signal faults can be observed in the spectrogram results of warped signals; however, directly identifying the mode order remains impossible, thus it is important to find a method to effectively identify the normal modes.

Identification of normal mode order can be achieved on the basis of the conventional beamforming of a horizontal line array [22]. The dispersion curves extracted by warping transform are used as the input signal, according to Bayesian theory, while the replica is calculated with the acoustic field model. Subsequently, the joint estimation of mode order and environmental parameters can be performed [23]. However, the calculation of the replica requires multiple environmental parameters regarding the water as well as the bottom. Too many inversion parameters reduce the inversion efficiency, and correlations between parameters increase the error. A inversion scheme that does not require mode identification is thus proposed.

The feature of this study is the identification of normal modes and source ranging effectively without *a priori* knowledge of the marine environment. Bayesian inversion theory has good tolerance for marine environmental parameters, and all unknown marine environmental parameters can be used as inversion parameters for inversion. The input function and replica are two important components of the Bayesian inversion methodology. This study differs from previous inversion work because the input function is easy to obtain and the replica is efficiently calculated. In the method described herein, the dispersion curves of normal modes with high energy and good energy focus are used as the input signal, and the replica is obtained from the dispersion formula. The computational speed of the replica affects the efficiency of the entire inversion process. For shallow environments in which the speed of sound on the seabed is higher than that in water, the bottom features can be approximated according to the bottom reflection phase shift parameter P for SRBR (surface-reflected-and-bottom- reflected) modes in the case of small angle incidence.

The dispersion formula can be obtained with four parameters. Therefore, for SRBR normal modes, the dispersion curve of the mode calculated by the dispersion formula is valid. Under the condition of unknown *a priori* knowledge of the ocean, when the replica is obtained with the dispersion formula, the number of inversion parameters is reduced, the errors caused by the coupling of environmental parameters are effectively avoided, and the inversion efficiency is improved.

The method is applied to the data measured from the South China Sea in October 2014 and the Yellow Sea of China in December 2018. The method provides a reliable estimate of the propagation range of the sound source.

2 Materials and methods

2.1 Modal propagation theory

In a shallow water waveguide, consider a broadband pulsed sound source S(f), located at depth z_s. The signal is received by a hydrophone located at depth z_r after a propagation range r. The received signal can be can be expressed as the sum of multi-order normal modes [24]:

$$\boldsymbol{pre}_f(\boldsymbol{f},\boldsymbol{r}) \approx \boldsymbol{S}(\boldsymbol{f})\sum_{n=1}^{N}\sqrt{\frac{2\pi}{\xi_n \boldsymbol{r}}}\boldsymbol{U}_n(\boldsymbol{z}_s)\boldsymbol{U}_n(\boldsymbol{z}_r)\boldsymbol{e}^{\boldsymbol{j}\left(\xi_n \boldsymbol{r}+\frac{\pi}{4}\right)} \tag{1}$$

where n is the normal mode order, and ξ_n is the horizontal wavenumber. The traveling wave characteristic of the normal mode in the direction of horizontal propagation range r is determined by $e^{j(\xi_n r+\frac{\pi}{4})}$, whereas the characteristic in the standing wave direction is determined by the Eigen function $U_n(z)$. Different modes show variations in the depth z direction. For the ideal shallow water waveguide, for example, the surface is a free-release boundary, and the seabed is a horizontal rigid boundary. The Eigen function can be expressed as:

$$\boldsymbol{Z}_n(\boldsymbol{z}) = \sin\left[\left(\boldsymbol{n}-\frac{1}{2}\right)\frac{\pi}{\boldsymbol{H}}\cdot\boldsymbol{z}\right] \tag{2}$$

From Eq. 2, when the depth of water is H, the normalized amplitude of the first 5-order normal modes varies with z, as shown in Figure 1.

As shown in Figure 1, the Eigen function of the normal mode has n points with zero energy value in the depth direction, and this point is called a node. The energy of the mode signal of each order in the received data varies with the source/receiver depth configuration. When the source/reception depth is just near the node, the modal excitation is insufficient and subsequently disappears. Marine environmental factors affect the propagation characteristics of normal modes. Therefore, the

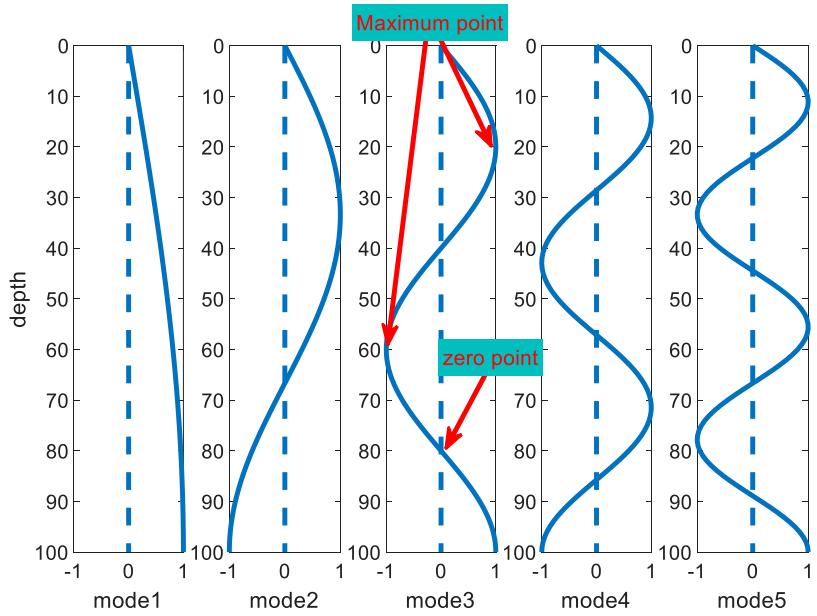

FIGURE 1
Normalized amplitude distribution of normal modes with depth.

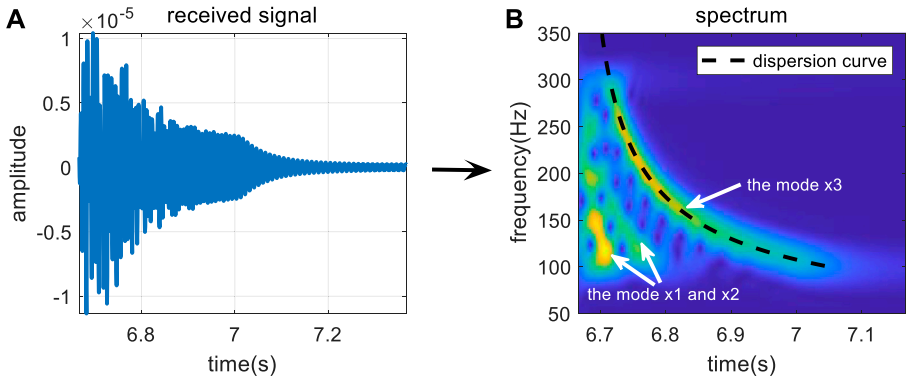

FIGURE 2
The received signal **(A)** in the time domain and **(B)** time-frequency domain.

mode contains a large amount of oceanographic information and is widely applied in underwater engineering. The analysis of normal mode characteristics is important in performing the inversion of geoacoustic parameters and source localization. However, the mode order cannot be determined directly from the received data, and the use of time-frequency analysis (TFA) and warping transform provides convenience in research.

The energy variation in normal modes can be observed through the TFA technique. Figures 2A, B show the received signal in the time domain and time–frequency domain after TFA for a broadband pulsed sound source in the frequency band of 100–300 Hz propagating for 10 km in a Pekeris waveguide. The environmental parameters are as follows: depth $H = 100$ m, SSP in water $c_0 = 1500$ m/s, depth of the sound source $z_s = 28$ m at the node of mode 4, seabed speed of sound $c_b = 1800$ m/s, and density $\rho_b = 1.6$ g/cm^3.

Figure 2A shows the total propagation characteristics of multi-order normal modes, which cannot reflect the characteristics of a single mode. However, multiple normal modes with higher energy can be seen in Figure 2B. Because the order of each mode cannot be determined directly, the order is assumed to be x1, x2, x3, ..., and xn. The energy of the normal mode is gathered in a curve associated with time and frequency (e.g., the black dotted line corresponding to the x3 order mode in Figure 2B), which is called the dispersion curve. The dispersion curves not only describe the energy variation characteristics of normal modes but also contain information on the marine environment. The characteristics of dispersion curves of different modes vary, and determining these characteristics is equivalent to obtaining multiple sets of data containing information about the environment in the case of one receiver.

2.2 Dispersion curve

Dispersion characteristics are very important aspects of shallow water waveguides. The dispersion characteristics can be explained by the group velocity and phase velocity, which are associated with the order of the normal mode and vary with frequency. The group velocity and phase velocity can be written as:

$$v_n^g = \frac{2\pi\partial f}{\partial \xi_n} \quad v_n^p = 2\pi f \Big/ \xi_n \tag{3}$$

The different group velocity of each mode leads to different arrival times; therefore, the dispersion curve is a function of time and frequency. The dispersion curve of mode n can be written as:

$$t_n(f) = \frac{r}{v_g^n(f)} = \frac{r\partial\xi_n}{\partial(2\pi f)} \tag{4}$$

The energy of the mode varies with the dispersion curve, according to the mode order n, propagation range, and horizontal wavenumber ξ_n. Therefore, using dispersion curves is favorable for source ranging.

2.2.1 The dispersion formula

In Beam-Displacement Ray-Mode (BDRM) theory, when a sound source with a small grazing angle propagates in a waveguide where the speed of sound of the seabed is larger than that in water, the dispersion curve of the SRBR normal mode can also be calculated with the dispersion formula [25]:

$$f_n(t) \approx \frac{n\pi c_0 t}{2\pi H\sqrt{t^2 - (r/c_0)^2}} - \frac{Pc_0}{4\pi H} - \frac{Pr}{4\pi H t^2 c_0} \tag{5}$$

where the P is the bottom reflection phase shift parameter, which is a quantity associated with the seabed parameter, expressed as:

$$P \approx \frac{\sqrt{2}\rho_2 \Big/ \rho_1\sqrt{\sqrt{\left(1-(c_0/c_b)^2\right)^2 + (c_0/c_b)^2\frac{\alpha c_b}{2\pi f}} + 1 - (c_0/c_b)^2}}{\sqrt{\left(1-(c_0/c_b)^2\right)^2 + (c_0/c_b)^2\frac{\alpha c_b}{2\pi f}}} \tag{6}$$

where ρ_1, ρ_2, c_b, and α are the water density, seabed density, and seabed absorption, respectively. According to Eq. 6, the P is a frequency-dependent quantity. However, when the attenuation of the seabed is minor, and the frequency exceeds 10 Hz, the effect of frequency on P can be neglected, and Eq. 6 can be simplified to:

$$P \approx \frac{2\rho_2}{\rho_1\sqrt{1-(c_0/c_b)^2}} \tag{7}$$

The inversion efficiency can be improved by reducing the number of inversion parameters by describing the bottom properties with parameter P. Moreover, the dispersion curve can be calculated more rapidly by using the dispersion formula compared with the sound field model (e.g., KRAKENC) [26].

According to the above, the dispersion curves of each order of simple positive waves can be calculated with Eq.5 and 6, when the parameters of the marine environment are known. KRAKENC is a more mature model for acoustic field calculation; therefore, the dispersion curves obtained by KRAKENC according to Eq. 5 are used as the reference curves.

However, the dispersion curves obtained with the dispersion formula Eq. 5 do not contain frequencies lower than Ariy frequency (Ariy frequency: The frequency corresponding to the minimum value of the group velocity of the normal mode). It is also an important part of our future work to obtain dispersion formulas that can calculate complete dispersion curves.

2.2.2 Extraction of dispersion curves

In practical applications, detailed environmental parameters are difficult to obtain, and the dispersion curves can be extracted through analysis of the received signals. The combination of time-frequency analysis techniques, warping transform, modal filtering, and ridge extraction techniques can achieve accurate extraction of dispersion curves in measured data.

The warping transform can transform the time domain signal $pre_t(r,t)$ (the time domain result of $pre_f(f,r)$) by a time transformation factor $h(t) = \sqrt{t^2 + (r/c_0)^2}$, thereby transforming the sound pressure signal into a superposition of multiple single frequency signals to achieve effective separation of different normal modes. The modal filtering technique can then be used to extract normal modes.

The extracted modes are inverted with the inverse warping operator $h(t) = \sqrt{t^2 - (r/c_0)^2}$, and finally the dispersion curve of each mode is extracted with techniques such as ridge extraction. In the above process, two parameters are used: the propagation distance r and the speed of sound in seawater c0. Because the warping transform is invertible, the two parameters are process quantities, and the final results are not dependent on the accuracy of the two parameters. However, the arrival time of each normal mode must be accurate, and great care must be taken in processing the received signal [27].

The above process can be described by the simulation results in the Pekeris waveguide, with the same simulation environment as in the previous section, taking the example of extracting the dispersion curve of normal mode x3.

In the spectrogram of the received signal shown in Figure 3A, the energy of mode ×3 is strong, thus facilitating its extraction. The received signal contains at least 5th-order normal modes, but the energy of different-order modes varies, and the energy of mode four is weak and appears blurry in Figure 3B. Mode x3 is extracted after modal filtering and unwarping transform, and the spectrogram and extracted dispersion curve of modal x3 are shown in Figures 3C, D, respectively.

The dispersion formula Eq. 5, data-extraction and theoretical calculation based on an acoustic model are three methods for calculating the dispersion curve. The accuracy of the calculated results is verified by comparing with the results from KRAKEN, used as reference value. The simulation analysis is performed in the Pekeris waveguide and the waveguide with a thermocline, respectively, whose simulation parameters are shown in Figure 4. The propagation range of source is r = 5 km, and the broadband of source is 100–200 Hz, the sampling rate is f_s = 1 kHz, the spectrum of the received signal is obtained by the short-time Fourier transform (STFT). The spectrum information is illustrated in Figure 3, where the information of RGB is given. The locations of the source and receiver, and the seabed environment are the same as in the Pekeris waveguide, but the speed of sound in water has a thermocline at 20–40 m. The difference between the speed of sound at the surface and the seabed is 9 m/s, and the source is located in the thermocline. Figure 5A and Figure 5B show the TFA results of the received signal in the two waveguides and the dispersion curves calculated with the three methods, respectively.

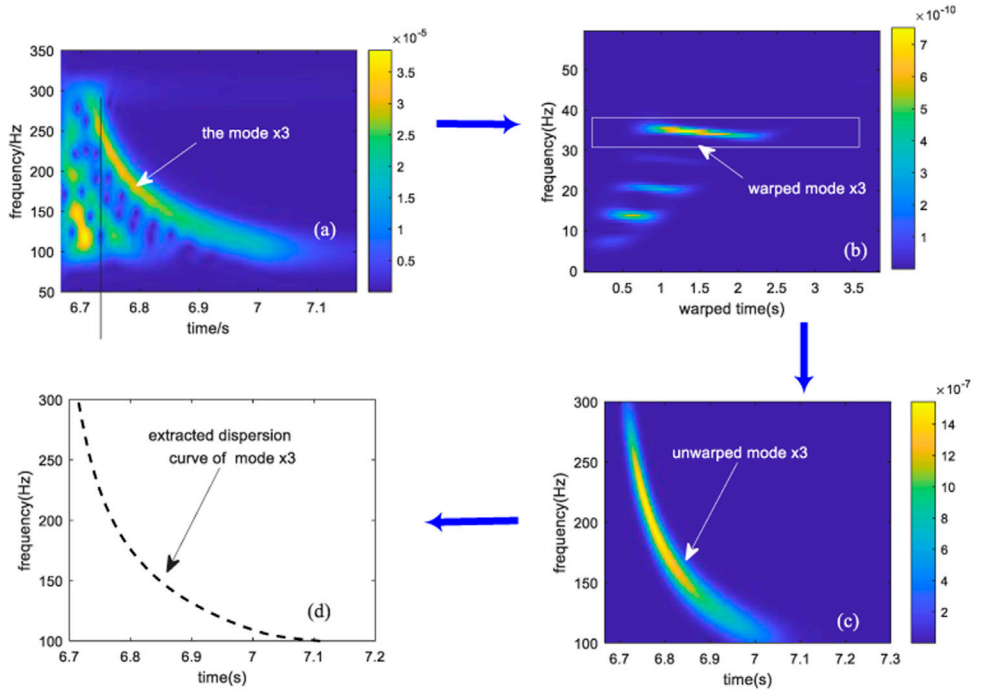

FIGURE 3
Structure of dispersion curve extraction: **(A)** spectrogram of the received signal; **(B)** spectrogram of the warped signal; **(C)** spectrogram of mode x3; **(D)** dispersion curve of mode x3.

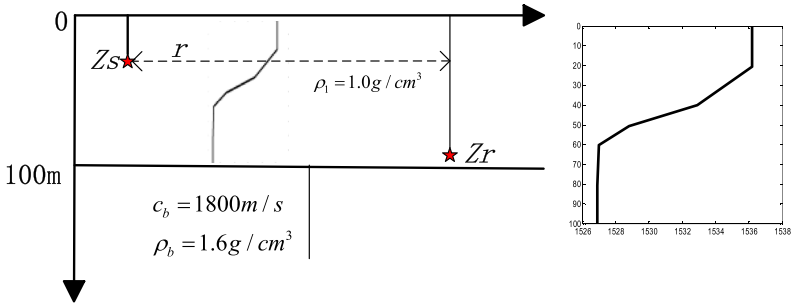

FIGURE 4
Parameters in a thermocline waveguide.

Figure 5 shows that the dispersion curves obtained through the three methods match well in the Pekeris waveguide, and are consistent with the mode energy change trend. In a thermocline waveguide, the dispersion curves extracted from data and calculated with Eq. 5 are consistent, but the low order normal modes do not fully conform to the characteristics of SRBR normal modes, and the consistency is poor. The results of the extracted dispersion curves, particularly the high energy modes, represent the energy variation trend of each mode and can be used in underwater applications.

In addition, Figure 5A shows that the mode order corresponding to the higher energy modes (modes x1, x2, and x3) in the received signal are 2, 3, and 5. The properties of the dispersion curves correspond to the mode order, and the accurate identification of the extracted modes is key to the passive ranging of sources by using the dispersion curves in the case of unknown marine environmental parameters. However, the identification of the modes in the case of unknown *a priori* knowledge presents the following difficulties.

1) Because of the weak intensity of the first-order mode, the first mode that can be detected in the TFA results of the received signal is not necessarily the true first-order normal mode.
2) The depth configuration of the source/receiver results in weak energy of several modes in the signal, but the number of missing modes cannot be determined, and thus the remaining mode orders cannot be determined.
3) When the frequency is high, the group velocity of two modes tends to be close to the speed of sound in water, the arrival times of the two modes are close, and the two modes are easily mixed into the same mode, thus making the identification of the mode order difficult.

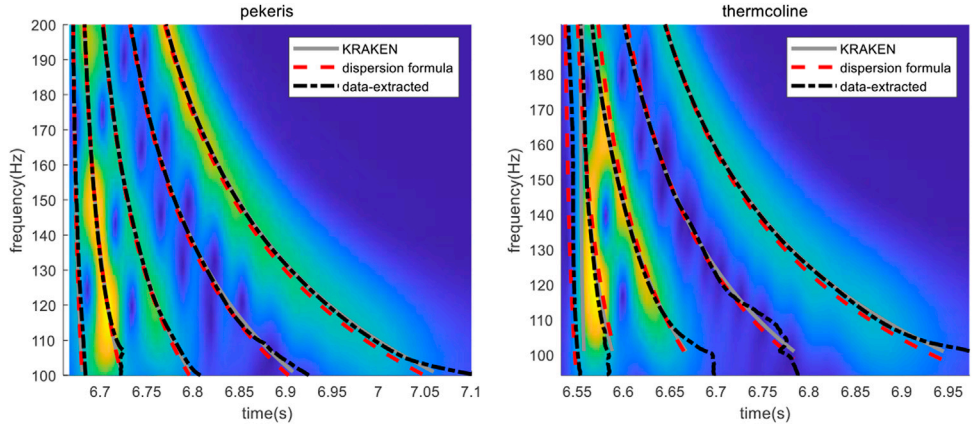

FIGURE 5
Dispersion curves calculated with different methods **(A)** in the Pekeris waveguide and **(B)** a thermocline waveguide.

2.3 The joint estimation algorithm

Under the condition of unknown prior knowledge, Bayesian theory is tolerant to environmental parameter mismatch and has a wide application in the passive location of underwater sound sources. In Bayesian theory, the joint inversion of mode order and source propagation range can improve the inversion efficiency. Therefore, a joint estimation method of normal mode order and range of underwater source is presented.

2.3.1 Bayesian inversion theory

The posterior probability density (PPD) of the parameters to be inverted is used as the estimation result, in an important feature of Bayesian theory. The PPD is associated with the conditional probability density of measured data $P_{ro}(\mathrm{d}\,|\,\mathrm{m})$ and the prior distribution of $\mathbf{m}$ and $\mathbf{d}$, $P_{ro}(\mathrm{m})$ and $P_{ro}(\mathrm{d})$, and the PPD can be written as [28]:

$$\boldsymbol{P_{ro}}(\mathbf{m}\,|\,\mathbf{d}) = \boldsymbol{P_{ro}}(\mathbf{d}\,|\,\mathbf{m})\boldsymbol{P_{ro}}(\mathbf{m})/\boldsymbol{P_{ro}}(\mathbf{d}) \tag{8}$$

where $\mathbf{m}$ is a vector of inversion parameters with length M, and $\mathbf{d}$ is the parameter vector of measurement data. In general, $P_{ro}(\mathrm{m}\,|\,\mathrm{d})$ a is positively correlated with the likelihood function $L(\mathrm{m})$, so $P_{ro}(\mathrm{m}\,|\,\mathrm{d})$ is:

$$\boldsymbol{P_{ro}}(\mathbf{m}\,|\,\mathbf{d}) \propto \boldsymbol{L}(\mathbf{m})\boldsymbol{P_{ro}}(\mathbf{m}) \tag{9}$$

The likelihood function $L(\mathrm{m})$ can be represented by the misfit function $E(\mathrm{m})$, as shown in the following equation:

$$\boldsymbol{L}(\mathrm{m}) = \boldsymbol{P_{ro}}(\mathrm{d}\,|\,\mathrm{m}) \propto \mathbf{exp}[-\boldsymbol{E}(\mathrm{m})] \tag{10}$$

Furthermore, where E(m) is the data matching function, a generalized misfit combining data and prior can be defined as

$$\boldsymbol{\varphi}(\mathbf{m}) = \boldsymbol{E}(\mathbf{m}) - \ln \boldsymbol{P_{ro}}(\mathbf{m}) \tag{11}$$

The $\varphi(\mathrm{m})$ is also known as the cost function. According to Eq.10 and Eq.11, the $P_{ro}(\mathbf{m}\,|\,\mathbf{d})$ can also be expressed as

$$\boldsymbol{P_{ro}}(\mathbf{m}\,|\,\mathbf{d}) = \frac{\mathbf{exp}[-\boldsymbol{\varphi}(\mathbf{m})]}{\int \mathbf{exp}[-\boldsymbol{\varphi}(\mathbf{m}',\mathbf{d})]d\mathbf{m}'} \tag{12}$$

To decrease the difficulty in calculating the integral in the above equation, the principle for parameter estimation is the maximum *a posteriori* (MAP). The inversion parameter values can initially be determined through the optimization search algorithm. The optimal value of a set of inversion parameters is obtained when the maximum likelihood function is maximal.

$$\hat{\mathbf{m}} = \boldsymbol{Arg}_{\ \min}\{\boldsymbol{L}(\mathbf{m})\} = \boldsymbol{Arg}_{\ \min}\{\boldsymbol{\varphi}(\mathbf{m})\} \tag{13}$$

The uncertainty of the inversion parameters is characterized by the one-dimensional marginal probability distribution of the parameters

$$P_{ro}(m_i\,|\,\mathbf{d}) = \int \delta\left(m_i' - m_i\right)P_{ro}(\mathbf{m}'\,|\,\mathbf{d})d\mathbf{m}' \tag{14}$$

Where m_i refers to the ith inversion parameter。

2.3.2 The joint cost function

As described above, the cost function can be derived from a likelihood function, which is key to achieving parameter estimation. The input function and the replica are two important components of the likelihood function. The dispersion curve F_n^m extracted from the data is taken as the input function, and the replica F_n^c is calculated with Eq. 5. The results in Figure 5 confirm the feasibility of calculating the replica with Eq. 5. If the data error satisfies a Gaussian distribution, the likelihood function is:

$$\boldsymbol{L}(\mathbf{m},\boldsymbol{r}) = \prod_{n=1}^{N}\frac{\mathbf{exp}\left\{-\frac{1}{2}\left(\mathbf{F}_n^m - \mathbf{F}_{nr}^c\right)^T\mathbf{C}_n^{-1}\left(\mathbf{F}_n^m - \mathbf{F}_{nr}^c\right)\right\}}{(2\pi)^{M_n/2}|\mathbf{C}_n|^{1/2}} \tag{15}$$

where $\sum_{n=1}^{N} n = N$ is the number of extracted dispersion curves, does not represent the exact order n of normal mode, and M_n is the length of the data. $\mathrm{C}_n = \upsilon_n\mathbf{I}$ is the covariance matrix, and υ_n and $\mathbf{I}$ are the unknown variance and the identity matrix, respectively. Therefore, the likelihood function is:

$$\boldsymbol{L}(\mathbf{m},\boldsymbol{r}) = \prod_{n=1}^{N}\frac{1}{(2\pi\boldsymbol{\upsilon}_n)^{1/2}}\mathbf{exp}\left\{-\frac{1}{2\boldsymbol{\upsilon}_n}\left(\mathbf{F}_n^m - \mathbf{F}_{nr}^c\right)^2\right\} \tag{16}$$

let $\frac{\partial L}{\partial \upsilon_n} = 0$, then υ_n is

$$\hat{\boldsymbol{\upsilon}}_n = \left|\mathbf{F}_n^m - \mathbf{F}_{nr}^c\right|^2/\boldsymbol{M}_n \tag{17}$$

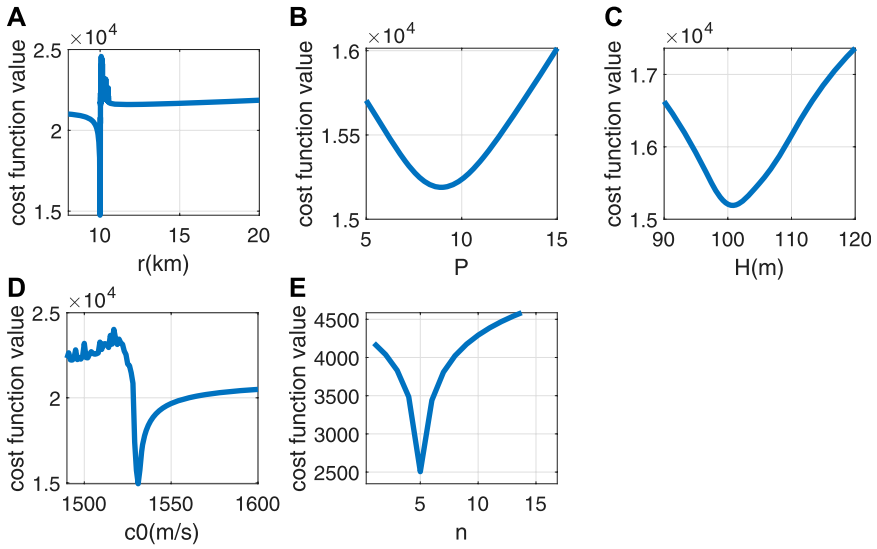

FIGURE 6
Sensitivity analysis results.

the cost function is:

$$\boldsymbol{\varphi}(\mathbf{m}, \boldsymbol{nr}) = \frac{1}{2}\sum_{n=1}^{N} \boldsymbol{M}_n \ln\left(\left|\mathbf{F}_n - \mathbf{F}_{nr}^{c}\right|^2\right) \tag{18}$$

In the absence of prior knowledge of the environment, the true order of mode n must be determined simultaneously, on the basis of the assumption that the true order is *nr* Therefore, each set of data also must satisfy:

$$\boldsymbol{\varphi}_n(\boldsymbol{nr}) = \frac{1}{2}\sum_{nx=1}^{Nx} \boldsymbol{M}_n \ln\left(\left|\mathbf{F}_n^{m} - \mathbf{F}_{nx}^{c}\right|^2\right) \tag{19}$$

where $nx \in [1, Nx]$ is the range of normal mode numbers, and N_x is sufficiently large to exceed the maximum order of modes obtained from the received data, thus ensuring the accuracy of the numerical determination.

Eq. 18 and Eq. 19 affect each other, and the order determination takes precedence over the parameter inversion in the optimization search process. After the order of normal mode numbers of the *n*th data set is determined by Eq. 19, the *n*th data set is then used to perform the parameter search and inversion according to Eq. 18. The optimal solution of the parameters is substituted into Eq. 12 to obtain the PPD of each inversion parameter, and then the effective inversion of the parameters is achieved. The Genetic Algorithm is used as a method of parameter search for optimization.

According to Eq. 5, the calculation of the replica in an unknown ocean environment requires the depth *H*, average speed of sound c_0, bottom reflection phase shift parameter P, and range *r*. Herein, the above four parameters are estimated jointly with the mode order.

2.3.3 Sensitivity analysis

The sensitivity of the four parameters to be inverted is analyzed in the waveguide with a thermocline. The simulation environment is shown in Figure 4. To fully verify the validity of the method for the mode order identification, the depth of the receiver is at the node of mode 5, which is also near the node of mode 2; i.e., theoretically the received signal has low energy of modes 5 and 2.

The input function is the dispersion curves extracted from the data, and the rest of the parameters are taken as true values when sensitivity analysis is performed for one parameter. The analysis results are shown in Figures 6A–E.

Figure 6 shows that the four inversion parameters are sensitive to the cost function. Compared with other parameters, the value cost function curve of *r* varies more sharply around the true value, thus fully demonstrating the sensitivity of the range to the cost function and the accuracy of inversion. The dispersion curve data of mode 5 from the received signal are selected to analyze the sensitivity of the normal mode order *n*. Figure 6E indicates that the cost function has the smallest value at the true order of the mode, thus indicating the validity of the cost function.

In addition, for a more adequate analysis of the validity of the cost function, two-dimensional correlations of inversion parameters are analyzed. The two parameters to be analyzed vary within the search interval, and the remaining parameters are taken as true values. The true values of the two parameters are marked with a white star. Figure 7 shows that the correlation between the range *r* and other parameters is low, with a nearly straight line at r_0, thus indicating that *r* plays a major role in the influence of the cost function with high sensitivity. However, the correlation between P and *H* is high, the correlation between c_0 and *H* gradually decreases with depth, and the speed of sound gradually dominates. Parameter coupling caused by correlation between parameters affects the accuracy of the inversion results. However, as shown in Figure 7, the parameter coupling does not affect the sensitivity of *r*. Comprehensively, the four inversion parameters and mode order have high sensitivity to the joint cost function.

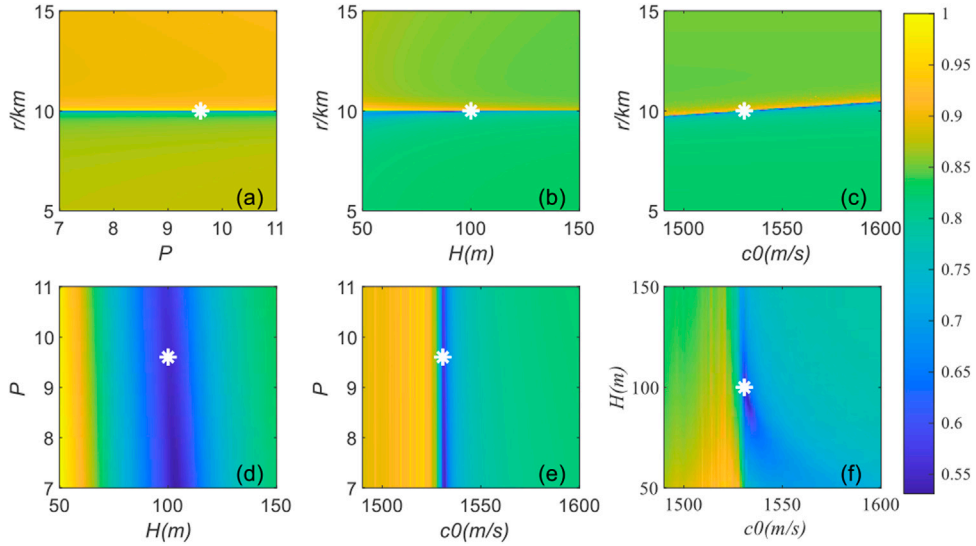

FIGURE 7
Sensitivity analysis results of the two parameters.

TABLE 1 Inversion parameter list.

Parameter	Reference value	Search bound	Inversion value	Error/%
r (km)	10	[8,20]	9.88	−0.12
P	6.0819	[5 15]	6.38	4.96
H(m)	100	[50,180]	96.74	−3.26
c_0 (m/s)	1530.7	[1600,2000]	1514.1	−1.08
Nr	[3 4 6 7 8]	[1,30]	[3 4 6 7 8]	0

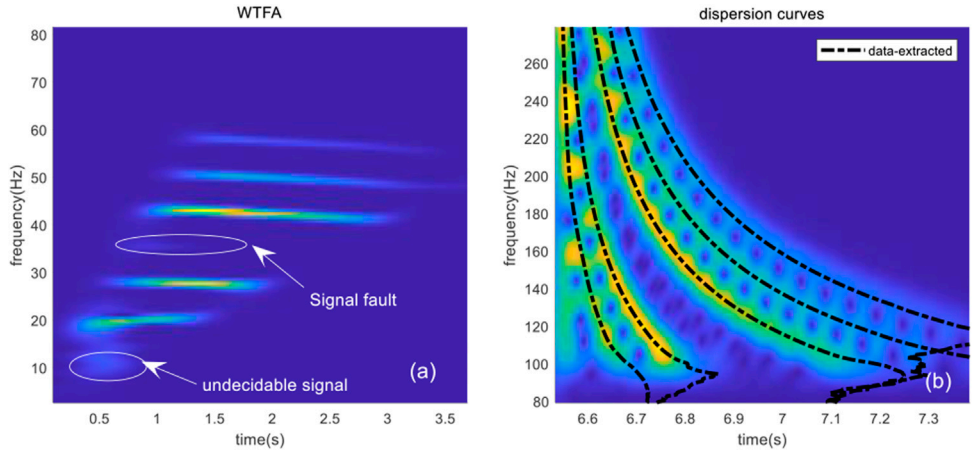

FIGURE 8
Received data: **(A)** spectrogram of the warped signal; **(B)** TFA results of the received data and the extracted dispersion curves.

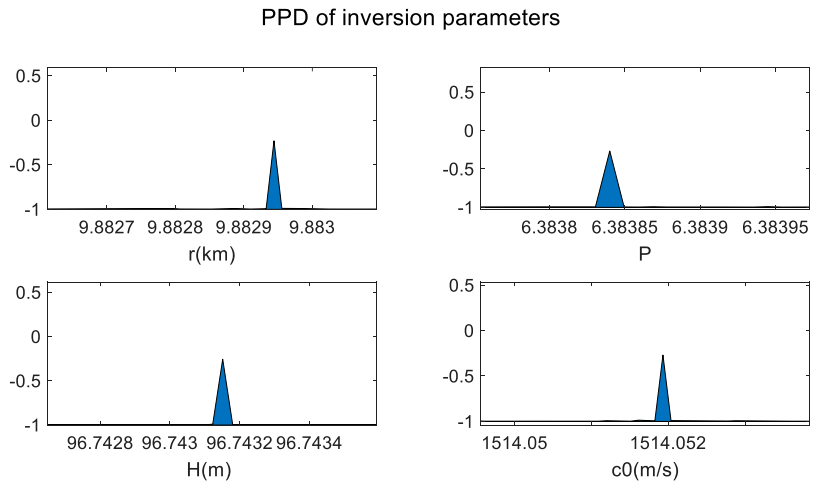

FIGURE 9
The 1-D MPD of inversion parameters.

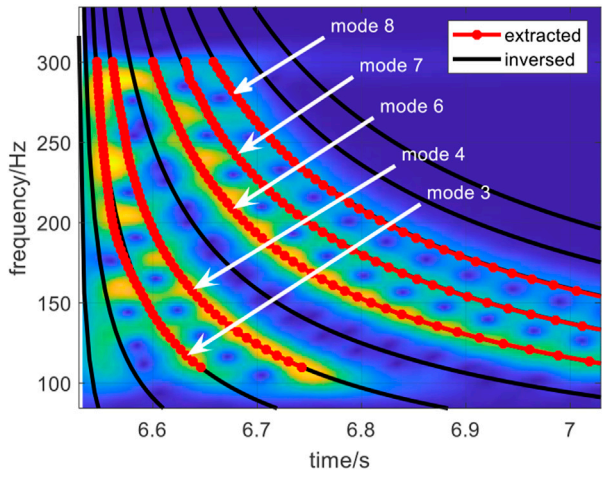

FIGURE 10
Mode determination results and dispersion curve comparison results.

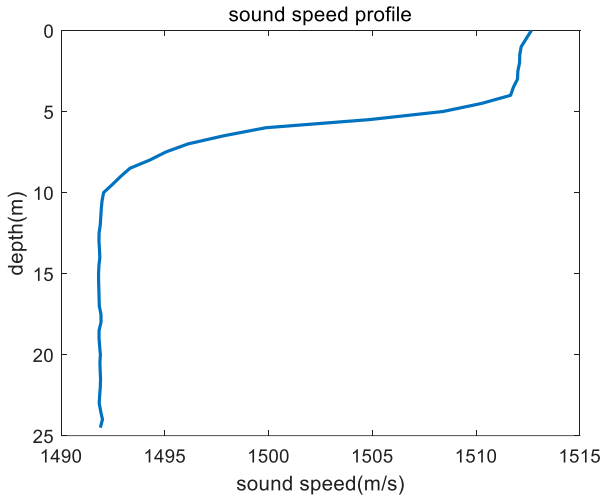

FIGURE 11
Sound speed profile of data 1.

3 Results

3.1 Theoretical simulation

The simulation environment is shown in Figure 4. When r = 10 km, the sound source is set at the node of mode 5, and the search interval of inversion parameters is shown in Table 1. The spectrogram results of the received signal and warped signal are shown in Figure 8A and Figure 8B. Five normal modes have higher energy in the received signal, and their dispersion curves can be chosen as the input signals to the inversion methods, as indicated by the black dashed line in Figure 8B.

As shown in Figure 8A, the received data contain two missing modes, thus preventing determination of the position of the first mode and the number of modes at the signal fault, and hindering accurate reversal of the parameters and determination of mode orders.

When the dispersion curve is extracted, the normal modes with high energy and good aggregation are the primary choice, and the frequency band of each mode larger than the Ariy frequency is chosen (the dispersion curve will have an inflection point at the Ariy frequency), and the extracted dispersion curves are the input function for parameter search. The convergence speed of all four parameters is very fast, and the time required for a 3,000 times optimization search is less than 3 min. Therefore, an improvement in the efficiency of the inversion method has been achieved.

Figure 9 shows the one-dimensional marginal probability densities (1-D MPD) of the parameters, which is calculated from the optimal values of the parameter search Figure 9 shows no clear side flap interference in the 1-D MPD of the four parameters, and the optimal search results are globally optimal. The one-dimensional MPD maximum of the inversion parameters is taken as the inversion result, as shown in Table 1.

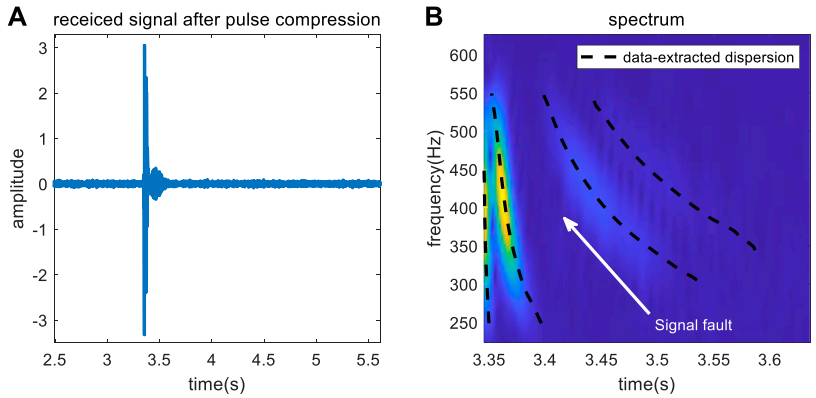

FIGURE 12
(A) Received data; **(B)** TFA of the warped signal.

TABLE 2 Inversion parameter list of measured data 1.

Parameter	Reference value	Search bound	Inversion value	Error/%
r (km)	4.96	[3,10]	5.00	0.008
P	6.33	[3,8]	5.01	−20.8
H(m)	24.5	[20,50]	26.54	2.04
c_0 (m/s)	1497	[1490,1550]	1499.2	0.002
Nr	—	[1,30]	[1,2,4,5]	0

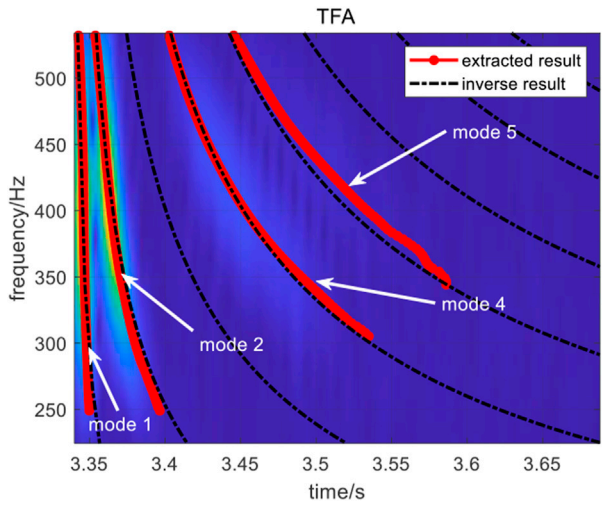

FIGURE 13
Mode determination results and dispersion curve comparison results of data 1.

As shown in Table 1, the results of the mode determination are accurate, and the numbers of extracted modes are 3, 4, 6, 7, and 8, in agreement with the low energy of modes 2 and 5 when the source is located at the node of mode 5 and near the node of mode 2. At this time, t, a possibility exists that mode 1 is also unexcited, owing to the existence of a thermocline in the water of the simulated environment. The error of r is 0.12%, thus indicating that the estimation result is accurate and reliable. Although the coupling between P and H causes the estimation errors for these two parameters to be much higher than r, the errors for all parameters are within 5%, which fully demonstrates the feasibility of the method proposed herein.

This work mainly considers the estimation of the propagation range, and the estimation errors of other parameters do not affect the estimation results of the range, thus demonstrating that the method has strong environmental adaptability.

Figure 10 provides the results of the mode order identification, and the results of comparing the dispersion curves obtained from the inversion parameters and Eq. 5 with the dispersion curves obtained from data and the spectrogram of the received signal. The findings demonstrate not only that the mode order identification results are accurate but also that the inversed dispersion curves match the results obtained through other methods, thus indicating the accuracy and validity of the joint estimation.

3.2 Experimental data analysis

Two sets of experimental data are selected for analysis to fully illustrate the validity of the method. The first set of experimental data was gathered in the South China Sea in October 2014, and the sound source was a broadband LFM signal; the second set of experimental data was obtained in the Yellow Sea of China in

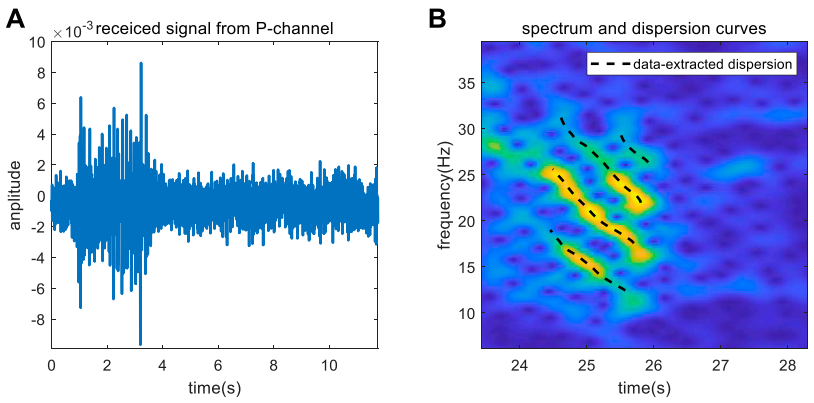

FIGURE 14
(A) Received data; **(B)** Dispersion curves selected as input signal.

TABLE 3 Inversion parameter list of measured data 2.

Parameter	Reference value	Search bound	Inversion value	Error/%
r (km)	35.12	[30,40]	35.21	0.26
P	5.43	[3,8]	5.18	−4.6
H(m)	350	[300,400]	344.45	−1.58
c_0 (m/s)	1460	[1450,1550]	1465.7	0.39
Nr	—	[1,30]	[3 4 5 6]	—

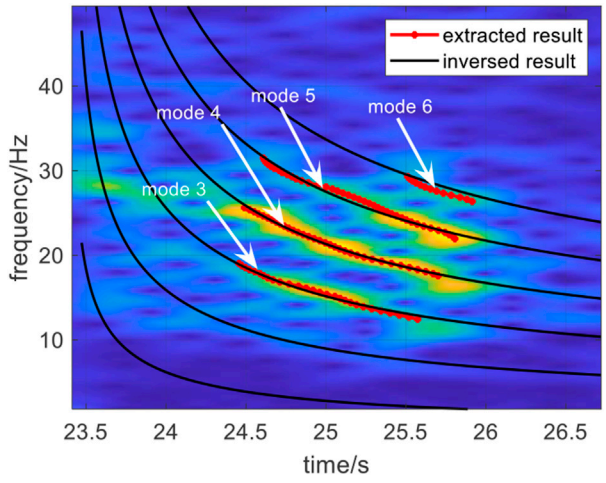

FIGURE 15
Mode determination results and dispersion curve comparison results of data 2.

December 2018, and the sound source was an explosion sound signal. The two sets of experimental data represent two cases; that is, there is an energy fault in two modes and the modes are missing, the first few orders of normal modes are missing, and the first-order mode cannot be determined.

3.2.1 Measured data 1

The depth of the experimental sea H = 24.5 m, and the SSP in the water has a thermocline, as shown in Figure 11, the average speed of sound is c0 = 1497 m/s, the broadband source with the broadband 200–500 Hz is located at z_s = 10 m, and p = 6.33. The signal is received by a single hydrophone at z_r = 9 m, and the receiving depth is near the node of mode 3. r_0 = 4.96 km, as measured by GPS. The source is a long pulse, and the received signal is processed by pulse compression for the next step of analysis.

The received signal is shown in Figure 12A, and the signal to noise ratio is high. The dispersion curves are extracted after warping transform. Figure 12B shows the time-frequency analysis result of the received signal. The normal modes with stronger energy are selected for dispersion curve extraction, and the extraction results are shown in Figure 12B. The received signal contains four orders modes with strong energy, and the position of mode 1 is clear, but several modes are missing after mode 2, and the number of the missing modes cannot be known, according to the figure. The part of the dispersion curve with high energy and strong aggregation is used as the input function. To ensure accuracy of the inversion, the frequency range matching the different orders of the simple positive waves is selected, and the final dispersion curve as the input function is shown in Figure12B. The search intervals of the parameters to be inverted and the reference values are shown in Table 2.

Parameter inversion and modal identification are performed according to the procedure described above, and the inversion results are shown in Table 2. As shown in Table 2 and Figure 13,

the results of normal mode number determination are accurate, and the results indicate that the missing mode is mode 3. Because of the location of the receiver, the energy of mode 3 is low and it is unobserved in the time-frequency domain of the received signal.

The errors of c0 and H are less than 5%, on the basis of comparison of the inversion results with the reference values, which are 2.04% and 0.002%, respectively. Although the error of P is larger, the estimated value of the propagation range is $r = 5.00$ km, which is a very accurate value with respect to the GPS result of $r_0 = 4.96$ km, and the error is only 0.008%. The inversion results fully illustrate that the method has strong stability with respect to marine environmental parameters. The inversed dispersion curves match well with the data extraction results and the spectrogram of the received data, thus demonstrating the superiority of the proposed method in passive ranging and normal mode order determination.

3.2.2 Measured data 2

The depth of the experiment sea is $H = 30$ m, the SSP is isovelocity with the speed c0 = 1460 m/s, and $p = 5.43$. An explosion sound signal was received by the ocean bottom seismometer located at the seabed after propagating 35.12 km, and four channels (P, X, Y, and Z) of data were obtained. The P-channel data were selected for inversion, and the received signal is shown in Figure 14A, which indicated that the signal to noise ratio of the measured data is lower than that in data 1.

Figure 14B shows the TFA result of the received signal, indicating four normal modes with strong energy. However, the first mode in the Figure is not the true mode 1 in the received signal; that is, the first few orders of the normal mode in the signal are missing. We therefore must determine the number of normal mode to achieve the inversion of parameters. The dispersion curves in Figure 14B are the parts after band selection and serve as the input signal. The search intervals, reference values, and inversion results of the parameters to be inverted are shown in Table 3.

The comparison result of dispersion curves obtained with the different methods is shown in Figure 15, which shows that the inversed dispersion curves are in good agreement with those from the other methods. From Figure 15 and Table 3, the orders of normal modes used for inversion are 3, 4, 5, and 6, and the mode identification results are accurate. Consequently, the first two modes did not appear in the time-frequency domain of the received signal and warped signal.

The error of the distance estimation results with respect to those obtained by GPS is only 0.26%, thus further validating the accuracy of the source ranging. In addition, the estimation errors of other parameters are within 5%.

4 Conclusion

We propose a joint estimation method for the normal mode number and propagation range of an underwater broadband impulse source based on a single hydrophone in an unknown marine environment. This method is based on Bayesian estimation theory and is applicable to a shallow sea waveguide. The characteristics of the dispersion curve of the normal mode correspond to the mode order. The dispersion curves with high energy and good aggregation are extracted by warping transform and used as the input signal for Bayesian methods. In a waveguide in which the seabed speed of sound is larger than that in water, the bottom properties can be approximated on the basis of the bottom reflection phase shift parameter P for SRBR modes in the case of small angle incidence. A dispersion formula based on four parameters is used to calculate the replica and reduce the number of inversion parameters in the unknown ocean environment. The inversion errors caused by the correlation of parameters can be effectively avoided.

The normal mode order and environmental parameters are jointly inversed as unknown parameters, and the joint cost function ensures the consistency of the results for mode order and inversion parameters. In this paper, the propagation ranges of two different shallow sea waveguides in two different types of broadband pulsed sound sources are measured. The mode identification results are accurate when there is modal missing in two modes, or the first few orders of normal modes are missing. In addition, the coupling of environmental parameters does not affect the accuracy of the results of mode order identification and range estimation, accurate identification of the normal mode order is achieved in different waveguides, the inversion error of environmental parameters is within 5%, and the error of propagation range measurement is less than 3%, thus demonstrating the good tolerance of the method to the environmental parameters. The simulation and experimental processing results fully illustrate the effectiveness and feasibility of the method.

Data availability statement

The original contributions presented in the study are included in the article/Supplementary Material, further inquiries can be directed to the corresponding author.

Author contributions

XL completed literature research, conceptualization, methodology, and manuscript writing. YM completed conceptualization, funding acquisition, and project management. HC, HL, and XB jointly completed the validation and visualization.

Funding

This research was funded by the Natural Science Foundation of China, grant number No. 12204199, the Natural Science Foundation of Jiangsu Higher Education Institutions of China, grant number No. 21KJD140001, the Open Foundation from Marine Sciences in the First-Class Subjects of Zhejiang, grant number No. OFMS004, the Rising Star Foundation of the Integrated Research Center for Islands and Reefs Sciences, CAS. Grant number No. ZDRW-XH-2021-2-04, and the Science Foundation of Donghai Laboratory (Grant No: DH-2022KF01018).

Conflict of interest

The authors declare that the research was conducted in the absence of any commercial or financial relationships that could be construed as a potential conflict of interest.

Publisher's note

References

1. Jensen FB, Kuperman WA, Porter MB, Schmidt H. *Computational Ocean acoustics*. New York: Spinger (2011). doi:10.1007/978-1-4419-8678-8_7

2. Donald FG, Peter G. Inversion for geometric and geoacoustic parameters in shallow water: Experimental results. *J Acoust Soc Am* (1995) 97(6):3589–98. doi:10.1121/1.412442

3. Liang X, Lin B, Liu B, Ma X. Study on dispersion and attenuation of laser-induced surface acoustic wave by grinding surface roughness. *Appl Acoust* (2022) 1999:109028. doi:10.1016/j.apacoust.2022.109028

4. Shi H, Li J, Chang H, Liu L. Research on passive localization method of shallow water acoustic source with single hydrophone based on hierarchical grid histogram filtering. *Appl Acoust* (2022) 194(15):108812. doi:10.1016/j.apacoust.2022.108812

5. Rui D, Kunde Y, Ma Y, Yang Q, Li H. Moving source localization with a single hydrophone using multipath time delays in the deep ocean. *J Acoust Soc Am* (2014) 136: EL159–65. doi:10.1121/1.4890664

6. Zhai D, Zhang B, Li F, Zhang Y, Yang X. Passive source depth estimation in shallow water using two horizontally separated hydrophones. *Appl Acoust* (2022) 192:108723. doi:10.1016/j.apacoust.2022.108723

7. Bonnel J. Acoustical oceanography with a single hydrophone: Propagation, physics-based processing and applications. *J Acoust Soc Am* (2019) 146(4):2931. doi:10.1121/1.5137181

8. Li Y, Tang B, Yi Y. A novel complexity-based mode feature representation for feature extraction of ship-radiated noise using VMD and slope entropy. *Appl Acoust* (2022) 196: 108899. doi:10.1016/j.apacoust.2022.108899

9. Li Y, Gao P, Tang B, Yi Y, Zhang J. Double feature extraction method of ship-radiated noise signal based on slope entropy and permutation entropy. *Entropy* (2022) 24(1):22. doi:10.3390/e24010022

10. Li Y, Geng B, Jiao S. Dispersion entropy-based lempel-ziv complexity: A new metric for signal analysis. *Chaos solitons & fractals* (2022) 161:112400. doi:10.1016/j.chaos.2022.112400

11. Bonnel J, Chapman NR. Geoacoustic inversion in a dispersive waveguide using warping operators. *J Acoust Soc Am* (2011) 130(2):101–7. doi:10.1121/1.3611395

12. Guo X, Yang K, Ma Y. A far distance wideband geoacoustic parameter inversion method based on a modal dispersion curve. *Acta Physica Sinica* (2015) 64(17):174302. doi:10.7498/aps.64.174302

13. Zoi-Heleni M, Nattapol A. Environmental inversion using dispersion tracking in a shallow water environment. *J Acoust Soc Am* (2018) 143:EL188–93. doi:10.1121/1.5026245

14. Graham AW, Stan ED, Jan D, Hannay DE. Bayesian environmental inversion of airgun modal dispersion using a single hydrophone in the Chukchi Sea. *J Acoust Soc Am* (2015) 137(6):3009–23. doi:10.1121/1.4921284

15. Bonnel J, Stan ED, Chapman NR. Bayesian geoacoustic inversion of single hydrophone light bulb data using warping dispersion analysis. *J Acoust Soc Am* (2013) 134(1):120–30. doi:10.1121/1.4809678

16. Bonnel J, AaronThode M, Blackwell SB, Kim K, Macrander AM. Range estimation of bowhead whale (Balaena mysticetus) calls in the Arctic using a single hydrophone. *J Acoust Soc Am* (2014) 136(1):145–55. doi:10.1121/1.4883358

17. Zhou SH, Qi YB, Ren Y. Frequency invariability of acoustic field and passive source range estimation in shallow water. *Sci China- Phys Mech-astron* (2014) 57(2):225–32. doi:10.1007/s11433-013-5359-z

18. Bonnel J, Gervaise C, Roux P, Nicolas B, Mars J. Modal depth function estimation using time-frequency analysis. *J Acoust Soc Am* (2011) 130(61):61–71. doi:10.1121/1.3592230

19. Sheri M, Stan ED, Iohn FC. Bayesian inversion of microtremor array dispersion data in southwestern British Columbia. *Geophys J Int* (2010) 183(2):923–40. doi:10.1111/j.1365-246X.2010.04761.x

20. Li Q, Yang F, Zhang K, Zheng BX. Moving source parameter estimation in an uncertain environment. *Acta Physica Sinica* (2016) 65(16):164304. doi:10.7498/aps.65.164304

21. Li X, Piao S, Zhang M, Liu Y. A passive source location method in a shallow water waveguide with a single sensor based on Bayesian Theory. *Sensors* (2019) 19(6):1452. doi:10.3390/s19061452

22. Meng R, Zhou S, Li F, Qi Y. Identification of interference normal mode pairs of low frequency sound in shallow water. *Acta Phys Sin* (2019) 68:134304. doi:10.7498/aps.68.20190221

23. Bonnel J, Lin YT, Eleftherakis D, Goff JA, Dosso S, Chapman R, et al. Geoacoustic inversion on the New England Mud Patch using warping and dispersion curves of high-order modes. *J Acoust Soc Am* (2018) 143:EL405–11. doi:10.1121/1.5039769

24. Jevgenija P, Kirill H, Bruno B, Groby J. An application of normal mode decomposition to measure the acoustical properties of low growing plants in a broad frequency range. *Appl Acoust* (2016) 117:39–50. doi:10.1016/j.apacoust.2016.09.028

25. Li X, Wang B, Bi X, Wu H. A fast inversion method for ocean parameters based on dispersion curves with a single hydrophone. *Acta Oceanologica Sinica* (2022) 41:71–85. doi:10.1007/s13131-022-1999-z

26. Porter MB. *The KRAKEN normal mode program*. NATO (1991). SACLANTCEN. Available at: https://openlibrary.cmre.nato.int/handle/20.500.12489/201?show=full.

27. Bonnel J, Aaron T, Dana W, Ross C. Nonlinear time-warping made simple: A step-by-step tutorial on underwater acoustic modal separation with a single hydrophone. *J Acoust Soc Am* (2020) 147(3):1897–926. doi:10.1121/10.0000937

28. Dosso S, Wilmut M. Uncertainty estimation in simultaneous Bayesian tracking and environmental inversion. *J Acoust Soc Am* (2008) 124(1):82–97. doi:10.1121/1.2918244

frontiers | Frontiers in Physics

TYPE Original Research
PUBLISHED 31 March 2023
DOI 10.3389/fphy.2023.1163767

OPEN ACCESS

EDITED BY
Govind Vashishtha,
Sant Longowal Institute of Engineering and Technology, India

REVIEWED BY
Ke Qu,
Guangdong Ocean University, China
Guanni Ji,
Xi'an Traffic Engineering Institute, China

*CORRESPONDENCE
Yingmin Yi,
yiym@xaut.edu.cn

SPECIALTY SECTION
This article was submitted to Physical Acoustics and Ultrasonics, a section of the journal Frontiers in Physics

RECEIVED 11 February 2023
ACCEPTED 03 March 2023
PUBLISHED 31 March 2023

CITATION
Jiang X, Yi Y and Wu J (2023), Analysis of the synergistic complementarity between bubble entropy and dispersion entropy in the application of feature extraction. *Front. Phys.* 11:1163767. doi: 10.3389/fphy.2023.1163767

Analysis of the synergistic complementarity between bubble entropy and dispersion entropy in the application of feature extraction

Xinru Jiang[1], Yingmin Yi[1,2]* and Junxian Wu[1]

[1]School of Automation and Information Engineering, Xi'an University of Technology, Xi'an, China, [2]Shaanxi Key Laboratory of Complex System Control and Intelligent Information Processing, Xi'an University of Technology, Xi'an, China

Most of the existing studies on the improvement of entropy are based on the theory of single entropy, ignoring the relationship between one entropy and another. Inspired by the synergistic relationship between bubble entropy (BE) and permutation entropy (PE), which has been pointed out by previous authors, this paper aims to explore the relationship between bubble entropy and dispersion entropy. Since dispersion entropy outperforms permutation entropy in many aspects, it provides better stability and enhances the computational efficiency of permutation entropy. We also speculate that there should be potential synergy between dispersion entropy and bubble entropy. Through experiments, we demonstrated the synergistic complementarity between BE and DE and proposed a double feature extraction method based on BE and DE. For the single feature extraction experiment, dispersion entropy and bubble entropy have better recognition performance for sea state signals and bearing signals, respectively; in double feature extraction, the combination of bubble entropy and dispersion entropy makes the recognition rate of sea state signals increase by 10.5% and the recognition rate of bearing signals reach 99.5%.

KEYWORDS

bubble entropy, permutation entropy, dispersion entropy, synergistic complementarity, feature extraction, sea state signals, bearing signals

1 Introduction

In the field of non-linear dynamics, it is important to study about the feature of complexity, which characterizes the complexity of the signal from a physical point of view [1, 2]. In fact, the existing time-domain and frequency-domain analysis techniques are applicable to periodic stationary signals and linear signals. However, for complex non-linear signals, the traditional methods cannot well reflect the non-linear characteristics and implied information. For time series, entropy and Lempel–Ziv complexity and other non-linear dynamic indexes are used as an evaluation criterion for signal complexity [3–10], among which the development of entropy is the most mature.

The entropy theory has been developed to date with a variety of characterizations in different forms. In 2002, Bandt et al. [11] first proposed the permutation entropy theory, which can represent the complexity of the permutation order of a one-dimensional time series with suitable parameters [12]. However, PE does not consider the relationship

between individual magnitudes in a time series and thus has limitations for the analysis of the time series [13]. Based on the original theory of PE, many scholars have studied various improvements, such as the proposed weighted-permutation entropy as a complexity measure for time series incorporating amplitude information [14], reverse permutation entropy as a method to identify different sleep stages by using electroencephalogram data [15], and multiscale permutation entropy to solve the problem of PE's inability to fully characterize the dynamics of complex EEG sequences [16] as well as refined composite processing based on multiscale cases [17].

In 2016, Mostafa Rostaghi and Hamed Azami [18] proposed dispersion entropy, an algorithm that overcomes the deficiencies of PE and provides better stability and increased computational efficiency. By processing the steps on the original DE algorithm accordingly, scholars have proposed refined composite multiscale dispersion entropy that is similar to refined composite multiscale permutation entropy [19], fluctuation-based dispersion entropy as a measure to deal with only the fluctuations of time series [20], reverse dispersion entropy as a new complexity measure for sensor signals [21], and hierarchical dispersion entropy as a new method of fault feature extraction [22].

In 2017, George Manis et al. [23] first proposed a new time series complexity metric, bubble entropy, which is an entropy with almost no parameters, and the algorithm is extensive by creating a more coarse-grained distribution through a sorting process that better reduces the impact of parameter selection.

Research on improvement and optimization based on a single entropy is more common, often adding weight, reverse, multiscale, refined composite, fluctuation, and other operations to the original entropy. Conversely, some scholars proposed new theories based on the combination of the core of a single primitive entropy approach; for example, permuted distribution entropy is the combination of PE and distribution entropy [24], fuzzy dispersion entropy is inspired by fuzzy entropy (FE) and DE [25], fractional order fuzzy dispersion entropy is proposed to introduce fractional order calculation and fuzzy membership function [26].

However, few people study the relationship between one entropy and another. David Cuesta-Frau and Borja Vargas studied the synergistic relationship between BE and PE in 2019 [27], and if DE is the improvement of PE, then BE and DE may also have a synergistic and complementary relationship with each other. Therefore, this paper proposed a double feature extraction method based on BE and DE and applied it to the sea state signal in the field of hydro-acoustics and the bearing signal for fault diagnosis.

The remainder of the paper is organized as follows: Section 2 describes detailed algorithm theories of BE and DE; Section 3 indicates the theoretical logic of BE, PE, DE, and FE and process of the proposed feature extraction method; Section 4 conducts the single feature extraction experiments of sea state signals and bearing signals; Section 5 performs the double feature extraction experiments of the same practical signals with different combinations, as well as carries out the analysis and comparison of experimental results; and ultimately, Section 6 elaborates the essential conclusion of this paper.

2 BE and DE

2.1 Theory of BE

As an entropy with almost no parameters, the theory of BE is very simple, similar to PE. The algorithm makes the distribution more coarse-grained by sorting, thus better reducing the impact of parameter selection and expanding the limitations of use.

Step 1: Given that the time series $x = x_1, x_2, \cdots, x_N$. According to the given embedding dimension m, the original signal is mapped to the m-dimensional phase space X in the way of time delay τ of 1, where each element is represented by X_i.

$$X = X_1, X_2, \cdots, X_{N-m+1}, \tag{1}$$

$$X_i = (x_i, x_{i+1}, \cdots, x_{i+m-1})\, i = 1, 2, \cdots, N - m + 1. \tag{2}$$

Step 2: The m elements in X_i are arranged in ascending order, and the number of swaps n_i can be obtained.
Step 3The probability p_i is derived by normalizing the individual n_i to the total number $N - m + 1$.

$$p_i = \frac{n_i}{N - m + 1}. \tag{3}$$

Step 3: The entropy value $H^m_{\text{swaps}}(X)$ can be calculated by substituting the probability into the following equation:

$$H^m_{\text{swaps}}(X) = -log \sum_{i=1}^{N-m+1} p_i^2. \tag{4}$$

Step 4: The value of $H^{m+1}_{\text{swaps}}(X)$ when embedding dimension m equals $m + 1$ is calculated by repeating Steps 1–4.

Step 5: The value of BE is available as follows:

$$bEn = \frac{\left(H^{m+1}_{\text{swaps}}(X) - H^m_{\text{swaps}}(X)\right)}{ln(m + 1/m - 1)}. \tag{5}$$

2.2 Theory of DE

DE often appears as the optimization of PE, and its characteristics lie in the mapping process and the selection of the dispersion mode. Compared with PE, this theory provides good stability and increased computational efficiency.
Step 1Given that the time series $x = x_1, x_2, \cdots, x_N$. $y = y_1, y_2, \cdots, y_N$ can be acquired by mapping x to a normal distribution function, after which $z = z_1, z_2, \cdots, z_N$ can be obtained by mapping to a linear equation.

$$y_i = \frac{1}{\sigma\sqrt{2\pi}} \int_{-\infty}^{x_i} e^{-(t-\mu)^2/2\sigma^2} dt, \tag{6}$$

$$z_i = round\left(c * y_i + 0.5\right), \tag{7}$$

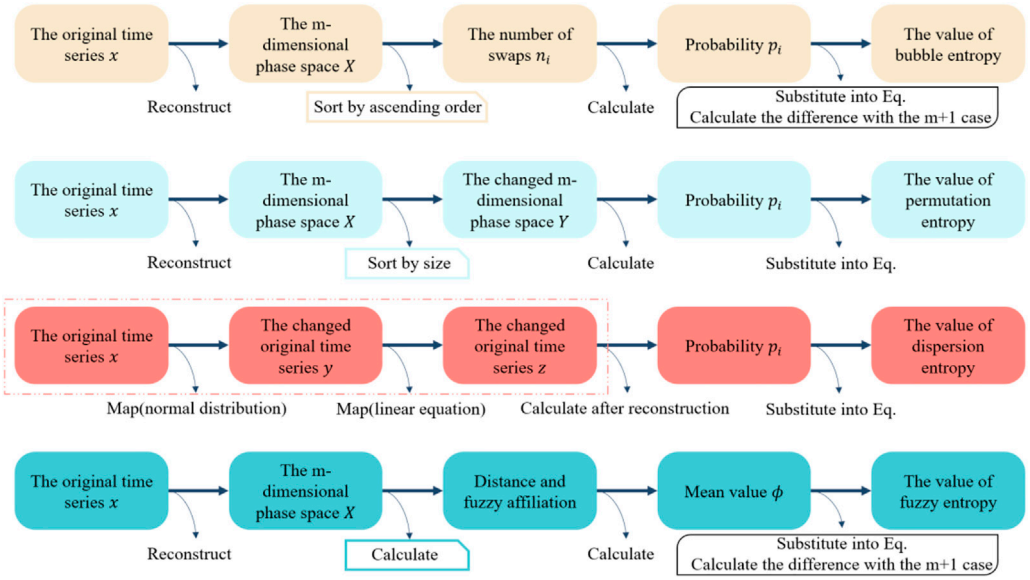

FIGURE 1
Theoretical logic of BE, PE, DE, and FE.

where μ and σ^2 are set to expectation and variance of x_i, respectively, c is the number of categories, and round denotes the integer function. Step 2 The phase space reconstruction of z based on the value of embedding dimension m is carried out to compose the corresponding $(N-m+1)\tau$ dispersion patterns $\pi_{v_0v_1\cdots v_{m-1}}$, and the probability of occurrence of different kinds of dispersion patterns is calculated. It is worth noting that the time delay τ in this step is 1.

$$p\left(\pi_{v_0v_1\cdots v_{m-1}}\right) = \frac{Num\{i \mid i \le N-m+1, \pi_{v_0v_1\cdots v_{m-1}}\}}{N-m+1}. \tag{8}$$

step 3 According to Step 1 and Step 2, each element in the component has c values, so there are c^m dispersion patterns. Therefore, the normalized DE is defined by the following formula:

$$dEn = -\sum_{\pi=1}^{c^m} p\left(\pi_{v_0v_1\cdots v_{m-1}}\right) \ln \frac{p\left(\pi_{v_0v_1\cdots v_{m-1}}\right)}{ln\left(c^m\right)}. \tag{9}$$

3 Algorithm analysis and method proposal

In this paper, four entropies are introduced and applied to sea state signals and bearing signals, each of which has a unique theory and different focus, so the algorithms are also different. Figure 1 briefly describes the theoretical logic of BE, PE, DE, and FE.

For BE, the original time series is first reconstructed to get the m-dimensional phase space, and then the number of swaps is obtained by sorting each vector in ascending order, then the corresponding probabilities are calculated, and finally the value is attained by substituting into the BE-specific formula.

For PE, the original time series is first reconstructed to get the m-dimensional phase space, and then the changed m-dimensional phase space is constructed by sorting each element in each vector according to the value size, then the corresponding probability is calculated, and finally the value is obtained by substituting into the PE-specific formula.

For DE, the original time series is first mapped by the normal distribution function to get the changed time series and then mapped again by using the linear equation to change the time series again. After this step, the m-dimensional phase space is obtained by reconstruction, then the dispersion pattern probability is calculated, and finally the value is obtained by substituting into the DE-specific formula.

For FE, the original time series is first reconstructed to obtain the m-dimensional phase space, then the distance and fuzzy affiliation are calculated, later its mean value is calculated, and finally the value is obtained by substituting into the FE-specific formula.

By comparing the four entropies as a whole, it is obvious that: BE, PE, and FE reconstruct the phase space first and then perform other operations afterward, where BE and PE both get the corresponding results by sorting, while DE is a direct processing of the time series through two mappings before reconstructing the phase space; both BE and FE need to calculate the difference in the $m+1$ case, and this step reduces the influence of the embedding dimension on the results to some extent.

The aforementioned description is the theoretical part of the four entropies, based on which we propose the feature extraction methods of single and double features. Figure 2 provides the flow chart of the feature extraction methods of single and double features taken in this paper.

Based on the analysis and comparison of the algorithm, we apply it to the feature extraction experiment for verification and further research. The feature extraction method includes four main steps:

Step 1: Diverse types of sea state signals (SSSs) and bearing signals (BSs) are applied as the input of the feature extraction experiment, where the length of each type of sea state or bearing signals is the same with identical sampling points.

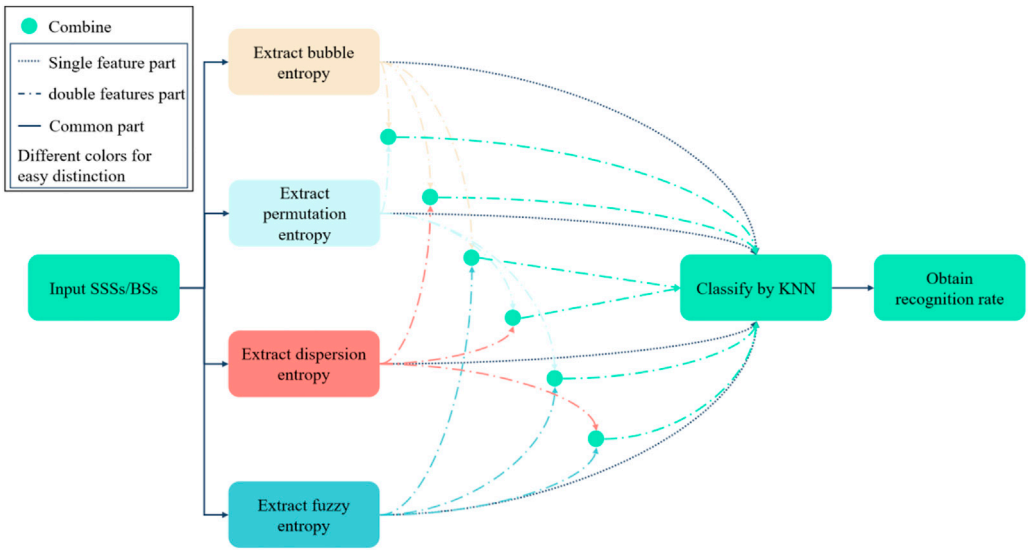

FIGURE 2
Flow chart of single and double feature extraction methods taken in this paper.

TABLE 1 Parameter settings for each type of entropy.

Complexity index	Embedding dimension m	Time delay τ	Category number c	Correlation coefficient r
BE	3	1	—	—
PE	3	1	—	—
DE	3	1	6	—
FE	3	1	-	0.2

Step 2: For four types of sea state or bearing signals, the values of BE, PE, DE, and FE can be extracted. For double feature extraction, one step needs to be added: the values of BE, PE, DE, and FE are combined two by two, and thus there are six combination forms.

Step 3: The K-nearest neighbor (KNN) [28] is accepted to classify each type of sea state or bearing signals.

Step 4: The recognition rate can be attained and employed for the expression of recognition ability.

4 Single feature extraction

4.1 Sea state signals and bearing signals

In this study, four different types of SSS and BS from website1 and website2 are selected for feature extraction and classification recognition in the form of complexity. For SSSs and BSs, the size of sample points is 1.3×10^6 and 1.2×10^5, respectively, and the sampling frequency for both are 44.1 kHz. Four diverse types of SSSs and BSs can be represented by sssI, sssII, sssIII, and sssIV and bsI, bsII, bsIII, and bsIV, respectively. Among these different types of signals, we selected 100 samples, starting from the sample point of the same serial number, and each sample consists of 2000 sampling points for sea state signals and 1,000 for bearing signals. Figure 3 shows the normalized time-domain waveforms of four diverse types of SSSs and BSs.

4.2 Feature extraction

For the 100 samples selected, we introduce BE, PE, DE, and FE and calculate the entropy values as the complexity feature. Table 1 illustrates the parameter settings for each type of entropy.

As can be seen from Table 1, the time delay τ and the embedding dimension m of all entropies are 1 and 3, respectively; only DE has the category number c and its value is 6; the correlation coefficient r of FE is 0.2. Figure 4 depicts the distributions of BE, PE, DE, and FE for the selected 100 samples under specific parameter settings for SSSs and BSs.

1 [Online]. Available: https://www.nps.gov/glba/learn/nature/soundclips.htm.

2 [Online]. Available: http://csegroups.case.edu/bearingdatacenter/pages/download-data-file.

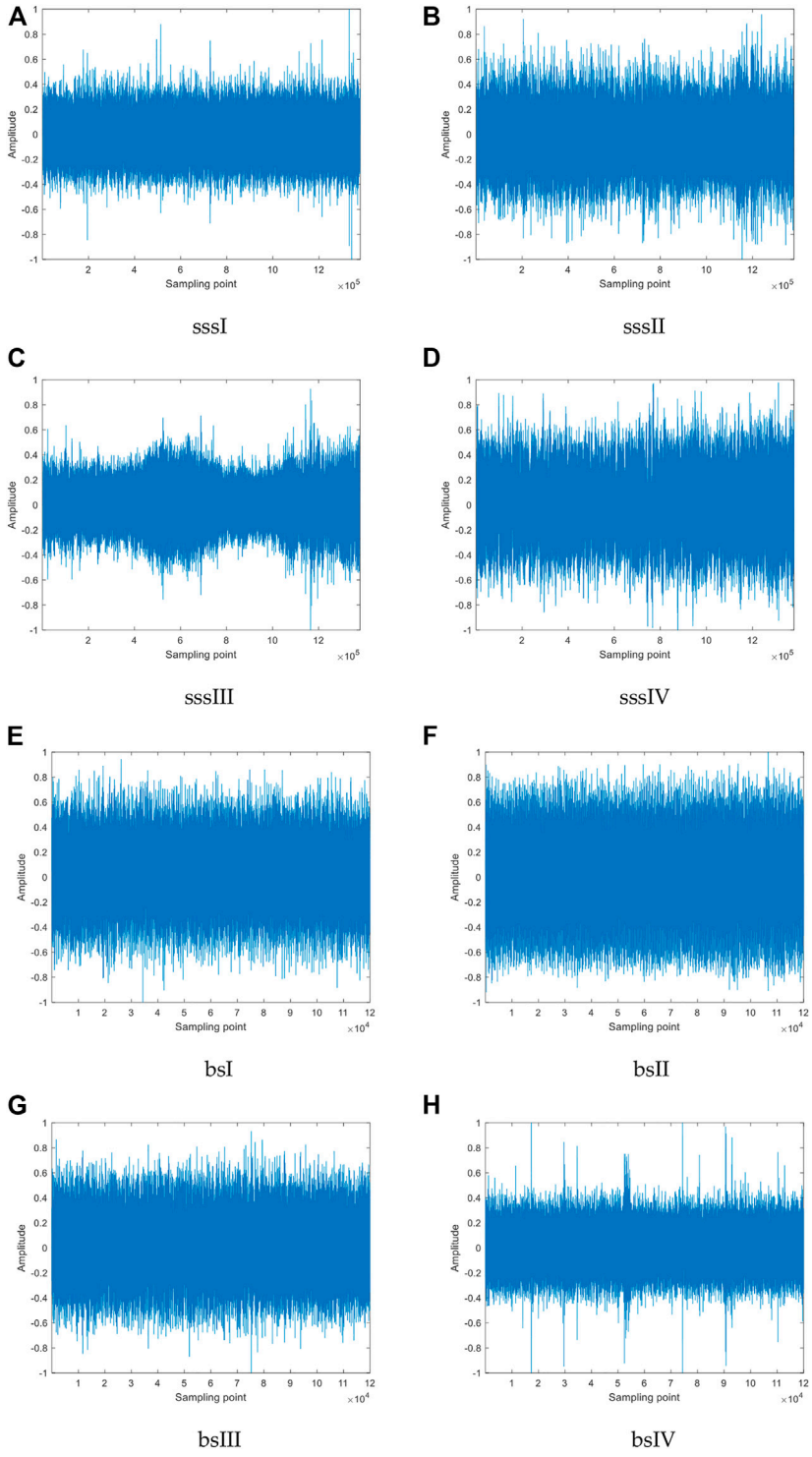

FIGURE 3
Normalized time-domain waveforms of four diverse types of SSSs and BSs: **(A)** sssI, **(B)** sssII, **(C)** sssIII, **(D)** sssIV, **(E)** bsI, **(F)** bsII, **(G)** bsIII, **(H)** bsIV.

According to the observation in Figure 4, the distributions of different entropies have specificity; for SSSs, DE has better distribution characteristics, and all kinds of signals are almost located in the same line with a small amount of an overlapping phenomenon, while BE and PE have obvious deficiencies in distinguishing sssI and sssIII, as well as sssII and sssIV; for BSs, the distribution of bsII and bsIII are too close to each other for PE, DE, and FE, and even a large mixing occurs, which is obviously not easy to differentiate, while BE overcomes this problem, and there appears only a small number of confusing sample points when differentiating bsIII and bsIV.

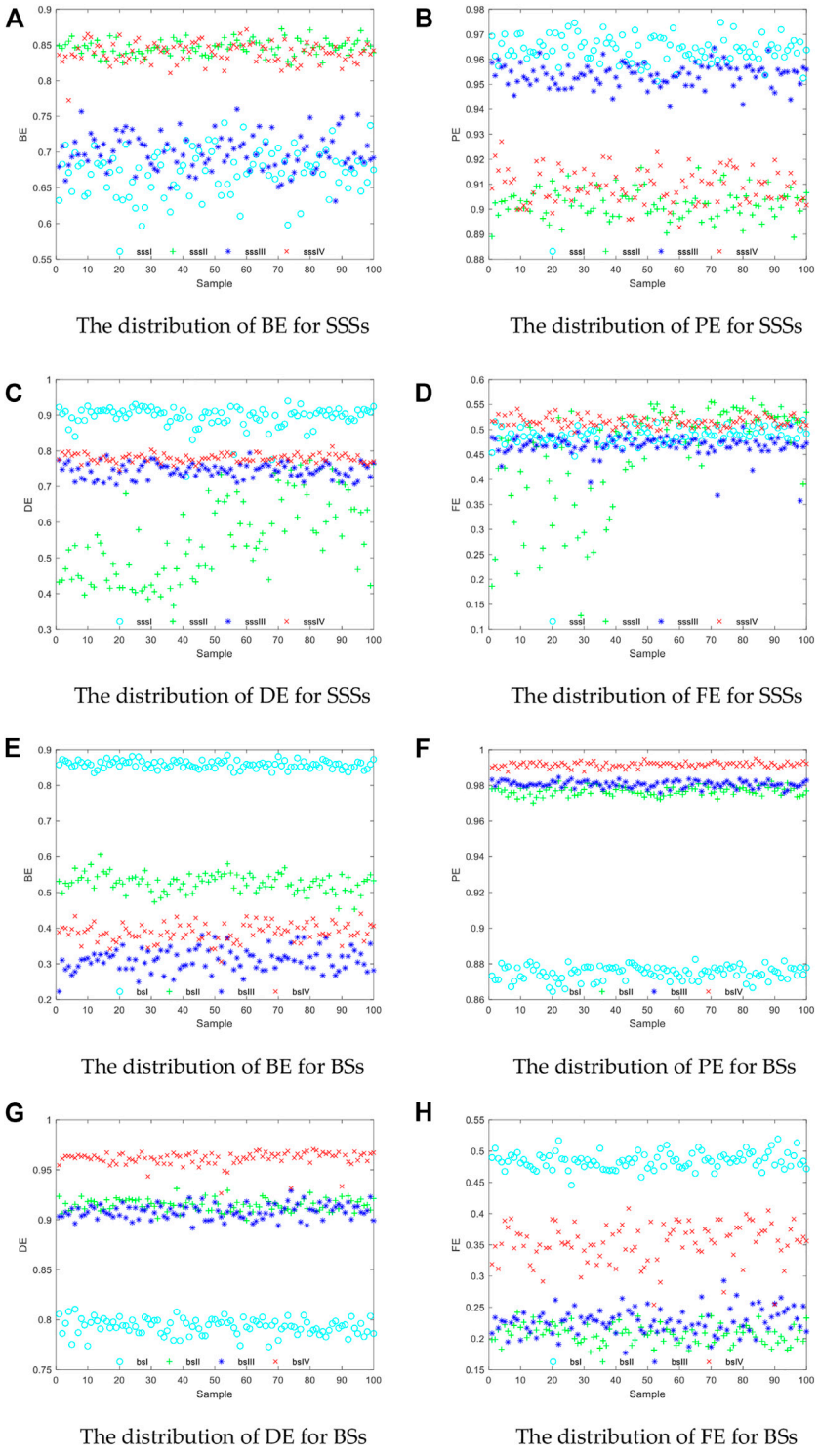

FIGURE 4
Distributions of BE, PE, DE, and FE for the selected 100 samples under specific parameter settings: **(A–D)** Distribution of SSSs, **(E–H)** Distribution of BSs.

4.3 Feature classification and recognition

To further explore the ability of BE, PE, DE, and FE to classify and recognize the four diverse types of SSSs and BSs, KNN was appointed to classify and recognize by taking the first 50 sample points as a training sample set and the rest as a test sample set. Table 2 and Table 3 summarize the feature classification and recognition results obtained for SSSs and BSs separately.

TABLE 2 Feature classification and recognition results obtained for SSSs.

Entropy	Number of misidentified samples for each type of sea state signals				Average recognition rate (%)
	sssI	sssII	sssIII	sssIV	
BE	23	20	14	3	60.0
PE	8	2	9	21	75.0
DE	2	14	8	8	84.0
FE	27	37	20	15	50.5

TABLE 3 Feature classification and recognition results obtained for BSs.

Entropy	Number of misidentified samples for each type of bearing signals				Average recognition rate (%)
	bsI	bsII	bsIII	bsIV	
BE	0	1	9	5	92.5
PE	0	11	18	0	85.5
DE	0	22	22	3	76.5
FE	0	17	22	3	79.0

From Table 2 and Table 3, it can be seen that BE, PE, DE, and FE have different numbers of misidentified samples for each type of sea state and bearing signals, meaning that they have specificity in recognizing the four diverse types of SSSs and BSs; as far as the average recognition rate is concerned, the average recognition rate of DE for SSSs is the highest, and that of PE, BE, and FE is in the decreasing trend; for BSs, BE has the best recognition capability, whose average recognition rate reaches up to 92.5%.

In the single feature extraction method, DE and BE have the best classification recognition properties to mine the unique features of different types of signals. Nevertheless, their average recognition rates under single feature still have a lot of room for improvement, especially for DE.

In order to further improve the average recognition rate, we propose to combine BE with other entropies to make full use of their specificity for the recognition of various types of signals, that is, the unique advantages of each other, to form a complementary double feature, so as to optimize the feature extraction method based on BE, which would make the final average recognition rate and the recognition efficiency better.

5 Double feature extraction

5.1 Double feature extraction method based on two-by-two combination

For the sake of the full utilization of specificity, we combine all the entropies mentioned two by two and denote the combination as A&B, where A and B represent any two of the four entropies. For example, BE&DE represents the combined form of BE and DE, and their order does not matter. Therefore, for BE, PE, DE, and FE, there exist six combination forms. Figures 5, 6 list the entropy distribution and classification recognition results for BE&PE, BE&DE, BE&FE, PE&DE, PE&FE, and DE&FE for SSSs and BSs separately.

Comparing the various combinations shown in Figures 5, 6, we can see that the entropy distributions for SSSs and BSs are different for each type of combination, and therefore have different classification recognition results.

For SSSs, the entropy values between sssI and sssIII as well as between sssII and sssIV are obviously mixed and consequently difficult to distinguish, especially for sssII, which are often misidentified as sssIV. By comparison, it is found that BE&DE has the best recognition rate among all combinations.

For BSs, the entropy distribution of bsI is far from the other signals and is distinguishable, while the misidentification mainly occurs in bsII, bsIII, and bsIV, among which the combination BE&DE has only one sample point misidentification and has an obvious classification advantage.

5.2 Comparison and analysis of the results of single and double feature extraction experiments

For the sake of more intuitively comparing the difference in the average recognition rates under single and double feature extraction methods, Table 4 indicates the average recognition rate of each combination of categories for SSSs and BSs under double features.

In accordance with the information in Table 4, the average recognition rate of the single and double features differed greatly before and after the combination of entropies, compared with Table 2 and Table 3; in the case of double feature extraction, the average recognition rate achieves 94% for all combinations involving DE for SSSs and up to 99% for all combinations involving BE for BSs,

10.3389/fphy.2023.1163767

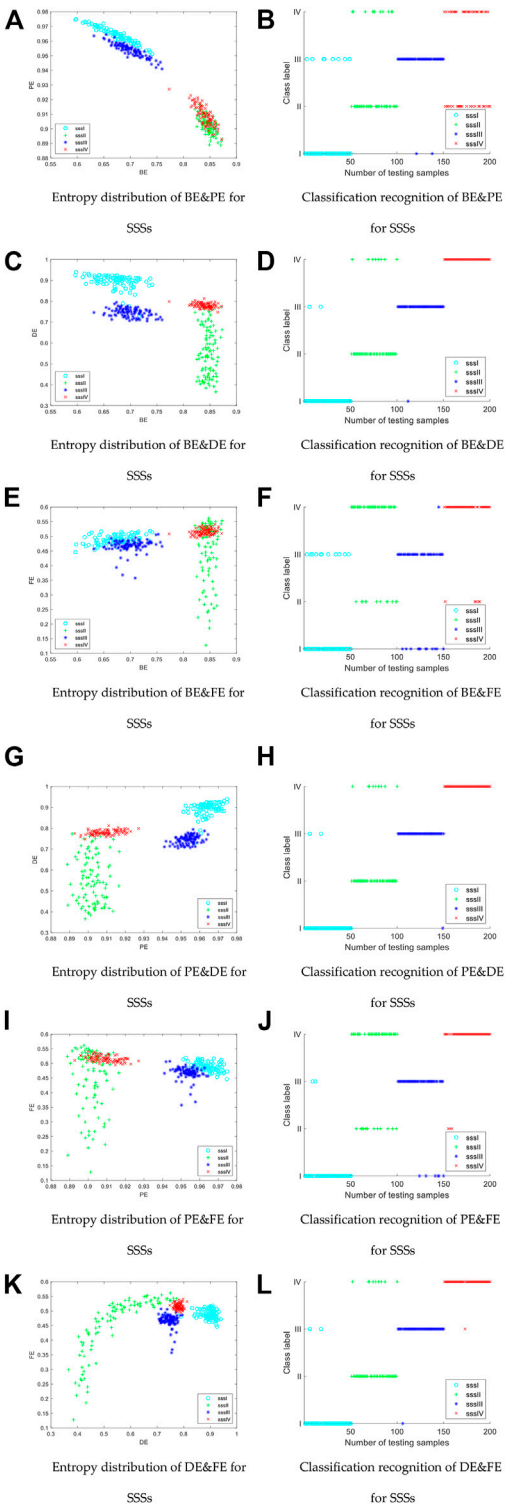

FIGURE 5
Entropy distribution and classification recognition results of BE&PE, BE&DE, BE&FE, PE&DE, PE&FE, and DE&FE of SSSs: distribution of different entropy combinations (Left column); classification recognition results (Right column).

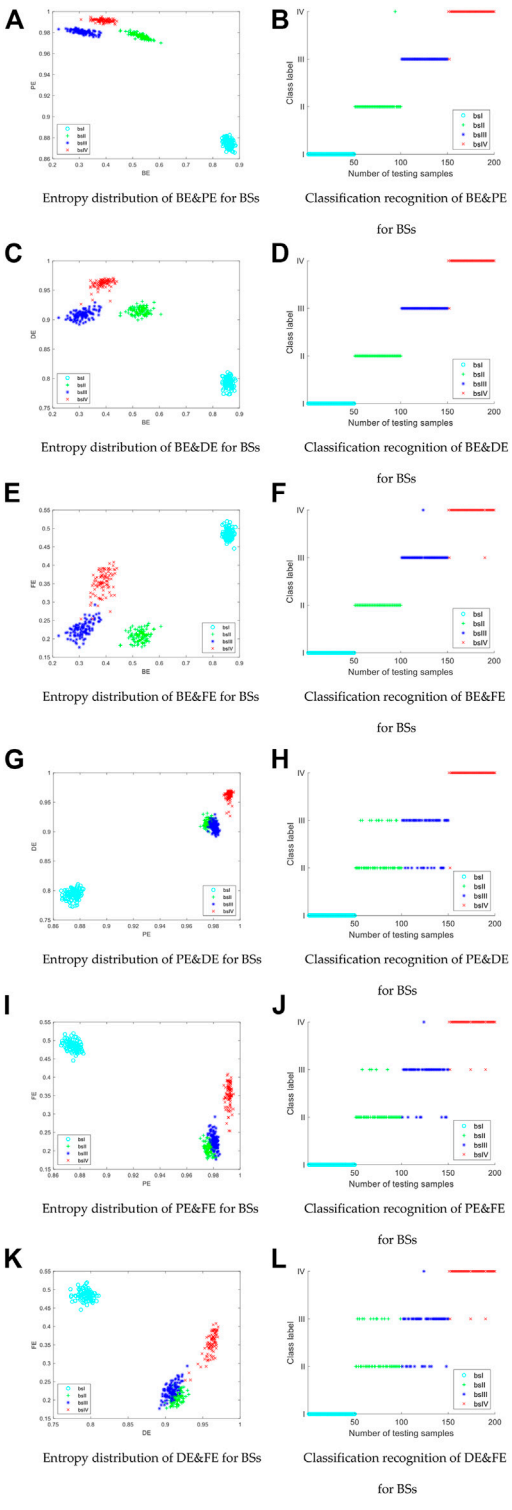

FIGURE 6
Entropy distribution and classification recognition results of BE&PE, BE&DE, BE&FE, PE&DE, PE&FE, and DE&FE of BSs: distribution of different entropy combinations (Left column); classification recognition results (Right column).

TABLE 4 Average recognition rate of each combination of categories for SSSs and BSs under double features.

Combination	Average recognition rate	
	SSSs (%)	BSs (%)
BE&PE	78.5	99.0
BE&DE	94.5	99.5
BE&FE	66.5	98.5
PE&DE	94.0	86.0
PE&FE	76.5	91.5
DE&FE	93.5	86.0

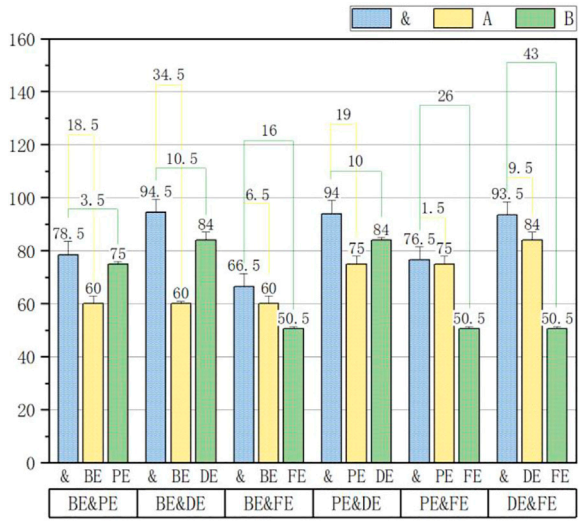

FIGURE 7
Average recognition rate and difference analysis of SSSs.

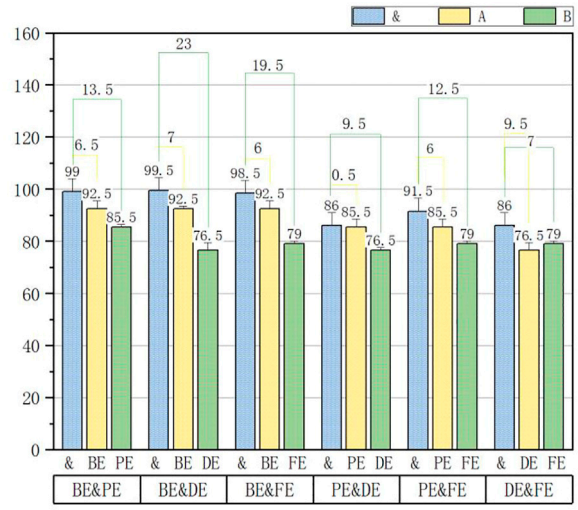

FIGURE 8
Average recognition rate and difference analysis of BSs.

which revealed that the initial capability to classify a single feature can be effectively modified by adding BE and DE as another feature; comparing the data in each column of the table confirms that BE&DE has the highest average recognition rate, that is, 94.5% for SSSs and 99.5% for BSs.

Figures 7, 8 show the average recognition rate and the difference analysis for SSSs and BSs, respectively. In the legend, & represents the combination, while A and B represent two of the four entropies, as described previously.

It is obvious from the aforementioned figures that the original recognition ability is improved by adding another feature. For SSSs, DE has the best recognition ability when used as a single feature and BE has a very poor recognition ability of 60%, while the combination of both achieves the highest recognition effect of 94.5%. For BSs, the situation is the opposite: BE is the entropy with the highest average recognition rate in the single feature extraction, while DE just has the lowest average recognition rate among the four entropies mentioned in this paper, but the combination of both can even reach 99.5%.

Generally speaking, combining two entropies with the highest average recognition rate and the second highest average recognition rate in single feature extraction should have a stronger combination to yield the highest final recognition rate, but for both SSSs and BSs, BE&DE has the best recognition rate, which implies that there is some synergy between BE and DE that can promote and improve each other.

6 Conclusion

In this study, we proposed BE&DE as a double feature extraction method based on the potential synergistic complementarity between BE and DE and applied it to the sea state signal in the field of hydro-acoustics and the bearing signal for fault diagnosis. The main conclusions drawn from this paper are as follows:

(1) Through the comparison and analysis of the algorithms, it can be seen that the essential difference between DE and BE is that DE makes use of the mapping relationship, while BE utilizes the number of exchanges to construct the vector, so it is speculated that there may be an assisting role between BE and DE.
(2) For sea state signals, DE has significant superiority, and for bearing signals, BE has better recognition performance. For different practical signals, different methods are applied in different suitable areas, but DE and BE are more effective compared to PE and FE.
(3) Based on the synergistic and complementary relationship between BE and DE, we proposed the combination form BE&DE and experimentally verified that the method possesses the best efficiency of signal classification and recognition.

Data availability statement

Publicly available datasets were analyzed in this study. These data can be found at: Sea state signal: https://www.nps.gov/glba/learn/nature/soundclips.htm. Bearing signal: https://engineering.case.edu/bearingdatacenter/download-data-file.

Author contributions

YY provided experimental ideas and financial support. XJ completed the experiment and wrote the article. JW was responsible for the revision of the article. All authors contributed to the article and approved the submitted version.

Funding

The research was supported by the Key Research and Development Plan of Shaanxi Province (2020ZDLGY06-01), Key Scientific Research Project of Education Department of Shaanxi Province (21JY033), and Science and Technology Plan of University Service Enterprise of Xi'an (2020KJRC0087).

Conflict of interest

The authors declare that the research was conducted in the absence of any commercial or financial relationships that could be construed as a potential conflict of interest.

Publisher's note

All claims expressed in this article are solely those of the authors and do not necessarily represent those of their affiliated organizations, or those of the publisher, the editors, and the reviewers. Any product that may be evaluated in this article, or claim that may be made by its manufacturer, is not guaranteed or endorsed by the publisher.

References

1. Berger A, Della Pietra SA, Della Pietra VJ. A maximum entropy approach to natural language processing. *Comput linguistics* (1996) 22:39–71.

2. Thuraisingham RA. Examining nonlinearity using complexity and entropy. *Chaos* (2019) 29:063109. doi:10.1063/1.5096903

3. Martyushev LM, Seleznev VD. Maximum entropy production principle in physics, chemistry and biology. *Phys Rep* (2006) 426:1–45. doi:10.1016/j.physrep.2005.12.001

4. Rajaram R, Castellani B. An entropy based measure for comparing distributions of complexity. *Physica A* (2016) 453:35–43. doi:10.1016/j.physa.2016.02.007

5. Li Y, Tang B, Yi Y. A novel complexity-based mode feature representation for feature extraction of ship-radiated noise using VMD and slope entropy. *Appl Acoust* (2022) 196:108899. doi:10.1016/j.apacoust.2022.108899

6. Li Y, Gao P, Tang B, Yi Y, Zhang J. Double feature extraction method of ship-radiated noise signal based on slope entropy and permutation entropy. *Entropy* (2022) 24(1):22. doi:10.3390/e24010022

7. Li Y, Geng B, Jiao S. Dispersion entropy-based Lempel-Ziv complexity: A new metric for signal analysis. *Chaos, Solitons Fractals* (2022) 161:112400. doi:10.1016/j.chaos.2022.112400

8. Yi Y, Li Y, Wu J. Multi-scale permutation Lempel-Ziv complexity and its application in feature extraction for Ship-radiated noise. *Front Mar Sci* (2022) 9:1047332. doi:10.3389/fmars.2022.1047332

9. Li Y, Jiao S, Geng B. Refined composite multiscale fluctuation-based dispersion Lempel–Ziv complexity for signal analysis. *ISA Trans* (2023) 133:273–84. doi:10.1016/j.isatra.2022.06.040

10. Li Y, Geng B, Tang B. Simplified coded dispersion entropy: A nonlinear metric for signal analysis. *Nonlinear Dyn* (2023). doi:10.1007/s11071-023-08339-4

11. Bandt C, Pompe B. Permutation entropy: A natural complexity measure for time series. *Phys Rev Lett* (2002) 88:174102. doi:10.1103/physrevlett.88.174102

12. Myers A, Khasawneh FA. On the automatic parameter selection for permutation entropy. *Chaos* (2020) 30:033130. doi:10.1063/1.5111719

13. Chen Z, Li Y, Liang H, Yu J. Improved permutation entropy for measuring complexity of time series under noisy condition. *Complexity* (2019) 2019:1–12. doi:10.1155/2019/1403829

14. Fadlallah B, Chen B, Keil A, Principe J. Weighted-permutation entropy: A complexity measure for time series incorporating amplitude information. *Phys Rev E* (2013) 87:022911. doi:10.1103/physreve.87.022911

15. Bandt C. A new kind of permutation entropy used to classify sleep stages from invisible EEG microstructure. *Entropy* (2017) 19:197. doi:10.3390/e19050197

16. Li D, Li X, Liang Z, Voss LJ, Sleigh JW. Multiscale permutation entropy analysis of EEG recordings during sevoflurane anesthesia. *J Neural Eng* (2010) 7:046010. doi:10.1088/1741-2560/7/4/046010

17. Humeau-Heurtier A, Wu CW, Wu SD. Refined composite multiscale permutation entropy to overcome multiscale permutation entropy length dependence. *IEEE Signal Processing Letters* (2015) 22:2364–7. doi:10.1109/lsp.2015.2482603

18. Rostaghi M, Azami H. Dispersion entropy: A measure for time-series analysis. *IEEE Signal Process. Lett* (2016) 23:610–4. doi:10.1109/lsp.2016.2542881

19. Azami H, Rostaghi M, Abásolo D, Escudero J. Refined composite multiscale dispersion entropy and its application to biomedical signals. *IEEE Trans Biomed Eng* (2017) 64:2872–9. doi:10.1109/TBME.2017.2679136

20. Azami H, Escudero J. Amplitude-and fluctuation-based dispersion entropy. *Entropy* (2018) 20:210. doi:10.3390/e20030210

21. Li Y, Gao X, Wang L. Reverse dispersion entropy: A new complexity measure for sensor signal. *Sensors* (2019) 19:5203. doi:10.3390/s19235203

22. Chen P, Zhao X, Jiang HM. A new method of fault feature extraction based on hierarchical dispersion entropy. *Shock and Vibration* (2021) 2021:1–11. doi:10.1155/2021/8824901

23. Manis G, Aktaruzzaman MD, Sassi R. Bubble entropy: An entropy almost free of parameters. *IEEE Trans Biomed Eng* (2017) 64:2711–8. doi:10.1109/TBME.2017.2664105

24. Dai Y, He J, Wu Y, Chen S, Shang P. Generalized entropy plane based on permutation entropy and distribution entropy analysis for complex time series. *Physica A* (2019) 520:217–31. doi:10.1016/j.physa.2019.01.017

25. Rostaghi M, Khatibi MM, Ashory MR, Azami H. Fuzzy dispersion entropy: A nonlinear measure for signal analysis. *IEEE Trans Fuzzy Syst* (2021) 30:3785–96. doi:10.1109/tfuzz.2021.3128957

26. Li Y, Tang B, Geng B, Jiao S. Fractional order fuzzy dispersion entropy and its application in bearing fault diagnosis. *Fractal and Fractional* (2022) 6(10):544. doi:10.3390/fractalfract6100544

27. Cuesta Frau D, Vargas-Rojo B. Permutation Entropy and Bubble Entropy: Possible interactions and synergies between order and sorting relations. *Math Biosciences Eng* (2020) 17:1637–58. doi:10.3934/mbe.2020086

28. Keller JM, Gray MR, Givens JA. A fuzzy K-nearest neighbor algorithm. *IEEE Trans Syst Man Cybernetics* (1985) 15(4):580–5. SMC-. doi:10.1109/tsmc.1985.6313426

frontiers | Frontiers in Physics

TYPE Original Research
PUBLISHED 04 April 2023
DOI 10.3389/fphy.2023.1180595

OPEN ACCESS

EDITED BY
Yuxing Li,
Xi'an University of Technology, China

REVIEWED BY
Xiaohui Yang,
Inner Mongolia University of Science and Technology, China
Guanni Ji,
Xi'an Traffic Engineering Institute, China

*CORRESPONDENCE
Nina Zhou,
summerm2023@126.com

SPECIALTY SECTION
This article was submitted to Physical Acoustics and Ultrasonics, a section of the journal Frontiers in Physics

RECEIVED 06 March 2023
ACCEPTED 24 March 2023
PUBLISHED 04 April 2023

CITATION
Zhou N and Wang L (2023), Triple feature extraction method based on multi-scale dispersion entropy and multi-scale permutation entropy in sound-based fault diagnosis.
Front. Phys. 11:1180595.
doi: 10.3389/fphy.2023.1180595

Triple feature extraction method based on multi-scale dispersion entropy and multi-scale permutation entropy in sound-based fault diagnosis

Nina Zhou[1]* and Li Wang[2]

[1]School of Electronic and Electrical Engineering, Baoji University of Arts and Sciences, Baoji, China, [2]School of Physical Education, Baoji University of Arts and Sciences, Baoji, China

Fault of rolling bearing signal is a common problem encountered in the production of life. Identifying the fault signal helps to locate the fault location and type quickly, react to the fault in time, and reduce the losses caused by the failure in production. In order to accurately identify the fault signal, this paper presents a triple feature extraction and classification method based on multi-scale dispersion entropy (MDE) and multi-scale permutation entropy (MPE), extracts the features of the signal of rolling bearing when it is working, and uses the classification algorithm to determine whether there is a fault in the bearing and the type of fault. Scale 2 of MDE is combined with scale 1 and scale 2 of MPE as the three features required for the experiment. As a comparison of recognition results, multi-scale entropy (MSE)is introduced. Ten scales of the three entropy are calculated, and all combinations of three feature extraction are obtained. K nearest neighbor algorithm is used for three feature recognition. The result shows that the combination recognition rate proposed in this paper reaches 96.2%, which is the best among all combinations.

KEYWORDS

rolling bearing signal, triple feature extraction, multi-scale dispersion entropy, multi-scale permutation entropy, fault diagnosis

1 Introduction

Today, mechanized equipment fault diagnosis is an unavoidable problem in all walks of life. Rolling bearing fault accounts for a large part of mechanical equipment fault [1, 2]. Rolling bearing, as a basic part of mechanical equipment, is easily damaged under long-term operation, resulting in many different types of faults, which affect the overall operation of equipment. However, early fault identification of bearings has always been a difficult problem to solve. In order to accurately identify and repair faults in time, various fault diagnosis methods have been put forward to distinguish fault types [3–5].

Vibration signals will be generated during normal operation of rolling bearings. By analyzing the characteristics of vibration signals, the fault categories of bearings can be effectively diagnosed. However, due to the influence of bearing load and friction between components, the vibration signals generated are always non-linear and non-stationary [6, 7]. For feature extraction and recognition of such signals, researchers have put forward many time-frequency analysis methods to extract information from the signals. For example, wavelet transform (WT), empirical mode decomposition (EMD) [8] and variational mode

decomposition (VMD) [9], however, these methods also have their own disadvantages, such as WT only decomposes low frequency band of signal, mode overlap of EMD, etc. To solve these problems, some improved methods have been put forward successively, such as empirical WT (EWT) [10], complete ensemble EMD with adaptive noise (CEEMDAN) and so on [11, 12].

In recent years, entropy, as a non-linear dynamic method, has also been applied in the fields of fault diagnosis and underwater acoustic signal recognition [13–15]. It is used to describe the complexity of the signal. Sample entropy (SE) [16], approximate entropy (AE) [17], permutation entropy (PE) [18], dispersion entropy (DE) [19] and so on have been put into use successively, and some achievements have been made [20]. However, single-scale entropy cannot completely reflect the fault information, especially the limitations of mutation information. As a result, multi-scale signal analysis methods are gradually applied to signal recognition [21, 22]. MSE was proposed by Costa et al. in 2002 [23], which successfully quantifies the information of time series on multi-scales. Based on the proposal of multi-scale SE (MSE), in 2005, Aziz et al. also made improvements on PE, proposed multi-scale PE (MPE) [24], and made PE obtain higher noise resistance. The proposed multi-scale DE (MDE) is faster to compute and better reflects the characteristics of the real signal than MSE. Both MPE and MDE are widely used in the field of signal recognition [25, 26].

Considering that the DE is faster and more stable, this paper uses the DE to extract fault features, but the DE contains less information. In order to obtain more information about the signal, we introduce the concept of multi-scale and propose a triple feature extraction method based on MDE and MPE in fault diagnosis.

The remainder of this paper is as follows: Section 2 introduces the principle and calculation method of multi-scale and DE; Section 3 describes the specific steps of the triple feature experiments proposed in this paper. Section 4 shows the feature distribution and recognition results of the triple feature extraction experiments, which proves the feasibility of the experiment. Section 5 summarizes the entire experiment.

2 Dispersion entropy

DE is a measure of time complexity. It has a faster calculation speed, is less affected by sudden changes in the signal and can reflect the magnitude relationship. The calculation steps of DE are as follows.

(1) For a given set of time series, $= \{x_1, x_2, \ldots, x_n\}$, the normal cumulative distribution function is used to map the original time series between 0 and 1.

$$y_j = \frac{1}{\sigma\sqrt{2\pi}} \int_{-\infty}^{x_i} e^{\frac{-(t-\mu)^2}{2\sigma^2}} dt \tag{1}$$

The standard deviation σ and mean μ of the time series x are respectively used in the formula.

(2) Use round function to convert the time series mapped in the first step into integers between 1 and c, where c is the number of categories.

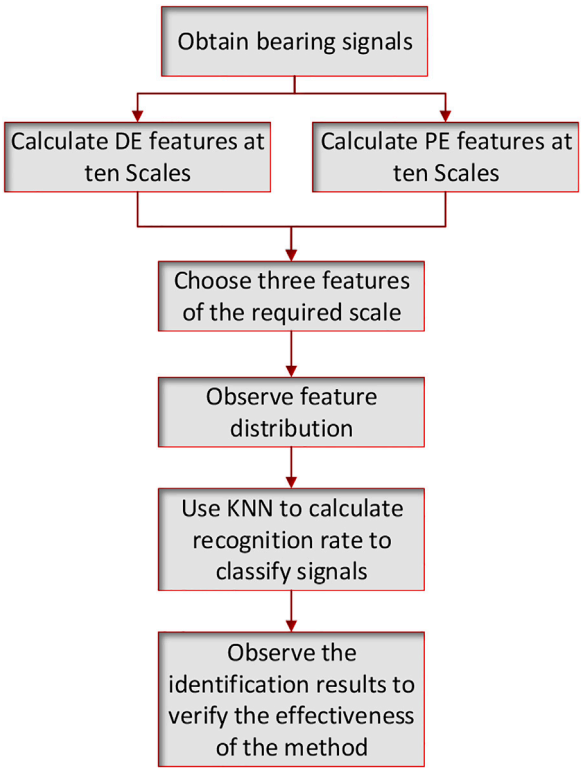

FIGURE 1
Detailed steps of the experiment.

$$z_j^c = Round\left(c \cdot y_j + 0.5\right) \tag{2}$$

(3) Construct the embedding vector based on the embedding dimension m and the time delay constant τ as follows:

$$z_j^{m,c} = \left\{z_j^c, z_{j+\tau}^c, \cdots z_{j+(m-1)\tau}^c\right\} \tag{3}$$

(4) Set $z_j^c = v_0, z_{j+\tau}^c = v_1, \cdots z_{j+(m-1)\tau}^c = v_{m-1}$, based on each embedded vector, a corresponding dispersion pattern can be obtained.

$$\pi_{v_0 v_1 \ldots v_{m-1}} (v = 1, 2, \cdots c) \tag{4}$$

(5) c^m dispersion patterns can be obtained in Step 4) with the following probabilities.

$$p\left(\pi_{v_0 v_1 \ldots v_{m-1}}\right) = \frac{Number\left\{t \mid t \le (m-1)\tau, \pi_{v_0 v_1 \ldots v_{m-1}}\right\}}{N - (m-1)\tau} \tag{5}$$

(6) Based on the above steps, the formula for calculating DE is as follows.

$$DE(x, c, m, \tau) = -\sum_{\pi=1}^{c^m} p\left(\pi_{v_0 v_1 \ldots v_{m-1}}\right) \ln\left(p\left(\pi_{v_0 v_1 \ldots v_{m-1}}\right)\right) \tag{6}$$

3 Steps of the experiment

The method proposed in this paper is a triple feature extraction method based on MDE and MPE, which is shown in Figure 1. The

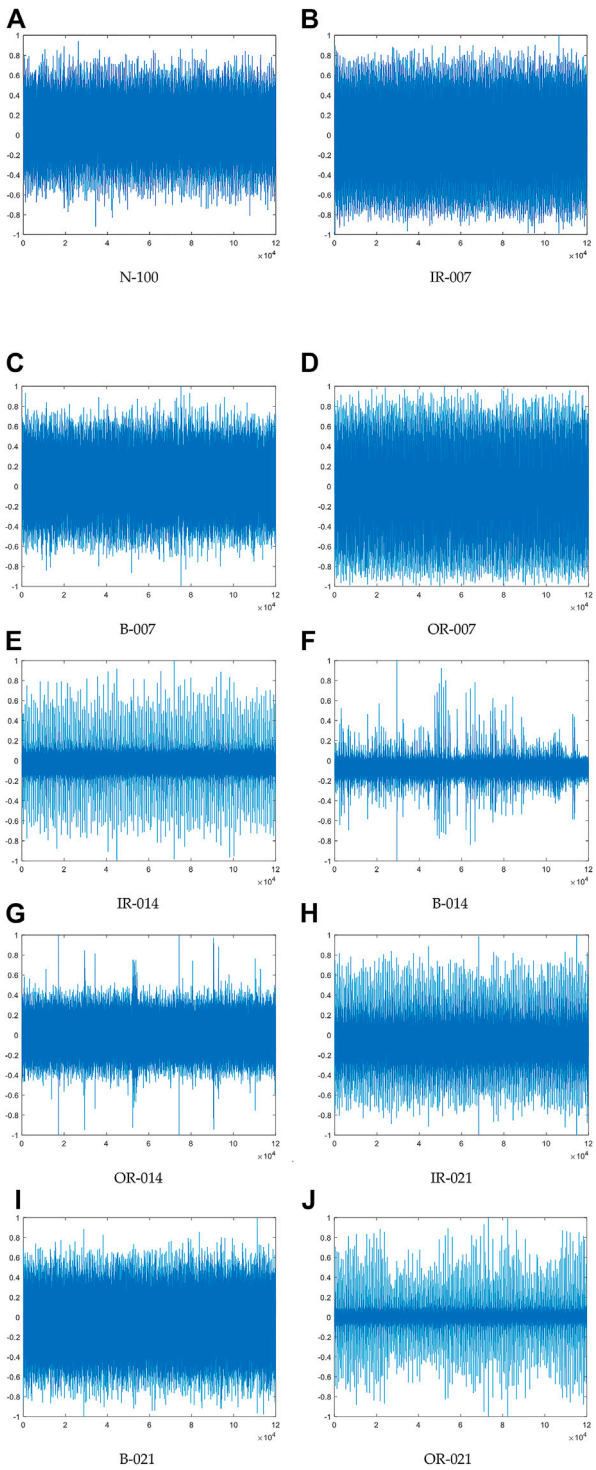

FIGURE 2
Ten types of bearing signals: **(A)** N-100, **(B)** IR-100, **(C)** B-100, **(D)** OR-100, **(E)** IR-014, **(F)** B-014, **(G)** OR-014, **(H)** IR-021, **(I)** B-021, **(J)** OR-021.

method combines scale 2 of MDE with scale 1 and 2 of MPE as three features of the signal, and combines these three features to identify the signal using a classifier. The specific experimental steps are as follows:

(1) Select bearing signals of different fault categories and sizes and divide the samples.
(2) Extract MDE and MPE features at ten scales from samples of these ten types of signals.
(3) Draw the triple feature distribution of the ten types of signals according to the selection principle of the highest recognition rate.
(4) Triple feature recognition by using KNN (k nearest neighbor) algorithm.
(5) Draw the recognition result and calculate the recognition rate to verify the validity of the method.

4 Rolling bearing signals

In order to identify the fault of bearing signal, this article has selected ten bearing signals in different states from Case Western Reserve University [27]. The first one is normal working signal, named N-100, the other nine are working signals in failure state. According to their three sizes (0.007, 0.014 and 0.021 feet) and three different fault locations (ball fault, inner race fault and outer race fault), the nine working signals are named IR-007, B-007, OR-007, IR-014, B-014, OR-014, IR-021, B-021, OR-021. Ten types of bearing signals are shown in Figure 2.

5 Feature extraction experiments

In this experiment, MDE at scale 2 and MPE at scale 1 and 2 are selected as the three features, and the entropy values at ten scales of these ten kinds of signals are calculated. When the scale is 1, the time series is itself. When the scale is larger than 1, the data used to calculate the entropy value is coarsened. The parameters used to calculate the entropy at different scales are the same. It is worth noting that after coarsening, the mean and variance of the data needed for calculating the normal distribution function within the dispersed entropy are still the original data. After calculating the entropy value features, the distribution and recognition of these features are observed and compared, and the feature extraction method used in this paper is verified.

5.1 Single feature extraction

Firstly, the parameters and sampling ranges are determined. The data used are from the ten types of bearing signals selected above. From the 1000th data point of the ten types of signals, 1,024 data points are taken as a sample, and 100 samples are taken for each type of signal. The parameters of these entropy are set as embedding dimension, number of classes, time delay, feature distribution of the ten scales of the two entropy is calculated and plotted. The ten scales of MDE are named as DE1, DE2,.DE10, and MPE is similarly named as PE1, PE2, . PE10. The horizontal coordinates of the graph are the number of samples. The vertical coordinate is the entropy value, and single feature distribution of ten scales of MDE for ten signals are shown in Figure 3.

It can be seen from Figure 3 that at scale 1, entropy values of these ten types of signals are arranged orderly, but there are still different degrees of

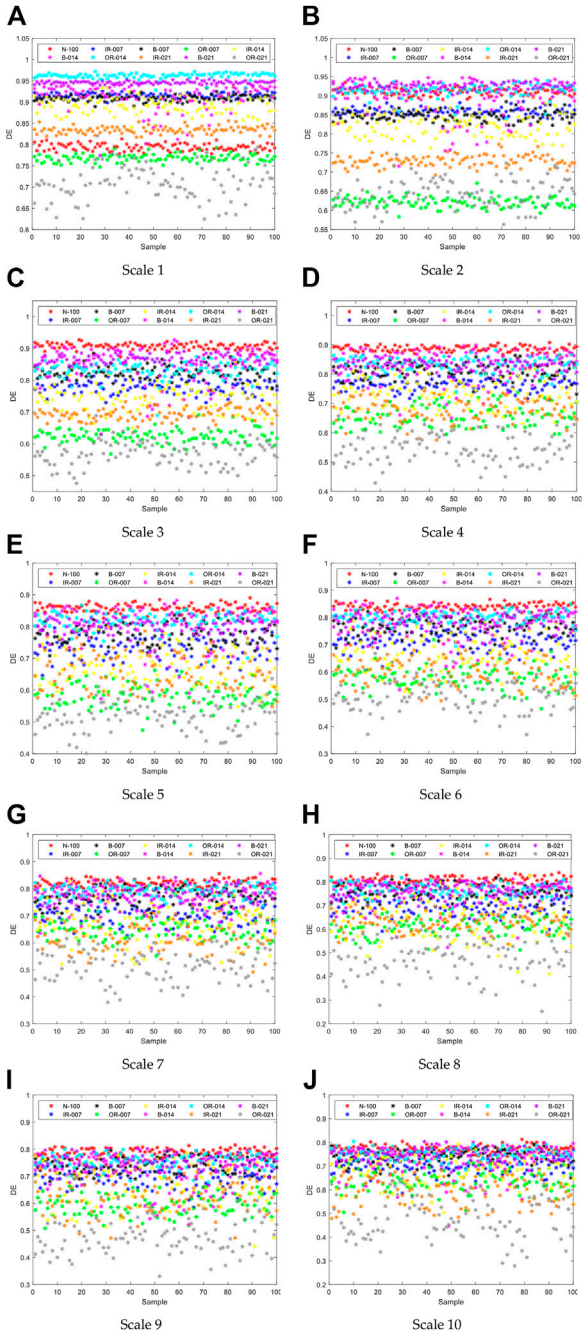

FIGURE 3
Single feature distribution of ten scales of MDE for ten signals: **(A-J)** represent Scale 1 to Scale10.

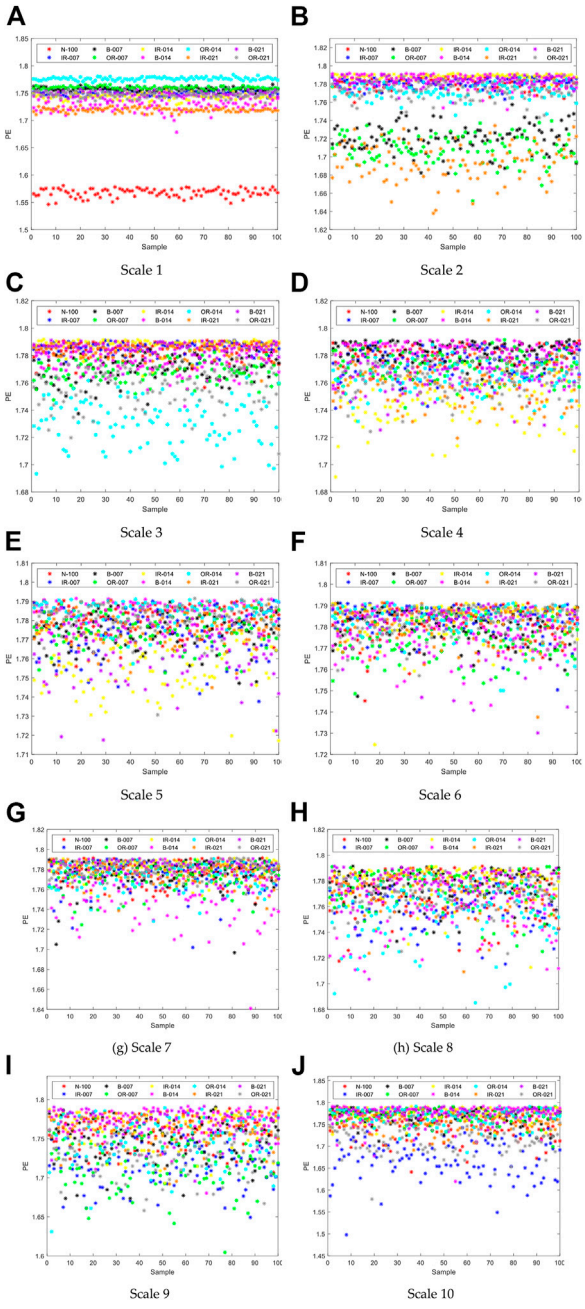

FIGURE 4
Single feature distribution of ten scales of MPE for ten signals: **(A-J)** represent Scale 1 to Scale10.

confusion between two different signals with adjacent distributions. With the increase of scale, the boundaries between various signals become blurred gradually, the effect of feature extraction becomes worse and the phenomenon of aliasing becomes more serious. From the point of view of distribution, the distribution of OR-021 is relatively scattered, while the distribution of other signals mostly concentrates in a certain interval. With the increase of scale, the entropy value gradually concentrates to around 0.8. Single feature distribution of ten scales of MPE for ten signals are drawn in Figure 4.

It can be seen from the Figure 4 that when scale 1 is used, the distribution of the entropy of all kinds of signals is relatively centralized, in which N-100 and OR-014 have less overlap with other signals. In other scales, the signal confusion is more serious. When the scale is 2, the signal entropy concentrates at 1.72 and 1.78. When the scale is greater than 3, the distribution of the ten types of signals is almost confounded. In order to obtain exact results, single feature recognition was performed on these features.

TABLE 1 Single feature recognition results for ten scales of MDE for ten types of signals.

Types	Recognition rate (%)									
	DE1	DE2	DE3	DE4	DE5	DE6	DE7	DE8	DE9	DE10
N-100	80	42	74	70	72	74	50	52	54	34
IR-007	38	60	62	40	22	40	30	34	26	26
B-007	34	38	44	20	40	36	10	18	20	18
OR-007	72	74	50	46	36	32	40	38	44	34
IR-014	62	50	18	28	26	20	20	18	12	8
S-014	30	18	26	22	14	8	6	4	16	10
OR-014	90	24	26	30	38	28	24	8	18	22
IR-021	90	84	74	32	28	32	26	30	10	34
B-021	86	44	54	26	32	26	10	24	6	16
OR-021	90	60	92	82	72	58	80	78	82	68
Average	67.2	49.4	52.0	39.6	38.0	35.4	29.6	30.4	28.8	27.0

According to Table 1, the recognition rate of ten kinds of signals under ten scales of MDE is not high. Except for scale 2 and scale 6, OR-021 had the highest recognition rate. Overall, the recognition rate shows a downward trend with the increase of the scale. When the scale increases to 6, the recognition rate for S-014 starts to be less than 10%. The recognition rate for the ten scales of B-007 and S-014 is less than 50%. Single feature recognition results for ten scales of MPE for ten types of signals are shown in Table 2.

TABLE 2 Single feature recognition results for ten scales of MPE for ten types of signals.

Types	Recognition rate (%)									
	PE1	PE2	PE3	PE4	PE5	PE6	PE7	PE8	PE9	PE10
N-100	100	20	16	16	14	10	20	20	20	16
IR-007	24	24	24	18	10	16	6	14	8	58
B-007	38	38	18	14	16	12	18	18	2	28
OR-007	54	40	24	10	6	16	10	12	46	24
IR-014	36	44	34	26	26	12	18	16	22	8
S-014	48	18	18	26	10	14	26	6	10	8
OR-014	100	32	62	22	14	10	8	22	6	8
IR-021	68	40	10	18	8	12	10	12	10	12
B-021	20	32	22	22	16	16	6	16	16	16
OR-021	20	24	28	12	10	10	8	8	16	20
Average	50.8	31.2	25.6	18.4	13.0	12.8	13.0	14.4	15.6	19.8

As can be seen from the Table 2, the performance of these ten kinds of signals using multi-scale permutation entropy is very poor, with an average recognition rate of 50.8% at scale 1 and less than 40% at the remaining nine scales. When the scale is larger than 3, the recognition rate is lower than 20%. When the scale is 1, the recognition effect is best. The recognition rates of N-100 and OR-014 are 100%, but the recognition rates of the remaining eight signals are not high. The recognition rate decreases significantly with the increase of scale, which is consistent with the feature distribution. The recognition rate of B-007 at scale 9 is only 2%.

5.2 Single feature recognition

After obtaining the characteristic distribution of these ten kinds of signals, a classification algorithm is needed to distinguish them. In this paper, KNN algorithm is selected, 50 of 100 samples are taken as training samples to train the algorithm, and the remaining 50 samples are taken as test samples to observe the classification effect. According to the results of single feature extraction, the single feature recognition results for ten scales with MDE for ten types of signals are shown in Table 1.

5.3 Triple feature extraction

To compare with the feature extraction method proposed in this paper, MSE is introduced in this section, and three features of the ten

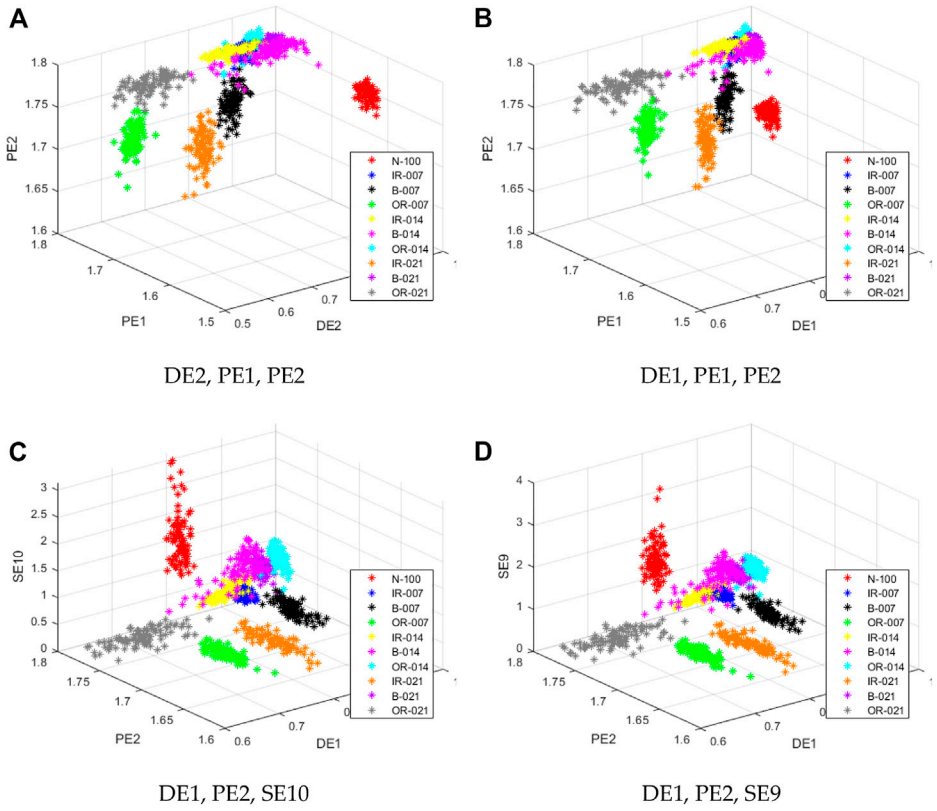

FIGURE 5
The distribution of features for the four best combinations of recognition results: **(A)** DE2, PE1, PE2 ; **(B)** DE1, PE1, PE2; **(C)** DE1, PE2, SE10; **(D)** DE1,PE2,SE9.

scales of the three entropies are combined. Sample selection and parameter setting of the entropy still follow the rules of single feature. Since there are 4,060 methods to select three of the 30 features, the selection of scale combination is based on the highest recognition rate in the experimental results and only four of the best results are obtained in this section: 1) Scale 2 of MDE and scale 1 and 2 of MPE; 2) Scale 1 of MDE and scale 1 and 2 of MPE; 3) Scale 1 of MDE, scale 2 of MPE and scale 10 of MSE; 4) Scale 1 of MDE, Scale 2 of MPE and Scale 9 of MSE. The distribution of features for the four best combinations of recognition results are shown in Figure 5.

From Figure 5, it can be seen that the distribution of all types of signals has been significantly different under the three features, among which N-100, B-007, OR-007, IR-021, OR-021 signals have little mixing with other signals. The remaining five signals have less mixing; All four of the best recognition results have the feature of MPE scale 2. To get a more specific and clear signal distinction, triple feature recognition is used for these features.

5.4 Triple feature recognition

In this section, KNN algorithm is still used to identify the three feature of the feature extraction results. 50 training samples and 50 test samples are still selected. The parameter settings are still the same as those of single feature recognition. Four recognition results maps with the highest recognition rate are drawn. The result figure and recognition rate table of triple feature recognition for ten types of signals are shown in Figure 6 and Table 3.

From Figure 6 and Table 3, it can be seen that the four combinations with the highest recognition rate have a considerable improvement over the recognition rate of single feature recognition, where the combination of scales are chosen based on the highest recognition rate in the experimental results. The average recognition rate of the four combinations has reached more than 90%, and only a few of the 100 samples of each type of signal have been misidentified. In the first combination with the highest recognition rate, the recognition rate of six types of signals is 100%, and the unreachable signals have considerable recognition

TABLE 3 Triple feature recognition rate for ten types of signals.

Combination of scales	DE2, PE1, PE2	DE1, PE1, PE2	DE1, PE2, SE10	DE1, PE2, SE9
Average recognition rate (%)	96.2	95.0	94.0	93.4

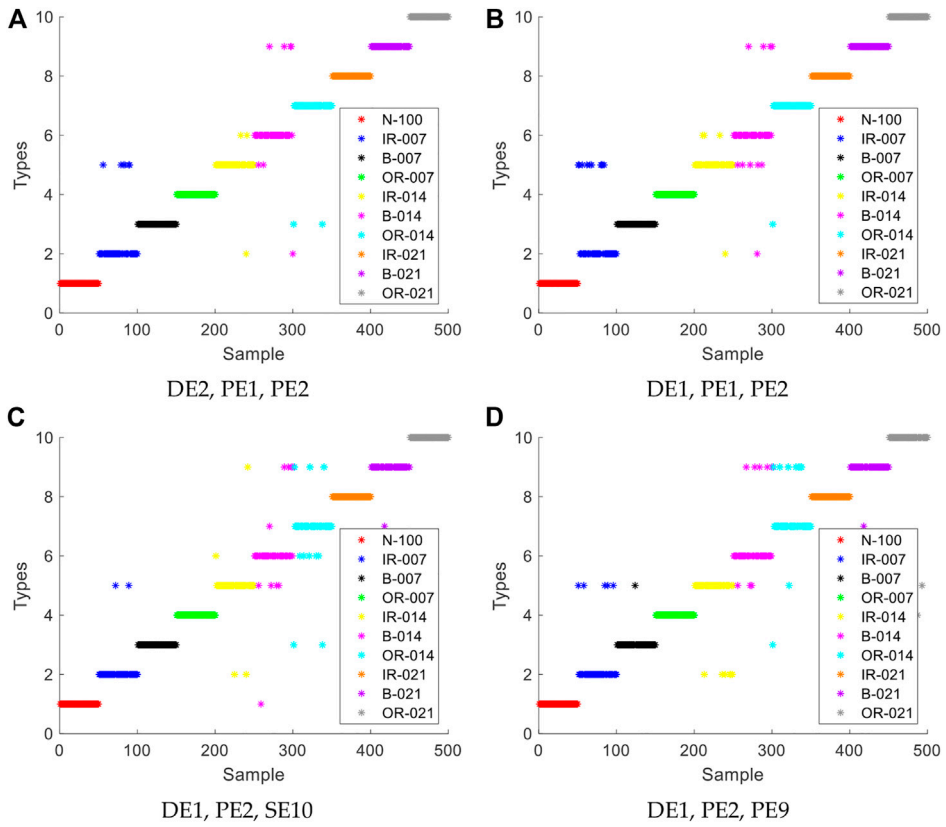

FIGURE 6
Triple feature recognition results for ten types of signals: **(A)** DE2, PE1, PE2 ; **(B)** DE1, PE1, PE2; **(C)** DE1, PE2, SE10; **(D)** DE1, PE2, SE9.

results. The combination of DE2, PE1 and PE2 presented in this paper has the highest recognition rate.

6 Conclusion

Fault signal recognition is the classification of time series, first extracts the features of the fault signal, and then uses the classification algorithm to classify the signal according to the features. In this paper, the multi-scale method is used to obtain the signal features at different scales, where the selection of scale combination is based on the highest recognition rate in the experimental results and only four of the best results are obtained in this section. Combining scale 2 of MDE with scale 1 and 2 of MPE, a triple feature extraction method is proposed to extract and identify the signal features. To verify the superiority of this method, ten types of rolling bearing fault signals are identified. The following are the main research conclusions:

(1) In the field of fault diagnosis, this paper introduces a triple feature extraction method based on scale 2 of MDE, scale 1 and 2 of MPE, and achieves good recognition results with the highest recognition rate of 96.2%.
(2) Combining the three types of entropy which have poor recognition effect in single feature experiment, the recognition ability has been improved significantly, and the recognition rate has been improved by 29%.
(3) The triple feature extraction methods proposed in this paper have a recognition rate of at least 1.2% higher than the other combinations of the three entropies, which can better diagnose the fault.

Data availability statement

Publicly available datasets were analyzed in this study. This data can be found here: [Online]. Available: http://csegroups.case.edu/bearingdatacenter/pages/download-data-file.

Author contributions

NZ and LW jointly discuss and determine the idea and method of the experiment. NZ is responsible for the whole feature extraction experiment, LW is responsible for the writing of the experiment part, and finally, NZ and LW are jointly responsible for the inspection and revision of the article.

Conflict of interest

The authors declare that the research was conducted in the absence of any commercial or financial relationships that could be construed as a potential conflict of interest.

Publisher's note

References

1. Wang T, Xu X, Pan H, Chang X, Yuan T, Zhang X, et al. Rolling bearing fault diagnosis based on depth-wise separable convolutions with multi-sensor data weighted fusion. *Appl Sci* (2022) 12(15):7640. doi:10.3390/app12157640

2. Yan X, Jia M. A novel optimized SVM classification algorithm with multi-domain feature and its application to fault diagnosis of rolling bearing. *Neurocomputing* (2018) 313:47–64. doi:10.1016/j.neucom.2018.05.002

3. Gao Y, Yu D. Intelligent fault diagnosis for rolling bearings based on graph shift regularization with directed graphs. *Adv Eng Inform* (2021) 47:101253. doi:10.1016/j.aei.2021.101253

4. Yao C, Wang S, Chen B, Mei G, Zhang W, Peng H, et al. An improved envelope spectrum via candidate fault frequency optimization-gram for bearing fault diagnosis. *J Sound Vibration* (2022) 523:116746. doi:10.1016/j.jsv.2022.116746

5. Li Y, Geng B, Jiao S. Dispersion entropy-based lempel-ziv complexity: A new metric for signal analysis. *Chaos, Solitons & Fractals*. (2022) 161:112400. doi:10.1016/j.chaos.2022.112400

6. Yuan X, Fan Y, Zhou C, Wang X, Zhang G. Research on twin extreme learning fault diagnosis method based on multi-scale weighted permutation entropy. *Entropy (Basel)* (2022) 24(9):1181. doi:10.3390/e24091181

7. Yang E, Wang Y, Wang P, Guan Z, Deng W. An intelligent identification approach using VMD-CMDE and PSO-dbn for bearing faults. *Electronics* (2022) 11(16):2582. doi:10.3390/electronics11162582

8. Huang NE, Shen Z, Long SR, Wu MC, Shih HH, Zheng Q, et al. The empirical mode decomposition and the hilbert spectrum for nonlinear and non-stationary time series analysis. *Proc Math Phys Eng Sci* (1998) 454(1971):903–95. doi:10.1098/rspa.1998.0193

9. Dragomiretskiy K, Zosso D. Variational mode decomposition. *IEEE Trans Signal Process* (2013) 62(3):531–44. doi:10.1109/tsp.2013.2288675

10. Prasannamoorthy V, Devarajan N. Fault detection and classification in power electronic circuits using wavelet transform and neural network. *J Comp Sci* (2011) 7(1):95–100. doi:10.3844/jcssp.2011.95.100

11. Li Y, Mu L, Gao P. Particle swarm optimization fractional slope entropy: A new time series complexity indicator for bearing fault diagnosis. *Fractal and Fractional* (2022) 6(7):345. doi:10.3390/fractalfract6070345

12. Li Y, Tang B, Yi Y. A novel complexity-based mode feature representation for feature extraction of ship-radiated noise using VMD and slope entropy. *Appl Acoust* (2022) 196:108899. doi:10.1016/j.apacoust.2022.108899

13. Ying W, Tong J, Dong Z, Pan H, Liu Q, Zheng J. Composite multivariate multi-scale permutation entropy and laplacian score based fault diagnosis of rolling bearing. *Entropy* (2022) 24(2):160. doi:10.3390/e24020160

14. Fei C, Tian W, Zhang L, Li J, Chen D, Chen D, et al. fault diagnosis of power transformer based on time-shift multiscale bubble entropy and stochastic configuration network. *Entropy* (2022) 24(8):1135. doi:10.3390/e24081135

15. Li Y, Geng B, Tang B. Simplified coded dispersion entropy: A nonlinear metric for signal analysis. *Nonlinear Dyn* (2023) 2023. doi:10.1007/s11071-023-08339-4

16. Luis M, Rossana C, Leandro P. On the use of approximate entropy and sample entropy with centre of pressure time-series. *J neuroengineering Rehabil* (2018) 15(1):116. doi:10.1186/s12984-018-0465-9

17. Pincus SM. Approximate entropy as a measure of system complexity. *Proc Natl Acad Sci United States America* (1991) 88(6):2297–301. doi:10.1073/pnas.88.6.2297

18. Yan R, Liu Y, Robert X. Permutation entropy: A nonlinear statistical measure for status characterization of rotary machines. *Mech Syst Signal Process* (2012) 29:474–84. doi:10.1016/j.ymssp.2011.11.022

19. Rostaghi M, Reza Ashory M, Azami H. Application of dispersion entropy to status characterization of rotary machines. *J Sound Vibration* (2019) 438:291–308. doi:10.1016/j.jsv.2018.08.025

20. Li Y, Tang B, Geng B, Jiao S. Fractional order fuzzy dispersion entropy and its application in bearing fault diagnosis. *Fractal and Fractional* (2022) 6(10):544. doi:10.3390/fractalfract6100544

21. Costa M, Goldberger Ary L, Peng C-K. Multiscale entropy analysis of complex physiologic time series. *Phys Rev Lett* (2002) 89(6):068102. doi:10.1103/physrevlett.89.068102

22. Li Y, Jiao S, Geng B. Refined composite multiscale fluctuation-based dispersion Lempel–Ziv complexity for signal analysis. *ISA Trans* (2023) 133:273–84. doi:10.1016/j.isatra.2022.06.040

23. Costa M, Goldberger AL, Peng C-K. Multiscale entropy analysis of complex physiologic time series. *Phys Rev Lett Americam Physiol Soc* (2002) 89(6):068102. doi:10.1103/physrevlett.89.068102

24. Aziz W, Arif M. Multiscale permutation entropy of physiological time series. In: Proceedings of the 9th International Multitopic Conference; December 23-24, 2005; Karachi, Pakistan (2005).

25. Azami H, Escudero J. Coarse-graining approaches in univariate multiscale sample and dispersion entropy. *Entropy* (2018) 20(2):138. doi:10.3390/e20020138

26. Azami H, Rostaghi M, Escudero J. Refined composite multiscale dispersion entropy: A fast measure of complexity. *IEEE Trans Biomed Eng* (2016) 64:01379. doi:10.1109/TBME.2017.2679136

27. Smith WA, Randall RB. Rolling element bearing diagnostics using the case western reserve university data: A benchmark study. *Mech Syst Signal Process* (2015) 64:100–31. doi:10.1016/j.ymssp.2015.04.021

frontiers | Frontiers in Physics

TYPE Methods
PUBLISHED 05 June 2023
DOI 10.3389/fphy.2023.1205935

OPEN ACCESS

EDITED BY
Yuxing Li,
Xi'an University of Technology, China

REVIEWED BY
Zhenan Yao,
East China University of Technology, China
Xiao Chen,
Shaanxi University of Science and Technology, China

*CORRESPONDENCE
Chuan He,
chuanheus@163.com

RECEIVED 14 April 2023
ACCEPTED 22 May 2023
PUBLISHED 05 June 2023

CITATION
Yu Z, Huang Y, Fang Z, Tan Y and He C (2023), Adaptive noise suppression for low-S/N microseismic data based on ambient-noise-assisted multivariate empirical mode decomposition. *Front. Phys.* 11:1205935. doi: 10.3389/fphy.2023.1205935

Adaptive noise suppression for low-S/N microseismic data based on ambient-noise-assisted multivariate empirical mode decomposition

Zhichao Yu[1,2], Yingkun Huang[1], Zisen Fang[1], Yuyang Tan[3] and Chuan He[4]*

[1]National Supercomputing Center in Shenzhen, Shenzhen, China, [2]State Key Laboratory of Lithospheric Evolution, Institute of Geology and Geophysics, Chinese Academy of Sciences, Beijing, China, [3]Key Lab of Submarine Geosciences and Prospecting Techniques MOE, Frontiers Science Center for Deep Ocean Multispheres and Earth System, College of Marine Geosciences, Ocean University of China, Qingdao, China, [4]School of Earth and Space Sciences, Peking University, Beijing, China

Microseismic monitoring data may be seriously contaminated by complex and nonstationary interference noises produced by mechanical vibration, which significantly impact the data quality and subsequent data-processing procedure. One challenge in microseismic data processing is separating weak seismic signals from varying noisy data. To address this issue, we proposed an ambient-noise-assisted multivariate empirical mode decomposition (ANA-MEMD) method for adaptively suppressing noise in low signal-to-noise (S/N) microseismic data. In the proposed method, a new multi-channel record is produced by combining the noisy microseismic signal with preceding ambient noises. The multi-channel record is then decomposed using multivariate empirical mode decomposition (MEMD) into multivariate intrinsic mode functions (MIMFs). Then, the MIMFs corresponding to the main ambient noises can be identified by calculating and sorting energy percentage in descending order. Finally, the IMFs associated with strong interference noise, high-frequency and low-frequency noise are filtered out and suppressed by the energy percentage and frequency range. We investigate the feasibility and reliability of the proposed method using both synthetic data and field data. The results demonstrate that the proposed method can mitigate the mode mixing problem and clarify the main noise contributors by adding additional ambient-noise-assisted channels, hence separating the microseismic signal and ambient noise effectively and enhancing the S/Ns of microseismic signals.

KEYWORDS

microseismic monitoring, seismic signal, interference noise, noise suppression, multivariate empirical mode decomposition

1 Introduction

Microseismic monitoring technology is a useful tool for characterizing the structures, physical properties, and dynamic processes in the subsurface within a target region. This technique has been widely used in the monitoring of hydraulic fracturing in hydro-carbon reservoirs [1–3], coal mining [4, 5], geothermal exploration [6, 7], and CO_2 capture and

storage (CCS) [8]. Single-component (1-C) or three-component (3-C) receivers installed at the surface and/or in the borehole are anticipated to record not only the seismic event signals but also high-energy interference noises and random noises generated by motions such as mechanical vibrations [9–11]. Various excitations and strong noises could significantly reduce the detectability of weak but useful seismic signals in the monitoring data, thereby compromising the reliability of data processing and interpretation [12–14]. Therefore, it is essential to develop an effective method to suppressing interference noise in microseismic monitoring data.

Low signal-to-noise (S/N) microseismic recordings are usually abandoned without applying adequate denoising methods due to the small magnitudes of microseismic events obscured by noisy recording environments. Frequency-domain band-pass filtering is the most commonly used method in seismic monitoring processing for attenuating background noises and extracting microseismic signals, but the effect of this method may not be very satisfying if the background noises and microseismic signals are in the same frequency range. Researchers have made a great effort to develop novel methods for noise suppression and microseismic signal enhancement, such as polarization filtering [15], median filtering [16], mathematical morphology filtering [17], the singular value decomposition-based method [18, 19], and the time-frequency transform-based method [20–24]. In addition to high-frequency noise, the background interference noises are also of concern [13, 17, 21, 22]. Because the characteristics of microseismic signals in the noisy monitoring data are usually unclear, conventional denoising methods struggle to suppress the strong-energy, long-duration interference noises and retain the energy of microseismic signals. Thus, the improvement in the S/N of microseismic data is often limited.

Mode decomposition algorithms can adaptively decompose the nonlinear and nonstationary signals to analyze the local characteristic time scale and have been widely applied in seismic/microseismic signal processing, mechanical fault detection, structural health monitoring, and biomedical signal analysis [19, 25–31]. To overcome the problems of mode mixing, end effect, and lack of adaptability, mode-decomposition algorithms have progressed from empirical mode decomposition (EMD) [25] to ensemble empirical mode decomposition (EEMD) [27], complementary ensemble empirical mode decomposition (CEEMD) [28, 29], and variational mode decomposition (VMD) [30, 31]. By iteratively extracting the high-frequency components and their associated envelopes, the complex signal is decomposed into a set of intrinsic mode functions (IMFs) in the empirical mode decomposition based algorithms. Similarly, the VMD methods employ an optimization framework to separate the complex signal into multiple modes. To deal with multivariate data, the multivariate extension of EMD (i.e., multivariate EMD, or MEMD for short) and VMD (i.e., multivariate VMD, or MVMD for short) are proposed for processing multivariate data to obtain the IMFs with aligned frequency ranges [32–35]. Noise-assisted MEMD (NA-MEMD) [33], partial noise-assisted MEMD (PNA-MEMD) [36], and sinusoidal signal-assisted MEMD (SA-MEMD) [37] and harmonic-assisted MEMD (HA-MEMD) [38] are subsequently proposed to improve the performance of the MEMD method by adding additional channels with independent white noise, high-frequency band-limited noise, and a sinusoidal assisted signal, respectively.

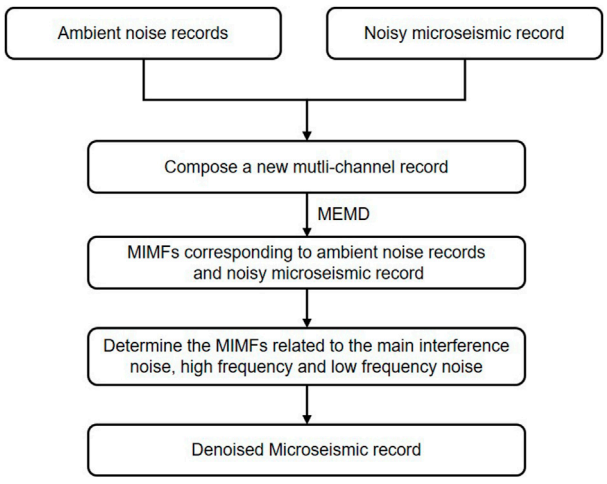

FIGURE 1
The flowchart of the proposed method.

These mode-decomposition algorithms have been widely employed in seismic/microseismic data denoising and arrival picking [19, 39–44]. The separation or reconstruction of signals is often accomplished in the mode decomposition based methods and their improvement approaches by the selection of IMF components. When reconstructing the signal, metrics like as correlation coefficient, kurtosis, mutual information entropy, and other parameters that characterize the signals of each IMF are calculated to provide various weight coefficients that emphasize the target signal. However, the study of low signal-to-noise ratio microseismic signals are hampered by noise because real-world signals are typically nonlinear and accompanied by strong ambient noise, and the features extracted directly from these signals usually contain a large amount of useless as well as noisy information that cannot effectively distinguish seismic signals from noise. Compared to the interference noises with long durations and high energies, the microseismic signals show very short duration (<1s) and unpredictable energies in the field data. The Low-S/N microseismic event may be identified from continuous recordings using rigorous detection thresholds, thus, the adaptive and effective separation of background noise and weak microseismic signal is critical for subsequent data processing. In this paper, we develop an adaptive noise suppressing method for microseismic data processing based on ambient-noise-assisted multivariate empirical mode decomposition (ANA-MEMD). In the proposed method, a new multichannel record that combines the noisy microseismic recording with preceding ambient noises is decomposed by the MEMD method into multivariate intrinsic mode functions (MIMFs). Then, the ambient records are utilized to assist in decomposing microseismic data and identifying main noise contributors. In this study, we first introduce the theory of EMD and MEMD, then elaborate on the ANA-MEMD method for noise suppression in microseismic data. Finally, we evaluate

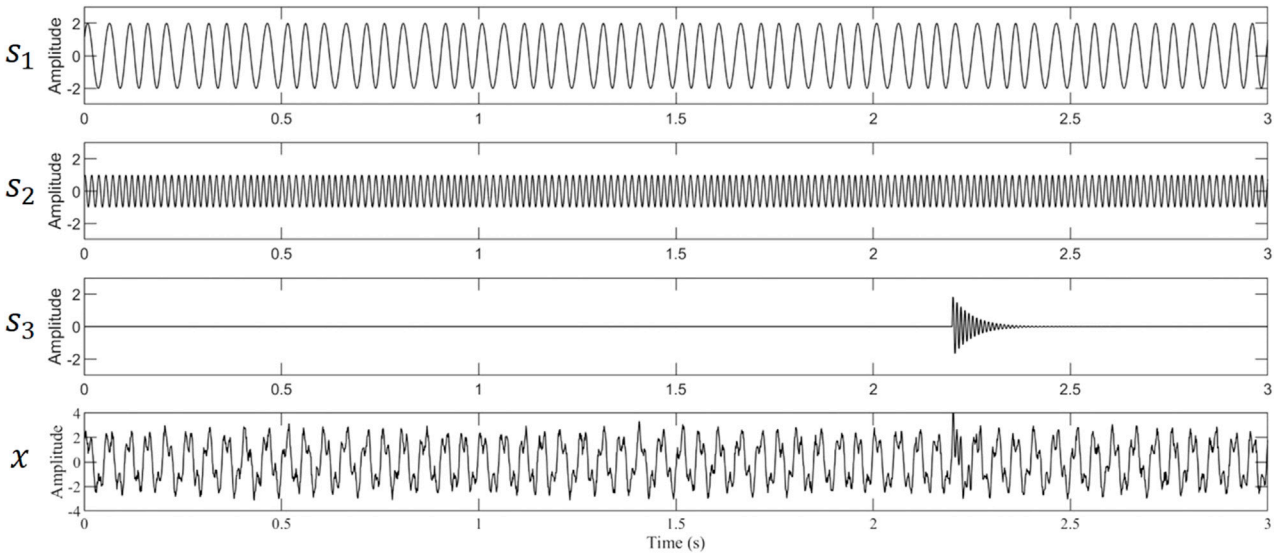

FIGURE 2
Single-component synthetic noisy microseismic recording.

the performance of the proposed method by using synthetic and field data.

2 Methods

2.1 Empirical mode decomposition

As a data-driven approach, empirical mode decomposition (EMD) decomposes a signal adaptively into a finite set of oscillatory components known as intrinsic mode functions (IMFs) [25]. The original signal can be recovered by reconstructing all IMFs, which represent different vibrations whose instantaneous frequency reflects the local characteristics of the input signal. Two conditions are essential for calculating an IMF: 1) the number of extrema and the number of zero crossings should be different only by one; 2) the mean value of the upper and lower envelopes should be roughly zero [25]. In the EMD method, the decomposition is accomplished by removing the slowly oscillatory modes and separating the rapidly oscillating modes from the data. For a real-valued signal $x(t)$, it can be decomposed into

$$x(t) = \sum_{m=1}^{M} d_m(t) + r(t), \tag{1}$$

where $d_m(t)$ represents the mth IMF and $r(t)$ is the residual component.

Although a complex signal can be decomposed into several IMFs by EMD, the application of real data may be restricted by the mode-mixing problem due to the intermittency of a signal component or closely spaced spectral tones. To address the limitation of mode mixings, ensemble empirical mode decomposition (EEMD) [27, 40] and complementary ensemble empirical mode decomposition (CEEMD) [28, 29] are proposed successively by taking the noises into consideration. The purpose of incorporating white noise is to perturb the signal in its true solution neighborhood and ensure the extreme value points are distributed uniformly during the sifting process, therefore restraining mode-mixing.

2.2 Multivariate empirical mode decomposition

Signal acquisition using multicomponent receivers or multiple receivers is prevalent in engineering applications. The characteristic analysis of the system may be impacted by a scale arrangement uncertainty problem when each signal is decomposed independently using the EMD approach. Multivariate empirical mode decomposition has been introduced to overcome this issue by performing the same mode analysis on multivariate signals in various frequency scales and ensuring that each signal's IMF number after decomposition is identical [32]. In the MEMD approach, a uniform sampling scheme based on the Hammersley sequence is used to calculate direction vectors. The n-dimensional signal envelops are obtained by taking a sequence of projection vectors along different directions in the n-dimensional space. After interpolating their extrema, the envelopes are averaged to generate the local mean of signals. One multivariate intrinsic mode function (MIMF) is produced by calculating the difference of the mean of all envelopes with respect to the original signals. This process is repeated until a sufficient number of MIMFs has been obtained or the stopping criterion is met. The MEMD decomposes a multivariate signal $\mathbf{X}(t)$ as

$$\mathbf{X}(t) = \sum_{m=1}^{M} \mathbf{d}_m(t) + \mathbf{r}(t), \tag{2}$$

where $\mathbf{d}_m(t)$ represents the *m-th* MIMF and the residual component $\mathbf{r}(t)$ represents the final trend. The detail procedures of the MEMD algorithm can be described as follows.

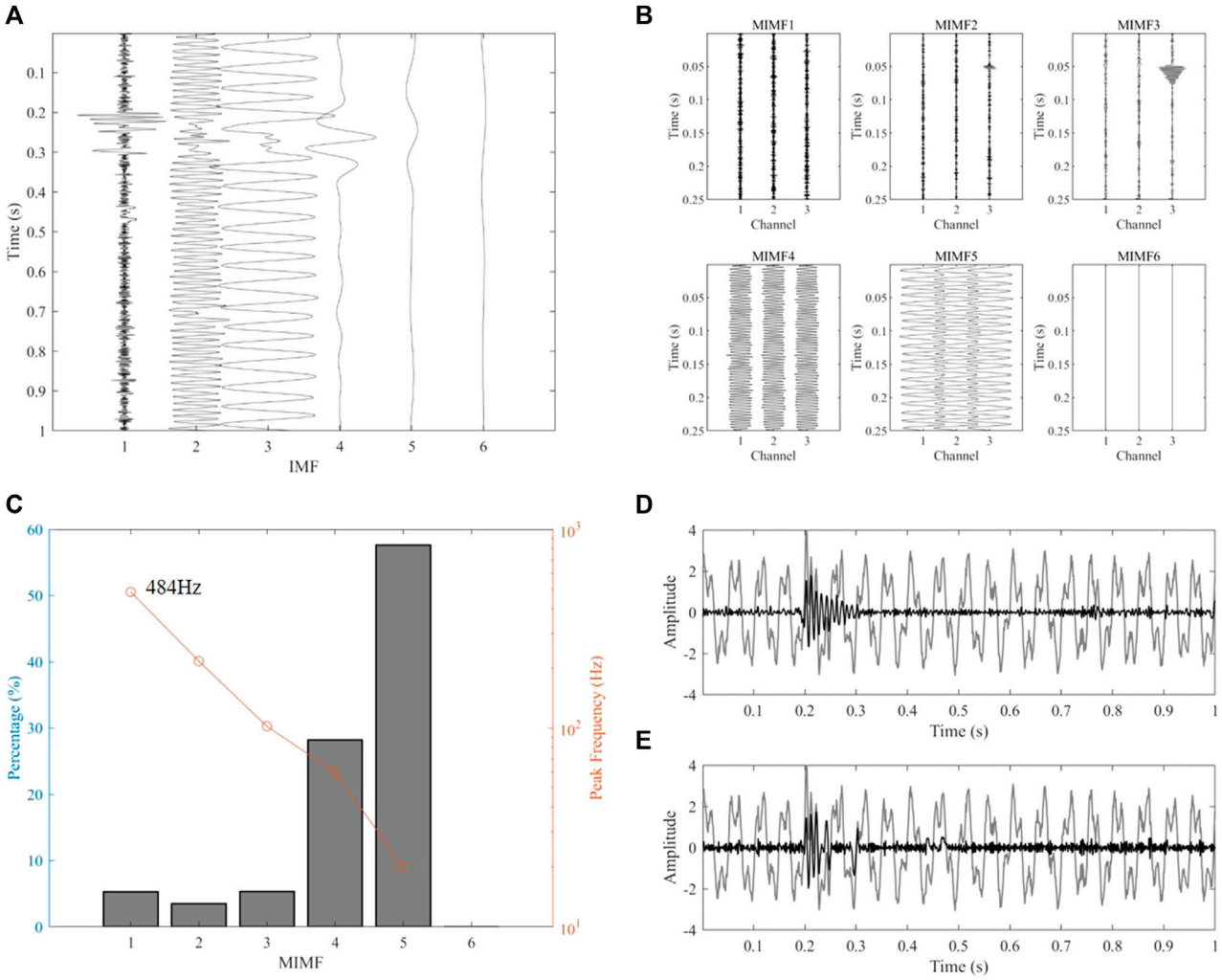

FIGURE 3
(A) Decomposition results of noisy microseismic waveform by the EMD method. **(B)** Decomposition results of the noisy microseismic waveform by the ANA-MEMD method. **(C)** The energy percentages of the IMFs in assisted channel and the peak frequencies of the IMFs in noisy microseismic record channel. **(D)** Comparison of the waveforms before (grey line) and after (black line) noise suppression by the proposed method. **(E)** Comparison of the waveforms before (grey line) and after (black line) noise suppression by the EMD method.

(1) Create a uniform sampling point set on an $(n\text{-}1)$-dimensional sphere using the Hammersly sequence, and establish an n-dimensional spatial direction vector.
(2) Obtain the project sets $P^{\theta_k}(t)$ of the input signal $\mathbf{X}(t)$ along all direction vector $\boldsymbol{V}^{\boldsymbol{\theta_k}}$ for a set of K direction vectors.
(3) Find the time instants $t_i{}^{\theta_k}$ corresponding to the maxima of the set of projected signals $P^{\theta_k}(t)$, and obtain multivariate envelop curves $\boldsymbol{e}^{\theta_k}(t)$ using the spline interpolation function.
(4) Calculate the mean value using $\mathbf{m}(\mathrm{t}) = \sum_{k=1}^{K} \boldsymbol{e}^{\theta_k}(t)/K$.
(5) Extract the detail $\mathbf{d}(t)$ by calculating $\mathbf{d}(t) = \mathbf{x}(t) - \mathbf{m}(t)$, and check whether $\mathbf{d}(t)$ satisfies the stopping criterion for a multivariate IMF. If $\mathbf{d}(t)$ satisfies the stopping criterion, apply the above procedure to $\mathbf{X}(\mathrm{t}) - \mathbf{d}(t)$; otherwise, apply it to $\mathbf{d}(t)$.

As a multivariate extension of EMD, the MEMD is a significant improvement in multichannel signal processing, allowing for adequate alignment between the same index IMFs and facilitating inherent multiscale analysis. Similar to the standard EMD method, the mode mixing problem still exists in the MEMD method. To solve this issue, additional channels containing auxiliary signals are used to help the decomposition of the original multivariate signal, such as noise-assisted MEMD (NA-MEMD) [33], partial noise-assisted multivariate EMD (PNA-MEMD) [36], a sinusoidal signal-assisted MEMD (SA-MEMD) [37], and high-frequency harmonic-assisted MEMD (HA-MEMD) [38]. For the original n-dimensional multivariate signal, l-dimensional extra channels are added and then processed using the MEMD method as an $(n + l)$-dimensional signal. These methods can be summarized as follows.

(1) Generate l-dimensional assisted channels that are of the same length as the original multivariate signal;
(2) Combine the n-dimensional input multivariate signal with the assisted channels created in Step **1**) to construct an $(n + l)$-dimensional signal;

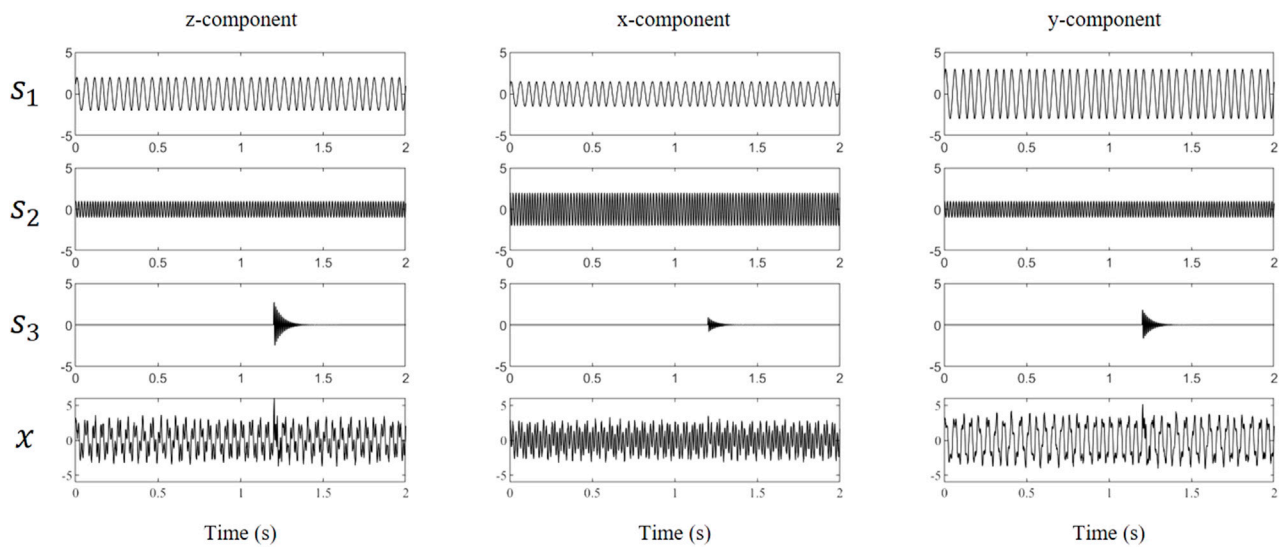

FIGURE 4
Three-component synthetic noisy microseismic recording.

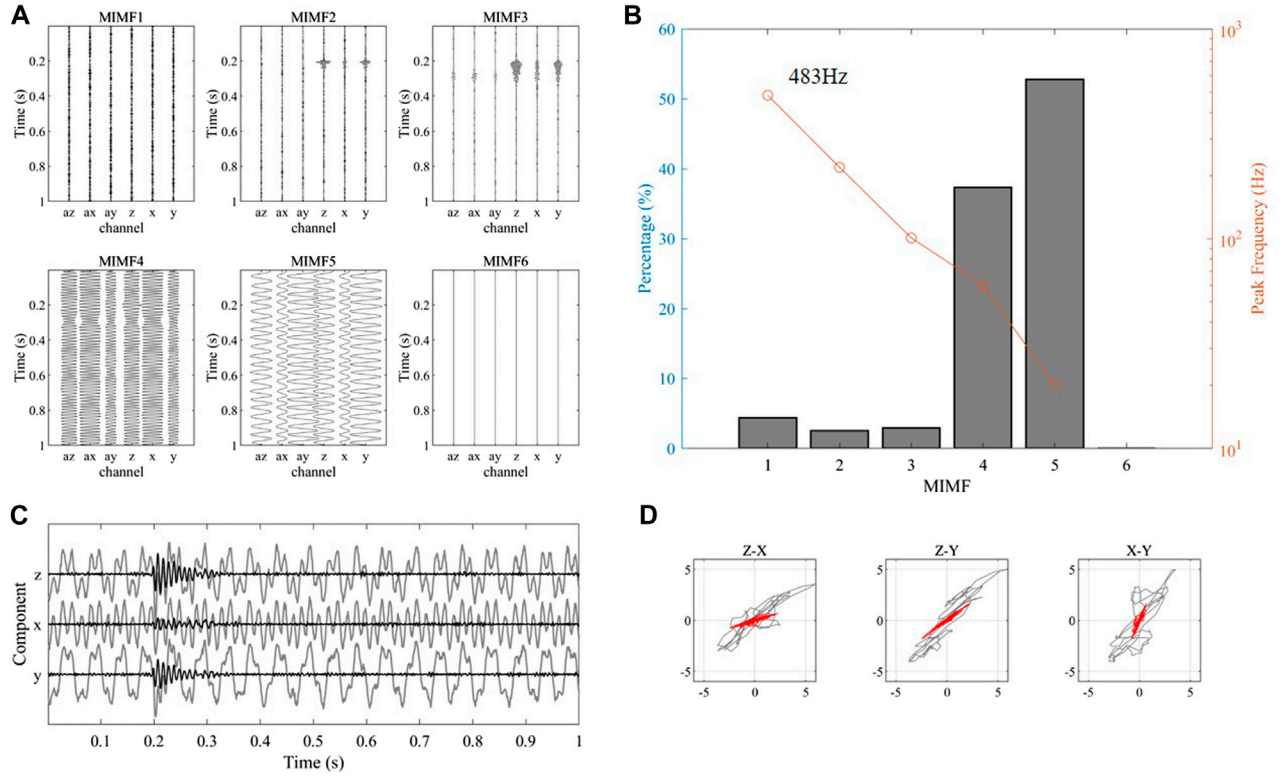

FIGURE 5
(A) Decomposition results of the 3-C noisy microseismic waveform by the ANA-MEMD method. **(B)** The energy percentages of the MIMFs in assisted channels and the peak frequencies of the MIMFs in noisy microseismic record channels. **(C)** Comparison of the waveforms before (grey lines) and after (black lines) noise suppression by the proposed method. **(D)** Comparison of the three-component seismic signal before (grey lines) and after (red lines) noise suppression by the proposed method.

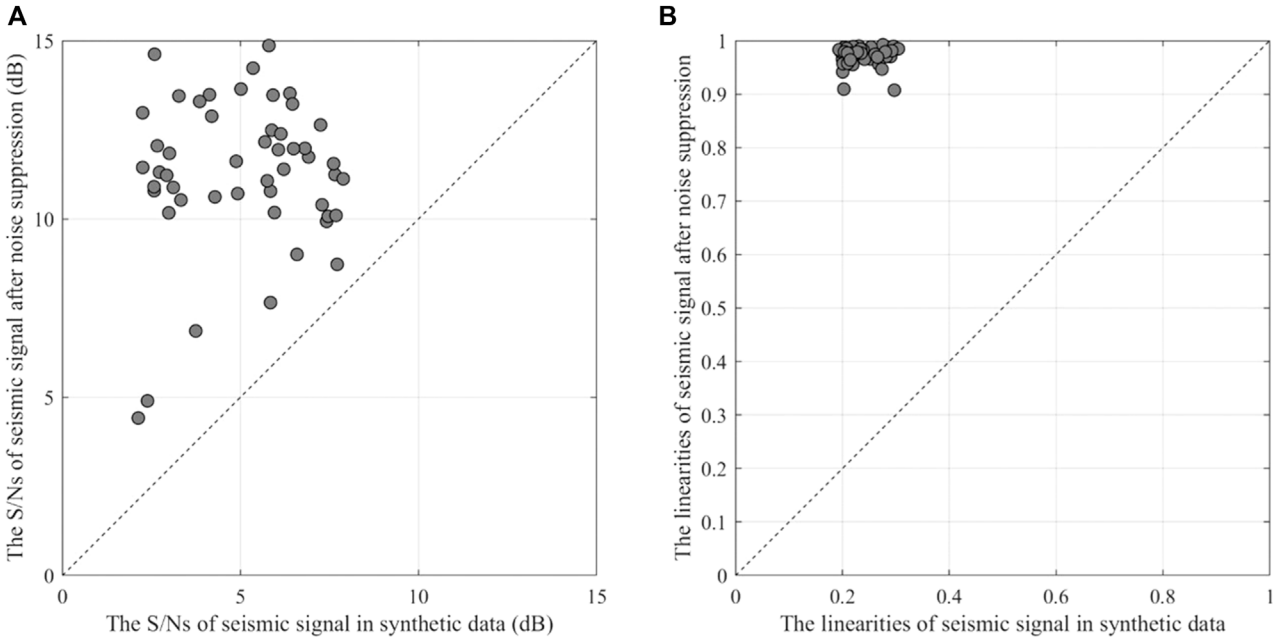

FIGURE 6
Comparison of S/Ns **(A)** and the linearities **(B)** of the three-component seismic signals before and after noise suppression by the proposed method in different tests.

(3) Decompose the new multivariate signal using the MEMD algorithm to extract the multivariate IMFs;
(4) Remove the l-dimensional IMFs related to the assisted signals from the multivariate IMFs in Step **3**) and retain the n-dimensional IMFs related to the original signal.

It is worth noting that, except from differences in additional channels, these improved methods maintain the same processing flow as standard MEMD method.

2.3 Adaptive noise suppression based on ambient-noise-assisted MEMD (ANA-MEMD)

Microseismic monitoring data can be expressed as

$$\mathbf{X} = \mathbf{AS}. \tag{3}$$

where $\mathbf{S} = [s_1, s_2, \ldots, s_K]^T$ represent K source signals, $\mathbf{X} = [x_1, x_2, \ldots, x_M]^T$ represent M observation signals, and $\mathbf{A}$ is the relation matrix between source signals and observation signals. The source signal could be seismic signal or noise. The observation signal can represent recordings at different locations, time windows, and components. In continuous recordings, the duration of ambient noise (e.g., interference noises produced by pumps or industries in continuous operation, >>1 min) is substantially longer than that of seismic events (<1 s). The interference noises in the ambient recording persist throughout successive time windows.

In this study, we present ambient-noise-assisted multivariate empirical mode decomposition (ANA-MEMD) for decomposing noisy microseismic data and remove non-effective components for S/N enhancement of microseismic data. The auxiliary channels containing ambient noise are introduced in the decomposition process, which differs from the standard MEMD technique. To determine whether one MIMF (or IMF for single-component microseismic data) contains ambient noise, we calculate the energy percentage of the assisted ambient noise in each decomposed MIMF (or IMF for single-component microseismic data). In our method, strong interference noise is considered to persist and constitute the predominant portion of the ambient record. Finally, the MIMFs (or IMFs) components associated with ambient noise and outside the desired signal band are eliminated during the reconstruction process. Our method is organized as follows.

(1) For a low-S/N microseismic signal recording with a time window length of Nwin, we select ambient recordings with the same time window length preceding the microseismic data as additional assisted channels. In general, two window for single-component microseismic data, and one window for 3-C microseismic data. Strong random signals (including coherent seismic signals) must not be present in the additional assisted channels.
(2) After constructing a new multivariate signal by adding the noisy microseismic data with the above-assisted channels, we obtain the multivariate IMFs $\mathbf{d}_m(t)$ and $\mathbf{c}_m(t)$ using the MEMD algorithm. $\mathbf{d}_m(t)$ and $\mathbf{c}_m(t)$ are the *m-th* MIMFs corresponding to noisy microseismic data and assisted ambient noise, respectively.
(3) We calculate and sort the energy percentage of each MIMF $\mathbf{c}_m(t)$ in descending order, and obtain the peak frequency of each MIMF $\mathbf{d}_m(t)$.

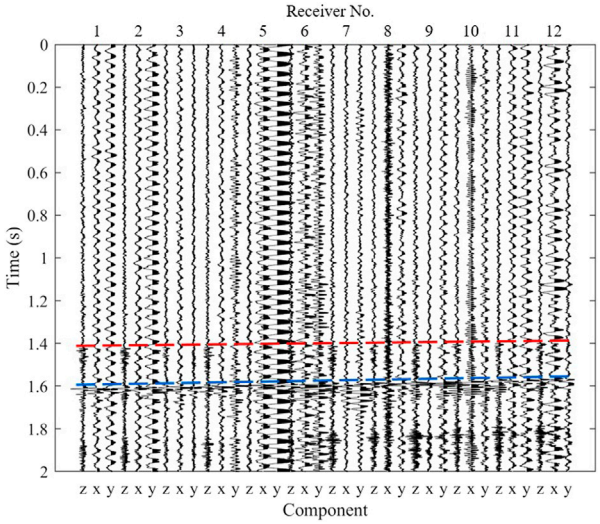

FIGURE 7
The waveforms of one low-S/N microseismic event. Red and blue dashed line represent the arrival times of P-wave and S-waves, respectively.

(4) Pre-set the band range $[f_l, f_h]$ determine high frequency and low frequency noise, and find the dominant noise according to a threshold value of the energy percentage. The IMFs with a large energy percentage are potential interference noise. The microseismic data after noise suppression can be reconstructed by $\boldsymbol{X}'(t) = \boldsymbol{X}(t) - \sum \boldsymbol{d}_{M_1}(t)$, where M_1 is the index of qualified MIMFs.

The above procedure is applicable to both single-component data and three-component microseismic data. The flowchart of the proposed method is shown in Figure 1.

3 Numerical examples

In this section, we demonstrate the performance of the proposed method using both single-component and three-component synthetic microseismic data. The synthetic signal is composed of two time-varying oscillation signals (regarded as persistent interference noises) with dominant frequencies of 20 Hz and 60 Hz, and an attenuated sine wave (regarded as seismic signal), which has the peak frequency of 100 Hz. Its composed components are expressed as the following equations.

$$\begin{cases} s_1 = \sin\ (2\pi 20t + 0.5\cos 2\pi 5t) \\ s_2 = \sin\ (2\pi 60t + 0.8\cos 2\pi 6t) \\ s_3 = \sin(2\pi 100(t - t_0))^* e^{-0.02(t-t_0)} \end{cases} \tag{4}$$

Where t_0 is the arrival time of seismic signal.

First, the above three source signals with the maximum amplitude ratio of 2:1:2 and Gaussian noise with the amplitude variance of 0.1 were applied to generate one single-component synthetic microseismic recording. The arrival time of seismic signal is 2.2 s and the sampling frequency is 1000 Hz. Figure 2 shows the waveforms of the synthetic microseismic data, it can be seen that the seismic signal becomes blurred due to the strong interference noise.

We compared the decomposition results of the synthetic microseismic record using the EMD method and the proposed ANA-MEMD method. Two 1-s long background noise recordings (0~1 s and 1~2 s) before the seismic signals were employed as extra assisted channels. Figures 3A, B illustrate the six IMFs that decomposed by above two methods, respectively. Channel 1, 2, and 3 in Figure 3B represent the IMFs corresponding to two background noise recordings and noisy microseismic signal, respectively. There is no doubt that the phenomenon of mode mixing has been alleviated by the addition of auxiliary noise channels. We demonstrated the viability of the proposed method in noise suppression using the aforementioned decomposition results. We calculated the energy percentage of each IMF in the ambient noise assisted channels (channel 1–2 in Figure 3B) and the peak frequency of each IMF in the noisy microseismic signal channel (channel 3 in Figure 3B), as shown in Figure 3C. By determining IMF related to the top two energy percentage (IMF 4 and 5, cumulative percentage greater than 80%), the high frequency noise (IMF1, the peak frequency >200 Hz), and the low frequency noise (IMF 6, the peak frequency <10 Hz), the IMF that contains the ambient noise can be identified. The denoised microseismic records by the proposed method and EMD method can be obtained by reconstructing the remaining IMFs, as shown in Figures 3D, E. Compared to the result of EMD method (black line in Figure 3E), the arrival of the seismic signal is clearly visible in the denoised waveform (black line in Figure 3D), while preserving as much the microseismic signal as possible.

Three-component synthetic microseismic recording was constructed by the above three source signals and a mixing matrix and Gaussian noise with the amplitude variance of 0.2. The mixing matrix is given as

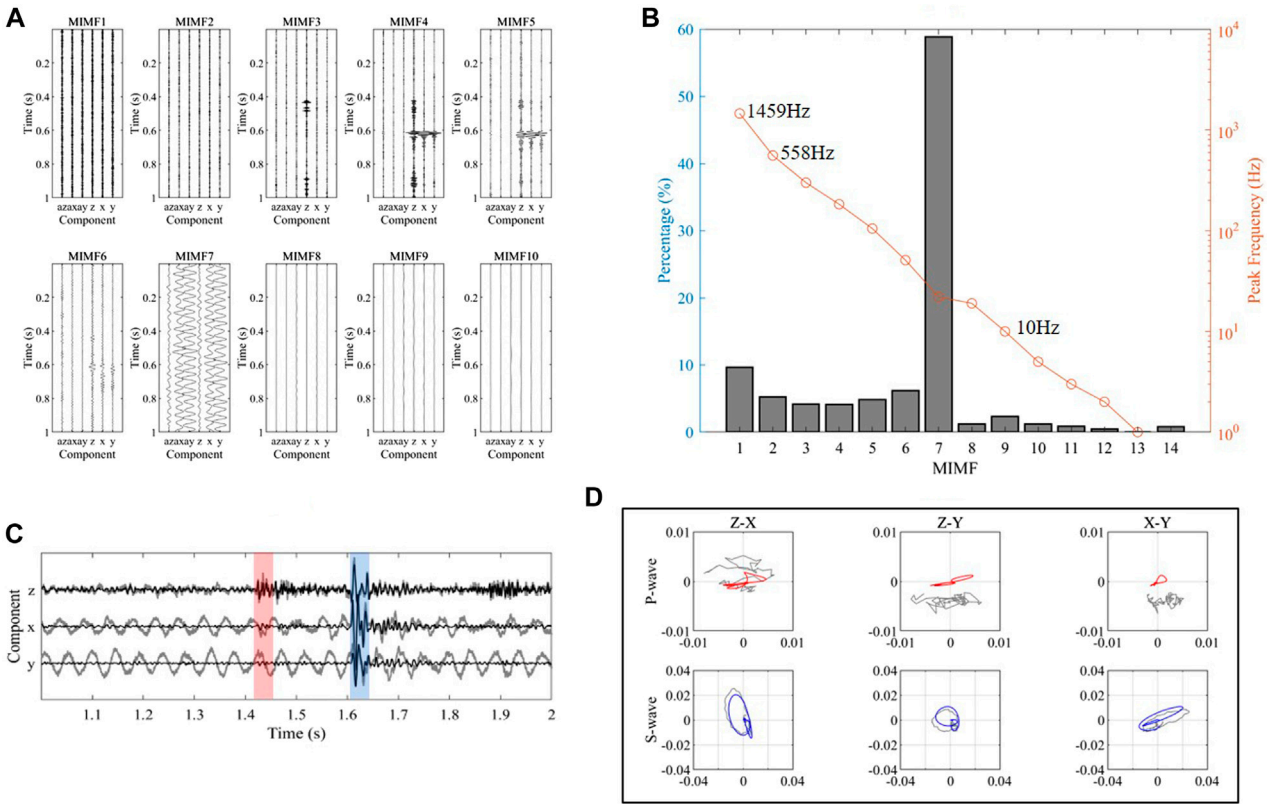

FIGURE 8
(A) Decomposition results of the recordings in Receiver No.1 by the ANA-MEMD method. **(B)** The energy percentages of the MIMFs in assisted channels and the peak frequencies of the MIMFs in noisy microseismic record channels. **(C)**. Comparison of the waveforms before (grey lines) and after (black lines) noise suppression by the proposed method. The P-wave and S-wave arrivals are denoted by the red box and blue box, respectively. **(D)** Comparison of P-wave and S-wave before and after noise suppression by the proposed method. Grey lines represent the raw waveforms. Red and blue lines represent P-wave and S-wave after noise suppression, respectively.

$$A = \begin{bmatrix} 2 & 1 & 3 \\ 1.5 & 2 & 1 \\ 3 & 1 & 2 \end{bmatrix} \quad (5)$$

The arrival time of seismic signal is 1.2s and the sampling frequency is 1000 Hz. Figure 4 shows the waveforms of the synthetic microseismic data.

In the process of three-component microseismic data, one 1-s long background noise recordings (0~1 s) before the seismic signals (1~2 s) were employed as extra assisted channels. Figure 5A illustrates the six MIMFs that decomposed by the ANA-MEMD method. Channels (az, ax, and ay) and (z, x, and y) in Figure 5B represent the MIMFs corresponding to the background noise recordings and noisy microseismic signals, respectively. Similar to the processing flow for the above single-component data. We calculated the energy percentage of each MIMF in the ambient noise assisted channels and the peak frequency of each MIMF in the noisy microseismic signal channels, as shown in Figure 5B. By determining MIMF related to the top two energy percentage (MIMF 4 and 5, cumulative percentage greater than 80%), the high frequency noise (MIMF1, the peak frequency >200 Hz), and the low frequency noise (MIMF 6, the peak frequency <10 Hz), the MIMFs that contains the ambient noise can be identified. The denoised microseismic record can be obtained by reconstructing the remaining MIMFs, as shown in Figure 5C. The arrivals of the seismic signals are obvious in the denoised waveform (black line in Figure 5C), and the linearity of the three-component seismic signal is significantly enhanced (as shown in red lines in Figure 5D).

Without loss of generality, the above test is repeated 50 times using synthetic three-component data with different S/Ns (1.9–5.5 dB) to verify the stability of the proposed method. To simulate varying S/Ns, we kept the amplitude of the background noise recordings and changed the amplitudes of the noise-free seismic signal. In addition, we also calculated the S/Ns and the linearities of the seismic signal before and after processing to quantitatively assess the method's performance. The S/N is calculated using the following equation [12]:

$$S/N = 20\log_{10}\left(\frac{A_{signal}}{A_{noise}}\right) \quad (6)$$

where A_{noise} and A_{signal} are the root-mean-square amplitudes of the signals before and after seismic arrivals, respectively. The linearity L for three component seismic data can calculated using the following quation,

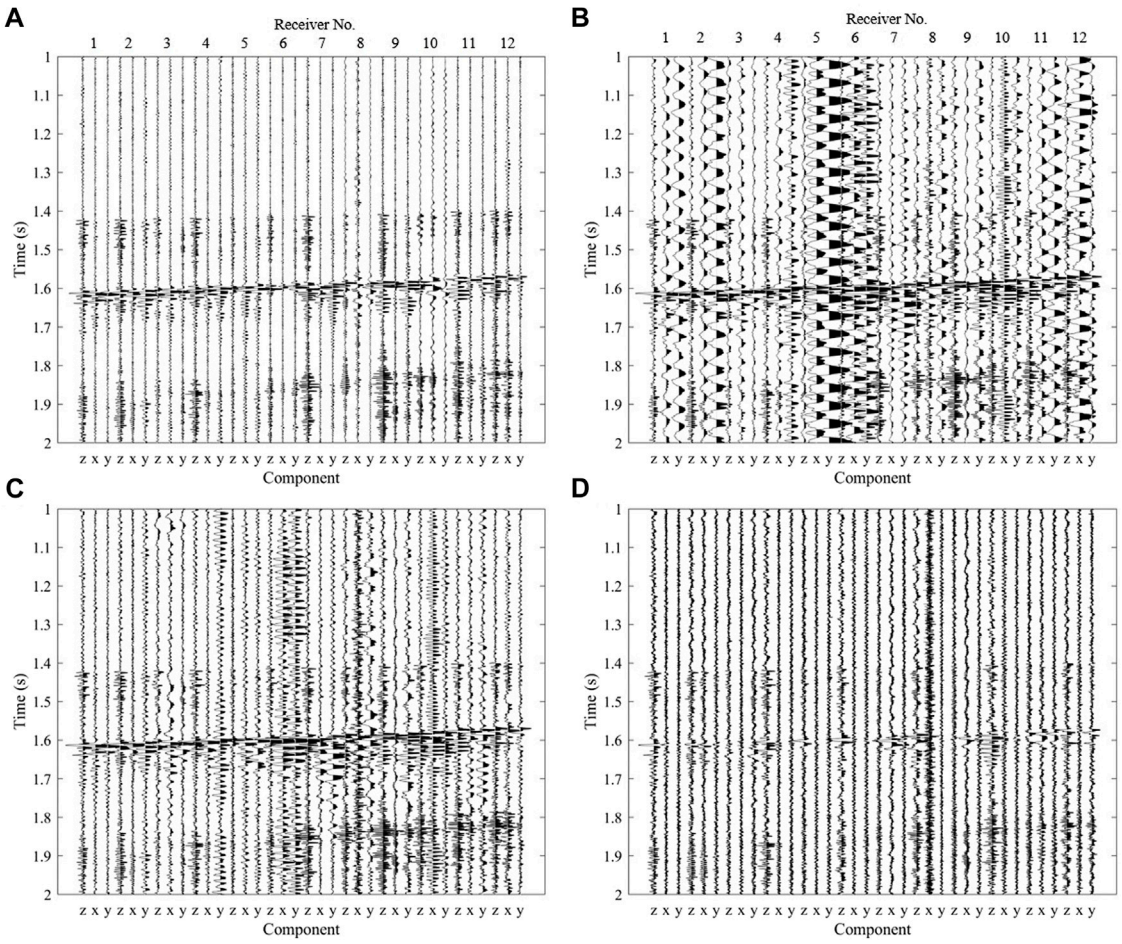

FIGURE 9
The microseismic signals after noise suppression using different methods. **(A)** The proposed method. **(B)** Band-pass filter method. **(C)** MEMD method with kurtosis criteria. **(D)** Multivariate wavelet denoising (MWD) method. The amplitude ranges of four microseismic waveforms subgraphs are the same.

$$L = \frac{(\lambda_1 - \lambda_2)^2 + (\lambda_2 - \lambda_3)^2 + (\lambda_1 - \lambda_3)^2}{2(\lambda_1 + \lambda_2 + \lambda_3)^2}. \quad (7)$$

Where $\lambda_1, \lambda_2, \lambda_3 (\lambda_1 > \lambda_2 > \lambda_3)$ are the eigenvalues of the convariance matrix for the three-component seismic signal. The S/Ns and the linearities of the microseismic signals before and after processing are shown in Figure 6. The S/Ns and the linearities of seismic signals in all tests increase using the proposed method demonstrate the effectiveness of this method for noise suppression reliability.

4 Field data application

In this section, we evaluated the performance of the proposed method using field microseismic data. The field data in this study come from a hydraulic fracturing surveillance job in a shale play in the Fulin gas field of China. A temporary array comprising 12 levels of triaxle 15 Hz geophones was placed in the inclined section (the inclination is about 40°) of a horizontal well adjacent to the treatment well and used for monitoring the stimulation. A total of 63 microseismic events were detected during a hydraulic fracturing stage. Figure 7 shows the 3-C waveforms of one Low-S/N microseismic event, in which the red and blue line represent the arrival times of P- and S-waves, respectively. It is evident that significant background noises obscure the microseismic signal, and the arrivals of direct P- and S-waves are masked by strong interference noise. Observed interferences are most likely due to pumping operations or pumping-fluid-wellbore interactions.

In this field data processing, we intercepted ambient noise recording with 1-s long time window (0~1s in Figure 7) before the microseismic signal (1~2s in Figure 7). The recordings in the shallowest receiver (Receiver No.1) were analyzed as an example. The multi-channel recordings are decomposed into 14 MIMFs, and their first ten MIMFs are shown in Figure 8A, with their frequencies decreasing sequentially. The seismic signal is divided into multiple MIMFs due to its wide frequency range. We calculated the energy proportion of each MIMF in the ambient noise assisted channels and the peak frequency of each MIMF in the noisy microseismic signal

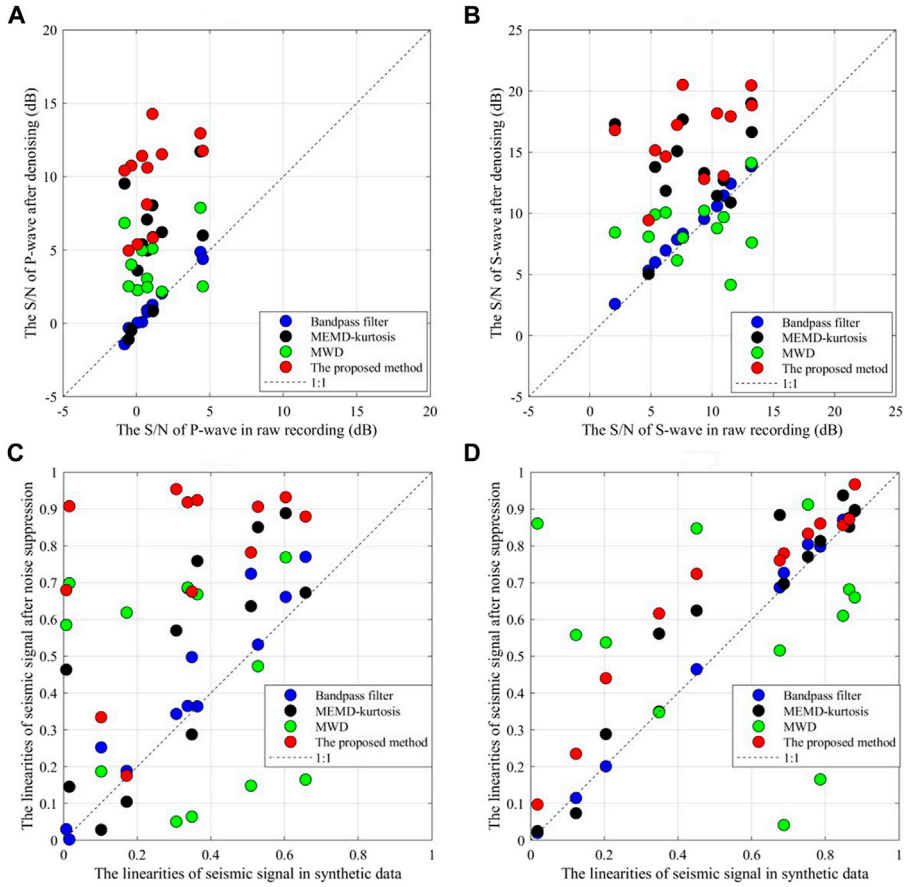

FIGURE 10
Comparison of S/Ns and the linearities of microseismic signals before and after noise suppression by the different methods. **(A)** the S/Ns of P-wave. **(B)** the S/Ns of S-wave. **(C)** the linearities of P-wave. **(D)** the linearities of S-wave.

channels, as shown in Figure 8B. The energy percentages of each MIMF shows that the energy of background noise accounts for about 60% of the total energy, demonstrating the necessity of removing these strong noises. By determining MIMF related to the top energy proportion (MIMF 7), the high frequency noise (MIMF1 and MIMF2, the peak frequencies >300 Hz), and the low frequency noise (MIMF 9–14, the peak frequencies <10 Hz), the MIMFs that contains the ambient noise can be identified. The denoised microseismic record can be obtained by reconstructing the remaining MIMFs, as shown in Figure 8C. The P-wave (denoted by the red box) and S-wave (denoted by the blue box) arrivals of the seismic signals are clearly visible in the denoised waveforms (black line in Figure 8C), and the linearities of the three-component microseismic signal are greatly improved, particularly in P-wave.

We have processed the microseismic recordings of all 12 receivers in Figure 7. Band-pass filter (10,300 Hz), traditional MEMD based method, and multivariate wavelet denoising (MWD) method were also used to process the field data for comparison. In the traditional MEMD method, we calculated the kurtosis value of each MIMFs, and the microseismic signal is regarded as existing if the threshold of the kurtosis value is surpassed (the threshold is set to 3). Figure 9 shows the results using these methods. The S/Ns and the linearities of the microseismic signals before and after processing are shown in Figure 10. Band-pass filter only removes high-frequency and partial low-frequency noise. There remain strong interferences in the denoised microseismic data. Part of the arrivals of P- wave and S-wave after MEMD method with kurtosis criteria are highlighted, there remain strong interferences in the several receiver recordings. It demonstrates that uniform kurtosis criteria are incapable of dealing with complicated and variable noise. The noise reduction effect on S-wave of MWD method is not obvious, which is also reflected in the S/Ns after denoising. Although the traditional MEMD method and MWD method can increase the S/Ns, they decrease the linearities of P-wave and S-wave, showing that the denoising result cannot effectively preserve the amplitude of the seismic signals. It can be seen that the proposed method performs better with the consideration of increasing the S/N and maintaining the microseismic signal adaptively.

We processed all 63 microseismic events using our method and compared the results with above three methods. For each event, we calculated the S/Ns and the linearities of P-wave and S-wave in different receivers and obtained the corresponding average values. Figure 11 displays the average values of the S/Ns and the linearities of P wave and S wave for all detected microseismic events before and after noise suppression by different methods. We can see that the proposed method can generally increase the S/Ns and the linearites

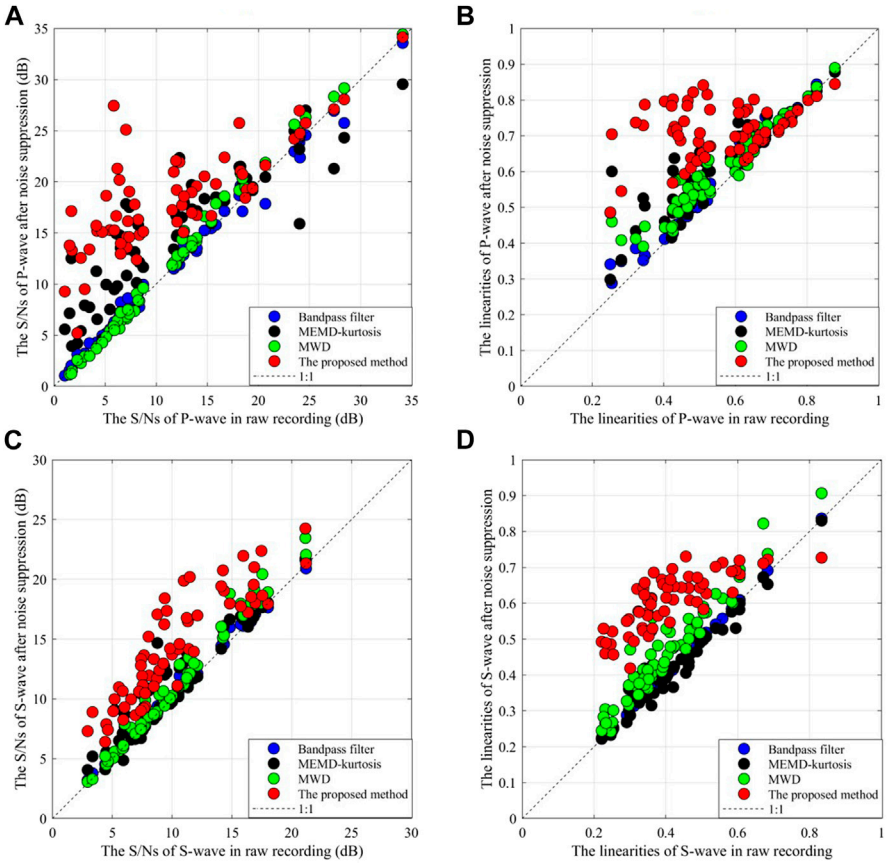

FIGURE 11
Comparison of the S/Ns and the linearities ofmicroseismic events before and after noise suppression by the different methods. **(A)** the S/Ns of P-wave for all events. **(B)** the linearities of P-wave for all events. **(C)** the S/Ns of S-wave for all events. **(D)** the linearities of S-wave for all events.

of the microseismic signals more robustly than the other methods, especially for the P-wave of low S/N microseismic events. It is worth noting that the results of the proposed method are not necessarily better than those of the other methods. This is because the proposed method may also retain part of the ambient noise while preserving as much the microseismic signal as possible. Nevertheless, the fact that the S/Ns of the majority of microseismic signals increase when using the proposed method demonstrate the effectiveness of this method for microseismic signal denoising.

5 Conclusion

In this study, we have developed an adaptive noise suppressing method based on ambient-noise-assisted multivariate empirical mode decomposition (ANA-MEMD) for microseismic data. Multivariate empirical mode decomposition (MEMD) is employed to decompose multichannel seismic recording into multivariate intrinsic mode functions (MIMFs). To address the problem of mode mixing, ambient noise is used as assisted channels. Additionally, the dominant noise can be removed by calculating energy percentage with the ambient noise in the assisted channels. We have applied the proposed method to synthetic data and field data. The decomposing results show that the proposed method can successfully separate and remove the strong background interference noises. In the comparison to the results of conventional filtering methods, the proposed method is demonstrated to be able to improve the S/Ns of the microseismic signals. Thus, it is favorable for microseismic signal denoising. We must emphasize that while this study tested the feasibility of the proposed method using microseismic data, this method can be applied straight forward to the active seismic data (i.e., artificial exploration seismic data) or any other multicomponent geophysical dataset that can be represented as time series.

Data availability statement

The raw data supporting the conclusions of this article will be made available by the authors, without undue reservation.

Author contributions

ZY developed the method and wrote the original draft. YT and CH revised the manuscript. All authors participated in designing this research work. All authors contributed to the article and approved the submitted version.

Funding

This work is supported by the Key-Area Research and Development Program of Guangdong Province (Grant No. 2021B0101310002), and Science and Technology Program of Shenzhen Science and Technology Innovation Commission (Grant No. JSGG20201102160200001), and the National Key R&D Program of China (No.2020YFB0204802), and the China Petroleum & Chemical Corporation Project (Grant No. 322083).

Acknowledgments

We would like to thank SINOPEC Geophysical Company, Shengli Branch for providing us the field data.

Conflict of interest

The authors declare that the research was conducted in the absence of any commercial or financial relationships that could be construed as a potential conflict of interest.

Publisher's note

All claims expressed in this article are solely those of the authors and do not necessarily represent those of their affiliated organizations, or those of the publisher, the editors and the reviewers. Any product that may be evaluated in this article, or claim that may be made by its manufacturer, is not guaranteed or endorsed by the publisher.

References

1. Maxwell S. *Microseismic imaging of hydraulic fracturing: Improved engineering of unconventional shale reservoirs*. Tulsa, OK: Society of Exploration Geophysicists (2014).

2. Eaton DW. *Passive seismic monitoring of induced seismicity: Fundamental principles and application to energy technologies*. Cambridge: Cambridge University Press (2018).

3. Li L, Tan J, Wood DA, Zhao Z, Becker D, Lyu Q, et al. A review of the current status of induced seismicity monitoring for hydraulic fracturing in unconventional tight oil and gas reservoirs. *Fuel* (2019) 242:195–210. doi:10.1016/j.fuel.2019.01.026

4. Westman E, Luxbacher K, Schafrik S. Passive seismic tomography for three-dimensional time-lapse imaging of mining-induced rock mass changes. *The Leading Edge* (2012) 31(3):338–45. doi:10.1190/1.3694902

5. Delplancke C, Fontbona J, Prado J. A scalable online algorithm for passive seismic tomography in underground mines. *Geophysics* (2020) 85(4):WA201–11. doi:10.1190/geo2019-0440.1

6. Foulger G. Geothermal exploration and reservoir monitoring using earthquakes and the passive seismic method. *Geothermics* (1982) 11(4):259–68. doi:10.1016/0375-6505(82)90032-3

7. Amoroso O, Festa G, Bruno PP, D'Auria L, De Landro G, Di Fiore V, et al. Integrated tomographic methods for seismic imaging and monitoring of volcanic caldera structures and geothermal areas. *J Appl Geophys* (2018) 156:16–30. doi:10.1016/j.jappgeo.2017.11.012

8. Verdon JP, Kendall JM, White DJ, Angus DA, Fisher QJ, Urbancic T. Passive seismic monitoring of carbon dioxide storage at Weyburn. *The Leading Edge* (2010) 29(2):200–6. doi:10.1190/1.3304825

9. Tary JB, Van der Baan M, Eaton DW. Interpretation of resonance frequencies recorded during hydraulic fracturing treatments. *J Geophys Res Solid Earth* (2014) 119(2):1295–315. doi:10.1002/2013JB010904

10. Vaezi Y, Van der Baan M. Interferometric assessment of clamping quality of borehole geophones. *Geophysics* (2015) 80(6):WC89–WC98. doi:10.1190/geo2015-0193.1

11. Harris D, Albaric J, Goertz-Allmann B, Kuehn D, Sikora S, Oye V. Interference suppression by adaptive cancellation in a high Arctic seismic experiment. *Geophysics* (2017) 82(4):V201–9. doi:10.1190/geo2016-0452.1

12. Tan Y, He C. Improved methods for detection and arrival picking of microseismic events with low signal-to-noise ratios. *Geophysics* (2016) 81(2):KS93–KS111. doi:10.1190/geo2015-0213.1

13. Huang W, Wang R, Li H, Chen Y. Unveiling the signals from extremely noisy microseismic data for high-resolution hydraulic fracturing monitoring. *Sci Rep* (2017) 7:11996. doi:10.1038/s41598-017-09711-2

14. Yu Z, Huang D, Tan Y, He C. Receiver orientation and event back-azimuth estimation for downhole microseismic monitoring using a probabilistic method based on P-wave polarization. *Front Earth Sci* (2023) 10:1027216. doi:10.3389/feart.2022.1027216

15. Akram J. An application of waveform denoising for microseismic data using polarization-linearity and time-frequency thresholding. *Geophys Prospecting* (2018) 66(5):872–93. doi:10.1111/1365-2478.12597

16. Zheng J, Lu JR, Jiang TQ, Liang Z. Microseismic event denoising via adaptive directional vector median filters. *Acta Geophysica* (2017) 65(1):47–54. doi:10.1007/s11600-017-0005-1

17. Li H, Wang R, Cao S, Chen Y, Huang W. A method for low-frequency noise suppression based on mathematical morphology in microseismic monitoring. *Geophysics* (2016) 81(3):V159–67. doi:10.1190/geo2015-0222.1

18. Lv H. Noise suppression of microseismic data based on a fast singular value decomposition algorithm. *J Appl Geophys* (2019) 170:103831. doi:10.1016/j.jappgeo.2019.103831

19. Zhang C, Shi Y, Liu J, Jiang S, Wang H, Wang Y. A denoising method of mine microseismic signal based on NAEEMD and frequency-constrained SVD. *The J Supercomputing* (2022) 78:17095–113. doi:10.1007/s11227-022-04554-9

20. Mousavi SM, Langston CA, Horton SP. Automatic microseismic denoising and onset detection using the synchrosqueezed continuous wavelet transform. *Geophysics* (2016) 81(4):V341–55. doi:10.1190/geo2015-0598.1

21. Mousavi SM, Langston CA. Automatic noise-removal/signal-removal based on general cross-validation thresholding in synchrosqueezed domain and its application on earthquake data. *Geophysics* (2017) 82(4):V211–27. doi:10.1190/geo2016-0433.1

22. Iqbal N, Liu E, McClellan JH, Al-Shuhail A, Kaka SI, Zerguine A. Detection and denoising of microseismic events using time-frequency representation and tensor decomposition. *IEEE access* (2018) 6:22993–3006. doi:10.1109/ACCESS.2018.2830975

23. Shao J, Wang Y, Yao Y, Wu S, Xue Q, Chang X. Simultaneous denoising of multicomponent microseismic data by joint sparse representation with dictionary learning. *Geophysics* (2019) 84(5):KS155–72. doi:10.1190/geo2018-0512.1

24. Li J, Li Y, Li Y, Qian Z. Downhole microseismic signal denoising via empirical wavelet transform and adaptive thresholding. *J Geophys Eng* (2018) 15(6):2469–80. doi:10.1088/1742-2140/aacf63

25. Huang NE, Shen Z, Long SR, Wu MC, Shih HH, Zheng Q, et al. The empirical mode decomposition and the Hilbert spectrum for nonlinear and non-stationary time series analysis. *Proc R Soc A Math Phys* (1998) 454:903–95. doi:10.1098/rspa.1998.0193

26. Barbosh M, Singh P, Sadhu A. Empirical mode decomposition and its variants: A review with applications in structural health monitoring. *Smart Mater Structures* (2020) 29(9):093001. doi:10.1088/1361-665X/aba539

27. Wu Z, Huang NE. Ensemble empirical mode decomposition: A noise-assisted data analysis method. *Adv adaptive Data Anal* (2009) 1(1):1–41. doi:10.1142/S1793536909000047

28. Yeh JR, Shieh JS, Huang NE. Complementary ensemble empirical mode decomposition: A novel noise enhanced data analysis method. *Adv adaptive Data Anal* (2010) 2(02):135–56. doi:10.1142/S1793536910000422

29. Torres ME, Colominas MA, Schlotthauer G, Flandrin P. A complete ensemble empirical mode decomposition with adaptive noise. In: 2011 IEEE international conference on acoustics, speech and signal processing (ICASSP); May 2011; Prague, Czech Republic. IEEE (2011). p. 4144–7.

30. Dragomiretskiy K, Zosso D. Variational mode decomposition. *IEEE Transactions Signal Processing* (2013) 62(3):531–44. doi:10.1109/TSP.2013.2288675

31. Li Y, Tang B, Jiao S. SO-Slope entropy coupled with svmd: A novel adaptive feature extraction method for ship-radiated noise. *Ocean Eng* (2023) 280:114677. doi:10.1016/j.oceaneng.2023.114677

32. Rehman N, Mandic DP. Multivariate empirical mode decomposition. *Proc R Soc A: Math Phys Eng Sci* (2010) 466(2117):1291–302. doi:10.1098/rspa.2009.0502

33. Rehman N, Park C, Huang NE, Mandic DP. EMD via MEMD: Multivariate noise-aided computation of standard EMD. *Adv adaptive Data Anal* (2013) 5(02):1350007. doi:10.1142/S1793536913500076

34. Rehman N, Aftab H. Multivariate variational mode decomposition. *IEEE Trans Signal Process* (2019) 67(23):6039–52. doi:10.1109/TSP.2019.2951223

35. Cao P, Wang H, Zhou K. Multichannel signal denoising using multivariate variational mode decomposition with subspace projection. *IEEE Access* (2020) 8: 74039–47. doi:10.1109/ACCESS.2020.2988552

36. Huang W, Zeng J, Wang Z, Liang J. Partial noise assisted multivariate EMD: An improved noise assisted method for multivariate signals decomposition. *Biomed Signal Process Control* (2017) 36:205–20. doi:10.1016/j.bspc.2017.04.003

37. Ge S, Shi YH, Wang RM, Wang RM, Lin P, Gao JF, et al. Sinusoidal signal assisted multivariate empirical mode decomposition for brain–computer interfaces. *IEEE J Biomed Health Inform* (2017) 22(5):1373–84. doi:10.1109/JBHI.2017.2775657

38. Wu Z, Zhang Q, Wang L, Cheng L, Zhou J. Early Fault detection method for rotating machinery based on harmonic-assisted multivariate empirical mode decomposition and transfer entropy. *Entropy* (2018) 20:873. doi:10.3390/e20110873

39. Kirbas I, Peker M. Signal detection based on empirical mode decomposition and Teager–Kaiser energy operator and its application to P and S wave arrival time detection in seismic signal analysis. *Neural Comput Appl* (2017) 28(10):3035–45. doi:10.1007/s00521-016-2333-5

40. Han J, van der Baan M. Microseismic and seismic denoising via ensemble empirical mode decomposition and adaptive thresholding. *Geophysics* (2015) 80(6): KS69–KS80. doi:10.1190/geo2014-0423.1

41. Li X, Dong L, Li B, Lei Y, Xu N. Microseismic signal denoising via empirical mode decomposition, compressed sensing, and soft-thresholding. *Appl Sci* (2020) 10:2191. doi:10.3390/app10062191

42. Chen Z, Wang P, Gui Z, Mao Q. Three-component microseismic data denoising based on Re-constrain variational mode decomposition. *Appl Sci* (2021) 11:10943. doi:10.3390/app112210943

43. Candra AD, Suryani PE. Application of multivariate empirical mode decomposition to noise reduction in seismic signal. *J Phys Conf Ser* (2019) 1204(1): 012004. doi:10.1088/1742-6596/1204/1/012004

44. Xiao L, Zhang Z, Gao J. Ground roll attenuation of multicomponent seismic data with the noise-assisted multivariate empirical mode decomposition (NA-MEMD) method. *Appl Sci* (2022) 12:2429. doi:10.3390/app12052429

Frontiers in Physics

Investigates complex questions in physics to understand the nature of the physical world

Addresses the biggest questions in physics, from macro to micro, and from theoretical to experimental and applied physics.

Discover the latest Research Topics

See more →

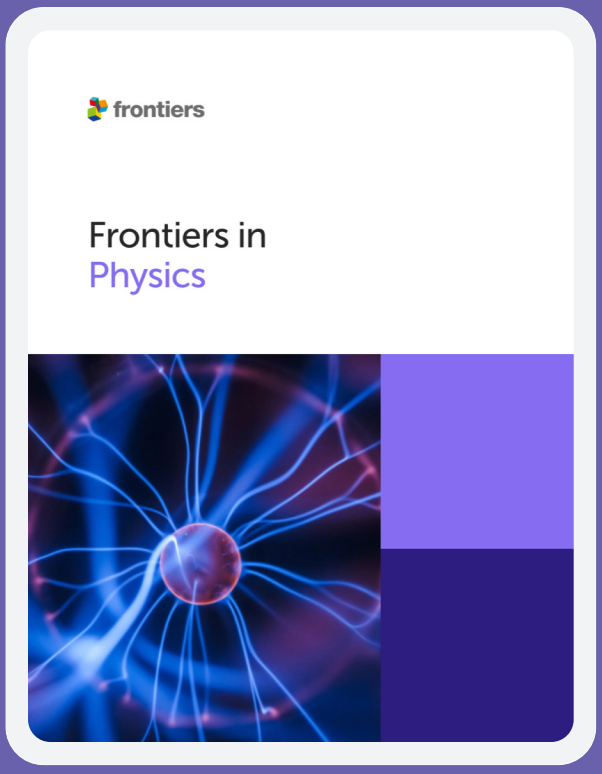

Frontiers

Avenue du Tribunal-Fédéral 34
1005 Lausanne, Switzerland
frontiersin.org

Contact us

+41 (0)21 510 17 00
frontiersin.org/about/contact